GEOCHEMICAL CHARACTERISTICS OF THE GOLD-BEARING QUARTZ VEINS IN THE LYKLING AREA, BØMLO, SW NORWAY

Frida Riple Forsberg

Master of Science thesis

Department of Earth Science
University of Bergen
August 2021

ABSTRACT

The Lower Ordovician ophiolitic terrane exposed in the Lykling area, on the island Bømlo, SW Norway, hosts numerous gold-bearing quartz veins. The mineralization shares many geologic features with the orogenic type of gold deposits.

The mineralization is hosted by the Lykling Ophiolite Complex and the associated trondhjemite intrusions. It is spatially associated with at least two generations of basaltic dikes that crosscuts both host lithologies. Considering their mineral assemblages, structural characteristics and spatial relationships with the host rocks, the veins can be subdivided into two types of mineralization: I) quartz-carbonate veins hosted by low-angle ductile shear zones and II) sulphide-rich quartz veins hosted by steeply dipping brittle faults. This study brings new mineralogical, geochemical, and stable isotope characteristics of the gold-bearing quartz veins, their host rocks and associated alteration products in the Lykling area. The study has also provided a better understanding of the ore-forming processes that resulted with deposition of gold in the study area.

The typical mineral assemblage of the ductile mineralization consists of carbonates (predominantly ankerite), quartz and hydrous silicates, mostly chlorite and epidote. The mineral assemblage indicates that hydrothermal fluids had a near-natural pH value, a high CO_2 fugacity and a low sulphur fugacity. The fluid inclusion study revealed boiling as a trigger for precipitation of gold from gold-bisulphide complexes.

The typical brittle mineralization consists of quartz and sulphides, predominantly pyrite and locally chalcopyrite. The mineral assemblage reflects a high sulphur fugacity. Fluid inclusions revealed mixing of a low temperature and low salinity fluid with higher temperature and moderate salinity fluids and consequent destabilisation of Au-chloride complexes as the trigger for precipitation of native gold and base-metal sulphides. Stabile isotope characteristics of the Lykling mineralization disclosed magmatic source of sulphur and CO_2 in both types of the mineralization.

Two theories are suggested for the timing of the ductile and brittle mineralization: (I) The ductile and brittle mineralization might be related to the change from compressional to extensional regime during the orogenic collapse following the Taconian Orogenes and the formation of the Siggjo Complex. (II) The ductile shear zone hosted mineralizations might be related to the compressional stage of the Caledonian Orogeny, whereas the brittle type of the

mineralization was formed during the extensional regime related to the Caledonian post-orogeny extension.

ACKNOWLEDGEMENT

This study has been supported by the EIT Raw Materials project “MinExTarget” (Grant agreement number 19217).

First, I would like to thank my thesis supervisors for support and guidance through these two years. Rolf Birger Pedersen, thank you for the opportunity to work with such an interesting project. Sabina Strmic Palinkas, thank you for great guidance and helpful feedback throughout this project. Håvard Hallås Stubseid, thank you for always being accessible for questions and giving good advice. It has been a pleasure to work with you all.

A special thank you to Ida Marie Gabrielsen and Andreas Viken for showing me how to correctly process my samples in the crushing lab and the thin section lab. Your advice and guidance have been much appreciated. I will also give a thanks to Siv Hjorth Dundas, Hildegunn Almelid and Yuval Ronen for sample preparations and analytical work.

A special word of gratitude to my partner Trond Fjellet for great help and company during field work and numerous discussions on and off topic during this period. I will also give a gracias to Matz Slotnes and Simen Saltvedt for two memorable field trips and for being great study partners. Ingvild Aarrestad, thank you for the helpful feedback on this thesis. Thank you everyone from the “black smoker” office for a fun time with laughter and coffee breaks when needed. I am thankful to all my fellow geology students at the University of Bergen for numerous social events and unforgettable field trips through these five years.

It has been a pleasure to study such an interesting area, that I have a personal attachment to. The time I have spent at Lykling as a child made this even more interesting and now, I have knowledge I will carry with me for the rest of my life. Finally, I would like to thank my family for the support during my studies.

Bergen, 29.08.21

Frida R. Forsberg

Frida Riple Forsberg

TABLE OF CONTENT

1 Introduction 1
2 Analytical methods 3
2.1 Field work 3
2.2 Petrography 3
Thin and thick section preparation 3
Optical microscopy 3
2.3 Lithogeochemical analyses 3
X-Ray fluorescence spectroscopy (XRF) 4
Inductively Coupled Plasma Mass Spectrometry (ICP-MS) 4
Inductively Coupled Plasma Atomic Emission Spectrometer (ICP-AES) 4
LA-ICP-MS analyses 5
Stable isotope 5
Ore grade 6
X-ray powder diffraction (XRD) 6
Chlorite thermometry 7
2.4 Fluid inclusion studies 7
Double polished thick sections 7
Fluid inclusion petrography and microthermometry 8
3 Regional geology 9
3.1 The Scandinavian Caledonides – SW Norway 9
Scandinavian Orogeny 9
The Caledonian nappes 9
The Caledonian extension 11
3.2 The ophiolitic terrane of SW Norway – Geology of Bømlo 13
3.3 Tectonic and magmatic evolution of the terrane in SW Norway 15
3.4 The Lykling area 17
4 Mining history 19
5 Theoretical background 20
5.1 Fluid inclusion studies in hydrothermal ore deposits 20
Introduction to fluid inclusion studies 20
Roedder's rules 21
Modification of fluid inclusion 22
Microthermometry 22
Fluid inclusions in hydrothermal deposits 26
5.2 Origin and characteristics of orogenic gold deposits 27
Ore Fluids 30
Hydrothermal alteration 32
5.3 Stable isotope systematics in hydrothermal ore deposits, with a focus to orogenic gold deposits 33
Stable isotopes 33
Stable isotopes in orogenic gold deposits 35
6 Results 37
6.1 Mineralogical characteristics of the Lykling gold mineralization 37
Gold mineralization hosted by brittle quartz veins 38

Mineralization hosted by ductile quartz-carbonate veins 43
6.2 Geochemical characteristics of the host rocks 46
Lykling Ophiolite gabbro 46
Trondhjemite 46
Mafic dikes 52
6.3 XRD analysis 60
6.4 Gold Assay 61
6.5 Fluid inclusion petrography and microthermometry 62
6.6 Stable isotope characteristics of the mineralization 66
6.7 Trace element composition of sulphide phases 69
6.8 Chlorite microthermometry 77
7 Discussion 79
7.1 Host rocks 79
7.2 Mafic dikes 79
7.3 The gold-bearing quartz veins 81
Quartz-carbonate veins hosted by ductile shear zones 81
Quartz-sulphide veins hosted by brittle fractures 82
7.4 Stable isotope characteristics of the Lykling mineralization 83
7.5 Ore-forming model 84
7.6 Similar systems 85
8 Conclusion 87
9 Further research 89
REFERENCES 90
Appendix 97

1 INTRODUCTION

The Lykling area, on the island of Bømlo, in Sunnhordland, SW Norway, host gold-bearing quartz veins. The gold mineralization was discovered in the 1860s. This finding initiated a gold rush followed by organized mining activities from 1883 till 1910. According to their mineralogical and structural features, the gold-bearing veins can be subdivided into two main types: (I) sulphide-rich quartz veins hosted by steeply dipping brittle faults and (II) quartz-carbonate veins hosted by low-angle ductile shear zones. Both types of veins are spatially associated with mafic dikes that crosscut the Lykling Ophiolite Complex and associated intruding trondhjemites. The host lithologies represent a part of the Upper Allochthone of the Scandinavian Caledonides (Fig. 1.1).

The gold-bearing quartz veins have formerly been described as a mesothermal (orogenic) mineralization precipitated from low saline fluids with variable CO_2-content (Christensen, 1994). Combining the findings of previous studies in the area with new geochemical data, this study will look further into the difference between the two types of quartz veins and compare them with orogenic gold deposits elsewhere. The general characteristics of orogenic gold deposits have been summarized by several authors including Groves et al. (1998), Goldfarb et al. (2001), Goldfarb & Groves (2015) and Gaboury (2019).

The primary goal of this study is to determine the mineralogical, geochemical, and stable isotope characteristics of the gold-bearing quartz veins, as well as their host rock and associated alteration products. This study combines field observations, reflected, and transmitted polarized light microscopy, scanning electron microscopy coupled with an energy dispersive system (SEM-EDS), lithogeochemistry, stable isotopes analyses ($\delta^{13}C$, $\delta^{18}O$, $\delta^{34}S$) and fluid inclusion analysis. In addition, laser ablation inductively coupled plasma mass spectrometry (LA-ICP-MS) is applied to identify gold and trace elements in sulphide phases, and chlorite thermometry is employed with an aim to determine the temperature of the ore-forming process.

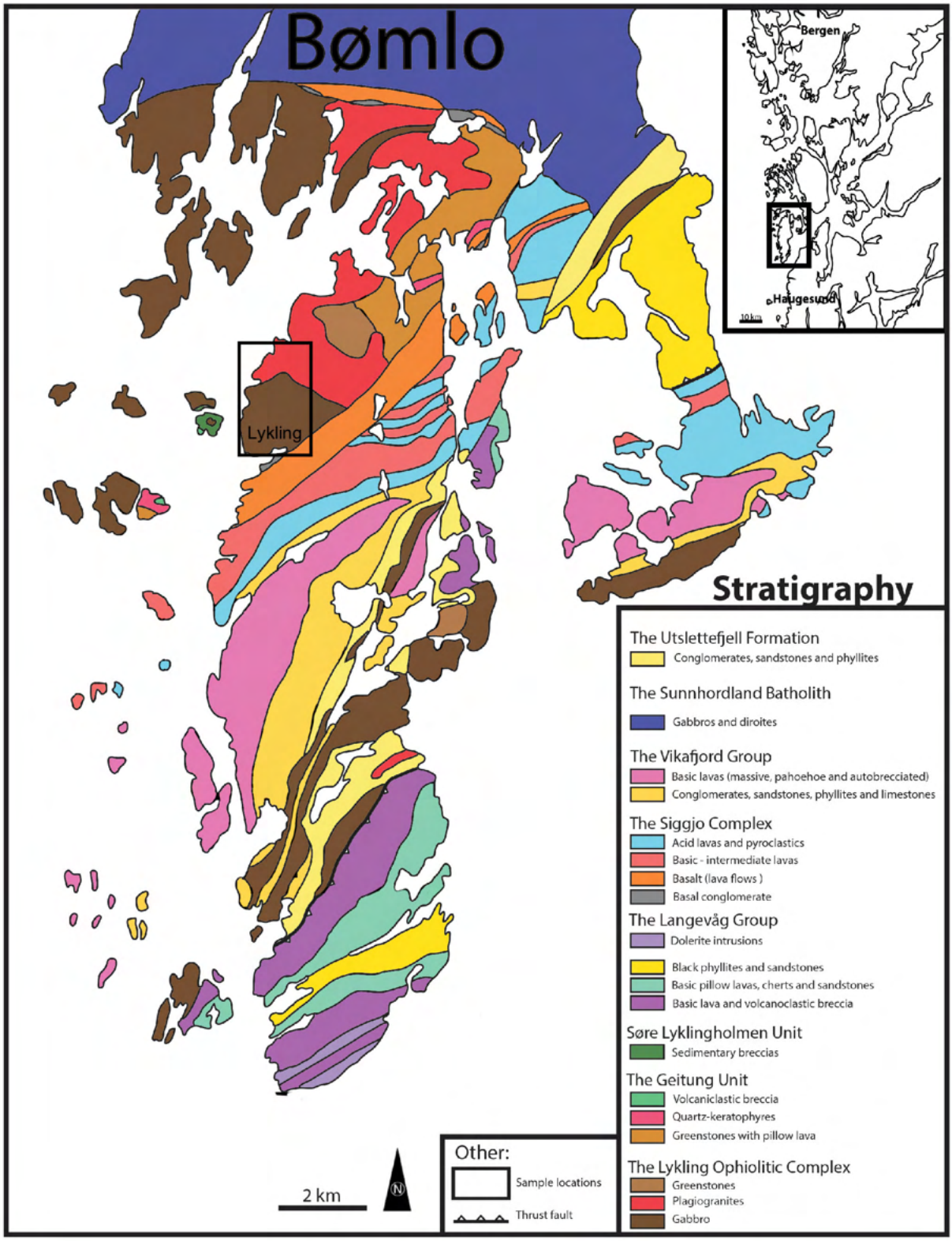

Figure 1.1 *Geological map of the island of Bømlo with the study area marked in a black box (Modified by Viken, 2017).*

2 ANALYTICAL METHODS

2.1 Field work

The field work was conducted in the Lykling area on the island of Bømlo. A preliminary set of samples was collected during a one-day excursion in August 2019. A detailed sampling campaign was conducted during a three-weeks fieldwork during the summer of 2020. In total, 40 samples were collected at 24 localities for further analyses. Appendix A gives an overview of the collected samples, the sampling positions and the analysis that have been carried out.

2.2 Petrography

Thin and thick section preparation

Rock samples were cut with a saw into blocks of suitable sizes that fit onto a microscopy glass slide. The sample blocks were impregnated with epoxy to secure fractures from breaking in following steps. After being impregnated, the samples blocks were glued with epoxy to glass slides. An Isomet 500 Linear precision saw was used to cut the sample thinner before grinding them by the Grinding Robot (Artech AS) to 400 µm for thick sections and 30 µm for thin sections. After grinding the samples to a suitable thickness, the thin and thick section were polished to 1 µm using Struers Tegramin-30 polishing machine. In total, eight thin and seventeen thick sections were prepared.

Optical microscopy

Petrographic observations were obtained on polished thin and thick sections, using an optical microscope at the Department of Geoscience, University of Bergen (UiB). Transparent minerals were studied using transmitted light microscopy, whereas opaque minerals were identified using reflected light microscopy. The optical microscope (Nikon eclipse LV100POL) is equipped with a microscope camera (Nikon DS -F/3) for taking photomicrographs of textures and minerals phases in the thin and thick section. An Epson Perfection V370 Photo scanner were used to scan photos of the thin and thick sections using the computer program EPSON Scan.

2.3 Lithogeochemical analyses

For lithogeochemical analyses the samples were crushed and milled to fine powder. The samples were first crushed with a hammer down to a grain size of approximately 2 mm, afterwards a portion of the crushed samples were milled to fine powder in an agate ball mill. In

the next step, the samples were ignited at 1000°C for two hours in a lab furnace to remove volatiles and organic components. Based on the weight difference after ignition the loss on ignition (L.O.I, wt.%) was calculated. After calculating the L.O.I.% the samples were handed to the geochemical lab of the Department of Geoscience at UiB for lithogeochemistry. The lithogeochemistry analyses is a combination of X-Ray Fluorescence (XRF) spectroscopy, Inductively Coupled Plasma Mass Spectrometry (ICP-MS) and Inductively Coupled Plasma Atomic Emission Spectrometer (ICP-AES).

X-Ray fluorescence spectroscopy (XRF)

Glass tablets were prepared for XRF analyses. For each tablet, 6.72 grams of lithium tetraborate ($Li_2B_4O_7$), a flux agent, was mixed with 0.96 grams of the finely crushed rock sample powder. The mixture of the flux agent and sample powder makes a homogenous solid solution when heated. A fusion furnance (Claisse, model Fluxy) was used to melt the mixture at approximately 1000°C for 30 minutes to produce the glass tablets used for analysis. The tablets were then inserted into a S4 PIONEER X-ray fluorescence spectrometer that measures the concentration of the major element Si. The standard used for the analysis was USGS CRM BCR-2 (Colombia River Basalt).

Inductively Coupled Plasma Mass Spectrometry (ICP-MS)

Beforehand, 0.1 g of each sample was weighed precisely in 25ml PFA Savillex beakers and dissolved in 3 ml concentrated hydrofluoric acid (HF). The compound was then heated for approximately 48 hours until all the acid evaporated to avoid fluoride formation and for the compound to be converted into a solvable nitrate. Continued, the nitrate was dissolved and diluted with 2% w/v HNO_3 into a suitable level for the Element XR (Thermo Scientific) Inductively Coupled Plasma Mass Spectrometer (ICP-MS) instrument that was used for the analyses. The results gave the concentrations of the elements (Li, Sc, Ti, V, Cr, Mn, Co, Ni, Cu, Zn, Rb, Sr, Y, Zr, Nb, Cs, Ba, Hf, Ta, Pb, Th and U) and Rare Earth Elements (REE). BCR2 (basalt, Columbia River) was used as a standard reference, and between each sample the synthetic seawater CRM SPS-SW2 was analysed to control the calibration curve and monitoring the performance of the instrument.

Inductively Coupled Plasma Atomic Emission Spectrometer (ICP-AES)

Similar as the ICP-MS method, 0.1 g of each sample was weighed precisely in 25 ml PFA Savillex beakers and dissolved in 3 ml concentrated hydrofluoric acid (HF). The compound was then heated for approximately 48 hours until all the acid evaporated, and the compound became a solvable nitrate. Continued, the nitrate was dissolved and diluted with 2% w/v HNO_3

into a suitable concentration. The Thermo Scientific ICap 7600 Inductively Coupled Plasma Atomic Emission Spectrometer (ICP-AES) instrument was used to measure the concentration of a series of major and trace elements (Al, B, Ba, Ca, Co, Cr, Cu, Fe, K, Li, Mg, Na Mn, Ni, P, Pb, S, Sr, Ti, V, Y, Zn, Zr). BCR2 (basalt, Columbia River) was used as a standard reference, and in-between the samples the synthetic seawater CRM SPS-SW2 was analysed to control the calibration curve and monitoring the performance of the instrument.

LA-ICP-MS analyses

Thick sections were sent to the Raw Materials Characterization Laboratory at Trinity Collage Dublin, Ireland, for LA-ICP-MS spot analyses and high-resolution trace element mapping of sulphide phases. A Photon Machines Excite 193 nm eximeter Ar-F laser system with Helex 2-volume ablation cell and He-Ar carrier gas (ca.0.8 1/min He and 0.7 1/min Ar) was used. The mass spectrometer used was a quadrupole Thermo iCapQc. The instrument was tuned with scans on UQAC FeS-1 and USGS MASS1 as reference materials at the beginning of each analytical session.

Stable isotope

Stable isotope analyses ($\delta^{13}C$, $\delta^{18}O$ and $\delta^{34}S$) were carried out on carbonate and sulphide mineral phases. Before analysing them, powders from carbonates and sulphides were drilled out with a DREMEL driller equipped with the bits: Dremel Diamond Wheel Point 7105 and 7144. The powder was collected and put in small glass containers at the Department of Geoscience, UiB. Between every sample the drill was cleaned using first water and dried of with paper. Then the drill bit was dipped in 10% hydrochloric acid (HCl). HCl reacts with any residual carbonate forming water, carbon dioxide, and calcium chloride:

$$(CaCO_3(s) + 2HCl(aq) \rightarrow H_2O(l) + CO_2(g) + CaCl_2(aq))$$

The drill was then cleaned again with water and dried with paper to remove residues of the HCl. The stable isotope analyses on carbon ($\delta^{13}C$), oxygen ($\delta^{18}O$) and sulphur ($\delta^{34}S$) were conducted at the Stable Isotope Laboratory at the Institute of Earth Surface Dynamics (University of Lausanne) in Switzerland. Measurements were carried out with an automated Thermo/Finnigan online preparation device Gas Bench II connected to an isotope ratio mass spectrometer (IRMS) using a continuous flow mode (Révész & Landwehr, 2002). Borosilicate sample bottles were washed in diluted acid, then twice in deionized water and overnight dried at 70°C. The powder samples (~250µg) were added to the vials in air, and air was removed from the sample vials by automatic autosampler-assisted flushing with He, using He flow of 100 ml/min for 5 minutes. The phosphoric acid, which is maintained at the reaction temperature (70°C for calcite and

90°C for Fe-carbonates and dolomite) was added dropwise under computer control to each individual reaction vessel. The reaction time was 60 minutes. Both the amount of the acid and the reaction time were controlled by the software. 16 Data was extracted to an EXCEL file by using the ISODAT NT EXCEL export utility and further calculation steps were carried out using a predefined EXCEL Worksheet. A linearity correction was applied based on the relationships between the intensity of the first sample peak (m/z 44) and $\delta^{18}O$ value of the standards. The stable carbon and oxygen isotope ratios are reported in the delta (δ) notation as per mil (‰) deviation relative to the Vienna Standard Mean Ocean Water (V-SMOW) for oxygen and Vienna Pee Dee Belemnite (V-PDB) for carbon. The analytical reproducibility was better than ±0.05‰ for δ 13C and ±0.1‰ for δ 18O. Sulfur isotope analyses were carried out at performed at the Stable isotope laboratory of Institute of Earth Surface Dynamics, University of Lausanne, Switzerland. Measurements were performed by on-line EA-IRMS system consisting of a Carlo Erba 1108 elemental analyzer (EA) coupled with a continuous helium flow interface to the Thermoquest/Finnigan Mat Delta S IRMS. The EA oxidizes all sample compounds under a stream of helium and oxygen by flash combustion in a single oxidation-reduction quartz tube filled with oxidizing (tungsten trioxide) and reducing (elemental copper) agents at 1030°C. Water was removed using anhydrous magnesium perchlorate, and the gases enter a chromatographic column (Poropak QS) for separation of SO_2 which is isotopically analyzed by IRMS (Giesemann et al., 1994). The sulfur isotope values are reported in the typical δ−notation relative to V-CDT standard. The reproducibility, assessed by replicate analyses of the laboratory standard (natural pyrite, +6.1 ‰, synthetic mercury sulfide, +15.5 ‰, barium sulfate, +12.5 ‰ δ 34S) was better than 0.2 ‰.

Ore grade

Twelve samples were sent to Bureau Veritas Minerals in Canada for precious mineral Fire Assay Au (method FA330-Au). The lower detection limit for the instrument is 2 ppb, and the upper limit is 10 ppm. For samples with Au >10 ppm a gravimetric method was applied (method FA530-Au).

X-ray powder diffraction (XRD)

Three samples were selected for X-ray powder diffraction (XRD) and firstly crushed and milled to a fine powder. XRD was conducted on the D8 ADVANCE ECO X-Ray Diffraction Scanner at the Department of Geoscience (UiB). The machine is a 1 kW copper X-Ray tube diffractometer and is used for mineral detection and quantification. Diffraction patterns were

documented by step scanning from 3-90° 2θ. After being scanned, the compounds were identified using a computer program with the reference database DIFFRAC.EVA.

Chlorite thermometry

Four thick sections containing chlorite were analysed using SEM-EDS at the Department of Geoscience in the University of Tromsø (UiT). From SEM-EDS measurement of chlorite, chlorite thermometry was conducted. The values were recalculated based on 28 oxygens and with Fe^{2+}/Fe^{3+} and OH calculated assuming full site occupancy. Temperatures were calculated using Cathelineau (1988) and Jowett (2021). The method is based on work from Cathelineau (1988) with modifications from Kranidiotis & MacLean, (1987). The full calculation and temperatures are presented in Appendix F.

2.4 Fluid inclusion studies

Double polished thick sections

Preparation of double polished thick sections were prepared at the Department of Geoscience, UiB. Seventeen samples were prepared with this method at the thin section lab. The procedure started with cutting the selected rock samples with a saw into suitable sizes to fit onto a glass slide. Next, each sample was grinded and polished on one side by hand, starting with a coarse diamond grinding surface to smooth out the surface for approximately 5-10 min. The samples were then polished progressively from 15 μm to 9 μm, then to 6 μm and finally at 1 μm to ensure the best polished result. All the samples contained quartz and because of the quartz hardness all samples were grinded and polished for approximately a total of 25-30 min. In between polishing a microscope with reflected light was used to determine if the sample was ready for the next step. Next step was mounting the polished sample side down to glass slides using superglue. Superglue or crystal balm is used because it can be dissolved, and the sample can be removed from the glass at a later step. After gluing the samples to glass slides, the samples were sawed down to 2mm with a Isomet 500 Linear precision saw. Afterwards, the samples were grinded and polished on the other side, using the Grinding Robot (Artech AS) down to 0.05mm – 0.3mm thickness. After being grinded down to an exactable thickness the samples were polished with 1 μm, using a polishing machine. It is also possible to do the grinding and polishing by hand, repeating the grinding and polishing step. Lastly, the samples were put in acetone to dissolve the glue, removing the sample from the glass.

Fluid inclusion petrography and microthermometry

Out of the seventeen thick sections prepared eleven was selected to be analysed by petrographic and microthermometric measurements of fluid inclusions. This was executed at the Department of Geoscience of UiT. Prior to the microthermometry, selected fluid inclusions assemblage (FIA) was identified and mapped by petrography. FIA is defined as a group of inclusions trapped simultaneously from the same fluid. If every fluid inclusion in an assemblage displays similar homogenization temperature, the inclusions is assumed to have been trapped at the same time from the same fluid. The microthermometric measurements were preformed using the temperature and environmental controlling Linkam THMS 600 stages, mounted on an Olympus BX 2 microscope using the objectives 10x and 50x. To calibrate the apparatus two synthetic fluid inclusion standards, SYN FLINC: pure H_2O and mixed H_2O-CO_2, were used. The precision for the acquired homogenization temperature was ±2.0 ºC and ±2.0 ºC for the temperature range between -60 ºC and +10 ºC. During microthermometric measurement the eutectic temperature (T_e), last melting temperature of ice ($T_{m\ ice}$) and the total homogenization temperature (T_h) was measured. Later, the salinity (w%, NaCl eq), density (g/cm^3) and dP/dT were calculated using the Steele-MacInnis et al. (2012) Microsoft Excel spreadsheet for interpreting microthermometric data from fluid inclusions based on the PVTX properties of H_2O-NaCl (Atkinson, 2002; Bodnar, 1983; Bodnar, 1993; Bodnar & Vityk, 1994)

3 REGIONAL GEOLOGY

3.1 The Scandinavian Caledonides – SW Norway

The Scandinavian Caledonides are a deeply eroded orogenic belt that stretches from the Stavanger region in southern Norway to the Barents Sea of the northern coast of Norway for about 1500 km and a width of 200 to 300 km (Corfu, et al., 2014; Hossack & Cooper, 1986; Gee, 1975). The development of the geology in SW Norway is very complex involving a series of tectonic events and numerous thrust sheets of various composition with diverse and wide-ranging metamorphic grade (Roberts, 2003).

Scandinavian Orogeny

Before the Scandinavian Orogeny initiated, Baltica drifted away from Laurentia during late Proterozoic, and the development of the Iapetus Ocean commenced (Corfu, et al., 2014). In late Cambrian (541-485Ma), Baltica and Laurentia started contracting closing the Iapetus Ocean, resulting in an oblique collision and subduction of Baltica underneath Laurentia in Late Silurian (443-419Ma) to Early Devonian (419-358Ma) (Roberts, 2003). During the collision of the tectonic plates, the continental crust of Baltica was subducted, and the slab was metamorphosed at depths of 65-80 km to eclogites (Griffin & Brueckner, 1980; Krogh, 1977). Fossen (1992) subdivides the Caledonian framework in South Norway into three tectonic units: (I) the Baltic Shield (Precambrian basement), (II) décollement zone, and (III) an overlying orogenic wedge of mostly far-travelled nappes. The unconformably overlying sediments on the Baltic Shield formed mechanically weak phyllites and phyllonites creating a basal detachment fault, enabling the Caledonian nappes to thrust above the décollement zone (Fossen, 1992).

The Caledonian nappes

The Caledonian nappes are divided into five tectonostratigraphic units; The Autochthon-Parautochthon, Lower, Middle, Upper and Uppermost Allochthon (Fig. 3.1; Roberts & Gee, 1985). The **Autochthon-Parautochthon** consist of Archean to Proterozoic rocks that constitute the Baltic Shield, unconformably overlain by a thin Neoproterozoic to Paleozoic sedimentary cover (Corfu et al., 2014). The **Lower Allochthons** consist primarily of Neoproterozoic to Ordovician low-grade sedimentary rocks (Stephens, 1988; Andersen & Andresen, 1994; Fossen & Hurich, 2005). The **Middle Allochthon** is dominated by crystalline Proterozoic gneiss complexes and late Proterozoic psammitic rocks (Andersen & Andresen, 1994). The upper part of the Middle Allochthon is intruded by rift-related metamorphosed diabase dikes (Hollocher,

et al., 2007; Solyom, 1979; Stephens & Gee, 1989). The **Upper Allochthon** consist of exotic nappes of outboard ophiolitic terrain, magmatic arcs, and marginal basins from unknown sources within or peripheral to the Iapetus Ocean (Gale & Roberts, 1974; Stephens & Gee, 1989; Stephens & Gee, 1985; Pedersen, et al., 1988; Pedersen & Furnes, 1991; Grenne, et al., 1999; Roberts, 2003). The unit display significant evidence of extensive igneous activity and is the most heterogeneous and complex tectonic allochthon (Stephens & Gee, 1985; Roberts & Gee, 1985). Pedersen et al. (1988) suggest that the ophiolite formation occurred close to the Laurentian margin and was first accreted westward onto the Laurentian margin during Ordovician. Later during late Ordovician early Silurian, the margin was emplaced eastward onto the Baltoscandian margin. Evidence supporting this model is faunal data and zircon provenance dating of S-type granites in SW Norway (Pedersen, et al., 1992; Pedersen & Dunning, 1997). The ophiolitic terrane of SW Norway is situated in the Upper Allochthon and is the predominating Allochthon in this thesis. The **Uppermost Allochthon** is dominated mainly by gneisses and migmatites, and has a range of psammitic, pelitic and calcareous schists (Stephens & Gee, 1985). Based on structural observations, stable isotope analysis and radiometric dating, the Upper Allochthon likely formed in a continental margin setting with Laurentian ancestry (Roberts, 2003 & references within).

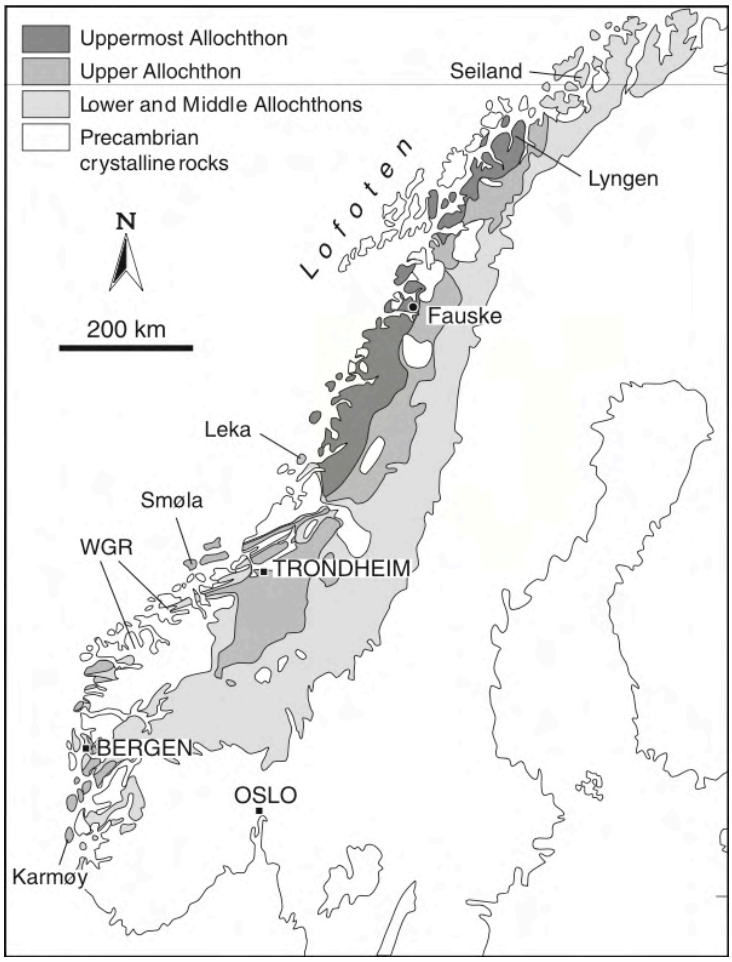

Figure 3.1 *Simplified tectonic map of the Scandinavian Caledonides (Roberts, 2003).*

The Caledonian extension

In Early Devonian, the convergent continent-continent collision shifted to a divergent movement (Fossen, 1992; 2000; Fossen & Hurich, 2005; Wilks & Cuthbert 1994; Rey & Casey, 1997). The shift in movement caused deformation. Fossen (1992) divides the extensional event into two modes of deformation. **Mode I** is represented by a backsliding low-angled extensional detachment in the basal Caledonian décollement zone (Fossen, 2000; Fossen & Hurich, 2005). The reactivated décollement zone transported the allochthons towards the northwest (Fossen, 1992). Further extension led to the second deformation mode (**Mode II**). The crust collapsed, which generated several kilometres of extensional oblique shear zone displacements (Fig. 3.2; Fossen, 2000). The transformation from Mode I to Mode II is the result of the strong contrast between the weaker decollement zone and the much stronger Proterozoic basement rocks. Most likely also contributing was the expulsion of fluids released due to metamorphic reactions within the decollement zone (Fossen et al., 2017). Ar/Ar ages of micas from the decollement zone suggest that the deformation changed between 408 and 402 Ma through (Fossen & Dunlap, 1998; Fossen et al., 2017). **The Hardanger Shear Zone** (HSZ) represent an example of the

Mode II deformation (Fossen, 1992). Located the foot side of the HSZ is the Precambrian basement, while the Caledonian nappes is located on the hanging wall (Fig. 3.2; Fossen & Hurich, 2005). Hardangerfjorden is a product of the HSZ and mouths out in Bømlafjorden close to the island Bømlo.

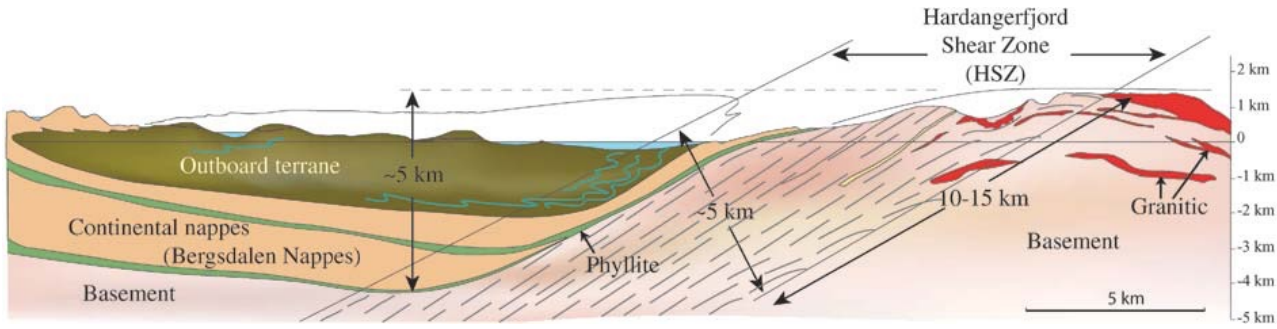

Figure 3.2 *Profile across the Hardangerfjord Shear Zone, with the Precambrian basement on the foot side and the continental nappes and outboard located on the hanging wall (Fossen & Hurich, 2005).*

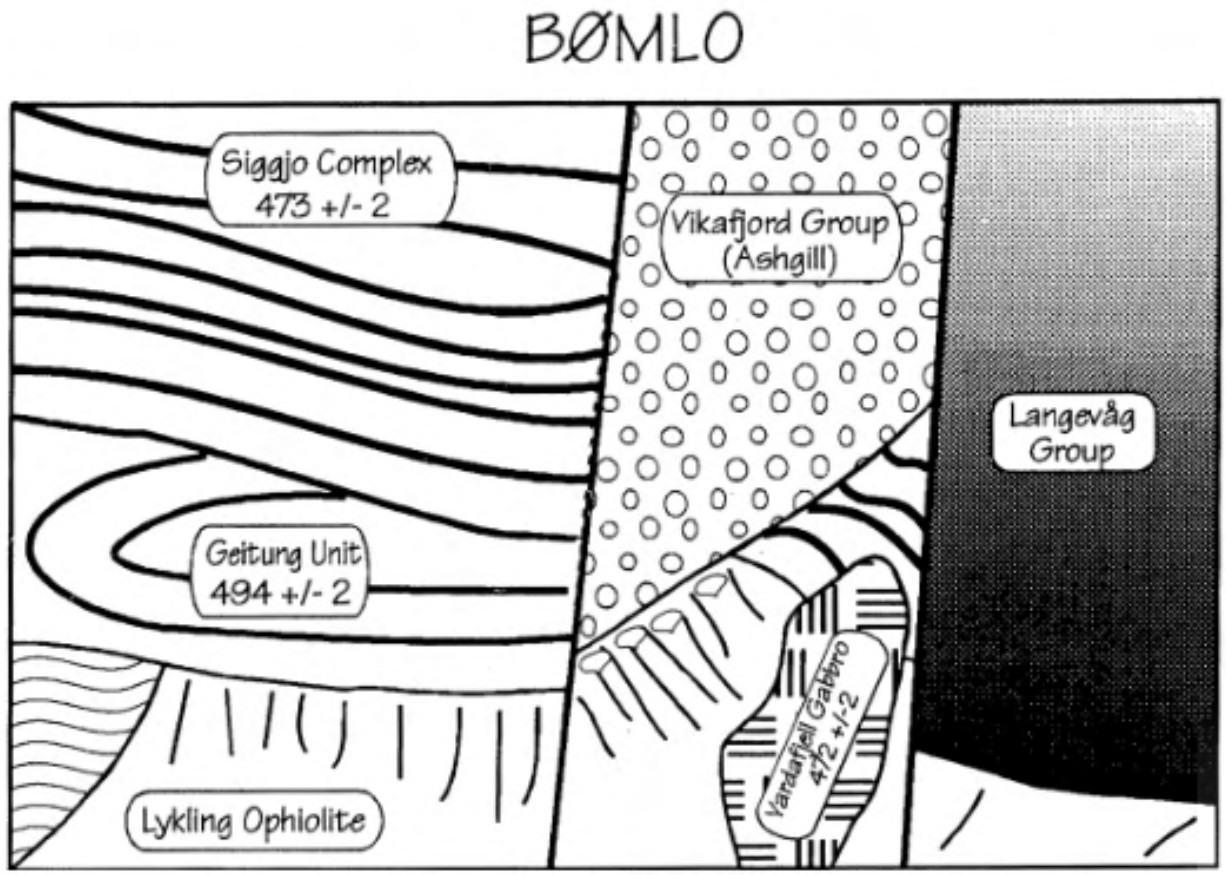

Figure 3.3 *Summary illustration of the geology of the Bømlo area with radiometric ages (Dunning & Pedersen, 1988; Pedersen & Dunning, 1997).*

3.2 The ophiolitic terrane of SW Norway – Geology of Bømlo

The ophiolitic terrane of SW Norway is visible along the coastline and fjords between Bergen and Stavanger and covers roughly 4000 km^2 (Pedersen & Dunning, 1997). This is where the study area is located, on the island Bømlo. The terrane is constituted by different ophiolite complexes, granitic complexes, island-arc sequences, and sedimentary units of varied ages and make up a large part of the Upper Allochthon (Pedersen et al., 1988; Pedersen & Dunning, 1997). Several of the ophiolite complexes in SW Norway show geochemical signatures of subduction zone magmatism with structures of ensimatic crust and are thought to have formed by divergent plate tectonics above a subduction zone (Pedersen & Dunning, 1997). In addition, some of the ophiolites display structures of island arc to near island arc origin (Pedersen & Dunning, 1997). The most prominent and best-preserved ophiolites of SW Norway is the Gullfjellet Ophiolite Complex and the Karmøy Ophiolite Complex and has been dated to 489 ± 3 Ma and 493 +7/-4 Ma by U/Pb (Dunning and Pedersen, 1988).

The rocks on Bømlo are subdivided into several lithostratigraphic units: The Lykling Ophiolite Complex, Geitung Unit, Søre Lyklingholmen Unit, Langevåg Group, Siggjo Complex, Vikafjord Group, and the Sunnhordland Batholith (Fig. 3.3, Brekke et al., 1984). The Early Ordovician **Lykling Ophiolite Complex** represents the oldest portion of the Upper Allochthone (Brekke et al., 1984). This ophiolite preserves an almost complete ophiolitic pseudostratigraphy (Nordås, 1985). Unconformably overlaying the Lykling Ophiolite is the **Geitung Unit** (Fig. 3.3), composed of a mixture of extrusive volcanic and sediments formed as a part of an immature island arc sequence (Brekke et al., 1984; Pedersen & Dunning, 1997). Parts of the Geitung Unit can be observed at the island Geitung just outside of Lykling (Fig. 1.1). The unit is dated to 494 ± 2 Ma with U-Pb and has a similar age to the tholeiitic rocks in the Karmøy ophiolite, dated to 493 +7/-5 Ma (Pedersen & Dunning 1997). The rocks in the Geitung Unit extents from basaltic to dacitic composition and is characterized by negative Nb and Ta anomalies (Pedersen & Dunning, 1997). Trace element studies done on this unit match the characteristics of immature island arc basalts (Pedersen & Dunning, 1997). The Lykling Ophiolite and the Geitung Unit is intruded by a voluminous amount of trondhjemite and tonalite (Nordås, 1985). The contact between the intruding trondhjemite and the Lykling Ophiolite can be observed north in the Lykling area (Fig. 1.1). **Søre Lyklingholmen Unit** overlies the Lykling Ophiolite and the Geitung Unit unconformably (Fig. 1.1). The unit consists of coarse, unsorted sedimentary breccias that are assumed to have been deposited at an escarpment along an old ocean fracture zone (Brekke et al., 1984; Amaliksen & Sturt, 1986). On southernmost Bømlo,

the **Langevåg Group** crops out (Fig. 1.1). The formation resulted from a progressive deepening of the back-arc marine basin and contains subaerial tuff-breccias, lavas, radiolarian chert, submarine volcaniclastic subaqueous debris flow, felspathic and tuffaceous turbidites and pillowed greenstone (Brekke et al., 1984). Unconformably overlaying the Geitung Unit is the **Siggjo Complex** (Fig. 3.3). Before the formation of the Siggjo Complex, the Lykling Ophiolite and the Geitung Unit were folded and eroded (Brekke et al., 1984). The Siggjo Complex contains various compositions of calc-alkaline subaerial basalts to rhyolites intermingled with sedimentary rocks (Furnes et al., 1986; Nordås, 1985) and can be observed NW along a line from Grutle-Børøya-Siggjo and on Moster (Nordås, 1985). Andesite from the Siggjo Complex is dated to 473 ± 3 Ma (Pedersen & Dunning, 1997). A similar age was obtained for the Katnakken Complex on Stord (476 ± 4 Ma). Cutting through the Siggjo Complex is the Sunnhordland fault zone (SFZ) (Andersen & Jansen, 1987). Discordant to the Siggjo Complex and the Lykling Ophiolite is the **Vikafjord Group** (Fig. 3.3). The group can be observed south of Grutle and is divided into four lithostratigraphic units (Brekke et al., 1984). Stratigraphically from the bottom up, the units are (I) The Roaldfjord Conglomerate, a polymict alluvial debris flow deposit. (II) The Bergsvatn Formation, indicating a transgression with fossiliferous limestones and calcareous phyllites. (III) The Sagvatn Formation, with grained phyllites, bedded chert and limestone transitioning to conglomerate and coarse sandstone representing a fast transgression. (IV) the Eriksvatn Formation defined by subaerial mafic lavas.

The **Sunnhordland Batholith** is a 1000km^2 igneous body located in SW Norway that ranges from gabbroic to granitic composition (Andersen & Jansen, 1987). Based on geochemical data the batholith is categorized as I-type complex with a differentiation trend from basic to acidic composition (Andersen & Jansen, 1987). The Sunnhordland Batholith is divided into three units based on age and composition. The oldest unit comprise of gabbro and diorites and is represented by the **Vardafjell Gabbro** (Pedersen & Dunning, 1997). The Vardafjell Gabbro crops out along a line north of Svortland, on Bømlo. The intrusive gabbros have been dated to 472 ± 2 by Pedersen & Dunning (1997). The age correlates with the ages found for the Siggjo Complex, the Katnakken Complex and the Feøy Gabbro on Karmøy, indicating they were all active at the same time. The next unit in the Sunnhordland Batholith, consist of granodiorites and foliated granites and the youngest unit consists of granitic rocks. Located north on Bømlo is the **Bremnes Migmatite**. The migmatite comprises meta-arkose, shists, quartzite and marble and is partly migmatized (Fonneland, 2002). The migmatite has similarities to the S-type granite in the West Karmøy Igneous Complex (WKIC), dated to 474 +3/-4 Ma (Pedersen & Dunning, 1997) and is associated with the Sunnhordland Batholith. The migmatite is in tectonic contact

with the Lykling Ophiolite (Fig. 1.1; Fonneland, 2002). Fonneland (2002) suggest that the Bremnes Migmatite Complex was accreted onto the ophiolitic terrane around 475 Ma, then later intruded by the Vardafjell gabbro. The sedimentary protolith of the migmatite is dominated by zircons with Paleoproterozoic and Archean ages, suggesting Laurentian affinity (Fonneland, 2002). This indicates that the SW ophiolitic terranes were located closer to the Laurentian margin at this point in the tectonic evolution. Alongside the batholith is the tectonic Sunnhordland Fault Zone (SFZ) (Andersen & Jansen, 1987). The fault changes direction from NW-SE to NE-SW with a steep to a vertical direction that can be followed 40 km from Tysnesøy to Siggjo (Andersen & Jansen, 1987). The structure in the SFZ appear to be from the same generation as a post-Caledonian large scale E-W trending fold that resulted from N-S compression (Andersen & Jansen, 1987).

3.3 Tectonic and magmatic evolution of the terrane in SW Norway

The ophiolitic terrane of SW Norway is recognized as a supra-subduction zone that has been active for at least 25 Myr (Pedersen & Dunning, 1997). The magmatism can be separated between the evolution from an immature island arc system (494 ± 2 Ma) to a mature island arc system (473 ± 2 Ma) over a 20 Myr period (Pedersen & Dunning, 1997). Pedersen et al. (1992) have constructed a tectonic model for the Early Ordovician ophiolite and island arc sequence, and the Late Ordovician to Early Silurian rift-related sequence (Fig. 3.4). The evolution is followed by the initiation of subduction and the development of the immature island arc, the Geitung Unit (494 ± 2 Ma), on top of the old oceanic crust (Fig. 3.4, step 1). Followed by the formation of the ophiolitic crusts exemplified by the Karmøy Ophiolite (494 ± 2 Ma) and the Gullfjellet Ophiolite (489 ± 2 Ma) (Pedersen & Dunning, 1997). In-between the transition from an immature to mature island arc spreading related magmatism took place, in the first 10 Myr, the system produced tholeiitic crust. At a later stage between 485 ± 2 Ma and 479 ± 5 Ma, the ophiolite was intruded by boninitic dike and island arc tholeiites (IAT) swarms (Fig. 3.4, step 2.). Subsequently, the region was intruded by tonalite, quartz diorite and granitic rocks containing inherited zircons of Precambrian age. Next follows the formation of the mature island arc, exemplified by extrusion of high-K calc-alkaline volcanics in the Siggjo Complex (473 ± 3 Ma) and the Vardafjell Gabbro (472 ± 2 Ma), and intrusions of calc-alkaline plutons found on Bømlo and Karmøy with build-up of shallow marine fauna (Fig. 3.4. step 3; Pedersen et al., 1992). The tectonic evolution continues with the accretion of the island arc systems to the Laurentia continental margin (Fig. 3.4, step 4). Lastly, as illustrated in Figure 3.4, step 5-6,

the rifting of the continental margin and the formation of the Late Ordovician to Early Silurian margin basin succession occurred.

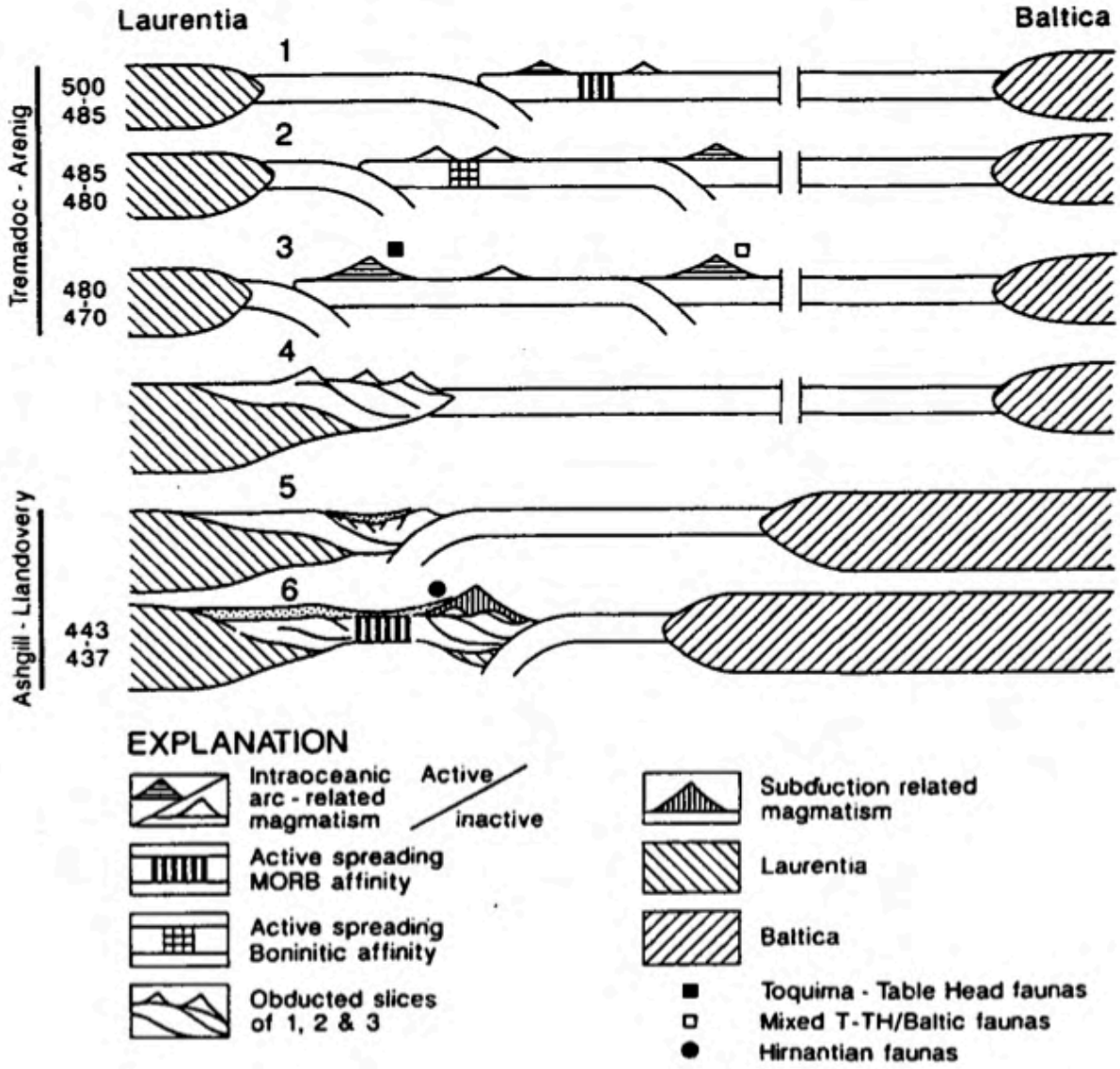

Figure 3.4 *The tectonic evolution model for the Ordovician ophiolite and island arc sequence (Pedersen et al,. 1992).*

3.4 The Lykling area

The island of Bømlo is situated along the coast of SW Norway, between Bergen and Stavanger. It comprises numerous gold-bearing hydrothermal quartz veins (Amaliksen, 1980a). The quartz veins follow small, mineralized shear zones scattered all over the island (Amaliksen, 1980a). The richest mineralization is in the Lykling area, located along the western part of the island (Fig. 3.5A). The mineralization has a mesothermal (450° C -250° C) character and has been precipitated from low salinity fluids and variable CO_2 content (Grenne et al., 1999). The first published work from Bømlo is from Reusch (1888). From 1971 to 1983, several theses have been written by Danish and Norwegian students on the geology of Bømlo (e.g., Amaliksen 1983; Christensen, 1994). Norwegian Geological Survey (NGU) has also published reports about the gold-bearing hydrothermal mineralization in the Lykling area (Amaliksen, 1980a; Wulff, 1996). The latest report on the Lykling area is a detailed "Competent Person's Report" by SRK Exploration Services Ltd (2018). In the Lykling area, the gold-bearing mineralization is hosted in the Lykling Ophiolite gabbro and the associated trondhjemite intrusions (Fig. 3.5B). The trondhjemite have in previous work been described as plagiogranite, tonalite and trondhjemite, but will further just be described as trondhjemite. According to Amaliksen (1983), the gold occurs both in masses and as fine disseminated grains, in the hydrothermal veins and along the shear zones and foliated rocks (Amaliksen, 1980b). There are large amounts of carbonate, pyrite and chalcopyrite recognized in the mineralization (Amaliksen, 1980a). Mineralization of chlorite, muscovite, and rutile have also been reported (Christensen & Stendal, 1995). Minerals like silver and galena were recorded in minor amounts (Reusch, 1888). The shear zones often follow sills and dikes (Amaliksen, 1980b). Two sets of doleritic dikes cut through the Lykling Ophiolite. The oldest dolerite dikes strike in the ESE-WNW orientation. The younger dikes crosscut the latter in the NNE-SSW orientation. Geochemical signatures of the older generation dikes correspond with tholeiitic basalts and the younger with calc-alkaline basalt (Amaliksen, 1983). Amaliksen (1983) compares the older generation dikes with the Eidesvatnet Formation from the Langevåg group and the younger generation to the Katnakken dolerites and Siggjo complex. The mineralizing veins on Bømlo are, according to Christensen and Stendal (1995) spatially related to the Sunnhordland Fault Zone (SFZ) and the Hardangerfjord Fault Zone (HFZ) (Fig. 3.5A; Wulff, 1996).

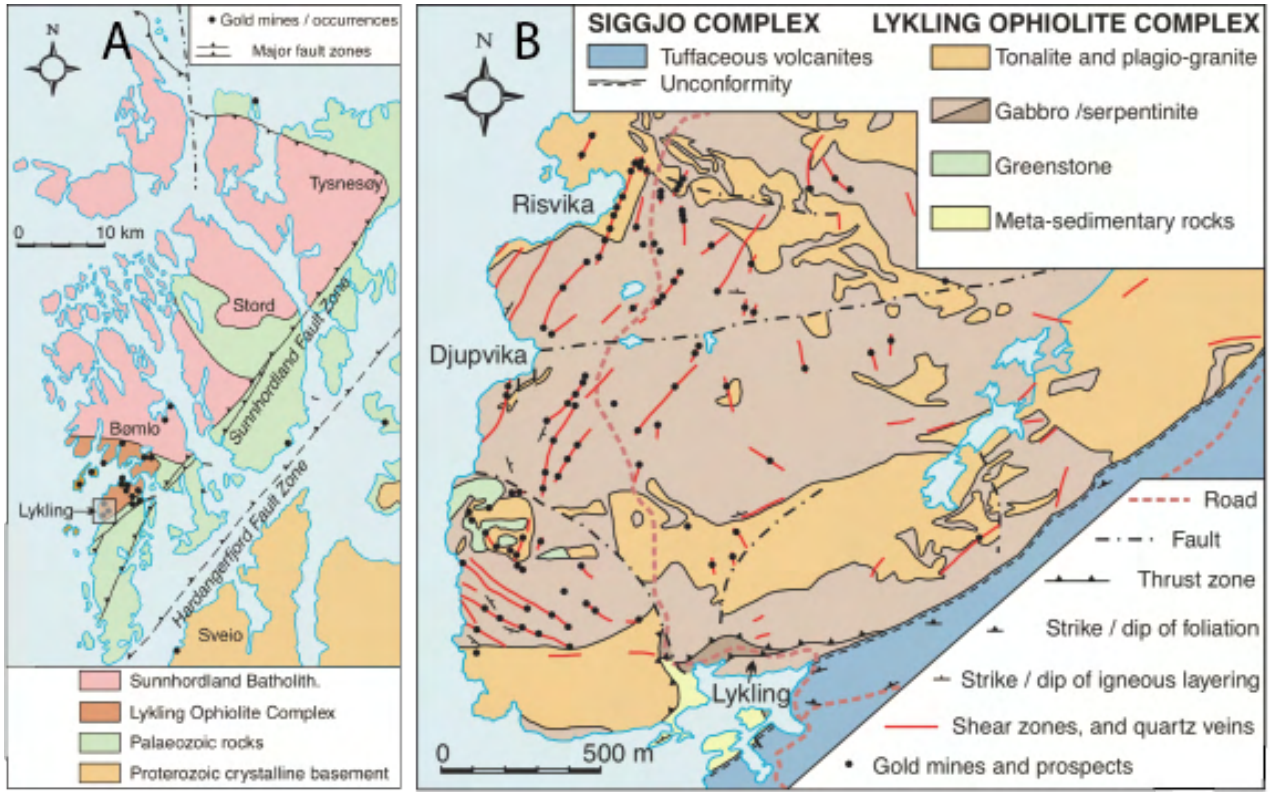

Figure 3.5 *Geological overview maps A: The island of Bømlo and B: The Lykling area Bømlo (Grenne et al., 1999).*

4 MINING HISTORY

The story tells that a local boy found the first gold nugget in 1862, and he flattened the nugget to repair his shoe. Later, the nugget was given to a worker that sold it for 8 Norwegian kroner to "Bergmester" Dahl. He later exhibited it in the mineralogy collection at the University of Oslo (Stautland, 2000). Gold was found in association with quartz veins with pyrite, chalcopyrite, carbonates, and hydrous silicate minerals. Geologist Amund Helland compared the gold occurrence at Lykling to gold provinces in Australia and California (Helland, 1884). During the 1860s, sulphur and copper were popular commodities to mine, mainly to use in medicine and ammunition and coins. The mining of pyrite and chalcopyrite commenced the mining history at Lykling. The gold mining started in 1883, around 20 years later (Amaliksen, 1980a). Three large mining companies operated in the area from 1883 to 1910. The Oscar Gold Mining Company Lmt. was the first and the most prominent company.

Approximately 93 individuals were working in the mines between 1883-1885, resulting in the production of 16 kg of gold. From 1886 to 1890, 64 kg was mined, with roughly 76 men at work. In 1891-1898, 57 kg of gold was collected from the mines with an average workforce of 48 men (Amaliksen, 1980a). The mine closed in 1898 but reopened again in 1906, and a few kilograms of gold were mined until 1909 (Amaliksen, 1980a). The total amount of gold that was mined from the area is estimated to be 152 kg, but it could potentially be larger (Stautland, 2000). Today, there is one mine, the Haugesund mine, that have licence for exploration of gold. The Haugesund mine is not highly active, but there is some mining action.

The Lykling area is not the only place in the region where exploration for gold in association with quartz veins occurred. In the period 1883 to 1910 exploration and mining activities were carried out at Hidle, Hiksjo, Meland and Sakseid (Fossen & Robin, 2015). Mining also occurred at at Vernøya on Reksteren (in association to arsenopyrite), on Varaldsøy and in Hyttevågen in Ølve all located in the hanging wall of the HSZ (Fossen & Robin, 2015). Gold findings have also been reported on Halsnøy and Hovdaneset in Sveio situated in the foot wall of the HSZ (Fig. 3.5A; Fossen & Robin, 2015).

5 THEORETICAL BACKGROUND

5.1 Fluid inclusion studies in hydrothermal ore deposits

Introduction to fluid inclusion studies

Fluid inclusions (FIs) are droplets of fluids trapped within a growing crystal, or within a fracture zone during the process of healing (Roedder & Bodnar, 1980) The fluids trapped during the crystal growth are called primary inclusions (Bodnar et al., 2014). Secondary inclusions are fluids trapped along fractures that develop after the host crystal has been formed. Inclusions developing along healed fracture zones in the continued growing crystal is termed pseudosecondary inclusions (Bodnar, 2018). If the inclusion is primary the temperature of the inclusion represents the minimum temperature of mineral growth and can give information about the original fluids, while secondary and pseudosecondary inclusions can provide an insight into later active hydrothermal processes (Bodnar et al., 2014). Fluid inclusions range in size from sub-microscopic to >100 µm in diameter, and usually contain 10^{-13} to 10^{-16} g of fluid (Roedder, 1984). Modern petrographic microscopes and heating/cooling stages allows for investigation of FIs larger than 2-3 mm (Bodnar et al., 2014). The shape of FIs may vary and is somewhat controlled by the crystallography of the host mineral (Shepherd et al., 1985).

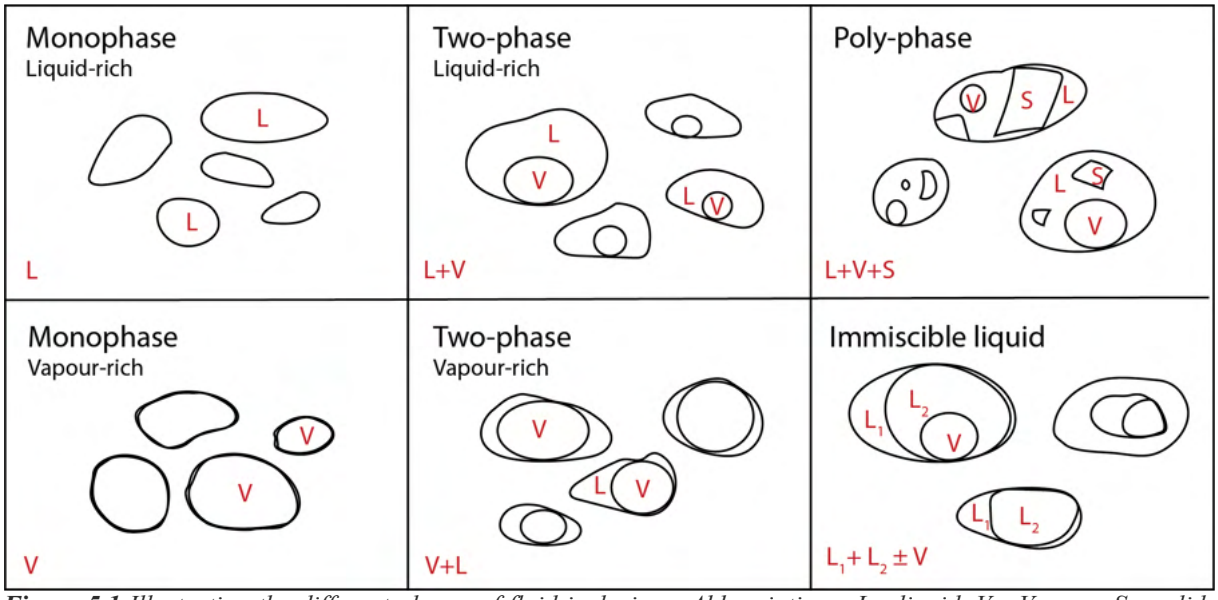

Figure 5.1 *Illustrating the different phases of fluid inclusions. Abbreviations; L= liquid, V= Vapour, S= solid. (Modified from Shepherd et al., 1985).*

At room temperature field inclusions can consist of one or more phases (Fig. 5.1). The mono-phase inclusions normally contain either liquid (L) or vapour (V) phase, but exclusively solid (S) phase inclusion are also found occasionally (Lambrecht & Diamond, 2014). Two-phase inclusions can appear as either vapour-rich or liquid-rich inclusions (Fig. 5.1) Two-phase inclusions are common in hydrothermal minerals. In addition to liquid and vapour, fluid inclusions may also contain one or more solid phases ($L+V+S_{1,2}\ldots$) (Fig. 5.1). Solids can be trapped in FIs as accidentally entrapped impurities or as daughter minerals (Fig. 5.2; Lambrecht & Diamond, 2014). Daughter solids are products of precipitation from the entrapped fluids (Lambrecht & Diamond, 2014).

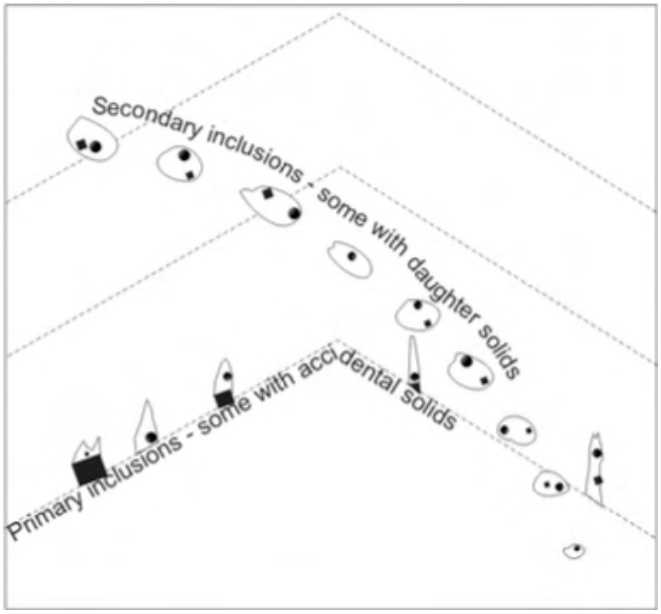

Figure 5.2 *Diagram illustrating primary and secondary inclusion with daughter solids and accidental solids. The primary fluid inclusions are parallel to the growth zone and is placed along the crystal growth direction. Black squares represent solids. The fluid-solid ratio differs in the primary fluid inclusion. The secondary fluid inclusions cut across the growth zoned making trail-bound inclusions. The fluid-solid ratio is similar in all secondary inclusions indicating daughter solids (Lambrecht and Diamond, 2014).*

Roedder's rules

Fluid inclusions studies have evolved over the years to aid the understanding of geological processes and events clearer and present important information about the composition, temperature, pressure, salinity, and density of the fluids. FIs can provide direct data on ore-forming solution properties and, on several occasions, are the most precise geobarometer and geothermometers accessible (Wilkinson, 2001). To achieve geothermometric knowledge, selected physical and chemical conditions must be in order and is referred to as Roedder's rule. The rules state that (I) the fluid inclusion traps a single, homogenous phase, (II) the volume system of the inclusion remains constant (isochoric) after the FI entrapment, and (III) nothing is added or removed after the entrapment i.e., the FIs has remained in a closed system (Bodnar,

2018). A group of FIs entrapped at the same time from the same fluid are called a fluid inclusion assemblage (FIA). This FIA concept was introduced by Goldstein & Reynolds (1994). If all fluid inclusions in a single FIA were trapped simultaneously, that implies entrapped at the same pressure and temperature from the fluid of same composition. Therefore, FIAs can be used to observe if Roedder's rules are fulfilled. Fluid inclusions can also be entrapped within the two-phase field, meaning that two phases were present at the time of entrapment. Boling systems or in general immiscible fluid systems are examples of two-phase fields (Fig. 5.1). Inclusions entrapped under these conditions may reveal important P-T information, for instance when the homogenization temperature is equal to the formation temperature (Roedder & Bodnar, 1980). This disregards the need for pressure correction to achieve the trapping temperature (Bodnar, 2003).

Modification of fluid inclusion

In some cases, Roedders's rules are not complied with, and the fluid inclusions are modified. Modification can trigger morphological change of the FIs and the information gained can be wrong. Randive et al. (2014) explained four common mechanisms causing modification: (I) recrystallization of solids and crystallization of fluids, (II) stretching and necking-down (III) explosion/ implosion decrepitation and (IV) leakage. Wilkinson (2001) describe two possible modifications of FIs within hydrothermal mineral deposits, diffusion and isotopic exchange. Diffusion can occur through grain boundaries, crystal defects or the bulk mineral lattice (Wilkinson. 2001). An example is observed in hydrogen diffusion in porphyry-copper deposits, where chalcopyrite has been observed as a daughter mineral in quartz-hosted inclusions (Wilkinson, 2001). The chalcopyrite did not dissolve when reheated with microthermometry, thus giving the wrong trapping temperature, and proving the chalcopyrite to be a modification of the fluid inclusions (Wilkinson, 2001).

Microthermometry

The temperature of the mineralization fluids is an important factor in the formation of ore deposits. Microthermometry of fluid inclusion is one of the most accurate techniques for estimating ore formation temperatures (Bodnar et al., 2014). Fluid inclusions can also give essential information about pressure, density, salinity, composition, P-T evolution, and gas composition. The method is based on controlled cooling and heating of inclusions with an aim to observe phase change during these controlled temperature changes. The methodology and problems concerning achieving microthermometric measurement have been discussed in detail in several studies (Roedder, 1984; Goldstein & Reynolds, 1994; Bodnar, 2003; Goldstein,

2003). By using microthermometric measurements it is possible to record the eutectic temperature (T_e), melting temperature of ice ($T_{m\ ice}$), melting temperature of hydrates (T_{hyd}), dissolution temperature of halite (T_s) and the total homogenization temperature (T_h). Microthermometry starts by freezing down the fluid inclusions. In H_2O-NaCl fluid inclusions with salinities between 0-23.0 wt.%, freezing the inclusion forms hydrohalite and ice (Fig. 5.3). After the complete content of the studied inclusion is frozen, process of controlled heating starts. Hydrohalite will disappear at the eutectic temperature -21.2 ºC (Fig. 5.3). Ice and liquid are present in the inclusion with the eutectic (T_e) composition (23.3 wt.%) (Bodnar, 2003). The inclusion is further heated so that the ice continues to melt, diluting the liquids salinity. The temperature where the ice is completely melted, represent the ice melting temperature ($T_{m\ ice}$). This temperature is a function of the fluid salinity (Fig. 5.3). The inclusions are further heated until the two-phase inclusion reaches the homogenization temperature (T_h) and the inclusion becomes a one-phase inclusion (Fig. 5.4). If the inclusions are trapped at "boiling" or as an immiscible fluid system, the T_h equals the trapping temperature, but if the inclusion is a mono-phase, pressure correction is needed to obtain trapping temperatures (Bodnar et al., 2014). To pressure correct the fluid inclusions the isochore slope needs to be calculated using the equation (Bodnar, 2003):

$$dP/dT\ (bar/\ ºC) = a_s + b_s * T_h + c_s + T_h^2 \qquad (1)$$

The dP/dT represent the slope of the isochore and a a_s, b_s, c_s are salinity-dependent fitting parameters (Bodnar, 2003).

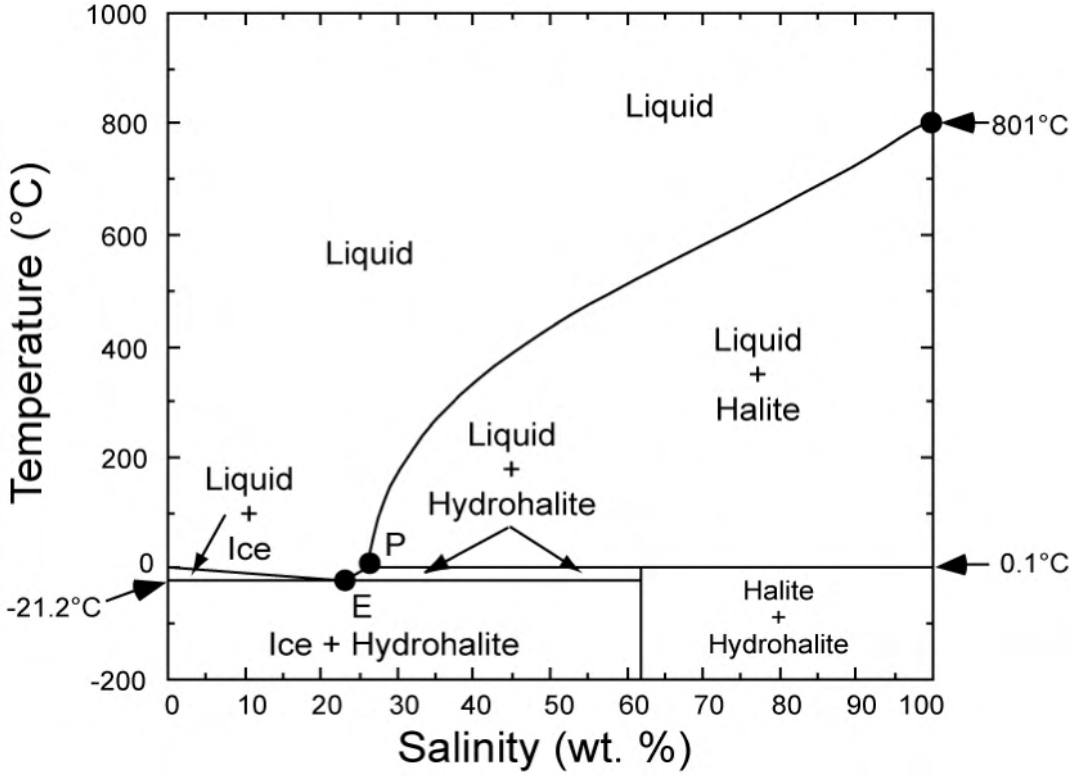

Figure 5.3 *T-X diagram of the NaCl-H_2O system displaying the different phases that are stable at changing temperatures and salinity. Abbreviations: I: ice; L: liquid; HH: hydrohalite; H: halite; P: peritectic (0.1 ºC, 26.3 wt.% NaCl); E: eutectic (-21.2 ºC, 23.2 wt.% NaCl) (Bodnar, 2003).*

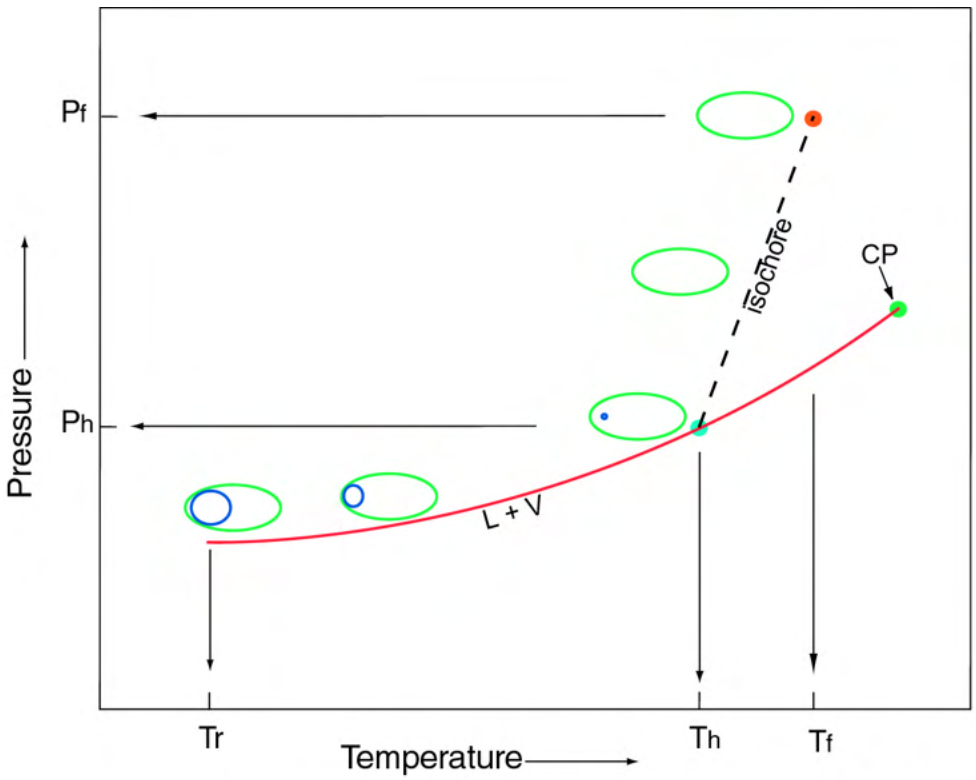

Figure 5.4 *Two-phased inclusion showing the change from two-phase to one-phase with increasing temperature and pressure, indicating the homogenization temperature and calculated isochore slope (Atkinson, 2002).*

H_2O-NaCl system

The H_2O-NaCl system is a binary system that can be used to interpret the PTX conditions of complex saline-aqueous solutions, including some fluid inclusions (Atkinson, 2002). Aqueous fluids can dissolve a number salts in different geological settings, but NaCl, KCl, $CaCl_2$, $MgCl_2$ and LiCl are the most common and abundant in the majority of geological fluids (Bodnar, 2003). In the NaCl-H_2O system Ice, halite (NaCl) and hydrohalite (NaCl-2H_2O) are the three possible solid phases that may form (Fig. 5.3; Davis et al., 1990). H_2O-NaCl fluid inclusions can give information about the trapping conditions using microthermometric analyses (Atkinson, 2002). The grey area in Figure 5.5 represent the possible PT conditions for which L+V two-phase immiscibility is possible in the H_2O-NaCl binary system (Bodnar, 2003). Within the grey area liquid and vapour is in immiscibility, whereas outside the area the inclusions would exist as a single-phase fluid.

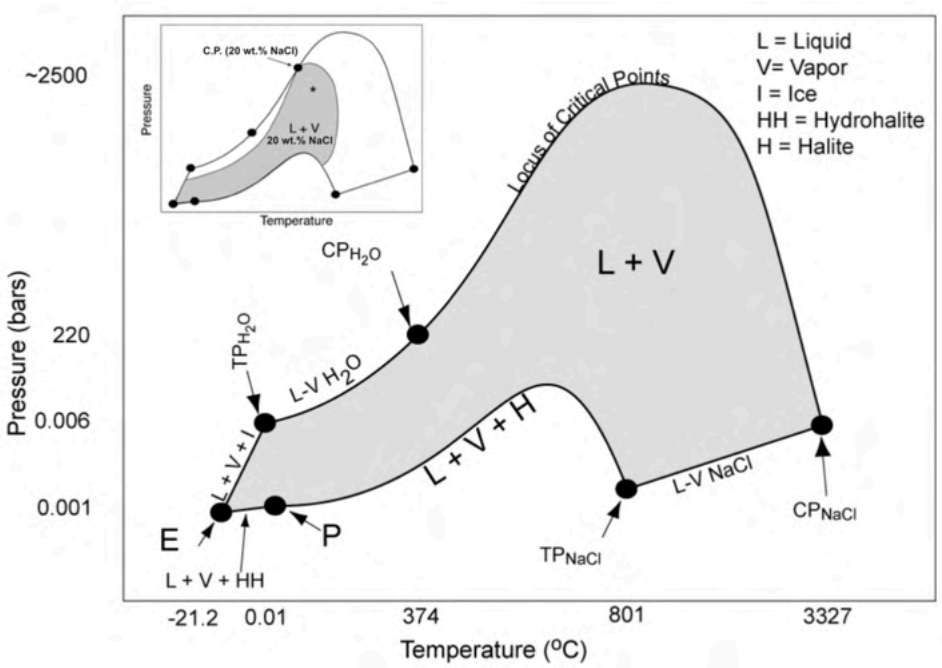

Figure 5.5 *Pressure-temperature diagram for the binary H2O-NaCl system. The "L+V" grey area represent the range where liquid and vapour would co-exist (immiscibility). The black dots represent E: eutectic point (L+V+I+HH)), TP: Triple point, CP: critical point and P: peritectic point (L+V+HH+H). The smaller box displays in the left corner the NaCl-H2O system with the salinity of 20 wt.% NaCl (Bodnar, 2003).*

H_2O-NaCl-$CaCl_2$ system

The ternary system H_2O-NaCl-$CaCl_2$, is commonly found in sedimentary basins and in metamorphic rocks (Bodnar, 2003). This system is recognized based on low first melting temperature in microthermometric measurements. In most liquid-vapour inclusions in this system form ice, hydrohalite and antarcticite ($CaCl_2$-6H_2O) when the inclusions are cooled down and when heated the eutectic point is - 52ºC (Bodnar, 2003).

Fluid inclusions in hydrothermal deposits

Hydrothermal ore deposit can be divided into different groups depending on their origin, including the Mississippi valley-type (MVT), Volcanogenic massive sulphide (VMS), Porphyry Cu, Mo or Sn-W, Epithermal, Skarn, Carlin-type Au and Orogenic gold deposits (Fig. 5.6; Wilkinson, 2001). All these different deposit types have distinctive fluid inclusion characteristic that separate them, but it is important to emphasise that fluid inclusion data alone is not enough to say something about the hydrothermal ore deposit. A combination of FIs studies together with geochemical and geological data is required in order to better understand the study area (Wilkinson, 2001). One way to characterize the FIs in mineralizing systems is by looking at the homogenization temperature and NaCl equivalent salinity (Wilkinson, 2001). Figure 5.6 illustrate the distinctive homogenization temperature (T_h) and salinity from different mineralizing deposit types. The focus in this thesis is the orogenic gold deposit, illustrated as lode Au. According to Bodnar et al. (2014), the homogenization temperature found in orogenic gold deposit for aqueous and aqueous-carbonic inclusions usually ranges from 150 to 650 °C.

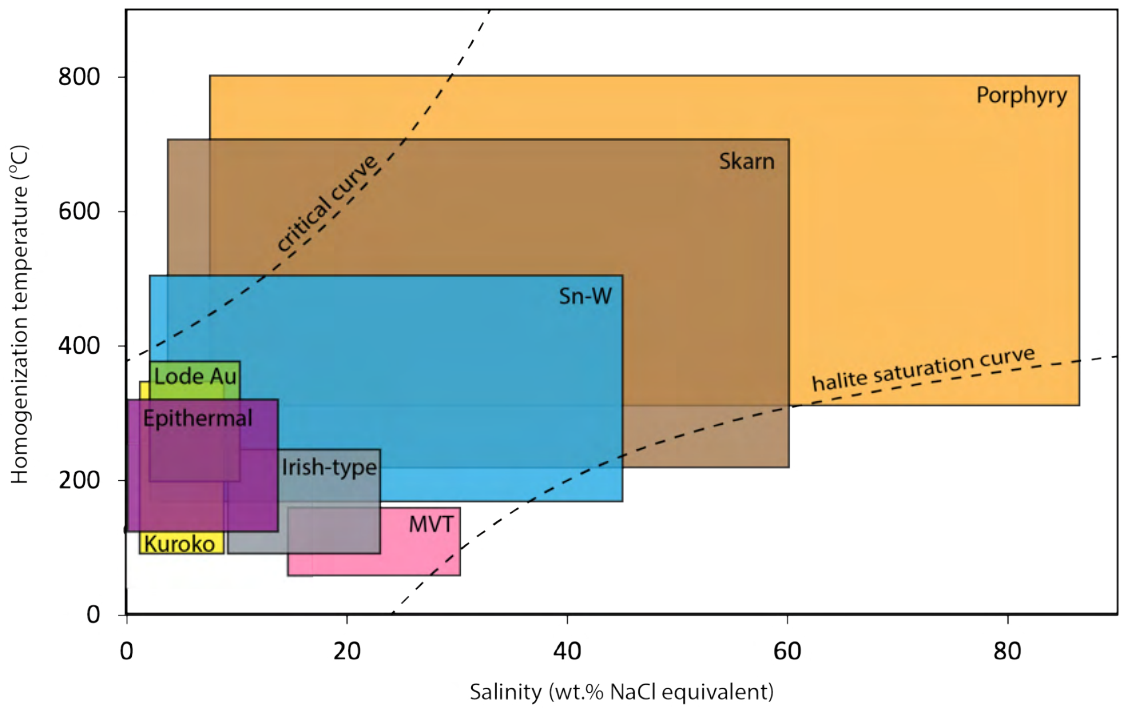

Figure 5.6 *Homogenization temperature (TH) – salinity diagram demonstrating the different hydrothermal deposit system (Modified from Wilkinson, 2001).*

Fluid inclusions in orogenic gold deposits can be illustrated by the H_2O-CO_2-NaCl ternary system (Fig. 5.7). FIs hosted in metasedimentary systems can also contain N_2 and/or CH_4 with concentrations similar to the CO_2 (Bodnar et al., 2014). The typical composition of H_2O-CO_2-NaCl inclusion in an orogenic gold deposit is illustrated in Figure 5.7 and show that most fluid inclusions is H_2O rich (Bodnar et al., 2014). The salinity in aqueous orogenic gold FIs is normally 0-10 wt.% NaCl, however, higher salinities have been found in some deposits (Bodnar et al., 2014). The CO_2 concentrations normally found in orogenic gold deposit fluid inclusion extends from 4 to 25 mol%, nevertheless higher intensities have been discovered occurring in deposits (Bodnar et al., 2014).

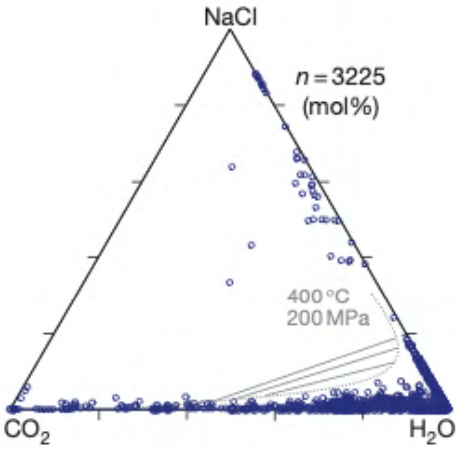

Figure 5.7 *H_2O-CO_2-NaCl ternary plot composition of fluid inclusions in orogenic gold deposits (Bodnar et al., 2014).*

5.2 Origin and characteristics of orogenic gold deposits

Orogenic gold deposits origin from hydrothermal fluids precipitating along convergent margins during accretion or collision, related to plate tectonics and/or lithospheric delamination (Groves et al., 2003). An orogenic gold deposit is an individual mineral deposit group and the term *orogenic* was first introduced by Bohlke (1982). The term *mesothermal gold deposit* has widely been used to describe orogenic gold deposits. The word "mesothermal" was initially used by Lindgren (1933), describing a metalliferous deposit developed at intermediate temperatures caused by rising hot fluids from intrusive rocks. The term *orogenic gold deposit* was later introduced by Groves et al. (1998) to replace assorted terms used, such as "lode gold deposit". Furthermore, Groves et al. (1998) suggested subdividing the orogenic gold deposits using the prefixes *epi-, meso-* and *hypo-* introduced by Lindgren (1907, 1933). Constructed on modern geothermobarometric studies the subdivision of orogenic gold deposit was divided into *epizonal, mesozonal* and *hypozonal* to reflect the gold deposition at different crustal depth (Fig.

5.8; Groves et al., 1998). *Epizonal* deposits is described to form at 6 km depth and temperatures of 150-300 ºC, *mesozonal* deposits form at deeper depth and at temperatures 300-475 ºC. Lastly, *hypozonal* deposits form below 12 km and at temperatures higher than 475 ºC (Groves et al., 1998).

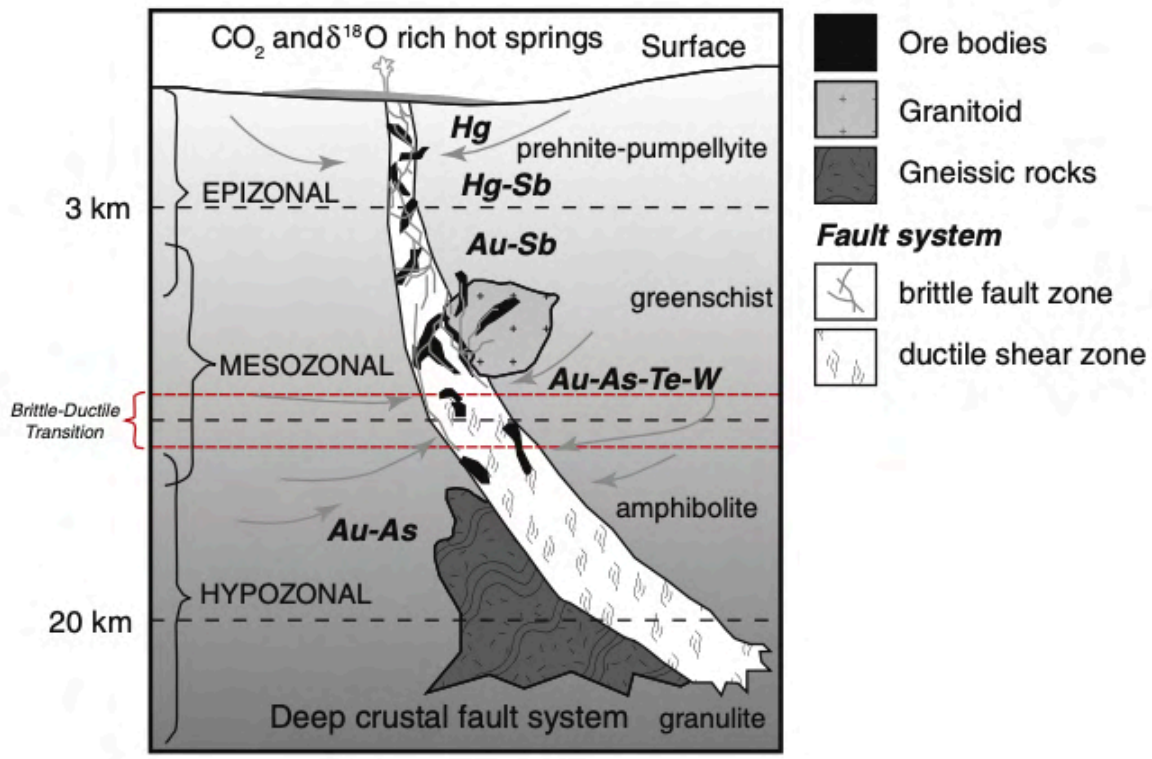

Figure 5.8 *Illustrating an orogenic gold deposit, with the different epizonal, mesozonal and hypozonal depth zones. (Modified from Groves et al. (1998) and sourced from Goldfarb & Groves (2015))*

Orogenic gold deposits are always associated with metamorphosed terrains. The age of known orogenic gold deposits range from Archean to Cenozoic time. Goldfarb et al. (2001) studied orogenic gold deposits though geological time and found that the deposits broadly correlate to thermal events that links to the growth of new continental crust. In the study, Goldfarb et al. (2001) found that the considerable amount of orogenic gold deposits in the world can be grouped into different geological time periods. The oldest substantial orogenic gold deposit resources are from the Middle Archean Barberton greenstone belt. The first period involves massive depositions of orogenic gold assembled during the Neoarchean, between 2.8 and 2.55 Ga in granitoid-greenstone terranes. The deposits from this period are found all over the world and some examples is the Yilgarn craton (Western Australia), Superior province (Canada), Tanzania craton (central Africa) and Dharwar (India). The Archean gold deposits in greenstone belts can be found in high or low metamorphic terranes of different ages (Groves et al., 1998).

The second period was assembled in Precambrian, between 2.1 and 1.8 Ga and includes, among others, the West African craton, Amazonian craton (South America), Trans Hudson orogen (North America), Svecofennian province and North Australian craton. In the period 1.8-0.6 Ga. fewer orogenic gold deposit has been recorded. According to Goldfarb et al. (2001) can the lack of significant gold ores from this period be explained by the change in continental growth and change in the plate motions. Lastly, the Phanerozoic orogens that formed along active continental margins throughout Paleozoic to Tertiary. Examples of orogenic gold deposit dated to this period is the North American Cordilleran orogen, Eastern Russia and the Central Asia orogenic belt. There have not been found any exposed orogenic gold deposits formed later than 50 Ma (Goldfarb et al., 2001). Contemporary geochronology suggests that within a given old continental crust, gold formation might be diachronous, as found in many Phanerozoic orogenic belts (Goldfarb et al., 2001).

Rowe & Zhou (2007) divide the orogenic gold deposits into three types; greenstone-hosted, turbidite-hosted and BIF-hosted (banded iron formation) type, based on their host rock environment (Fig. 5.9). The different types of orogenic gold deposits have several shared characteristics. Orogenic gold deposits are characterized by quartz-dominant veins systems ≤ 3-5% with sulphide minerals (mainly Fe-sulphides) and ≤5-15% carbonate minerals (Groves et al., 1998). The orogenic ore structures can range from brittle faults to ductile shear zones with low-angle to high-angle reverse motion to strike-slip or oblique-slip motion, fracture arrays, stockwork network, breccia zones in competent rocks, foliated zones or fold hinges in ductile turbidite sequences (Groves et al., 1998). These structures act as a conduit for hydrothermal fluid migration (Gaboury, 2019). Gold in hydrothermal orogenic gold deposits are precipitated as a result of instability of gold complexes transported by fluids in the crust. Changes in temperature, pressure, ligand activity, phase separation, boiling, mixing, and sulphide mineral precipitation can lead to precipitation of gold (Stefánsson & Seward, 2004).

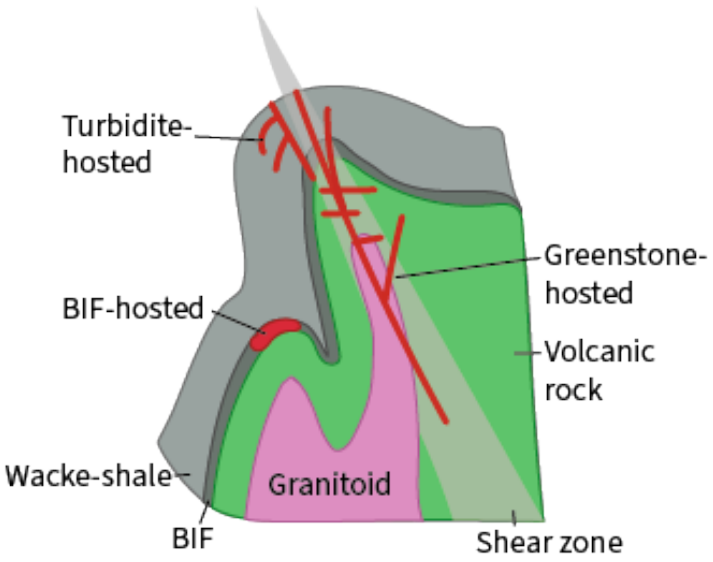

Figure 5.9 *Figure illustrating the orogenic hydrothermal system for gold deposition (Modified from Rowe & Zhou, 2007)*

Ore Fluids

Aqueous fluids are the dominant fluid type in orogenic gold deposits. The gold carrying ore-fluids have been interpreted to be of low salinity, near neutral pH and mixed aqueous-carbonic fluids. Orogenic gold deposits have an enrichment of trace metals: As, Sb, Se, B, Te, Hg, Bi, Mo, W and have small or lacking concentrations of Cu and Zn (Gaboury, 2019). Pinpointing the exact fluid source for orogenic gold deposits has been widely discussed and magmatic, metamorphic-derived, and deeply circulating meteoric water has all been proposed as the mineralization source (Bodnar et al., 2014). Ridley & Diamond (2000) discuss different models for the origin of the gold-transporting fluids for orogenic gold deposits. The first model entails devolatilization of felsic magma, where the fluids have exsolved from the granitic magmas and gold concentration is a consequence of gold being an incompatible element during crystallization. The driving force of deposition of gold would be changing fluid-rock equilibrium with the cooling or intrusion of country rock. The second model propose metamorphic dehydration of seafloor rocks. The gold is proposed to be leached from the dehydrating rocks or from nearby rocks along the fluid flow path. It is suggested that the fluid is released from mafic rocks in the transition from greenschist to amphibolite. The driving force for precipitation of gold and other minerals are considered to follow changes in equilibrium with cooling. Gold is a noble metal that is non-reactive under atmospheric conditions. In orogenic gold deposits, gold will commonly appear as native gold particles or in sulphides as micro- to nanometric inclusions (Gaboury, 2019). Various authors and studies have tried to find the link of orogenic gold and the specific sources of gold. Tomkins (2013) describe two likely

sources for gold: (I) Metamorphic rocks, producing fluids by temperature increase; and (II) felsic rocks to intermediate magmas, releasing fluids as they crystallize. Gold in orogenic gold deposits contain an average of 1-20 ppm Au, which is three times more than the average crustal rock (Saunders et al., 2014). The precipitation mechanics for gold can be described by the following reactions:

$$Au + HS^- + H^+ + \frac{1}{4}O_2 = Au(HS)^0 + \frac{1}{2}H_2O \qquad (2)$$

$$Au + 2HS^- + H^+ + \frac{1}{4}O_2 = Au(HS)_2^- + \frac{1}{2}H_2O \qquad (3)$$

$$Au(HS)_2^- + Fe^{2+} = FeS_2 + Au + 2H^+ \qquad (4)$$

$$HAu(HS)_2 + FeO = FeS_2 + Au + H_2O + \frac{1}{2}H_2 \qquad (5)$$

Based on Le Châtelier's principle, reaction (1) and (2) will precipitate gold if the bisulphide activity is decreased and for reaction (3) and (4) HS^- is consumed when pyrite is formed, leading to precipitation of gold within pyrite (Gaboury, 2019). Contrary, when HS^- is not consumed by pyrite or other sulphides, native gold will precipitate (Gaboury, 2019). The main ligand in ore forming fluids is therefore bisulphide and the dominant species in slightly acidic solutions is $AuHS^o$ (Saunders et al., 2014). $Au(HS)_2^-$ is stable at hydrothermal temperatures of 250-400ºC in neutral to slightly acidic solutions (Saunders et al., 2014). Figure 5.10 shows a binary diagram of gold solubility in an aqueous solution as a function of oxygen fugacity (fO_2) and pH (Gaboury, 2019). The illustration reveals that gold solubility is controlled by the two parameters: (I) limited pH range from neutral to slightly acidic conditions and (II) fO_2 just below mineral stability limit for sulphate-sulphide (oxide-sulphide) (Gaboury, 2019). At temperatures higher than 400 ºC and/or in highly saline fluids, chlorite (Cl^-) will operate as the main ligand (Gammons & Williams-Jones, 1997). To deposit gold in the $AuCl_2^-$ system the temperature needs to decrease (Zhu et al., 2011)

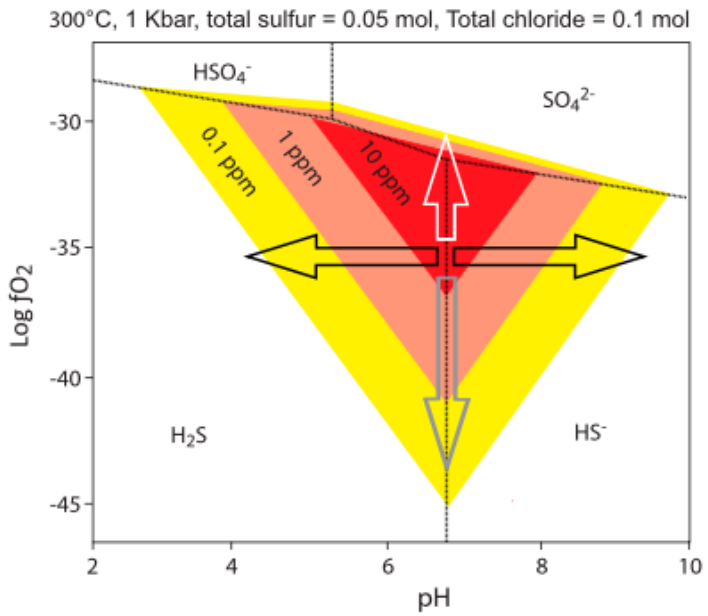

Figure 5.10 *Oxygen fugacity – pH diagram for gold solubility in aqueous solution at 300 ºC. Gold is precipitated most effectively at natural to slightly acidic condition and close to the oxidation limit of sulphate (Gaboury, 2019).*

Hydrothermal alteration

The mineralization associated with hydrothermal alteration assemblages may vary with the wall-rock compositions, water/rock ratio and crustal depth (Groves et al., 1998). The standard types of alteration found in orogenic gold deposits are sulphidation, (de)-silicification, carbonization and sericitization that indicate mobilization of Si, S, K, and CO_2 within the hydrothermal system (Saunders et al., 2014). The dominantly precipitated sulphide minerals are pyrite, arsenopyrite and pyrrhotite with high amounts in the ore zone and decreasing amount further away from the ore zone (Saunders et al., 2014). Pyrite is usually found in igneous rocks and greenschist grade metamorphosed rocks, pyrrhotite becomes more abundant in high temperature deposit like amphibolite grade rocks and BIFs (Rowe & Zhou, 2007; Saunders et al., 2014). Arsenopyrite can be found in clastic-sedimentary-hosted ores at the greenschist grade (Rowe & Zhou, 2007). The precipitation of sulphidation is massive in BIF and Fe-rich mafic host rocks (Groves et al., 1998). In greenschist facies the alteration implicates significant accumulation of CO_2, S, K, H_2O, SiO_2 ± Na and LILE (Groves, 1998).

5.3 Stable isotope systematics in hydrothermal ore deposits, with a focus to orogenic gold deposits

Stable isotopes

Isotopes are atoms that have the same number of protons in the nuclei but a different number of neutrons (Hoefs, 2018). They can be divided into two different categories, stable and unstable isotopes. Unstable isotopes are radioactive, and they spontaneously undergo radioactive decay (Shanks, 2014). The principle of stable isotopes was first recognized by Briscoe & Robinson (1925) on boron isotope ratios (Sharp, 2017). Stable isotope fractionation occurs as response to the difference in mass and thermodynamic properties of the same element although the isotopes have similar chemical and physical properties (Sharp, 2017). The difference in physicochemical processes may result in their fractionation. There are two types of isotope fractionation, (I) kinetic fractionation and (II) equilibrium fractionation. Kinetic isotope fractionation is irreversible and is associated with fast and incomplete processes like evaporation, diffusion, and dissociation reactions (Sharp, 2017). Kinetic isotope fractionation commonly occurs in nature but is relatively rarely in high temperature processes, therefore less important in this study. Equilibrium fractionation is described below. The relative difference in isotopic ratios can be determined by the delta (δ) notation, given by:

$$\delta = \left(\frac{R_X - R_{std}}{R_{std}}\right) \times 1000 \qquad (6)$$

The delta value is expressed in per mil (‰) and R is the measured ratio of abundance of heavy to light isotopes of the same element (Sharp, 2017). R_x represents the sample and R_{std} represents the standard ratio. Isotopic ratios are usually expressed as the ratio of heavy isotope to light isotope, for example $^{13}C/^{12}C$, $^{18}O/^{16}O$, $^{34}S/^{32}S$, etc. or as $\delta^{13}C$, $\delta^{18}O$, $\delta^{34}S$ (Sharp, 2017). The international standard ratio used for $\delta^{13}C$ and $\delta^{18}O$ is Vienna Standard Mean Ocean Water (V-SMOW) or Pee Dee Belemnite (PDB). For $\delta^{34}S$, the standard Vienna Canyon Diablo Troilite meteorite (V-CDT). The isotopic delta value is ether negative or positive. Positive delta values indicate depletion of light isotopes compared to the standard. Similarly, negative delta values indicate depletion of heavy isotopes.

Equilibrium isotope fractionation

Equilibrium isotope fractionation is a reversible reaction where the forward and backward rates are identical (7).

$$aA_1 + bB_2 = aA_2 + bB_1 \qquad (7)$$

The subfix describe the different substances as A and B with either light or heavy isotopes. The reactions equilibrium constant (K) is known as:

$$K = \frac{\left(\frac{A_2}{A_1}\right)^a}{\left(\frac{B_2}{B_1}\right)^b} \qquad (8)$$

The parentheses in the equation represent concentrations within the different isotopic species i.e. molar ratio. The equilibrium constant (K) is often replaced by the fractionation factor α in geochemistry (Hoefs, 2018). The fractionation factor is defined by the relative abundance of the light and heavy isotopes, reflected in the equation:

$$\alpha_{A-B} = R_A/R_B \qquad (9)$$

The R represent the ratio of the heavy to light isotopes i.e., $^{18}O/^{16}O$ and $^{13}C/^{12}C$. The fractionation factor can also be explained by the equilibrium constant:

$$\alpha = K^{1/n} \qquad (10)$$

The *n* serves as the total number of atoms exchanged in the reaction. The temperature in the system is a significant factor in isotopic fractionation and the effect is determined by the molecules structure and vibrational frequency in the reaction (Hoefs, 2018). In high temperature systems isotopic fractionation tends to become zero, meaning that the two phases are equal (Hoefs, 2018). It can be explained by the equilibrium constant being: $\alpha^{eq} = 1$ and is named "crossover". By measuring two different coexisting phases the isotopic temperature can be determined using a known calculated fractionation (Chriss, 1999).

Isotope geothermometry

Isotope thermometry is a well-established method used to determine the thermodynamic properties of isotopes substances (Hoefs, 2018; Urey et al., 1947). Finding the temperature in rocks based on isotopic exchange can give critical information about the formation temperature of e.g., hydrothermal orogenic gold deposits. Isotope thermometry is depended on the isotopic equilibrium. Isotopic equilibrium is mostly achieved at high temperatures (Hoefs, 2018). "*Theoretical studies show that the fractionation factor (α) for isotopic exchange between minerals is a linear function of $1/T^2$, where "T" is temperature in degrees Kelvin*" (Hoefs, 2018 p. 23). A weakness to the method is apparent in slowly cooled metamorphic and magmatic rocks, where the temperature estimations often are lower than seen in other geothermometers (Hoefs, 2018). There are three isotope thermometry methods used to determine the equilibrium fractionation for isotopic exchange reactions, (I) theoretical calculations, (II) experimental

determinations in the laboratory, and (III) empirical or semi-empirical calibrations (Hoefs, 2018).

Stable isotopes in orogenic gold deposits

Stable isotope data on hydrothermal ore deposits have given a useful understanding of the mineralizing systems during the last couple of decades (Shanks, 2014). Still, it is important to take precautions when interpreting isotopic data. The primary isotopic fluid values might have been altered by different factors. Goldfarb & Groves (2015) list four possible problems when interpreting stable isotope data: (I) fluid-rock interactions along the pathway of the fluids, (II) fluid-rock interaction at the mineralizing location, (III) overlapping isotopic fluid sources and (IV) uncertainties in the data source. Characteristically hydrothermal ore deposits show a significant yet variable enrichment in δD, δ^{18}O, and δ^{34}S values (Shank, 2014). Oxygen isotopes (δ^{18}O) measured in quartz from orogenic gold deposits range between +10 and +17‰ SMOW and fluids are calculated to be between +5 and +10‰ (Saunders et al., 2014). δ^{13}C in hydrothermal carbonates related to orogenic gold ores display values between -1 and +10‰ (Zoheir et al., 2019). Sulphur isotopes (δ^{34}S) reflect extremely variable signatures at different deposits of different ages (Saunders et al., 2014) and there is no distinctive signature for δ^{34}S-values for orogenic gold forming fluids (Goldfarb & Groves, 2015). The δ^{34}S-value tend to reflect rocks undergoing devitalization (Saunders et al., 2014). Changes in isotopic composition at the site of deposition can only shift a few per mill, indicating that the large variation of sulphur isotopes in orogenic gold is unlikely to be the result of the on-site precipitation conditions but rather the source of fluids (Goldfarb & Groves, 2015). However, as sulphur is assumed to be the main complexing agent for transporting gold (Gaboury, 2019), the understanding of sulphur and determining the source of sulphur might be critical to better understand the orogenic gold system (Goldfarb & Groves, 2015).

Hydrogen and oxygen isotopes

Isotope composition of hydrogen (δD) versus oxygen (δ^{18}O) provides very useful information about the water source of hydrothermal fluids. Studies on fluid inclusion and hydrous silica minerals of oxygen and hydrogen isotopes from orogenic gold deposit indicate mineralizing fluids in general are from metamorphic waters (Fig. 5.11; Shank, 2014). The fluid source of orogenic gold deposit is diverse and deposits with evidence of both magmatic and metamorphic water components (Shank, 2014)

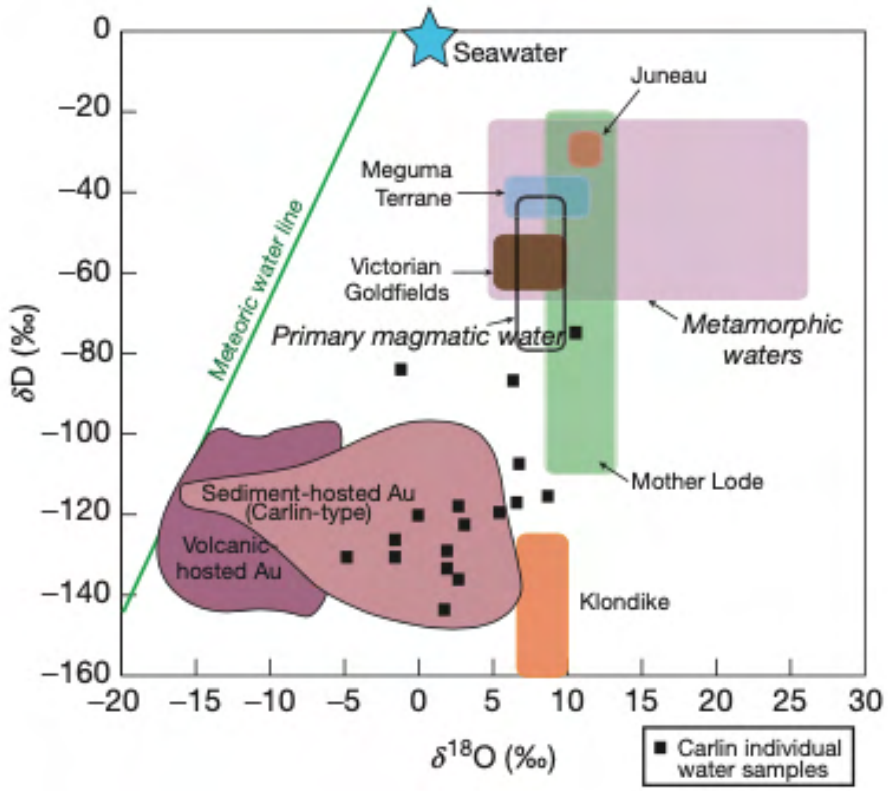

Figure 5.11 *Delta deuterium (δD) and oxygen isotopes ($\delta^{18}O$) plotted against each other in permil (‰) relative to the Standard Mean Ocean Water (SMOW). Outlined is a variation of mineralizing fluids from different orogenic gold deposits. (Modified from Goldfarb et al. (2005) and sourced from Shanks (2014)).*

6 RESULTS

6.1 Mineralogical characteristics of the Lykling gold mineralization

Based on structural and mineralogical characteristics the gold mineralization of the Lykling area can be subdivided into two main types, (I) quartz-sulphide veins hosted by steeply dipping brittle fractures and (II) quartz-carbonate veins hosted by ductile shear zones (Fig. 6.1).

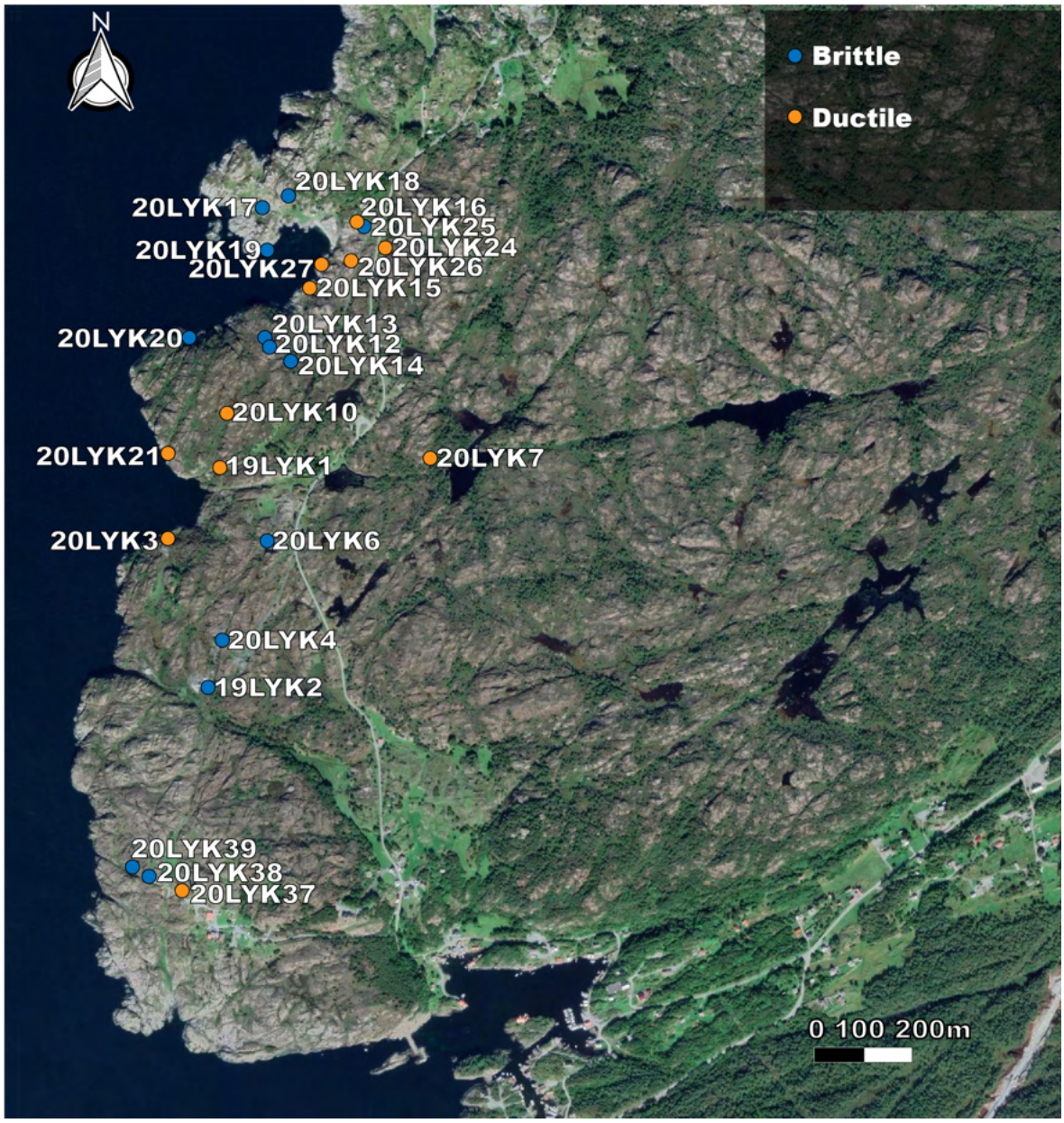

Figure 6.1 *Overview map of the Lykling area with sampling locations. The samples has been divided into brittle and ductile mineralization depending on their structural charachterstics (Google maps, 2021)*

Gold mineralization hosted by brittle quartz veins

Mineralized brittle quartz veins are observed within the Lykling Ophiolite gabbro and the associated trondhjemite intrusions (Fig. 6.2). This type of veins is often associated with mafic dikes that crosscut the Lykling Ophiolite gabbro and the overlying trondhjemite (Fig. 6.3A). In the northern part of the Lykling area most of the veins are controlled by an NNE-SSW-trending system of brittle fractures, while the southern part of the area is characterized by ESE-WNW oriented veins (Fig. 6.2). Figure 6.3 illustrates the typical spatial relations between the mineralized quartz and the NNE-SSW trending dikes. Figure 6.3C suggest emplacement of the mafic dikes preceded the brittle deformation event and deposition of the quartz veins. The quartz veins are massive, milky white and vary in thickness from a couple of centimetres to 1-2 meter. The most prominent example of the brittle NNE-SSW trending quartz veins is located at the historical Haugesund mine and the most prominent example of the ESE-WNW trending quartz veins has been found at the Harald Haarfagre mine (Fig. 6.2). The mineralization at the Harald Haarfagre mine host both brittle and ductile mineralization (Fig. 6.1). Most of the veins are hosted either by the Lykling Ophiolite gabbro or by the overlying trondhjemite, but the brittle NNE-SSW trending quartz veins represented by 20LYK20 (Fig. 6.1 is hosted in both (Fig. 6.3C).

Samples collected in-situ as well as samples collected from historical tailing sites in the study area revealed quartz as the main gangue mineral, while pyrite and chalcopyrite represent the most abundant ore minerals (Fig. 6.4). Pyrite occurs a massive and anhedral mineral (Fig. 6.4) and chalcopyrite usually comes in association with pyrite, ether synchronously or as inter-grain fillings (Fig. 6.4B, D). Disseminated sulphide mineralization is also observed in the surrounding host rock along the mineralized vein. Native gold is mostly spatially associated with chalcopyrite (Fig. 6.4B). Locally, the quartz veins host only chalcopyrite observed in sample 20LYK4C (Fig. 6.5A) and sample 20LYK4D. Two thick sections samples analysed by the SEM-EDS technique (Fig. 6.5A-D) confirmed observations from reflected light microscopy. The SEM-EDS also revealed traces of galena and muscovite (Fig. 6.5A).

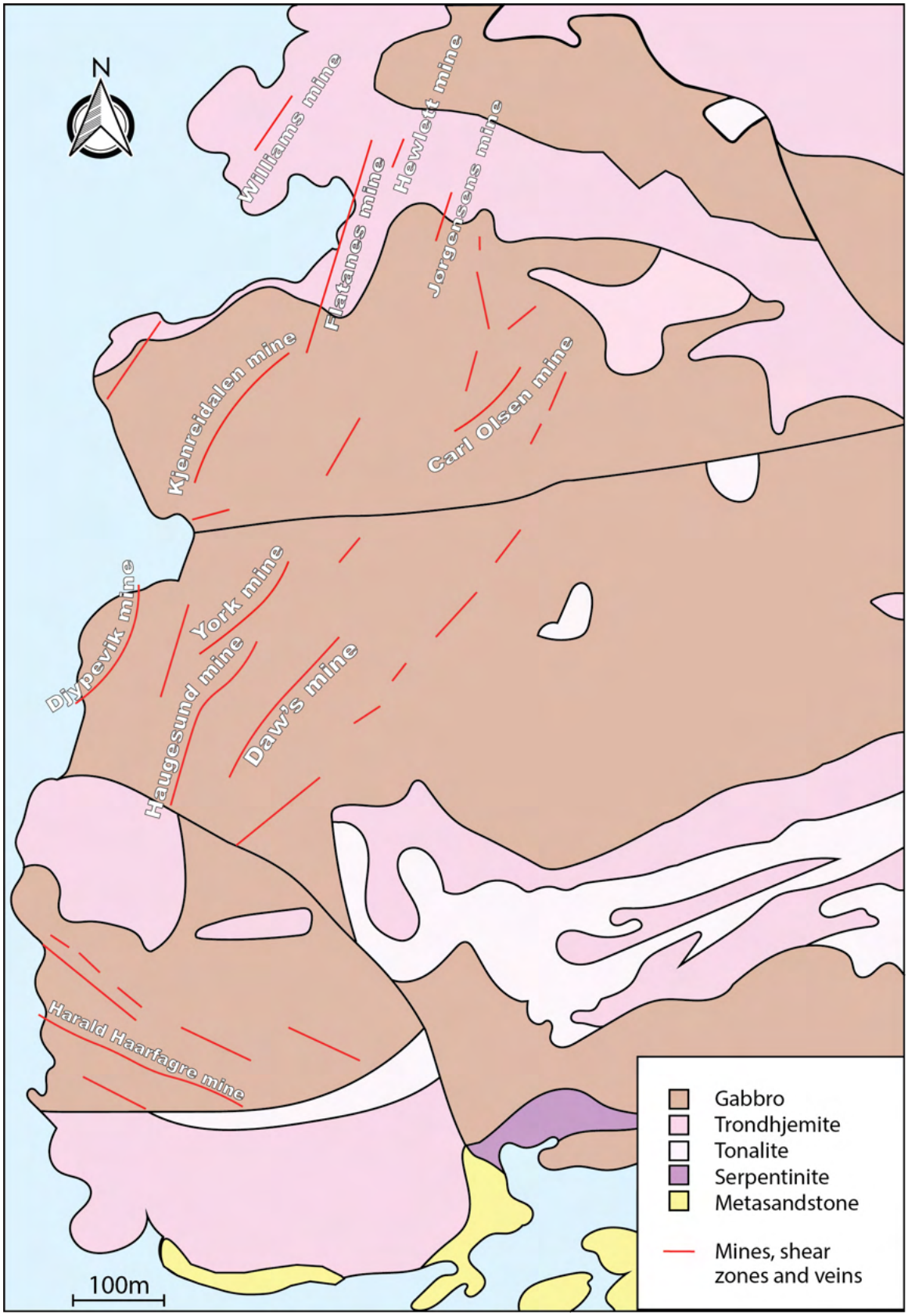

Figure 6.2 *Map of the Lykling area with lithology and mine names (Modified from Amaliksen, 1983).*

Figure 6.3 *Field pictures of brittle structures and mineralization. A: Mafic dikes and quartz cutting though the trondhjemite. The quartz is mineralized along the dike. B: Large quartz vein inside one of the mines tilted in a 182/30 plane. Hammer for scale. C: location 20LYK20, vertical quartz vein in NNE-SSW direction crossing trough the hosts, the trondhjemite and Lykling Ophiolite gabbro. The yellow lines: the NNE-SSW dike and red line is a normal fault.*

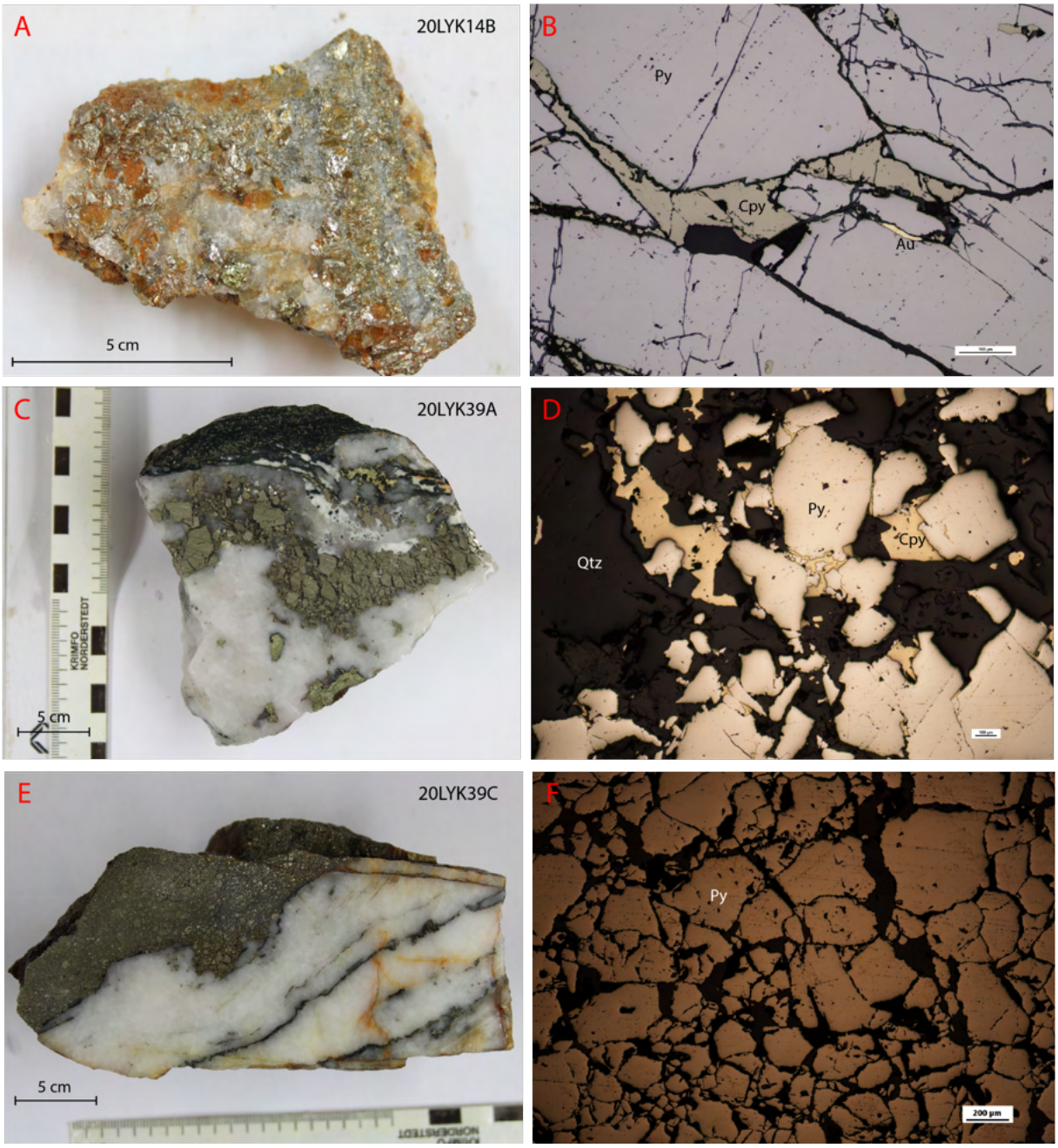

Figure 6.4 *Examples of the brittle type of mineralization A: Hand specimen of sample 20LYK14B. B: Reflected light microscopy picture of sample 20LYK14B showing the chalcopyrite (Cpy) in-between the pyrite (Py) and small amount of gold (Au). C: Hand specimen of sample 20LYK39A. D: Reflected light photomicrograph of sample 20LYK39A with quartz (Qtz), overgrown pyrite (Py) and chalcopyrite (Cpy). E: Hand specimen of sample 20LYK39C. F: Reflected light photomicrograph of the pyrite in sample 20LYK39C.*

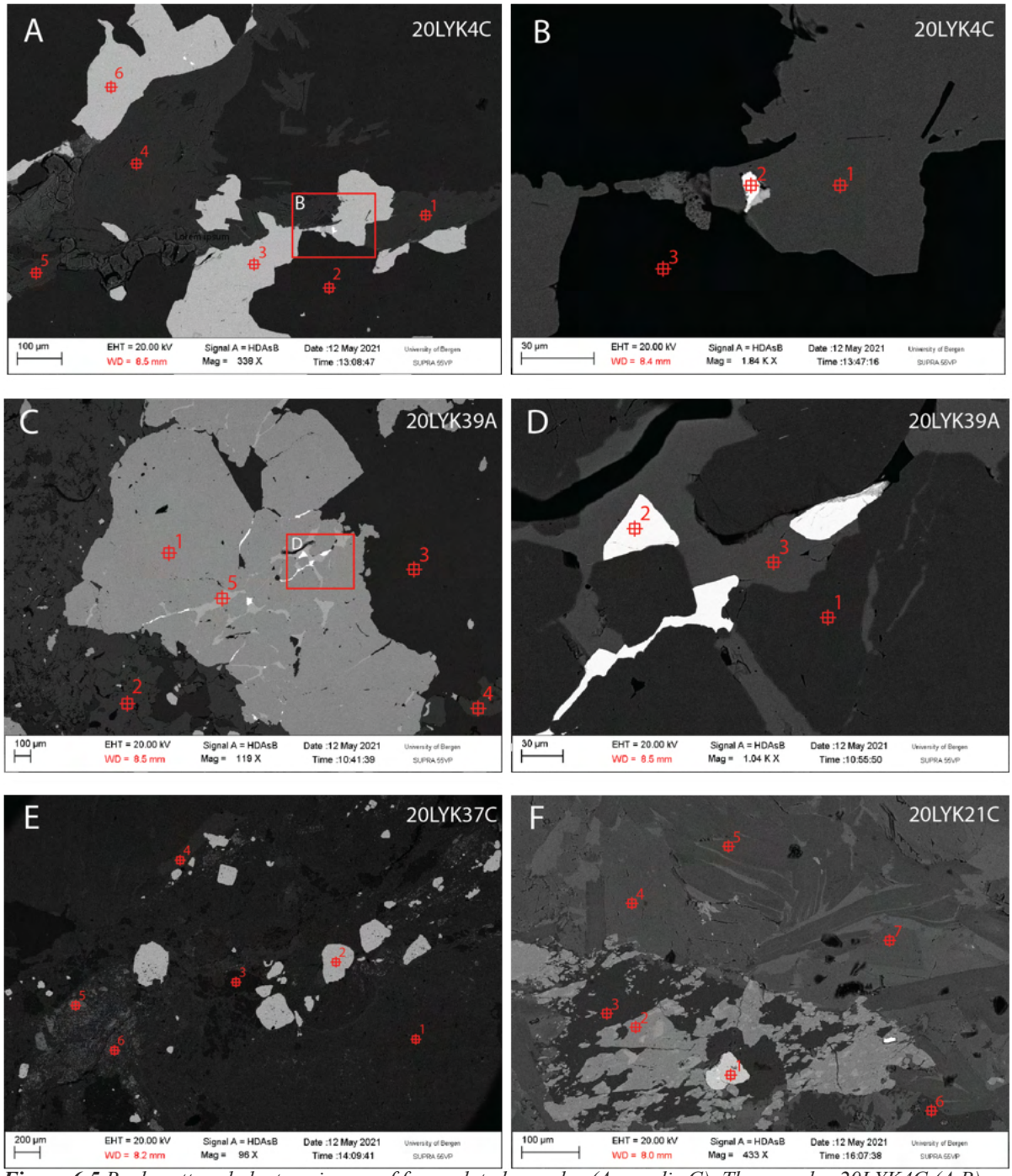

Figure 6.5 *Backscattered electron image of four selcted samples (Appendix C). The samples 20LYK4C (A,B) and 20LYK39A (C,D) represent the brittle type of mineralization, while 20LYK37C (E) and 20LYK21C (F) are from the ductile mineralization type. A: 20LYK4C with six points. 1; muscovite, 2; quartz, 3; chalcopyrite, 4; muscovite, 5; muscovite, 6; chalcopyrite. B: 20LYK4C, zoom in from A with three points. 1; chalcopyrite, 2; galena, 3; quartz. C: 20LYK39A with five points. 1; pyrite, 2; ankerite, 3; quartz, 4; ankerite, 5; chalcopyrite. D: 20LYK39A, zoom in from C with three points. 1; pyrite, 2; galena, 3; chalcopyrite. E: 20LYK37C with six points. 1; ankerite, 2; pyrite, 3; albite, 4; chlorite, 5; rutile, 6; muscovite. F: 20LYK21C with seven points. 1; pyrite, 2; rutile, 3; quartz, 4; ankerite, 5; muscovite, 6; albite, 7; ankerite.*

Mineralization hosted by ductile quartz-carbonate veins

The ductile mineralization is associated with shear zones in E-W, ESE-WNW and NNE-SSW orientation. The mineralization is situated in folded and strongly deformed rocks in both the trondhjemite and the Lykling Ophiolite gabbro. The most prominent example of the E-W ductile mineralization is located at 19LYK1 (Fig. 6.1; Fig. 6.6A, B) and the most prominent ESE-WNW mineralization is located along the historical Harald Haarfagre mine (Fig. 6.1; Fig. 6.6C). The shear zones hosted by the Lykling Ophiolite gabbro have been altered to greenschist (Fig. 6.6B). A typical ductile shear zone mineral assemblage consists of quartz, carbonate, and a mixture of hydrous silicate minerals (Fig. 6.6A). The SEM-EDS analyses revealed chlorite and muscovite as the main hydrous silicates (Fig. 6.5E, F). Variable amount of ankerite, albite, rutile, quartz, and pyrite were also identified. Pyrite crystals are in general larger and have more idiomorphic habits compared to pyrite in brittle quartz veins (Fig. 6.7). Chalcopyrite has not been recorded in the ductile mineralization. Compared to the brittle mineralization, the ductile type has higher amounts of carbonate and hydrous silicates but lower concentrations of quartz and sulphides (Fig. 6.6). In contrast to the brittle veins, where the quartz is massive, quartz in ductile shear zones mostly comes in combinations with carbonates and hydrous silicates (Fig. 6.6A).

Figure 6.6 *Field pictures of ductile structures and associated mineralization. A: Close up of ductile mineralization of quartz (Qtz), carbonate (C) and chlorite (Chl). B: Ductile structure in the gabbro with red lines showing the folding. Hammer for scale. C: Ductile ESE-WNW mineralization at the historical Harald Haarfagre mine with hammer for scale.*

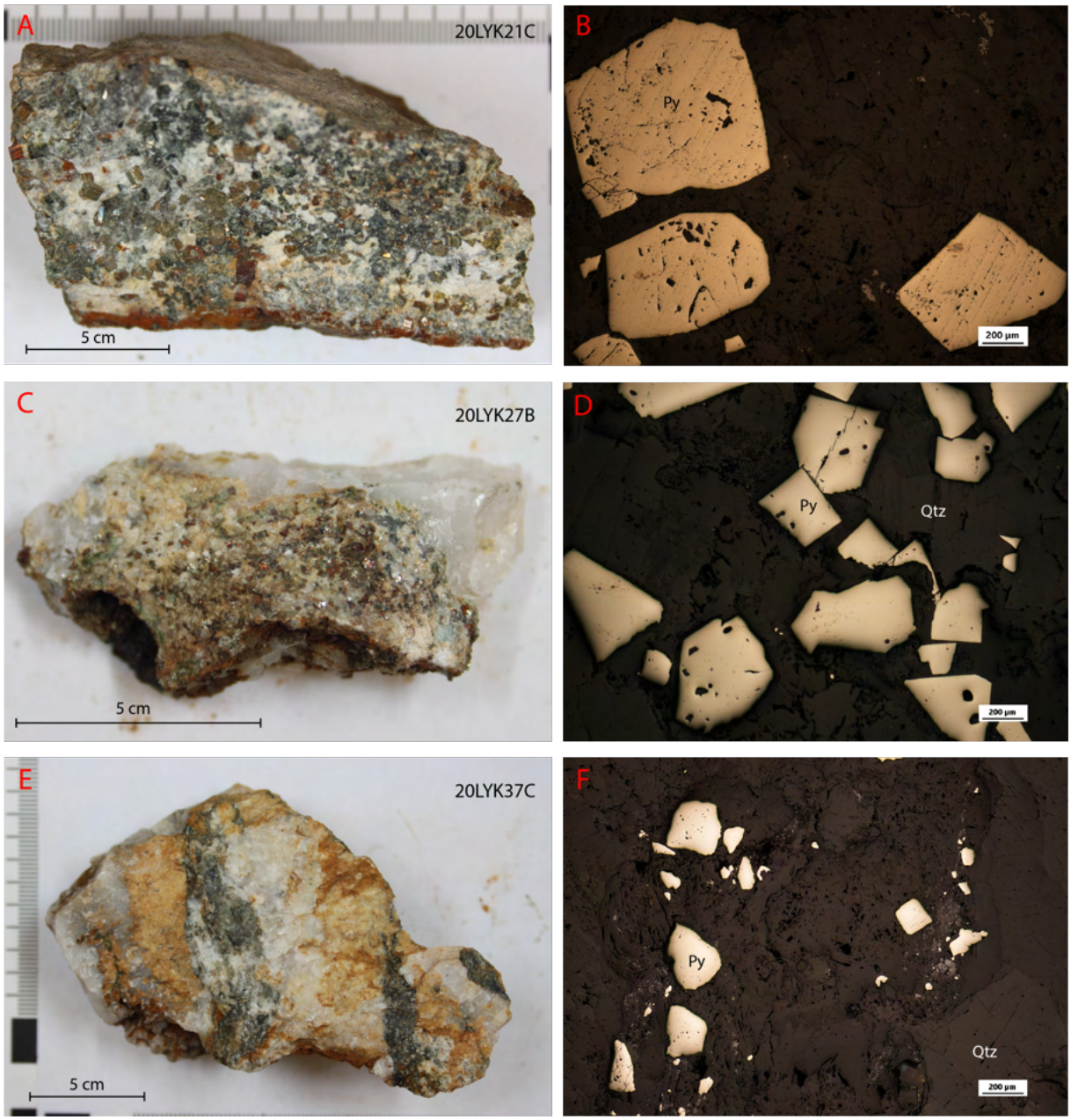

Figure 6.7 *Examples of ductile mineralization. A: Hand specimen of sample 20LYK21C. B: Reflected light photomicrograph of sample 20LYK21C with euhedral pyrite (Py). C: Hand specimen of sample 20LYK27B. D: Reflected light microscopy of 20LYK27B of pyrite (Py) and quartz (Qtz). E: Hand specimen of sample 20LYK37C. F: Reflected light microscopy of sample 20LYK37C with pyrite, quartz.*

6.2 Geochemical characteristics of the host rocks

Lykling Ophiolite gabbro

The Lykling Ophiolite gabbro in the study area occurs in forms of layered and massive varieties. The layered gabbro is characterized by rhythmically changing dark melanocratic and light leucocratic layers. The melanocratic layers are magnetic, while the leucocratic layers are not. Small-scale faulting has affected the layered gabbro (Fig. 6.8A). The layers vary in thickness from centimetres to metres. The orientation of the layered gabbro varies and is strongly affected by the faulting that has affected the area. The Lykling Ophiolite Complex was metamorphosed during the Caledonian orogeny but also it has also been hydrothermally altered during the ore-forming events (Amaliksen, 1983). Microscopic investigations revealed that both the layered and massive gabbro, in the Lykling area, are strongly hydrothermally altered (Fig. 6.8D, E). The identified minerals are pyroxene and plagioclase altered to saussurite. Along the mineralized shear zones, the gabbro appears more altered to greenschist (Fig. 6.6B). The gabbro samples have also been overprinted with hydrothermal veinlets composed of quartz and minor amounts of carbonates (Fig. 6.8B). Previous studies (e.g., Amaliksen, 1983) suggest that the Lykling Ophiolite gabbro has a tholeiitic character, a low REE content and a negative Ce anomaly.

Trondhjemite

Trondhjemite plutons intrude the Lykling Ophiolite and the Geitung Unit. The rock was observed in the northern and southern part of the study area (Fig. 6.2). Results from this study as well from Saltvedt (2021) show that this type of lithology in the study area plots as an albite-rich (Ab) trondhjemite (Fig. 6.9). The samples 20LYK19C and 20LYK26C in Fig. 6.10 presented the typical mineralization assemblage of the trondhjemite. The samples are medium grained and microscopic investigation of the trondhjemite revealed chloritization. Trondhjemite consist mostly of quartz with 77.51 wt.% (Table 1), altered plagioclase and evenly distributed chlorite. Quartz occurs as ≤100 μm grains. The smaller veins and grains appear as secondary mineralization, mineralized by hydrothermal fluids (Fig. 6.10). Figures 6.10 G-H exemplify that plagioclase has been hydrothermally altered to saussurite. The degree of saussurization varies between samples. Sporadically, trondhjemite is crosscut by quartz and muscovite veinlets (Fig. 10C, D). Minor amounts of disseminated sulphides have been recorded as well.

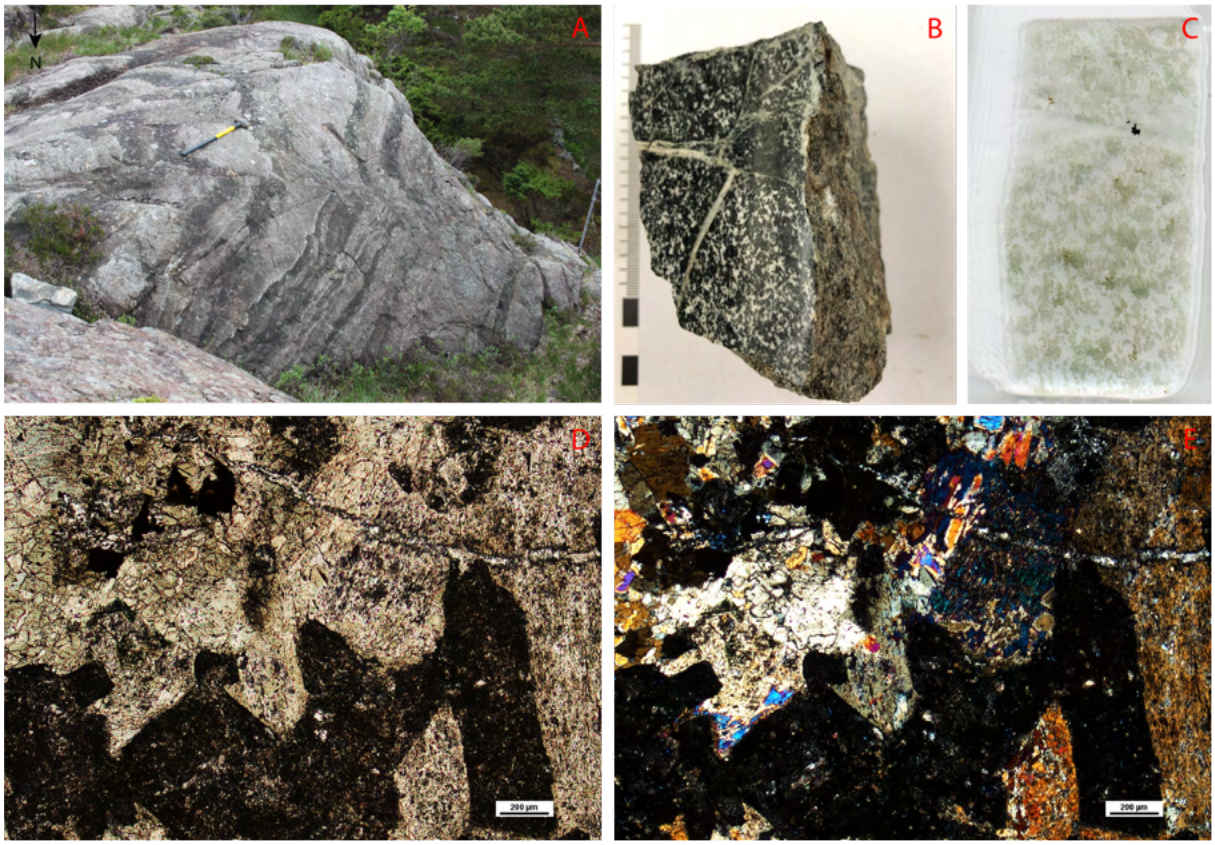

Figure 6.8 *A: Photo of the layered gabbro with small-scale faulting close to the Haugesund mine. Sledgehammer for scale. B: Hand specimen of gabbro with mineralized veins. C: Thin section of the hand specimen. D: PPL photomicrograph from the thin section of strongly hydrothermally altered gabbro. E: XPL photomicrograph of strongly hydrothermally altered gabbro.*

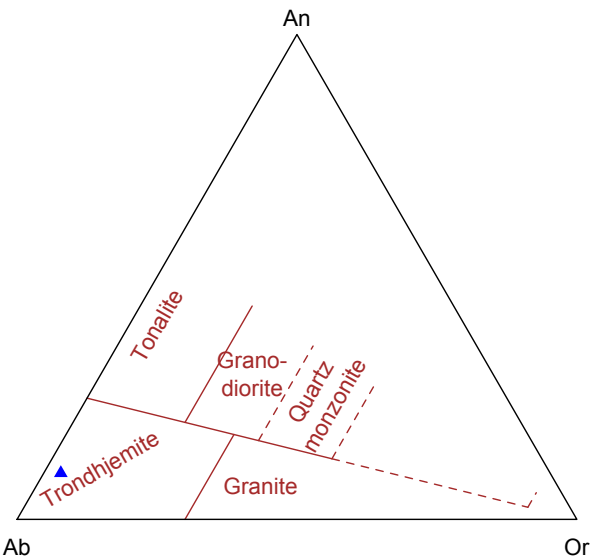

Figure 6.9 *The feldspar triangle classifying the samples as trondhjemite with a blue triangle (O'Connor, 1965).*

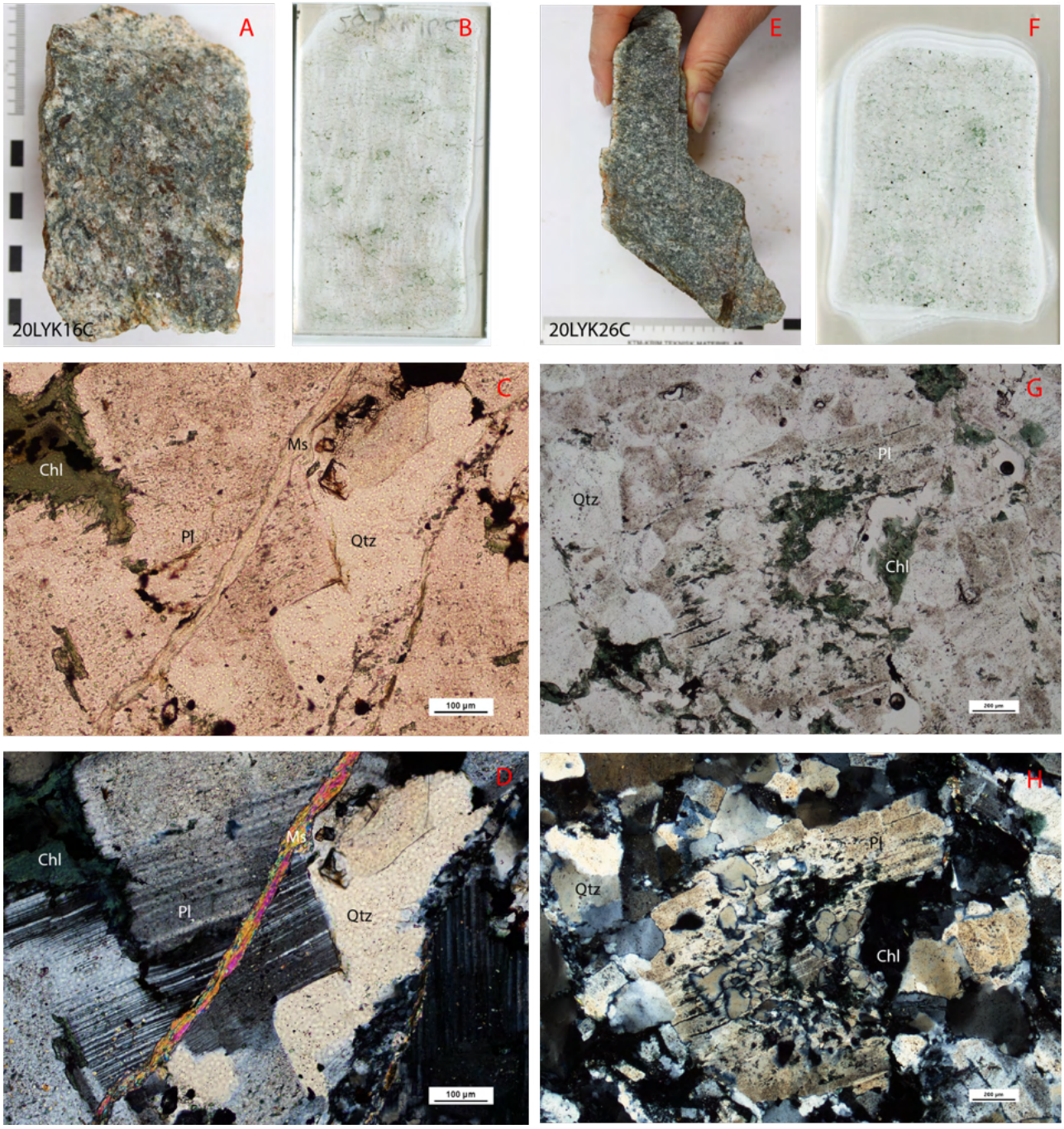

Figure 6.10 *Trondhjemite samples; A: Hand specimen of sample 20LYK16C. B: Thin section from the sample from A. C: PPL photomicrograph from microscopy with quartz (Qtz), plagioclase (Pl), chlorite (Chl) and a Muscovite vein (Ms). D: XPL photomicrograph of the 20LYK16C sample from the same area as C. E: Hand specimen of sample 20LYK26C. F: Thin section from the hand specimen in E. G: PPL photomicrograph from microscopy of quartz (Qtz), plagioclase (Pl) and chlorite (Chl). The plagioclase has been hydrothermally altered to saussurite. H: XPL photomicrograph of the 20LYK26C sample from the same area as H.*

The composition of trondhjemite from the study area normalized to NMORB and shows depletion in Nb, Sr, P, Zr and Ti (Fig. 6.11A). The composition show enrichment in Cs, Rb, Ba, Th, K and Pb compared to NMORB. The trondhjemite REE spider diagram normalized to a chondrite shows a gradual increase in LREE, a flat trend for HREE and a pronounced negative Eu anomaly (Fig. 6.11B). The negative Eu anomalies reflect plagioclase fractionation.

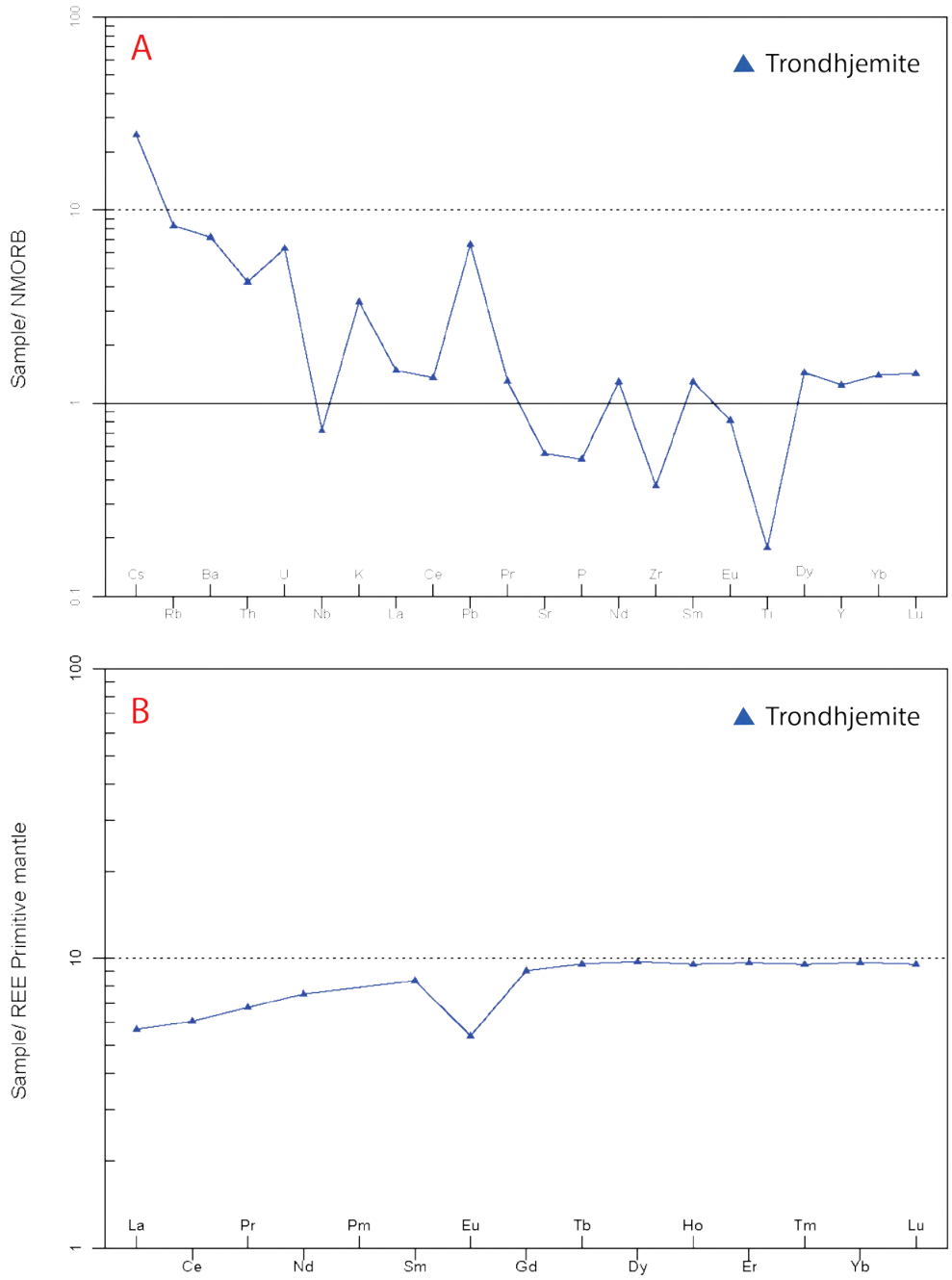

Figure 6.11 *Trondhjemite sample plotted in spider diagrams A: Trondhjemite sample/NMORB vs. elements (Sun & McDonough, 1989) and trondhjemite sample/REE primitive mantle vs. REE (Anders & Grevesse, 1989).*

Table 1. *Major and trace element compostions of selected mafic dikes and trondhjemite from the Lykling area.*

	19LYK2A	**20LYK12**	**20LYK13B**	**20LYK20K**	**20LYK20L**	**20LYK27E1**	**20LYK38C**	**20LYK26C**
Petrology	Mafic dike	Mafic dike	Mafic dike	Mafic dike east	Mafic dike west	Mafic dike	Mafic dike	Trondhjemite
Direction	NNE-SSW	ESE-WNW	ESE-WNW	NNE-SSW	NNE-SSW	ESE-WNW	ESE-WNW	
Mineralization	Brittle with mineralization	Brittle barren	Brittle with mineralization	Brittle with mineralization	Brittle with mineralization	Ductile with mineralization	Brittle with mineralization	Trondhjemite
Major elements (wt.%)								
SiO_2	47.77	46.95	36.78	49.92	54.06	44.20	42.05	77.51
TiO	0.87	1.38	2.53	0.77	0.51	0.47	1.58	0.23
Al_2O_3	13.11	15.10	11.99	15.26	16.57	12.27	10.68	11.10
Fe_2O_3	9.69	9.79	26.91	8.35	5.23	9.38	18.23	2.81
MnO	0.17	0.14	0.22	0.17	0.11	0.21	0.17	0.06
MgO	4.92	7.17	8.22	3.53	1.93	8.43	9.05	0.90
CaO	8.02	9.08	6.35	6.82	5.46	7.28	8.96	0.98
Na_2O	3.97	3.64	1.76	1.71	2.92	0.79	1.55	4.84
K_2O	0.07	0.11	0.07	3.43	3.98	1.74	0.21	0.24
P_2O_5	0.44	0.17	0.07	0.41	0.27	0.07	0.06	0.06
Trace elements (ppm)								
Lu	27.66	22.14	19.74	15.12	10.84	33.97	13.49	4.93
Sc	28.03	31.51	63.72	18.40	8.29	30.30	74.61	11.31
V	350.70	216.80	1119.50	194.90	98.29	197.10	932.60	6.09
Cr	88.50	343.90	1.82	9.44	1.04	579.90	190.40	0.98
Co	25.41	37.76	91.37	14.83	9.83	27.27	77.98	1.67
Ni	35.37	35.43	4.03	5.12	0.68	162.10	51.61	0.87
Cu	169.00	21.75	114.10	2.31	67.57	59.40	145.30	16.24
Zn	115.10	70.69	115.60	40.35	40.34	139.70	70.31	26.46
Rb	0.77	1.16	0.24	109.70	152.20	41.30	5.61	4.64
Sr	270.30	143.20	75.22	338.50	430.90	78.31	117.50	49.34
Y	13.35	21.67	8.96	19.26	19.24	15.63	10.38	34.81
Zr	109.70	97.67	7.64	100.60	112.60	24.51	8.98	27.58

Nb	12.21	7.77	0.15	9.22	9.77	0.32	0.14	1.68
Cs	0.34	0.15	0.10	2.53	3.37	0.59	0.77	0.17
Ba	25.12	17.31	4.10	648.70	815.60	112.60	32.46	45.57
Hf	3.25	2.72	0.33	2.73	2.92	0.82	0.40	1.27
Ta	0.64	0.53	0.01	0.52	0.58	0.03	0.02	0.11
Pb	5.23	0.87	1.02	5.10	6.96	11.29	4.89	1.99
Th	9.84	1.99	0.00	7.28	8.69	0.20	0.00	0.51
U	3.84	0.41	0.01	2.78	3.03	0.12	0.01	0.30
Y	14.06	21.76	8.52	19.73	18.95	15.97	10.52	33.71
La	19.74	12.10	0.37	28.07	32.53	2.54	0.37	3.69
Ce	45.46	25.92	1.10	56.02	63.09	5.81	1.38	10.16
Pr	6.25	3.60	0.21	7.05	7.63	0.93	0.28	1.72
Nd	26.81	16.16	1.54	29.18	30.88	5.27	2.08	9.41
Sm	5.14	4.04	0.70	5.88	5.80	1.82	0.96	3.40
Eu	1.29	1.40	0.44	1.65	1.58	0.66	0.38	0.83
Gd	4.09	4.51	1.22	5.00	4.73	2.59	1.49	4.93
Tb	0.55	0.75	0.23	0.71	0.70	0.42	0.29	0.95
Dy	2.98	4.64	1.70	4.00	3.97	2.65	2.04	6.55
Ho	0.59	0.93	0.38	0.77	0.79	0.57	0.44	1.42
Er	1.71	2.59	1.10	2.21	2.25	1.64	1.24	4.22
Tm	0.24	0.36	0.16	0.31	0.32	0.23	0.18	0.65
Yb	1.60	2.28	1.08	2.01	2.11	1.46	1.13	4.26
Lu	0.26	0.34	0.17	0.30	0.34	0.23	0.17	0.65

Mafic dikes

At least two generations of mafic dikes crosscut the Lykling Ophiolite gabbro and the associated trondhjemite intrusions (Fig. 6.12). The NNE-SSW oriented dikes have been observed cutting the ESE-WNW oriented dike, giving a relative age (Fig. 6.12B). The older generation dikes have an ESE-WNW orientation, and the younger generation goes in NNE-SSW direction. The ESE-WNW oriented dikes are coarse grained and are highly affected by deformation and faulting (Fig. 6.12). The NNE-SSW oriented dikes are fine to medium grained and is lighter than the ESE-WNW dikes. The NNE-SSW oriented dikes are most frequently observed in the northern part of the study area (Fig. 6.2). Established from microscopic observations, the NNE-SSW dikes are basalts overprinted by hydrothermal alterations (Fig. 6.13). The high degree of alteration makes it difficult to extinguish the different mineral phases (Fig. 6.13G, H) but one recognized alteration product in the basalt is chlorite. Seven samples from the mafic dikes were selected for lithogeochemistry (Table 1). The ESE-WNW mineralized samples 20LYK13B and 20LYK38C have tholeiitic signature and has low SiO_2 and alkali content relative to the NNE-SSW oriented dikes (Fig. 6.14). In contrast, the barren ESE-WNW plots as calc-alkaline in the AFM diagram and as a basalt in the TAS diagram with higher concentrations of SiO_2 than in the ESE-WNW mineralized dikes. The NNE-SSW oriented dikes have calc-alkaline character and varies from basaltic to andesitic in their composition. They have higher SiO_2 concentrations relative to the ESE-WNW dikes. Harker diagrams with major elements versus SiO_2 of the mafic dikes reveals higher concentrations of MgO, Ti_2O and FeOt in the ESE-WNW dikes relative to the NNE-SSW dikes that contain higher concentrations of Al_2O_3, P_2O_5 and K_2O (Fig. 6.15). The barren ESE-WNW sample plots different than the mineralized ESE-WNW with higher concentrations of Na_2O, Al_2O_3, P_2O_5 and lower concentrations of FeOt and MgO.

Figure 6.12 *A: ESE-WNW deformed mafic dike hosted in trondhjemite. B: ESE-WNW mafic dike (red dots) cut by the NNE-SSW mafic dike (yellow dots) hosted in the Lykling Ophiolite gabbro.*

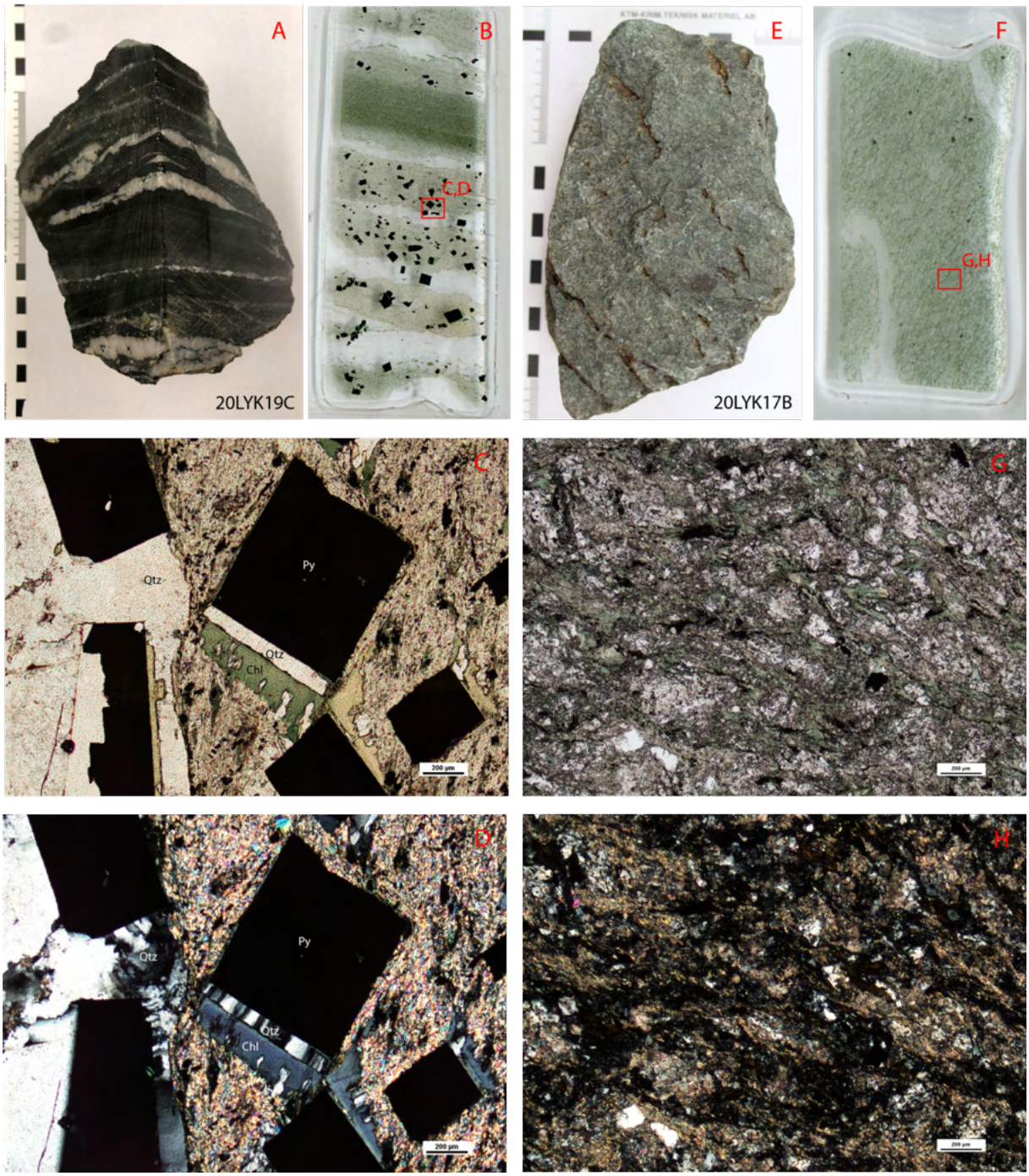

Figure 6.13 *Two NNE-SSW trending mafic dike; A: Hand specimen of mineralized NNE-SSW dike. B: Thin section of A with red box indicating where the photomicrographs C,D is from. C: PPL photomicrograph of thin section B, with quartz (Qtz) veins and large euhedral pyrite (Py) minerals, chlorite (Chl) and hydrothermal altered basalt matrix. D: XPL photomicrograph of thin section B. E: Hand specimen of NNE-SSW mafic dike. F: Thin section of E with red box indicating where microscope photos G,H is from. G: PPL photomicrograph of thin section D with hydrothermally altered basalt containing the alteration mineral chlorite. H: XPL photomicrograph of thin section D.*

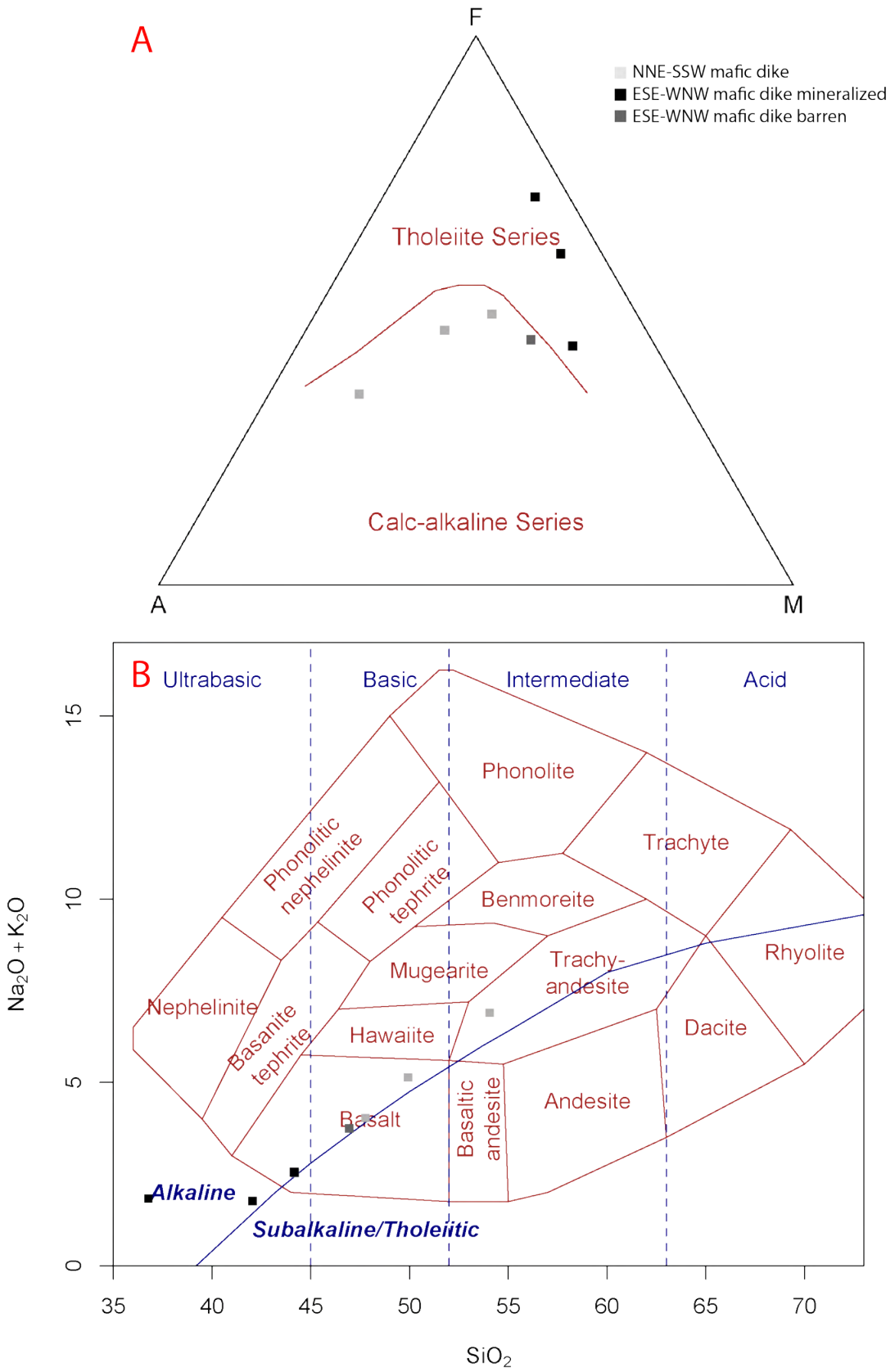

Figure 6.14 *A: Compostion of the mafic dikes plotted in an AFM diagram (Irvine & Baragar, 1971). B: Compostion of the mafic dikes plotted in a TAS diagram (Cox et al., 1979).*

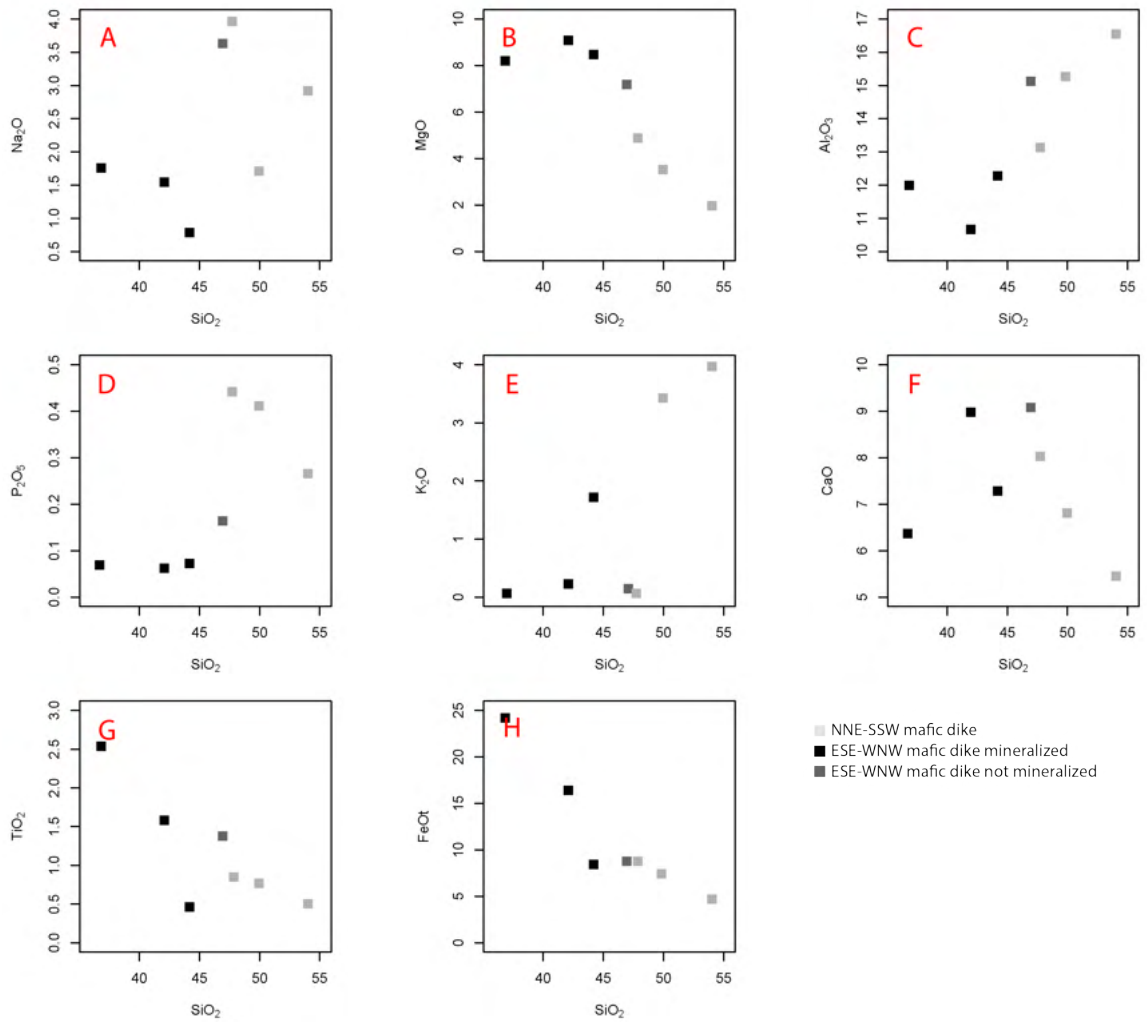

Figure 6.15 *Harker diagrams for selected dikes from the Lykling area with major elements.*

The NNE-SSW mafic dike samples reveal an enrichment in LILE elements compared to normalized MORB (Fig. 6.16A). They exhibit negative Nb, Ce, Zr anomalies and positive Pb, K anomalies. The NNE-SSW trending dike represented by sample 19LYK2A is a bit different with negative Rb, Cs and Ba anomalies relative to the other dikes with the same orientation. The ESE-WNW mineralized samples have pronounced negative Th anomalies and negative anomalies for Zr, La, Ce. They show positive Cs, Rb, K, Pb, Ti anomalies. The ESE-WNW oriented dike 20LYK27E1 stands out from the other ESE-WNW samples with generally higher composition of Cs, Rb, Th and U. The barren ESE-WNW is unlike the ESE-WNW mineralized samples with generally higher composition and positive Th anomaly and negative Rb, Ba, K anomaly.

The NNE-SSW mafic dikes are relatively enriched in REE compared to the primitive mantle (Fig. 6.16B). The spider diagram show enrichment in LREE, with lower abundance of HREE. The ESE-WNW mineralized dike samples are depleted in LREE, with negative La, Ce, Pr anomalies (Fig. 6.16B). The barren ESE-WNW dike sample contrasts with the ESE-WNW mineralized dike and is very different with generally higher in composition of REE and enrichment in LREE. The ESE-WNW trending dike represented by sample 20LYK27E1, has a different composition than the other ESE-WNW dike samples. The sample 20LYK27E1 show a linear content at four times primitive mantle. The barren ESE-WNW sample is more alike the NNE-SSW dikes in composition.

In Figure 6.17 the mafic dikes are demonstrated Harker diagrams with SiO_2 versus different trace elements. The NNE-SSW oriented dikes have generally higher concentrations in all the Harker diagrams. All samples plot in a similar pattern for Sr, La, Rb and Ce with an increasing amount of silica and trace elements from very low concentrations ESE-WSW dikes to higher concentrations of the NNE-SSW mafic dikes. The NNE-SSW dikes have in general higher concentrations of trace elements except for Cr (Fig. 6.17A). The sample 20LYK27E1 deviates from the rest of the ESE-WNW dikes with the highest Cr and Ni value (Fig. 6.17
A, B).

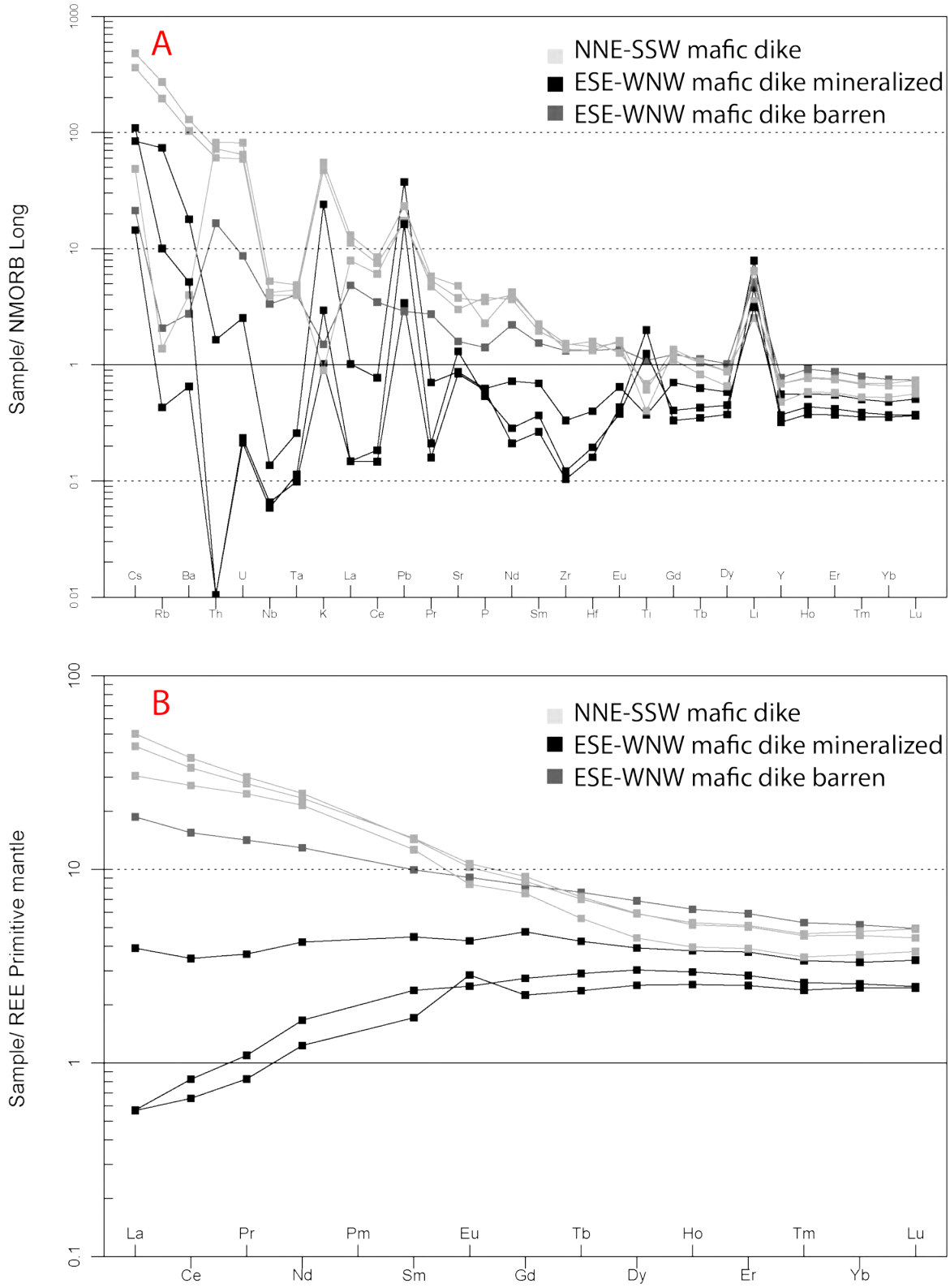

Figure 6.16 *A: The MORB-normalized trace element pattern for the mafic dikes. B: The REE primitive mantle pattern for the mafic dikes (McDonough & Sun,1995; Sun & McDonough, 1989).*

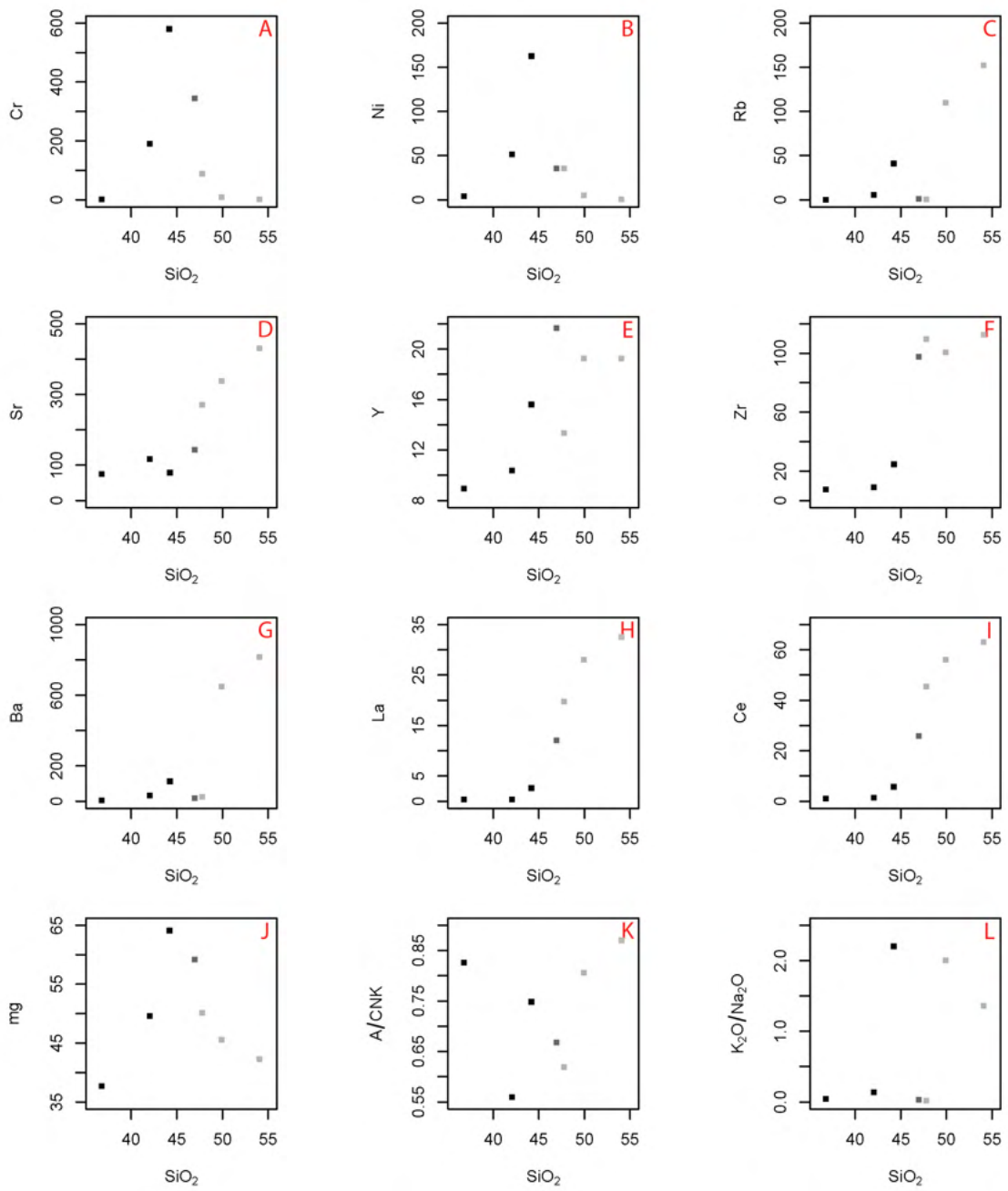

Figure 6.17 Harker diagrams for selcted dikes from the Lykling area with trace elements.

6.3 XRD analysis

Three samples of hydrothermal alteration assemblage were analysed by X-ray diffraction (XRD) technique. The results are illustrated in Figure 6.18. Two of the samples, 19LYK1A and 20LYK7D, are from a ductile mineralization, while sample 20LYK6 is from brittle mineralization (Fig. 6.1). All samples contain quartz and carbonate. The brittle sample 20LYK6 resembles the 20LYK7D sample, with both containing quartz, carbonate and chlorite, but the 20LYK6 has a much lower intensity in general for all peaks. The ductile samples are located approximately along the same fault seen in Figure 6.1. Sample 19LYK1A contains hedenbergite and epidote, and sample 20LYK7D comprise of chlorite.

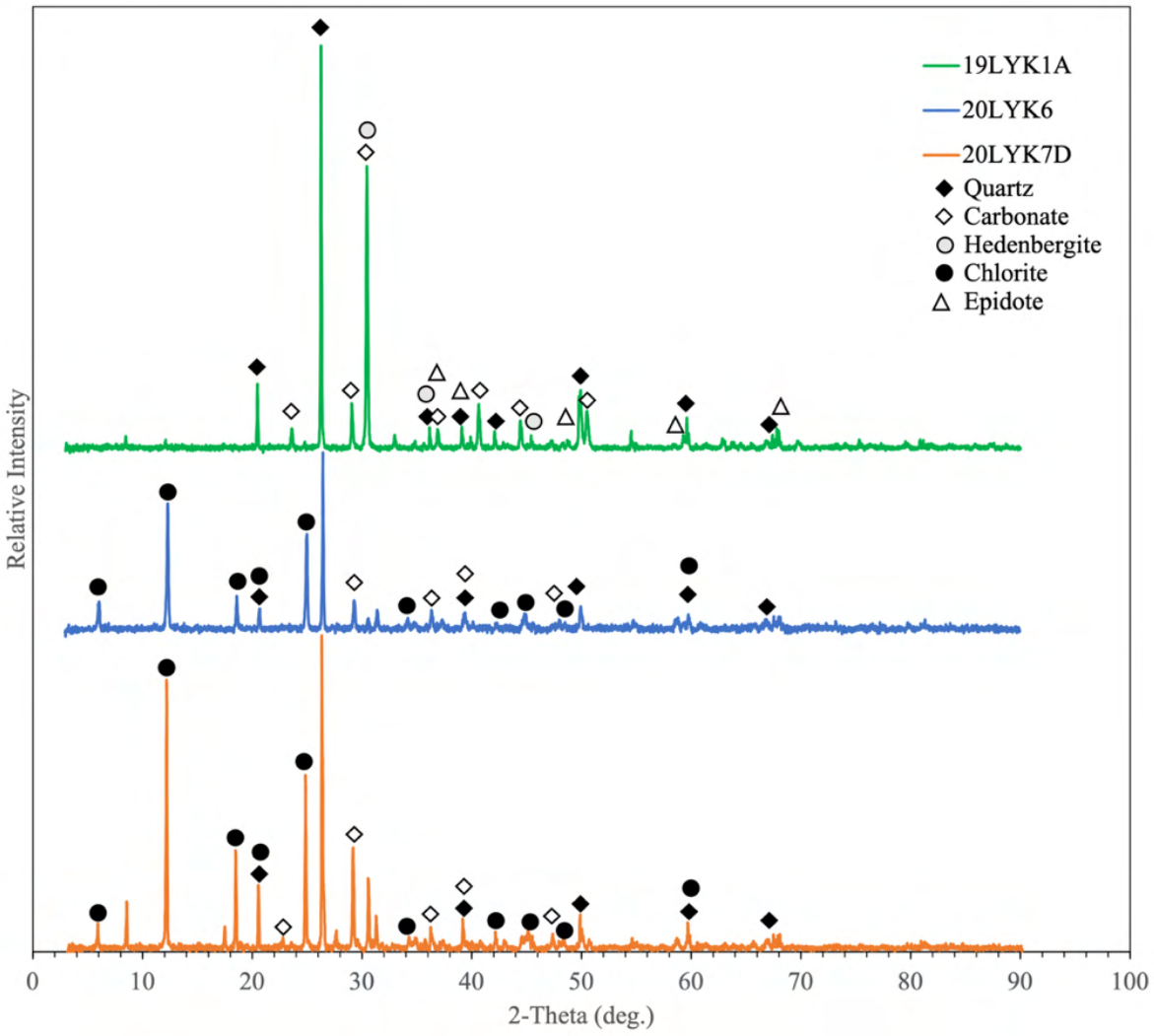

Figure 6.18 *XRD analysis results of sample 19LYK1A, 20LYK6 and 20LYK7D.*

6.4 Gold Assay

Table 1 *Results of the Au assay analyses. All values are expressed in part per bilion (ppb).*

Sample name	Au (ppb)	Mineralization	Direction	Host
20LYK18A	6	Brittle	NNE-SSW	Trondhjemite
20LYK25B	2044	Ductile	NNE-SSW	Trondhjemite
20LYK24B	8	Ductile	E-W	Trondhjemite
20LYK15D	4	Ductile	NNE-SSW	Trondhjemite
20LYK13A	4	Brittle	NNE-SSW	Gabbro
20LYK20B	154	Brittle	NNE-SSW	Trondhjemite
19LYK1A	17	Ductile	E-W	Gabbro
20LYK4C	275	Brittle	NNE-SSW	Gabbro
19LYK2A	107	Brittle	NNE-SSW	Gabbro
20LYK39A	785	Brittle	ESE-WNW	Gabbro
20LYK39C	29 000	Brittle	ESE-WNW	Gabbro
20LYK37C	240	Ductile	ESE-WNW	Gabbro

Twelve samples from both brittle and ductile type of quartz veins were sent for assay to determine their Au concentration. The results are presented in Table 2. The gold content in the different samples varies very in concentration for brittle and ductile structure and between the two host rocks. The highest concentration of 29 ppm Au is found in the brittle quartz vein from Harald Haarfagre mine (sample 20LYK39C; Figure 6.4E). The second highest concentration of 2.044 ppm Au has been recorded for the ductile type of the mineralization represented by sample 20LYK25B. Sample 20LYK20B, 20LYK4C, 19LYK2A, 20LYK39A and 20LYK37C have a moderate Au concentration between 107-785 ppb. Samples 20LYK18A, 20LYK24B, 20LYK15D, 20LYK13A and 19LYK1A have the lowest concentration between 4-17 ppb.

6.5 Fluid inclusion petrography and microthermometry

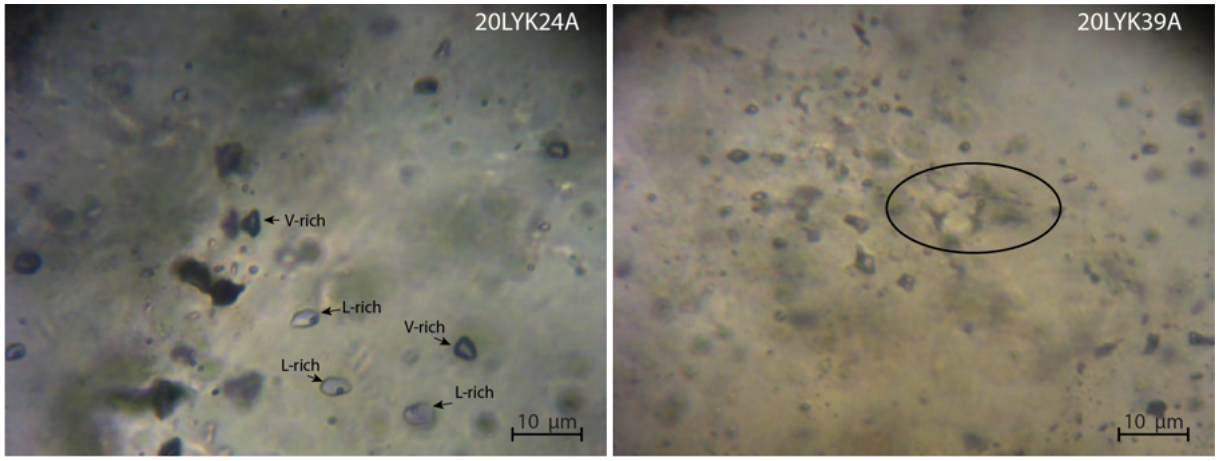

Figure 6.19 *Photomicrographs of fluid inclusions A: Fluid inclusion assemblage (FIA) hosted in quartz from the ductile shear zone hosted sample 20LYK24A. B: Decrepitated fluid inclusions in quartz from brittle mineralization 20LYK39A*

Eleven thick sections were prepared and analysed for fluid inclusions to identify the properties of the ore-forming fluids. Fluid inclusions suitable for microthermometry were found in quartz. Based on their petrographic features at room temperature, the fluid inclusions from the Lykling area can be divided into three types; Type 1: aqueous two phase (L+V) liquid-rich inclusions; Type 2: two phase (L+V) vapuor-rich inclusions; and Type 3: decrepitated and relict fluid inclusions (Fig. 6.19). A few fluid inclusion assemblages (FIA) consist of coexisting Type 1 and Type 2 inclusions (Fig. 6.19A) reflecting entrapment from a boiling fluid. The Type 3 fluid inclusions are arranged in linear arrays and is suggested to be decrepitated because of fluid overpressure (Sterner & Bodnar, 1989) and deviatoric stress (Tarantola et al., 2010; Zoheir et al., 2019). The majority of fluid inclusions assemblage (FIA) show post-entrapment reequilibration.

Microthermometry of the fluid inclusions in the brittle quartz type indicate large variation with homogenization temperatures between 120 to 190 °C, low to moderate salinities (0.2-12 wt.% NaCl) and ice melting temperature (Tm-ice) between -0.1 to -8.4 ºC (Fig. 6.19; Appendix B). Brittle quartz vein indicates mixing of fluids represented in the NNE-SSW sample 19LYK2A hosted in gabbro. The sample revealed the eutectic temperature -21 ºC in FIA 1 and -52 ºC in FIA 2 (Appendix B). The eutectic temperature -21 ºC reflect NaCl-H_2O inclusions and the eutectic temperature -52 ºC indicate the presence of the dissolved salts NaCl-$CaCl_2$ in the inclusions (Crawford, 1981). The FIA 1 exhibited ice melting temperature (Tm-ice) between (-0.1 to -0.5 ºC), low salinity (0.18-0.88 w.%, NaCl eq) and homogenization temperatures (Th) at between 125 to 128 ºC. The FIA 2 exhibited lower Tm-ice between -8.0 ºC to -8.4 ºC,

moderate salinity (11.7-12.16 w.%, NaCl eq) and higher homogenization temperatures at 175 to 180 ºC.

The ductile quartz type revealed general higher temperatures and constant salinity relative to the brittle type (Fig. 6.20), exhibiting homogenization temperature between 165 to 182 ºC, salinity between 3.23 to 6.45 w.%, NaCl eq. and ice melting temperature between -1.9 to -3.5 ºC (Appendix B). Indication of boiling FIA is observed in the sample 20LYK37C, i.e., in a ESE-WNW trending ductile vein from the historical Harald Haarfagre (Fig. 6.20). The ductile quartz type indicates boiling but does not indicate mixing of fluids in comparison to the brittle quartz type. There is little indication that the host rock (gabbro and trondhjemite) had any effect on the fluid inclusions. Based on Wilkinson (2001) model, the homogenization temperature and the average salinity the mineralized quartz veins are formed under the condition of epithermal system (Fig. 6.21).

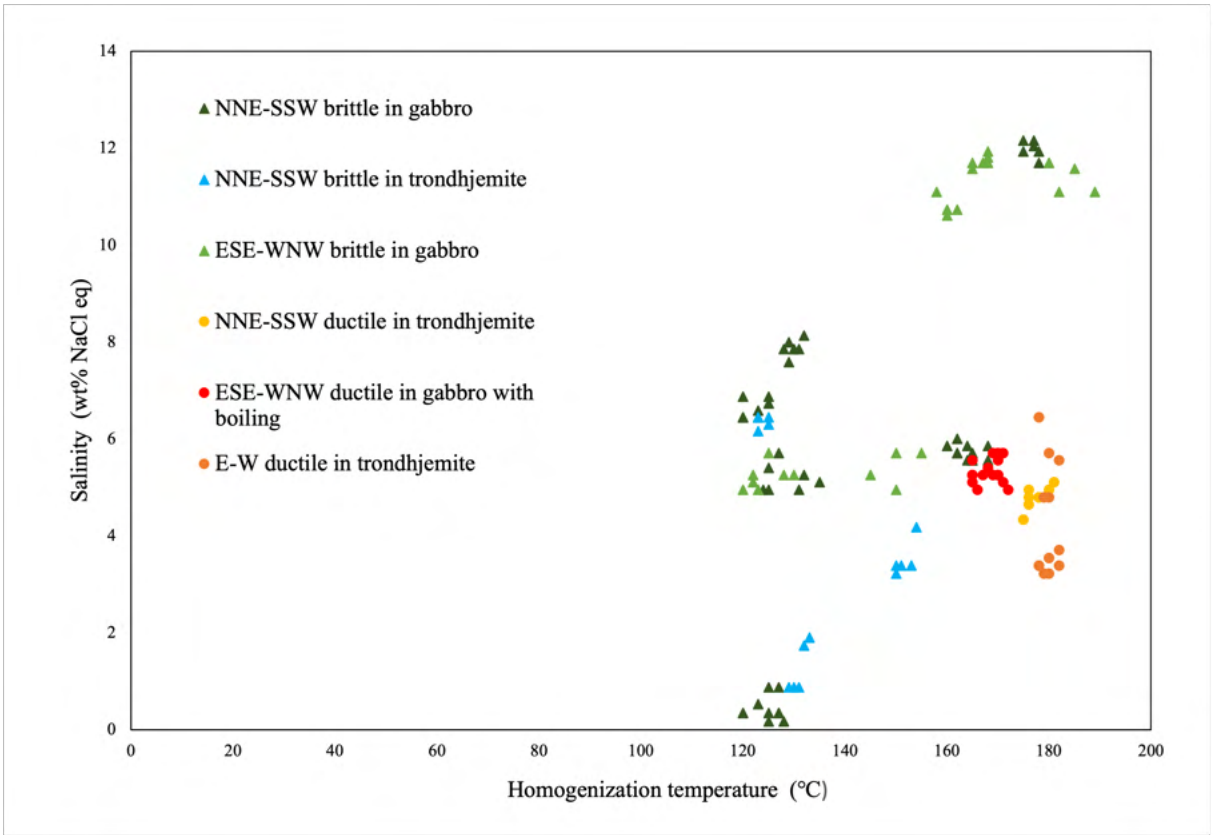

Figure 6.20 *Fluid inclusion presented in salinity - homogenization temperature diagram.*

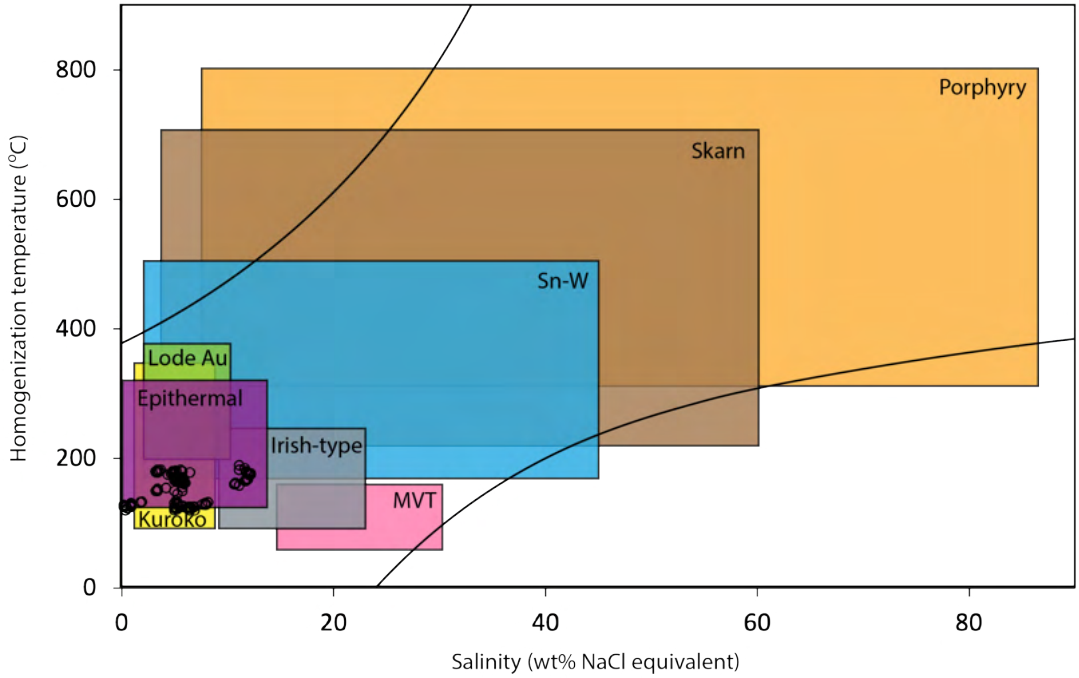

Figure 6.21 *The fluid inclusion results plotted in a homogenisation temperature – salinity diagram illustrating typical ranges for inclusions from different deposit types. The all the fluid inclusions plot inside the Epithermal box (purple) (Modified from Wilkinson, 2001).*

Table 2 *$\delta^{13}C$ and $\delta^{18}O$ data obtained from carbonates assciated with the Au-bearing quartz veins in the Lykling area*

Sample name	Mineralogy	Direction	Mineralization and host	$\delta^{13}C$ (VPDB)	$\delta^{18}O$ (VPDB)	$\delta^{18}O$ (VSMOW)	$\delta^{18}O$ ankerite (VSMOW)
20LYK6	Ankerite	NNE-SSW	Brittle in gabbro	-3.5	-19.6	10.7	10.7
20LYK20J	Ankerite	NNE-SSW	Brittle in trondhjemite	-5.2	-20.8	9.5	9.5
20LYK39A	Ankerite	ESE-WNW	Brittle + sulphides in gabbro	-3.8	-19.7	10.6	10.6
19LYK1A	Ankerite	E-W shear zone	Ductile in gabbro	-3.7	-18.9	11.4	11.4
20LYK3B	Ankerite	NNE-SSW	Ductile in gabbro	-3.7	-16.9	13.5	13.5
20LYK7D	Ankerite	NNE-SSW	Ductile in gabbro	-4.0	-19.8	10.5	10.5
20LYK10C	Ankerite	NNE-SSW	Ductile in gabbro	-4.1	-20.4	9.9	9.9
20LYK15D	Ankerite	NNE-SSW	Ductile in gabbro	-4.2	-20.4	9.9	9.9
20LYK24A	Ankerite	E-W shear zone	Ductile in gabbro	-4.1	-20.1	10.1	10.1
20LYK24B	Ankerite	E-W shear zone	Ductile in gabbro	-4.2	-20.1	10.1	10.1
20LYK25B	Ankerite	NNE-SSW	Ductile in gabbro	-4.0	-20.7	9.6	9.6
20LYK37C	Ankerite	ESE-WNW	Ductile in trondhjemite	-3.8	-19.8	10.5	10.5
20LYK21C	Ankerite	NNE-SSW	Ductile + sulphides in gabbro	-4.5	-20.3	10.0	10.0
20LYK21B	Ankerite	NNE-SSW	Ductile + sulphides in gabbro	-4.4	-20.5	9.8	9.8

6.6 Stable isotope characteristics of the mineralization

Oxygen and carbon isotopes

Measurements of $\delta^{13}C$ and $\delta^{18}O$ for carbonates (ankerite) have been conducted for 13 samples (Table 4). The stable isotope measurements reveal little difference in the isotopic measurements between carbonates associated with the brittle and ductile mineralizing. The measured $\delta^{13}C$ values range between -5.2 and -3.5 ‰ V-PDB and $\delta^{18}O$-values between 9.5 and 13.5 ‰ V-SMOW. The obtained $\delta^{13}C$ versus $\delta^{18}O$ data reflect a strong input of magmatic CO_2 (Fig. 6.22).

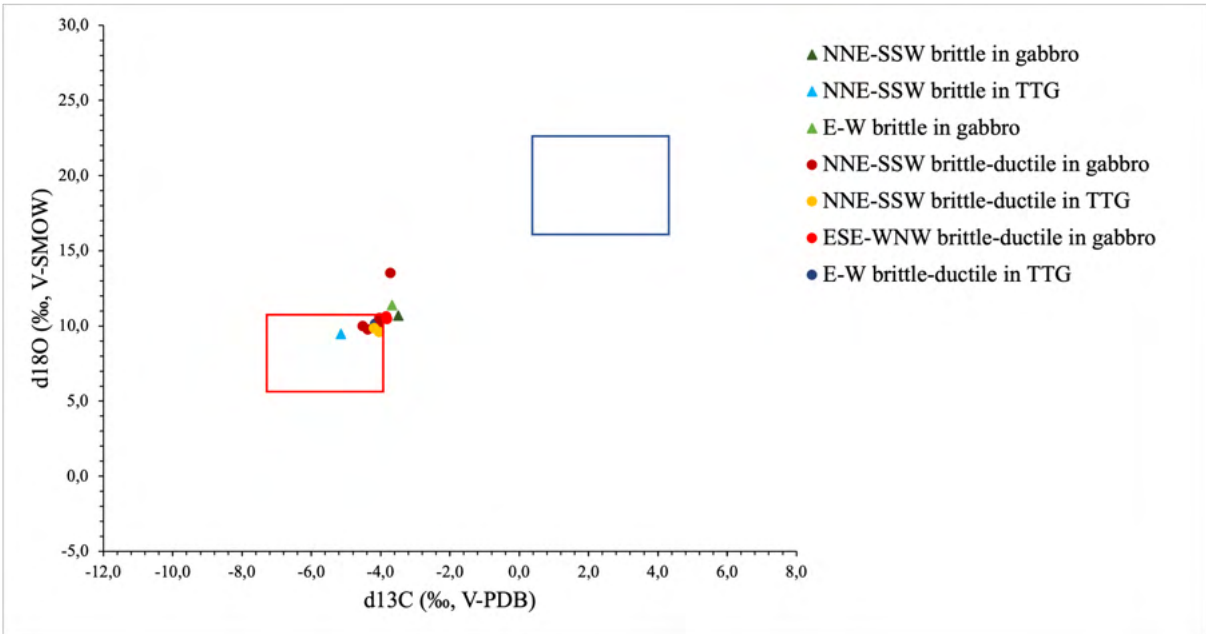

Figure 6.22 *$\delta^{18}O$ (V-SMOW) vs $\delta^{13}C$ (V-PDB) plot. The blue box represents values for marine carbonates (Veizer & Hoefs, 1976)) and the red box represent the values for magmatic carbonates (Stakes & O'Neil, 1982).*

Sulphur isotopes

Table 3. *Sulphide isotope data obstained from sulphides associated with the Au-bearing quartz veind in the Lyklung area.*

Sample	Mineralization and host	Direction	Mineralogy	δ^{34}S V-CDT (‰)
20LYK4C	Brittle in gabbro	NNE-SSW	Chalcopyrite	6.87
20LYK4D	Brittle in gabbro	NNE-SSW	Chalcopyrite	7.17
20LYK39A po2	Brittle in gabbro	ESE-WNW	Chalcopyrite	6.73
20LYK14B	Brittle in gabbro	NNE-SSW	Pyrite	5.96
20LYK20B	Brittle in trondhjemite	NNE-SSW	Pyrite	4.81
20LYK39A po1	Brittle in gabbro	ESE-WNW	Pyrite	7.20
20LYK39C	Brittle in gabbro	ESE-WNW	Pyrite	7.20
20LYK21B	Ductile in trondhjemite	NNE-SSW	Pyrite	3.08
20LYK27B	Ductile in trondhjemite	NNE-SSW	Pyrite	0.23
20LYK37C	Ductile in gabbro	ESE-WNW	Pyrite	7.24

The δ^{34}S (V-CDT ‰) values obtained for sulphides from the brittle and ductile type gold-bearing quartz vein is listed in Table 4. Chalcopyrite from the brittle veins show the δ^{34}S-value between 6.73 and 7.17‰. There was no observed precipitation of chalcopyrite in the ductile type of mineralization. Pyrite in brittle mineralization yields the δ^{34}S-values 4.81 to 7.2‰ and in ductile veins δ^{34}S-value between 0.23 to 7.24‰. There is a distinct difference between the samples hosted in the Lykling Ophiolite gabbro and the trondhjemite (Fig. 6.23). The isotope value is lower in the trondhjemite compared to the gabbro. In general, veins hosted by trondhjemite are depleted in ^{34}S comparing to the veins hosted by gabbro (Table 4).

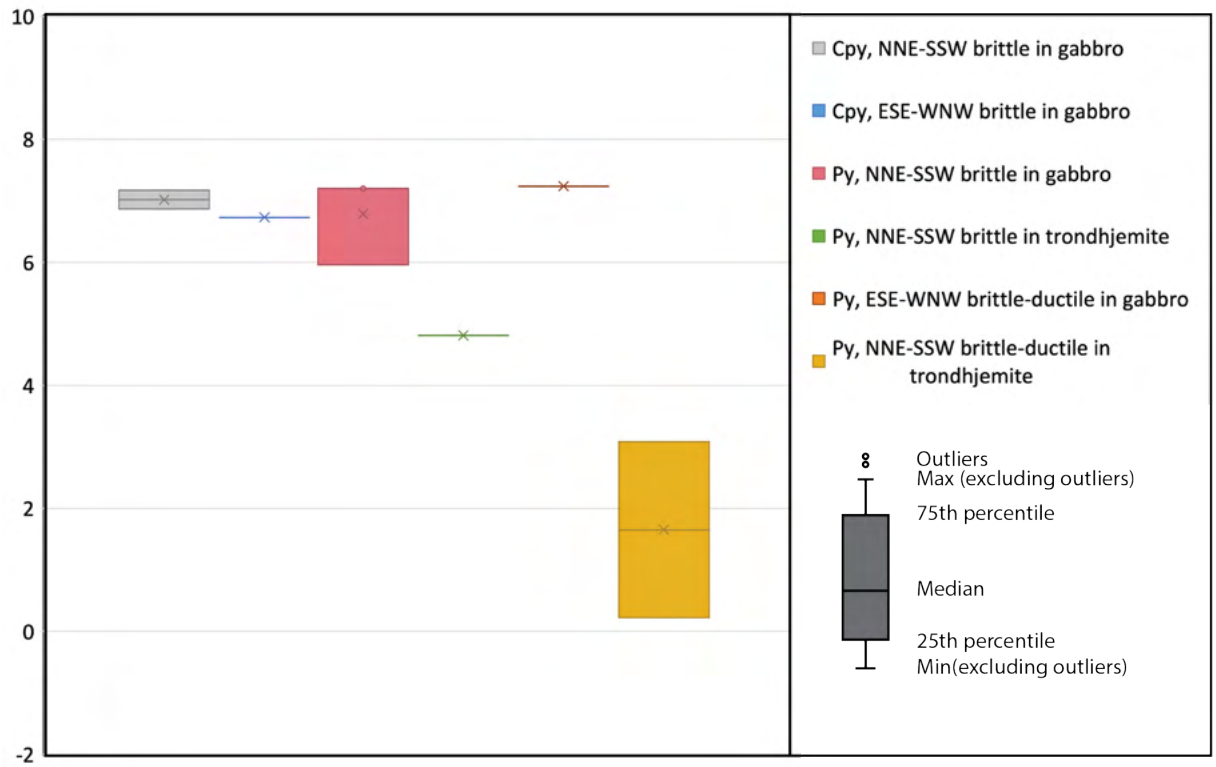

Figure 6.23 *Box diagram presenting $\delta^{34}S$-values (V-CDT ‰) measurements for chalcopyrite (Cpy) and pyrite (Py) from brittle and ductile mineralized veins hosted by Lykling Ophiolite gabbro and the associated trondhjemite.*

6.7 Trace element composition of sulphide phases

Five thick sections (20LYK4D, 20LYK14B, 20LYK20B, 20LYK27B and 20LYK39C) were analysed by the LA-ICP-MS technique (Appendix D, E). Figure 6.24 demonstrated the spatial distribution of selected trace elements in a typical NNE-SSW oriented brittle quartz vein (Sample 20LYK14B, area 1). The sample present pyrite with inter-grained chalcopyrite. Cobalt, Ni and As is chemically bonded with pyrite, although the elements are further enriched around the pyrite grains. Inter-grained between the pyrite are Cu, Mo, Sb, Pb and Hg with lower concentrations of Zn, Ag and Te, implying mineralization at a later phase than the pyrite. Gold occurs native in the sample 20LYK14B. Figure 6.25 present a typical NNE-SSW chalcopyrite-rich brittle vein sample (Sample 20LYK4D, area 1) with pyrite and chalcopyrite. Pyrite is chemically bonded to Co, Ni, Se, Ag, Te, Pb, Bi whereas chalcopyrite is bonded to Zn. Silver and Se is chemically bonded to both pyrite and chalcopyrite with higher concentrations in pyrite (Fig. 6.25). Arsenic seems to be inter-grained between both pyrite and chalcopyrite indicating a later mineralizing phase. Gold in the sample 20LYK4D appears to be chemically bonded to pyrite. Figure 6.26 demonstrate a typical NNE-SSW oriented ductile mineralization (Sample 20LYK27B, area 2) with euhedral pyrite grains. Pyrite is chemically bonded to Co, Ni, Cu, As. The rest of the map have generally low concentrations of other trace elements, but Mo, Ag, Pb and Bi looks to be concentrated around the pyrite grains (Fig. 6.26). Cobalt generally shows zonation in all maps (Fig. 6.24-6.26; Appendix D). The rest of the analysed spatial distributions with selected trace element maps are accessible in Appendix D.

In addition, all samples were explored with spot analysis on pyrite and chalcopyrite (Appendix E). The spot analysis is summarized with median, maximum, and minimum ppm concentrations in Table 5 (pyrite) and Table 6 (chalcopyrite) and illustrated in log-scale boxplots in Figure 6.27, 6.28. The spot analysis on brittle type pyrite revealed general enrichment in the concentration of Co, Ni, As, Se, Ag, Te and Pb. The ductile type of pyrite is very similar to the brittle vein type and show the same enrichment in trace elements. However, the ductile type of pyrite has higher concentrations in Ni, with the median value 716ppm (Fig. 6.27; Table 5). The spot analysis on chalcopyrite revealed a general enrichment in concentration of Co, Ni, Zn, As, Se, Ag, Sn, Sb, Te, Hg, Pb, Bi. Chalcopyrite is generally enriched in trace elements relative to pyrite, e.g. Sn, Sb and Hg (Fig. 6.28; Table 6). However, cobalt and Ni is less enriched in chalcopyrite relative to pyrite with the medians 39ppm, 43ppm Co and 8ppm, 19ppm Ni indicating mobilization of the trace elements in pyrite. Chalcopyrite has high concentration of Zn with 218ppm and 127 ppm. Silver have concentration with 50ppm median in NNE-SSW

oriented mineralization and 20 ppm in ESE-WNW oriented mineralization in chalcopyrite. In comparison, pyrite has the median 1.5ppm and 2.4ppm in NNE-SSW oriented and ESE-WNW oriented mineralization. Indicating Ag to be chemically bonded to chalcopyrite and not pyrite. Low content of Au in sulphide phases (Table 5, 6) suggest that Au has not been chemically bonded in pyrite nor chalcopyrite (Fig. 6.24) (Table 5) and occur in native form.

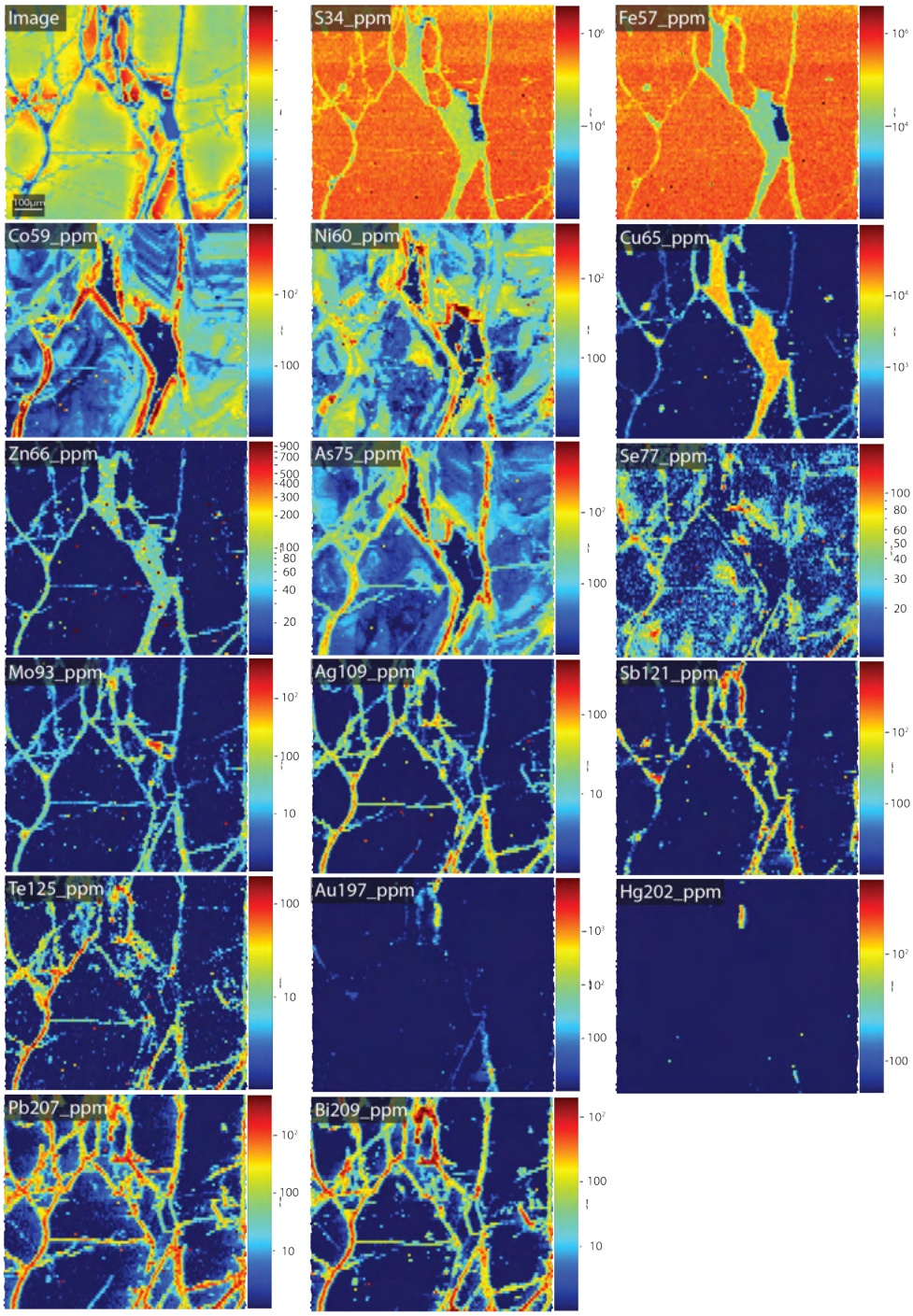

Figure 6.24 *Spatial distribution of trace elements of the brittle NNE-SSW oriented sample 20LYK14B, area 1 in log-scale ppm.*

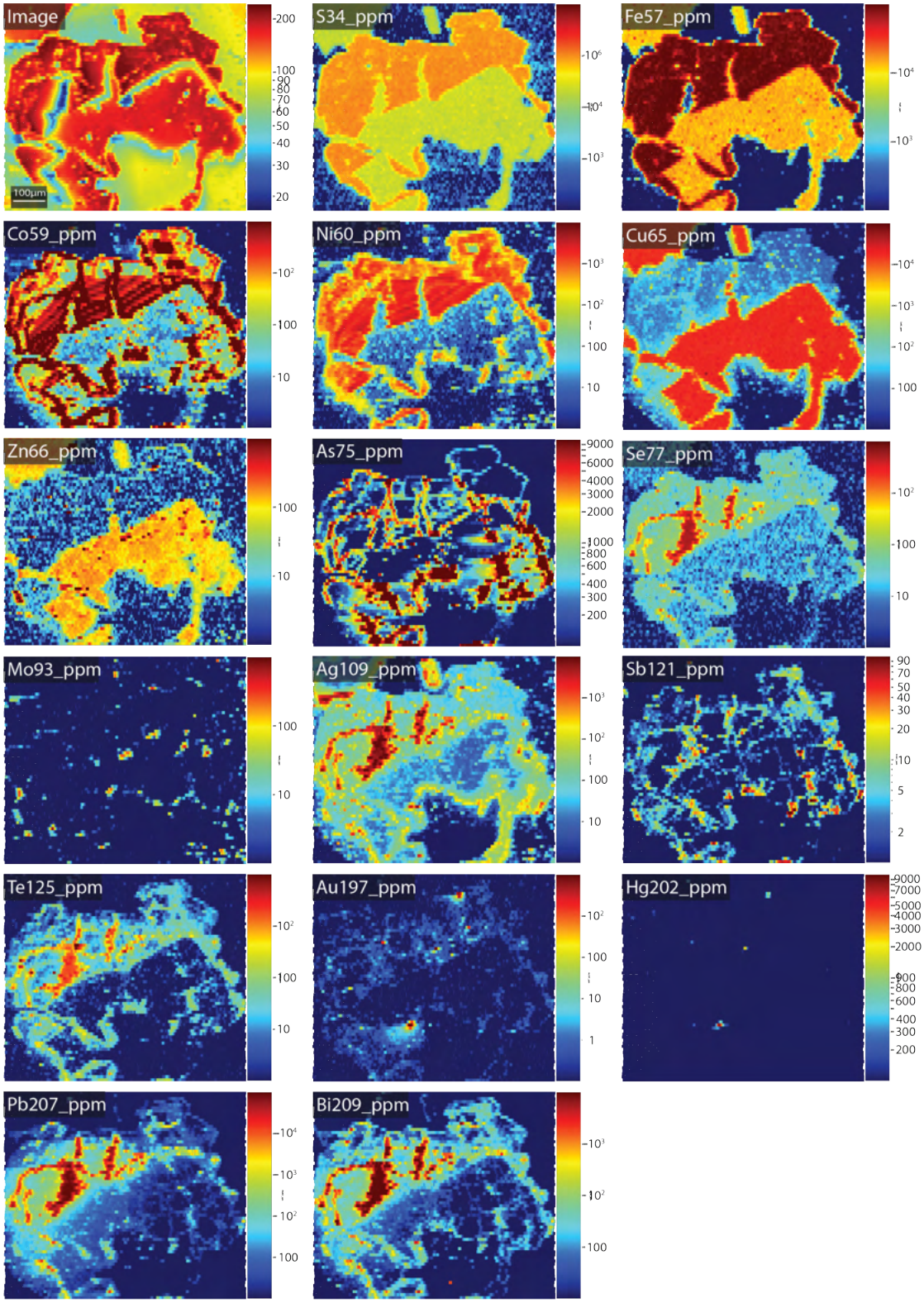

Figure 6.25 *Spatial distribution of trace elements of the brittle NNE-SSW oriented chalcopyrite-rich sample 20LYK4D, area 1 in log-scale ppm.*

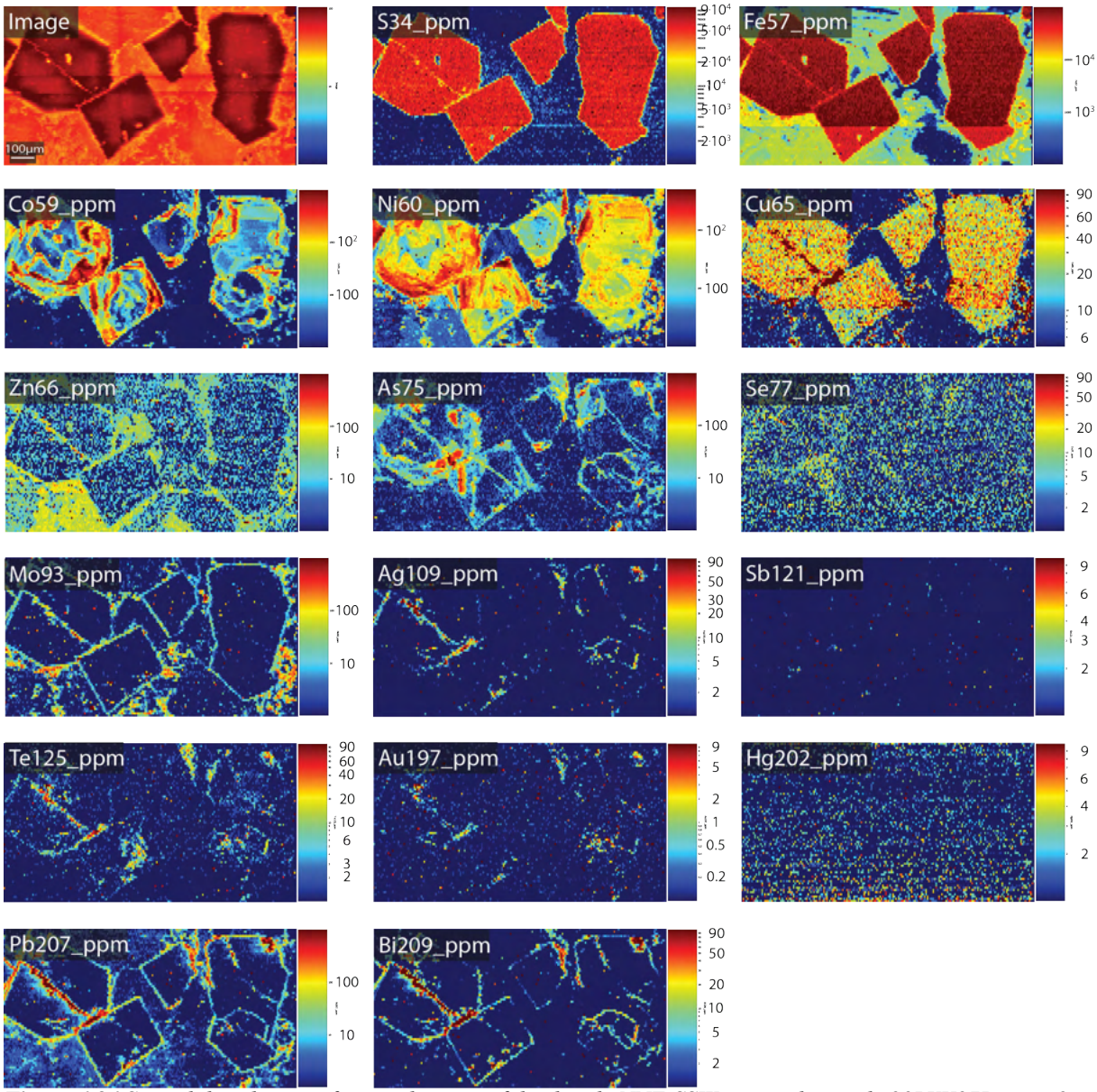

Figure 6.26 *Spatial distribution of trace elements of the ductile NNE-SSW oriented sample 20LYK27B, area 2 in log-scale ppm.*

Table 4 *Descriptive statistics for a selection of minor and trace elements in pyrite. All values are reported in part per milion (ppm). Median = median concentration, Max = maximum concentration, Min = minimum concentration, N= number of spot analyses by LA-ICP-MS on individual grains and <d.l. = below detection limit. The median was calculated using <d.l./2 for samples with measured concentration over and below the detection limit.*

	Py, NNE-SSW brittle in gabbro (20LYK14B) n=8			Py, NNE-SSW brittle in trondhjemite (20LYK20B) N=9		
ppm	Median	Max	Min	Median	Max	Min
S34	642976	707308	563261	604164	623077	581098
Co59	71	146	18	386	1172	33
Ni60	84	281	11	134	388	13
Cu65	121	956	<D.I.	2	10	<D.I.
Zn66	5	24	<D.I.	<D.I.	<D.I.	<D.I.
As75	54	217	5	8	25	2
Se77	19	57	10	4	7	<D.I.
Mo92	0	1	<D.I.	0	1	<D.I.
Ag109	2	11	<D.I.	0	0	<D.I.
Sn117	<D.I.	<D.I.	<D.I.	<D.I.	<D.I.	<D.I.
Sb121	1	4	<D.I.	<D.I.	<D.I.	<D.I.
Te125	1	3	<D.I.	7	42	<D.I.
Au197	0	0	<D.I.	0	0	<D.I.
Hg202	<D.I.	<D.I.	<D.I.	<D.I.	<D.I.	<D.I.
Pb207	57	451	<D.I.	2	13	<D.I.
Bi209	5	38	<D.I.	7	46	<D.I.
	Py, ESE-WNW brittle in gabbro (20LYK39C) n=10			Py, NNE-WNW ductile in trondhjemite (29LYK27B) n=9		
ppm	**Median**	**Max**	**Min**	**Median**	**Max**	**Min**
S34	610974	660256	577434	583638	650341	519038
Co59	195	943	<D.I.	474	1414	7
Ni60	572	2275	25	716	1677	56
Cu65	13	92	<D.I.	3	13	<D.I.
Zn66	<D.I.	<D.I.	<D.I.	5	17	<D.I.
As75	347	1745	13	52	327	<D.I.
Se77	12	18	7	3	7	<D.I.
Mo92	0	0	<D.I.	3	20	<D.I.
Ag109	2	20	<D.I.	0	2	<D.I.
Sn117	<D.I.	<D.I.	<D.I.	<D.I.	<D.I.	<D.I.
Sb121	0	0	<D.I.	0	1	<D.I.
Te125	7	32	<D.I.	3	9	<D.I.
Au197	0	1	<D.I.	<D.I.	<D.I.	<D.I.
Hg202	1	1	<D.I.	<D.I.	<D.I.	<D.I.
Pb207	16	136	<D.I.	50	424	<D.I.
Bi209	14	95	<D.I.	9	41	<D.I.

Table 5 *Descriptive statistics for a selection of minor and trace elements in pyrite. All values are reported in part per milion (ppm). Median = median concentration, Max = maximum concentration, Min = minimum concentration, N= number of spot analyses by LA-ICP-MS on individual grains and <d.l. = below detection limit. The median was calculated using <d.l./2 for samples with measured concentration over and below the detection limit.*

	Cpy, NNE-SSW brittle in gabbro (20LYK14B, 20LYK4D) n=7			Cpy, ESE-WNW brittle in gabbro (20LYK39C) n=7		
ppm	**Median**	**Max**	**Min**	**Median**	**Max**	**Min**
S34	541449	744686	436746	499388	527332	469101
Co59	39	198	<D.I	43	284	<D.I
Ni60	8	23	<D.I	19	100	<D.I
Cu65	374851	383017	364655	357665	384398	262433
Zn66	218	317	148	127	290	88
As75	111	748	<D.I	15	93	<D.I
Se77	18	27	<D.I	25	34	21
Mo92	0.5	1	<D.I	<D.I	<D.I	<D.I
Ag109	50	185	2	21	135	1
Sn117	3	5	<D.I	6	8	<D.I
Sb121	6	23	<D.I	1	1	<D.I
Te125	1	3	<D.I	2	7	<D.I
Au197	1	3	<D.I	<D.I	<D.I	<D.I
Hg202	5	8	<D.I	10	20	<D.I
Pb207	22	54	<D.I	4	12	<D.I
Bi209	15	27	<D.I	16	47	1

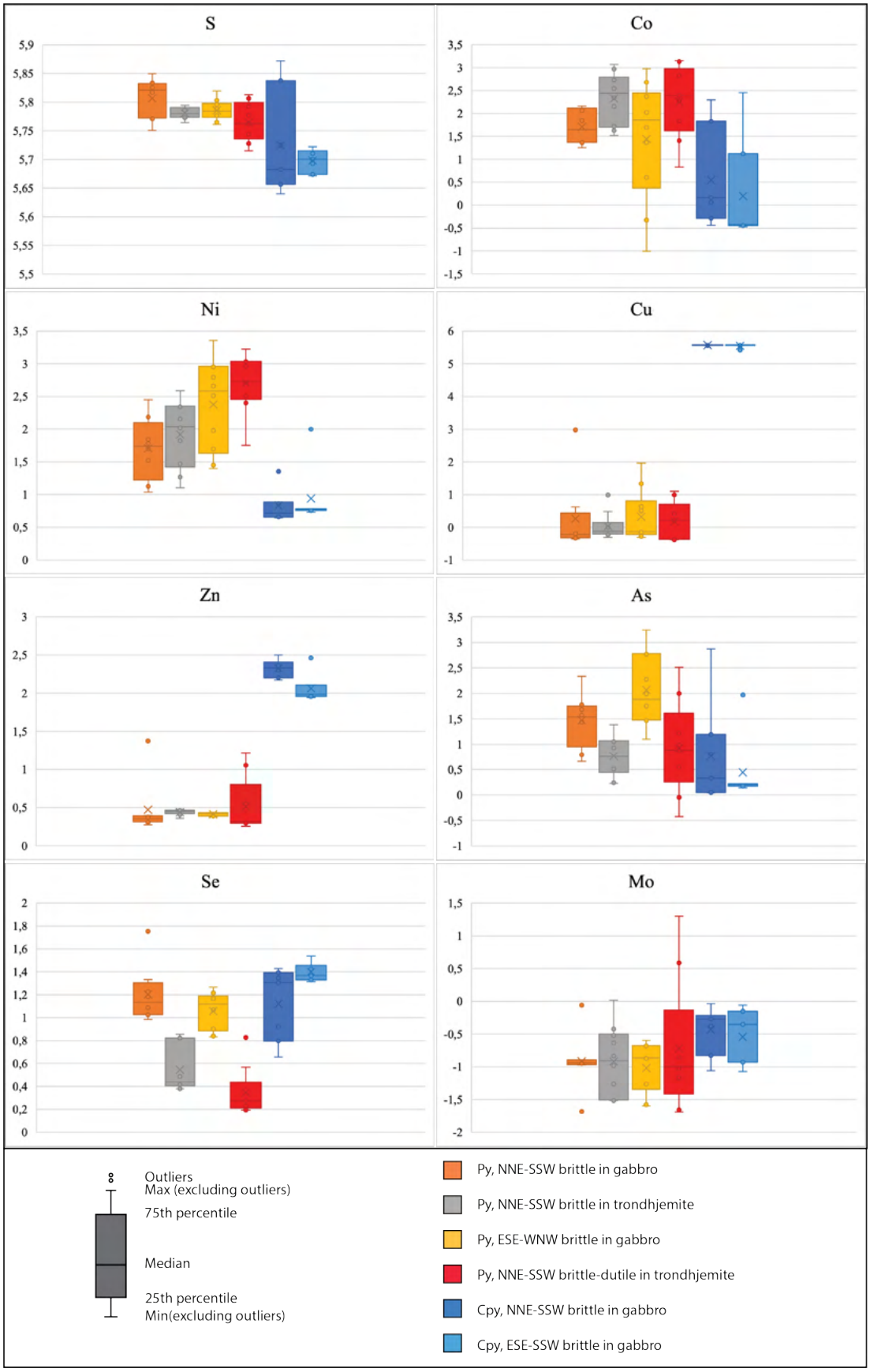

Figure 6.27 *LA-ICP-MS point analysis calculated into boxplots with the elements S, Co, Ni, Cu, An, As, Se and Mo. All values are reported as part per milion (ppm) in log-scale*

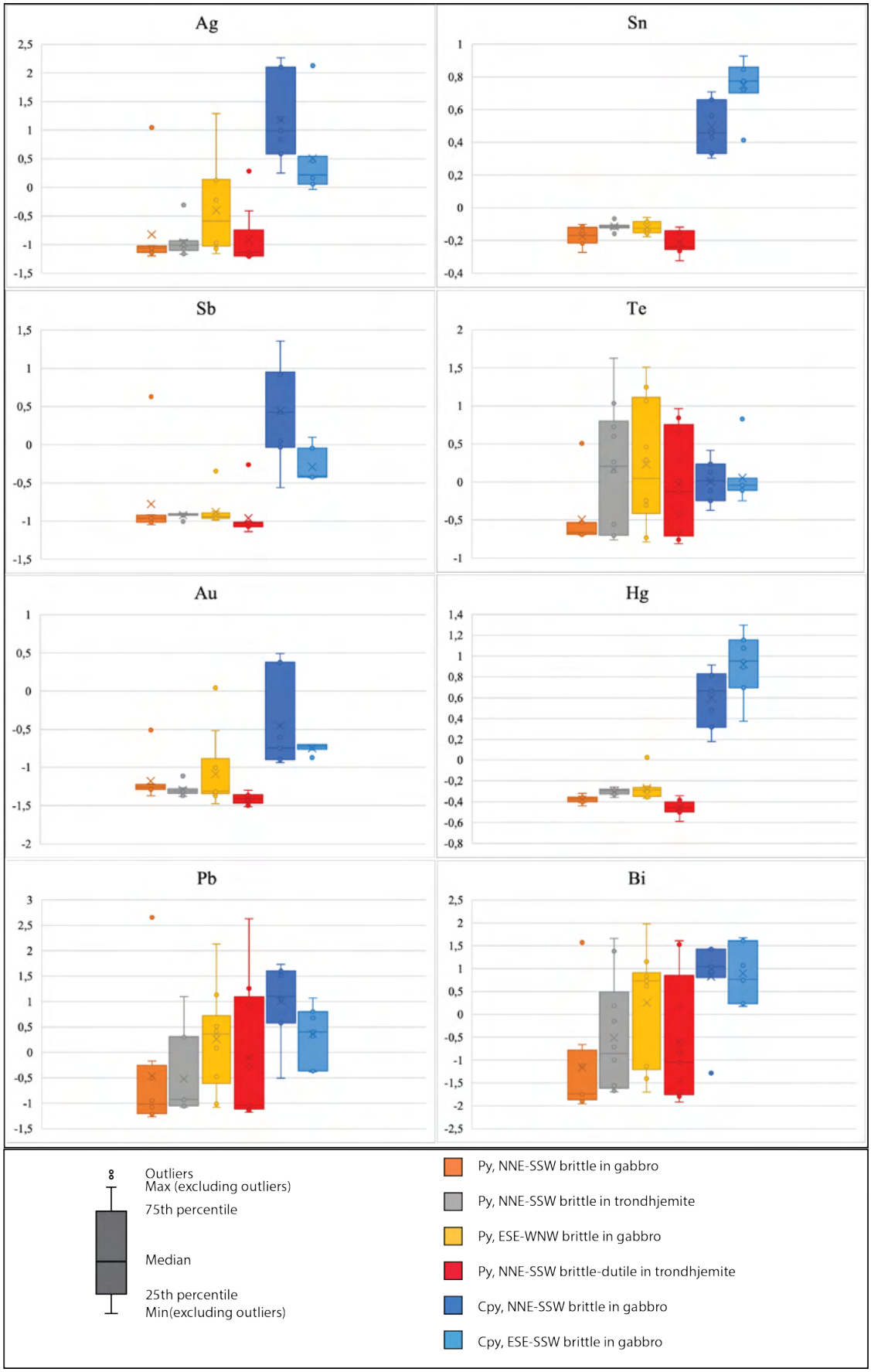

Figure 6.28 *LA-ICP-MS point analysis calculated into boxplots with the elements Ag, Sn, Sb, Te, Au, Hg, Pb and Bi. All values are reported as part per milion (ppm) in log-scale*

6.8 Chlorite microthermometry

Chlorite thermometry was applied to four sample (20LYK3B, 20LYK13B, 20LYK19C and 20LYK39A). The sample 20LYK3B represent hydrothermal alteration assemblage associated with ductile mineralization type of auriferous quartz veins. The other three samples represent alteration halos along the mineralized brittle quartz veins. The aim of chlorite thermometry was to determine the temperature of the chlorite crystallization to find the approximately formation temperature of the Au mineralization at the Lykling area. The calculated temperatures vary between 260 ºC to 349 ºC with the mean value at 316 ºC applying the method proposed by Cathelineau (1998) (Table 7). Similar temperatures (261 ºC to 359 ºC) were obtained from the model suggested by Jowitt (1991) with the mean value 322 ºC. The chlorite composition classifies as ripidolite, pycnochlorite and brunsvigite. The results show little difference in temperatures between brittle and ductile samples, but the ESE-WNW 20LYK39A reflect some lower temperatures (260 ºC-278 ºC) than the rest of the NNE-SSW oriented samples (Table 7).

Table 6 *Overview of SEM-EDS data and calculated temperatures using Catherlineau (1988) and Jowitt (1991).*

Sample	Spec. Nr.	SiO2	Al2O3	FeO	MgO	SUM	Temperature Cathelineau (1988), (ºC)	Temperature Jowitt (1991), (ºC)	Variary
20LYK3B site1	**36**	28.24	19.65	27.27	17.25	92.41	316	320	Pycnochlorite
	37	28.03	19.65	28.17	16.58	92.43	318	323	Pycnochlorite
	38	28.67	19.84	27.53	17.58	93.62	314	319	Pycnochlorite
	39	28.03	20.78	27.27	17.08	93.16	331	335	Ripidolite
	40	28.24	19.65	26.89	17.41	92.19	315	319	Pycnochlorite
20LYK3B 2-site1	**58**	28.88	19.27	27.15	18.08	93.38	307	311	Pycnochlorite
	59	29.1	19.08	27.27	17.25	92.70	293	297	Pycnochlorite
	60	28.67	19.46	27.79	16.42	92.34	300	305	Pycnochlorite
20LYK13B site1	**3**	14.98	10.77	16.60	7.79	50.14	320	327	Brunsvigite
	13	27.60	20.22	31.13	14.43	93.38	328	335	Ripidolite
	14	27.60	20.60	31.65	13.93	93.78	330	337	Ripidolite
	15	28.03	20.03	31.52	14.10	93.68	317	324	Brunsvigite
20LYK13B site2	**25**	28.24	20.22	31.13	14.43	94.02	316	323	Brunsvigite
	26	27.60	20.22	31.26	13.93	93.01	324	331	Brunsvigite
	27	27.38	20.78	31.52	14.10	93.78	338	345	Ripidolite
	34	28.03	20.41	31.00	14.26	93.70	320	327	Brunsvigite
	35	28.03	20.60	31.13	14.26	94.02	323	330	Brunsvigite
20LYK19C 1-site1	**91**	28.67	21.73	35.12	12.44	97.96	327	337	Ripidolite

	92	27.81	21.73	37.44	10.61	97.59	339	349	Ripidolite
	93	28.24	21.92	36.28	10.94	97.38	331	341	Ripidolite
20LYK19C 1-site2	**105**	27.81	22.11	35.25	11.11	96.28	337	347	Ripidolite
	106	28.45	21.73	34.86	11.44	96.48	323	332	Brunsvigite
	116	28.45	21.92	34.86	11.94	97.17	329	338	Ripidolite
20LYK19C-2-site1	**122**	26.96	21.54	32.68	11.94	93.12	341	350	Ripidolite
	123	26.53	20.60	35.38	10.45	92.96	339	349	Ripidolite
	124	26.10	20.97	34.09	10.94	92.10	349	359	Ripidolite
	127	27.38	21.54	35.89	11.28	96.09	343	353	Ripidolite
20LYK39A-1-site1	**133**	31.66	18.89	21.23	23.55	95.33	272	273	Pycnochlorite
	135	31.88	19.46	20.97	24.05	96.36	278	278	Pycnochlorite
	136	32.52	19.08	21.10	23.55	96.25	260	261	Pycnochlorite
	137	32.09	18.89	20.58	24.05	95.61	266	267	Pycnochlorite
	138	33.16	19.27	21.74	24.38	98.55	262	262	Pycnochlorite

7 DISCUSSION

7.1 Host rocks

The gold-bearing quartz veins in the Lykling area are hosted by the Lykling Ophiolite gabbro and intruding trondhjemite. The Early Ordovician Lykling Ophiolite Complex represents the oldest portion of the Upper Allochthone (Brekke et al., 1984). Trondhjemite in the Lykling area have been dated to 484 ±6 Ma and is thought to be a differentiation product of the Lykling Ophiolite gabbro (Saltvedt, 2021). Based on microscopical observations both lithologies, i.e., Lykling Ophiolite gabbro and intruding trondhjemite, have been strongly altered by hydrothermal fluids. The degree of alteration in the study area varies, but the hydrothermal alteration assemblages in general consist of quartz, chlorite, sulphides and saussurite resembling the greenschist facies alteration (Fig. 6.8, 6.10).

7.2 Mafic dikes

The gold-bearing quartz veins in the Lykling area are spatially associated with two generations of mafic dikes that crosscut the Lykling Ophiolite gabbro and the intruding trondhjemite. Field relationships suggest that the ESE-WNW trending mafic dikes are older than the NNE-SSW (Fig. 6.12B), and that the mineralized veins are younger relative to the two dike generations (Fig. 6.3C). The ESE-WNW mafic dikes have tholeiitic affinity (Fig. 6.14A) and their geochemical signature corresponds to the Lykling Ophiolite gabbro (Fig. 7.1; Saltvedt, 2021) suggesting that they may represent the sheeted dike complex of the Lykling Ophiolite complex. The NNE-SSW oriented mafic dikes have a calc-alkaline affinity and their composition ranges from basaltic to andesitic (Fig. 6.14B). This generation of dikes are relatively enriched in Al_2O_3, P_2O_5 and K_2O (Fig. 6.15), with negative Ta and Nb anomalies compared to NMORB (Fig. 6.16A) and have general enrichment in REE with highest enrichment in LREE compared primitive mantle (Fig. 6.16B). This geochemical signature suggests a genetic link between the NNE-SSW oriented mafic dikes and the calc-alkaline Siggjo and Katnakken volcanic rocks. Katnakken is presumed to be a later continuation of the Siggjo Complex and are dated at 476±4 Ma and 473±2 Ma, respectively (Pedersen & Dunning, 1997). In addition to the calc-alkaline character, the Siggjo Complex is characterized by a high K_2O content and negative Ta and Nb anomalies. The Th/Nb vs. La/Yb ratios classify the majority of the NNE-SSW trending dikes to the alkaline arc category (Fig. 7.2) supporting their genetic link with the mature island arc of the Siggjo Complex (Pedersen et al., 1992). Amaliksen (1983) also suggested that the NEE-

SSW dikes in the Lykling area are genetically associated with the Katnakken dolerites and the Siggjo complex.

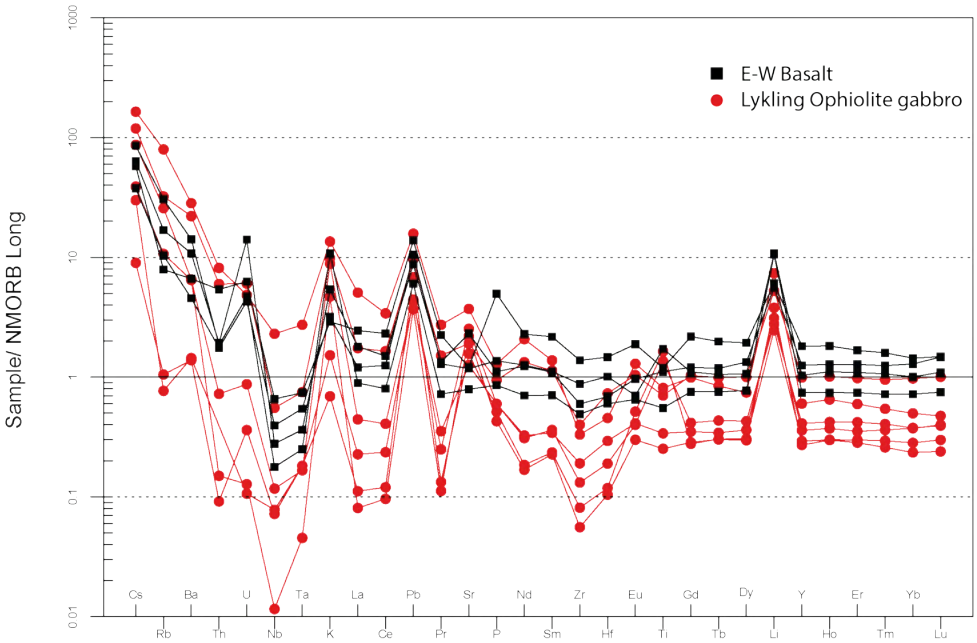

Figure 7.1 *Geochemical signaure of the ESE-WNW trending mafic dikes compared with the Lykling Ophiolite gabbro in the Lykling area. The composition of the Lykling Ophiolite gabbro is from Saltvedt (2021). The NMORB values are from Sun & McDonough (1989).*

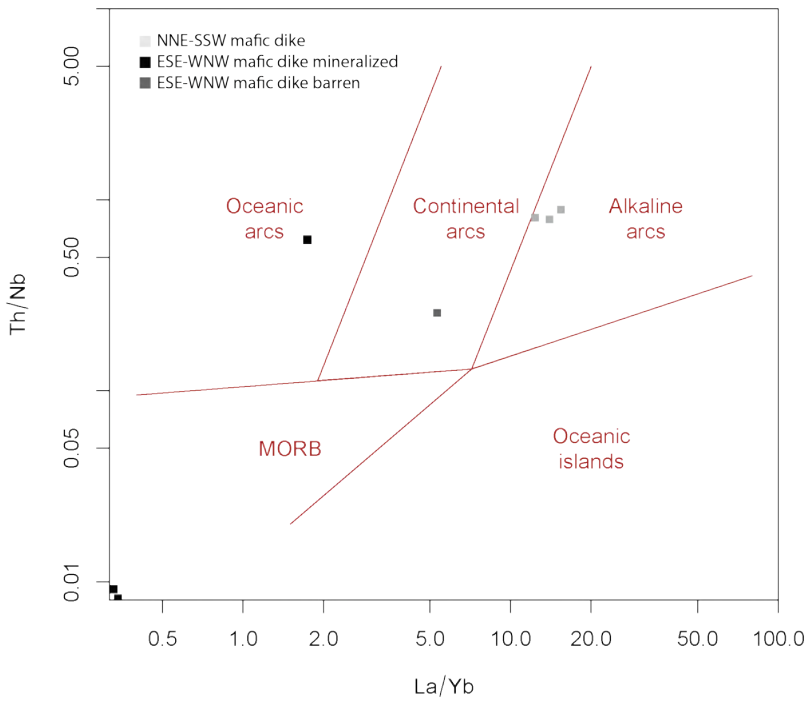

Figure 7.2 *Tectonic discimination diagram (after Hollocher et al., 2012) for the two main generations of mafic dikes in the Lykling area.*

7.3 The gold-bearing quartz veins

Based on their structural and mineralogical characteristics, the gold-bearing quartz veins in the Lykling area can be divided into two main types: (I) quartz-carbonate veins hosted by ductile shear zones; and (II) quartz veins, rich in sulphides hosted by brittle fractures.

Quartz-carbonate veins hosted by ductile shear zones

The gold-bearing quartz-carbonate mineralization is hosted by low-angled ductile shear zones in the Lykling Ophiolite gabbro and the intruding trondhjemites. A typical mineral assemblage consists of quartz, carbonates (mostly ankerite), and hydrous silicates, predominantly chlorite and epidote. Minor amounts of pyrite were recorded in the shear zones. This type of mineral assemblage reflects a near-neutral character of the mineralizing fluids, relatively high CO_2 fugacity and low sulphur fugacity. Microthermometry of fluid inclusions from the ductile quartz veins revealed homogenization temperature between 165 to 182ºC, relatively constant salinity (3.23 to 6.45 w.% NaCl eq.) and sporadically occurring coexistence of two-phase liquid-rich and vapour-rich inclusions indicating entrapment from boiling fluids (Fig. 6.20; Appendix B). In hydrothermal solutions, gold is transported in forms of Au-chloride or Au-bisulphide complexes, depending on temperature, salinity, sulphur fugacity and pH conditions (Seward, 1973; Zhu et al., 2011; Gaboury, 2019). Under low-temperature conditions, estimated for the deposition of the quartz-carbonate veins hosted by ductile shear zones, Au-bisulphide complexes would prevail. Previous fluid inclusion studies on the Lykling area observed mostly H_2O-NaCl inclusion with temperatures between 130-211 ºC and low salinities (0.8-3.5 wt.% NaCl), but they also found H_2O-CO_2-NaCl inclusions with 5-10 vol.% CO_2 with temperatures between 169 ºC to 240 ºC and low salinities (4.3-6.1 wt.% NaCl) (Christensen & Stendal, 1995). Carbonic acids (H_2CO_3, HCO_3-, CO_3^{-2}) acts as a pH buffer for gold solubility (Philips & Evans, 2004), keeping the pH at close to neutral level (Gaboury, 2019). Boling is an outcome of fluid immiscibility triggered by a drop in pressure, removing the CO_2 from the initial one-fluid phase making the fluids more acidic and consequently precipitating native gold as a result of destabilization of $Au(HS)_2^-$ complex (Gaboury, 2019):

$$Au(HS)_2^- + 2H^+ \leftrightarrow Au^0 + 2H_2S\ (g)$$

Correspondingly, reflected light microscopy, SEM analyses and LA-ICP-MS revealed gold was predominantly deposited in its native form in the ductile type of mineralization (Fig. 6.26; Table 5).

The structural elements suggest that the mineralization hosted by the ductile shear zones was emplaced during a compressional regime. Christensen & Stendal (1995) do not differentiate

between the ductile and brittle mineralization but argues that most quartz veins are brittle and suggest that the ductile mineralization shear movements were contemporaneous with the vein emplacement or was caused by later reactivation. Alternatively, the compressional regime seen in the ductile mineralization could be a result from the Caledonian orogeny while the extensional regime recorded by the brittle mineralization might be related to the Caledonian post-collisional extension (Fossen & Hurich, 2005).

Quartz-sulphide veins hosted by brittle fractures

The brittle veins cut through the Lykling Ophiolite gabbro and the intruding trondhjemite. Field observations revealed a close spatial relationship between the veins and the mafic dikes with both NEE-SSW and ESE-WNW orientation, suggesting that the contacts between the dikes and their host lithologies may represent a weak zone that efficiently channelled hydrothermal fluids. The contact between the veins and their host rocks is sharp and the alteration halo is very limited (up to few centimetres thick) or even completely absent. The steeply dipping orientation of these veins suggest that they were emplaced during an extensional event. As previously discussed, the brittle mineralization could be related to the Caledonian post-collisional extension. It has been suggested that the gold-bearing veins are a product of the Hardangerfjord Fault Zone (HFZ) and the Sunnhordland Fault Zone (SFZ) (Fig. 3.5; Christensen & Stendal, 1995). The HFZ and SFZ has been dated to have moved between 408Ma and 402Ma (Fossen et al., 2014).

A typical brittle mineral assemblage consists of quartz and sulphides, predominantly pyrite and locally chalcopyrite, implying a low CO_2 fugacity and a high sulphur fugacity. Fluid inclusion study of the brittle quartz veins revealed a coexistence of NaCl-H_2O (with eutectic temperatures around -21°C) and NaCl-$CaCl_2$-H_2O fluid inclusions (with eutectic temperatures around -52°C), implying mixing of at least two fluids. There are distinct differences in the measured salinity and homogenization temperatures (Appendix B). The NaCl-H_2O inclusions have lower homogenization temperatures (125 to 168 ºC) and low salinity (0.18 to 5.86 wt.% NaCl) whereas the NaCl-H_2O-$CaCl_2$ inclusions have higher homogenization temperatures (150 ºC to 182 ºC) and moderate salinity between (11.1 wt.% to 12,.6 wt.% NaCl). The obtained fluid inclusion data suggest that this type of quartz veins was deposited due to a mixing of high temperature and high salinity fluids with low temperature and low salinity fluids caused cooling and dilution affecting the metal solubility. As discussed earlier, in hydrothermal solutions gold can be transported by chlorite (Cl-) and bisulfide (HS-) (Seward, 1973; Zhu et al., 2011; Gaboury, 2019). Under the conditions of high temperatures, high salinity and/or low sulphur

fugacity, Au-chlorite complex prevails (Gammons and Williams-Jones, 1997; Abdelnasser & Kumar, 2017). At the estimated sulphur fugacity, measured homogenization temperatures and fluid salinity as well as the results of chlorite thermometry, suggest that gold was introduced as $Au(HS)^-_2$ to the ductile type of the mineralization. In contrast, a higher salinity and higher homogenization temperatures recorded for the brittle type of veins, indicate that gold was rather transported as Au-chloride complex, even under conditions of an increased sulphur fugacity (Zhu et al., 2011; Gaboury, 2019). Consequently, the mixing of the high temperature and high salinity fluids with low temperature and low saline fluids caused destabilisation of Au-chloride complexes and resulted in deposition of native gold:

$$AuCl_2^- \leftrightarrow Au^0 + 2Cl^- \qquad \Delta_r H<0$$

The LA-ICP-MS maps (Fig. 6.24; Appendix D) confirm that gold is deposited in its native form and that the amount of chemically bonded gold in sulphide phases is very limited.

7.4 Stable isotope characteristics of the Lykling mineralization

The $\delta^{34}S$-values for the Lykling area yield isotopic values from 0.23‰ to 7.24‰ for pyrite and between 6.73-7.17‰ for chalcopyrite. There is a distinct difference between the sulphur isotope values measured for pyrite hosted by the Lykling Ophiolite gabbro (5.96-7.24‰ $\delta^{34}S$) compared to pyrite hosted by trondhjemite (0.23-4.81‰ $\delta^{34}S$). A difference between the ductile and brittle types of the mineralization has not been recorded (Fig. 6.23). Sulphides hosted by the trondhjemite have sulphur isotopes values similar to expected values for fluids with a magmatic or mantle source. In contrast, sulphides hosted by gabbro are enriched in ^{34}S and overlap with values of basalt-hosted volcanogenic massive sulphide deposits associated with the Lykling Ophiolite Complex (Fjellet, 2021).

In comparison, the measured $\delta^{13}C$-values of ankerite range between -5.2 and -3.5 ‰ V-PDB and $\delta^{18}O$-values between 9.5 and 13.5 ‰ V-SMOW suggesting a magmatic origin of CO_2 (Fig. 6.22). Previous studies on carbonates from the Lykling area observed similar values with $\delta^{13}C$-values of -3.8 to -2.9‰ V-PDB and $\delta^{18}O$-values of 10.4 to 11.3 % V-SMOW (Christensen & Stendal). A difference between the ductile and brittle mineralization types has not been recorded, indicating a same source of CO_2 for both types of mineralization.

7.5 Ore-forming model

The Lykling area contains a vein-type gold mineralization that shares many geologic features with orogenic type of gold deposits (Fig. 7.3; Groves et al., 2003). The quartz-carbonate veins hosted by low-angle ductile shear zones are sporadically crosscut by the quartz-sulphide veins associated with brittle fractures, suggesting that gold was deposited as a result of at least two mineralizing events.

Mineral assemblages and the fluid inclusion study show that gold in the quartz-carbonate veins, that are linked to low-angle ductile shear zones, was deposited from aqueous fluids of relatively low temperature, low salinity and near-neutral pH character, and under conditions of a low sulphur fugacity and a high CO_2 fugacity. The structural elements associated of this type of the mineralization suggest that gold was deposited in a compressional setting. The fluid inclusion assemblages consisting of coexisting liquid-rich and vapour-rich fluid inclusions revealed that ore-bearing fluids periodically underwent boiling episodes that might have contributed to deposition of gold by destabilization of gold-bisulphide complexes. Boiling has been recognized as an efficient mechanism for deposition of would promote deposition of quartz and silica from low salinity hydrothermal fluids (e.g. Simpson et al., 2015).

In contrast, mineral assemblages and the fluid inclusion study indicate that gold in the quartz-sulphide veins hosted by steeply-dipping brittle fractures was deposited from relatively hot and saline aqueous fluids under conditions of a high sulphur fugacity and a low CO_2 fugacity. The structural elements of this type of the mineralization suggest that gold was deposited in an extensional setting. The fluid inclusion data reflect that a mixing of hot, moderately saline, $NaCl$-$CaCl_2$-H_2O fluids with cold, diluted, $NaCl$-H_2O might have fluids triggered destabilization of gold-chloride complexes. The mixing also would contribute to precipitation of quartz and base-metal sulphides, such as pyrite and chalcopyrite (e.g. Seward et al., 2014).

Orogenic gold deposits worldwide have been described as products of both brittle and ductile processes (Groves et al., 2003). Anyhow, some of orogenic gold deposits re associated with brittle-ductile transition zones, at mezosonal depths and temperatures (Fig. 7.3; Groves et al., 2003; Groves et al., 2018; Zoheir et al., 2019).

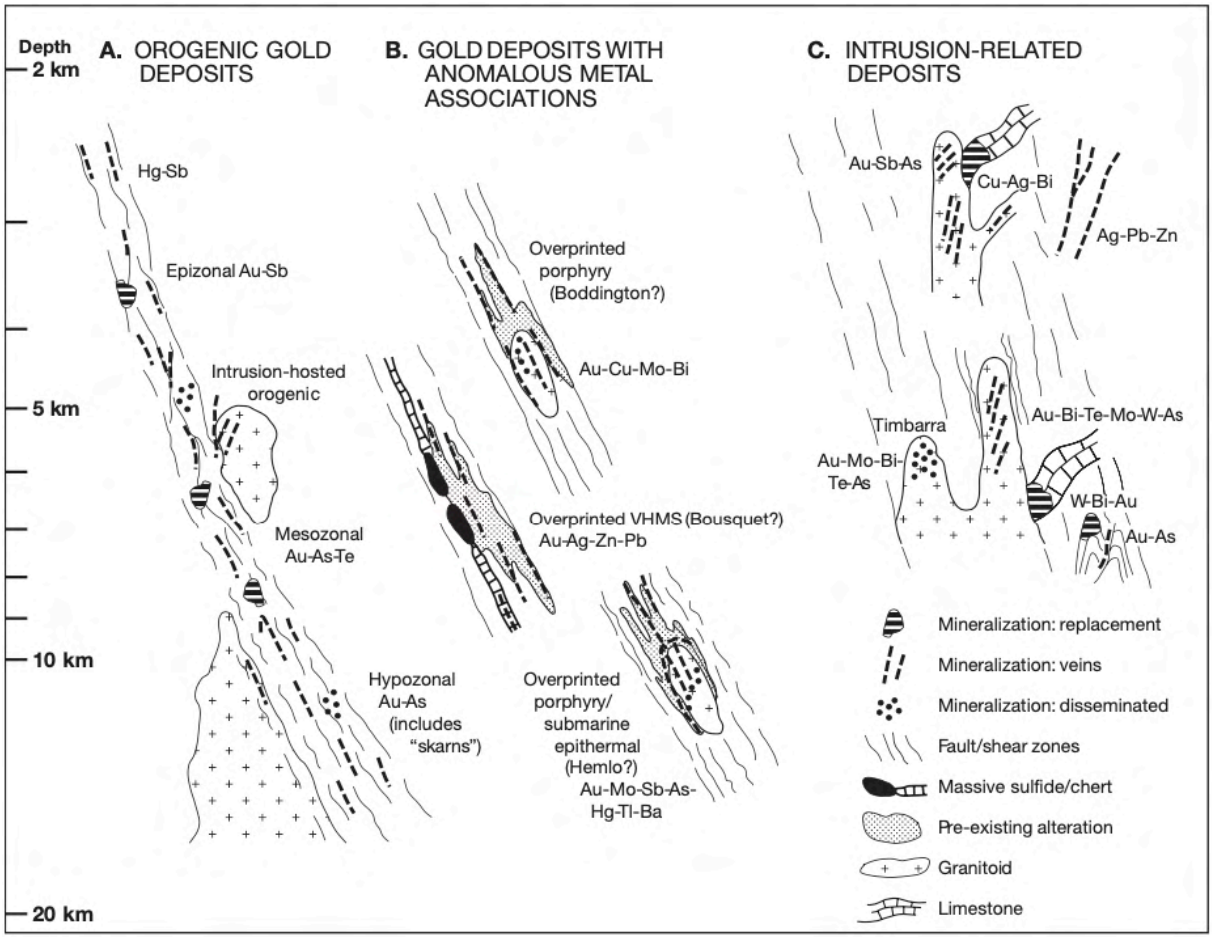

Figure 7.3 *Ilustration of the crustal environment of orgenic gold deposits, gold deposits with anomalous metal associations and intrusion related deposits (modified by Grove et al. (1998) and sourced from Lang et al., (2000)).*

7.6 Similar systems

The Lykling area has similarities with other orogenic gold deposit systems in the world. The Eastern Desert orogenic gold occurrences in Egypt represent similar but older orogenic gold deposit system (Zoheir, 2019). Comparably, it consists of gold-bearing quartz-carbonate veins located in fractures and shear zones related to a major strike-slip fault and thrusts during Neoproterozoic. The mineralization in the Eastern Desert is hosted by greenschist-facies arc rocks and late-tectonic granitoids (Zoheir, 2019). The Eastern Desert has a similar tectonic history to SW Norway, with both going through the Wilson cycle with the formation of ocean with continental rifting, then formation of volcanic arcs and fore-and back arc ophiolites, followed by closure of the ocean and accretion of arc terranes by subduction, continental collision, transgressional orogeny with faulting (Zoheir, 2019). The change from compressional to extensional regime in the Eastern Desert is suggested to be the main event for hydrothermal fluid flow (Zoheir, 2019). The deposition of gold from hydrothermal fluids at Lykling could be linked to a similar type of event, as the tectono-magmatic evolution at Bømlo strongly suggests

that there was a change from compressional to extensional regime linked to the orogenic collapse following the Taconian Orogenes (Slotnes, 2021). Following the collapse, thinning of the crust allowed for renewed magmatism resulting in the magmatism linked to the Sunnhordland Batholith, the volcanisms of the Siggjo Complex and the dyke swarm (Pedersen, 2021, personal communication; Slotnes, 2021) associated with the gold mineralization.

The El Sid deposit within the Eastern Desert orogenic gold deposit is hosted, just like the Lykling, deposit in granitic intrusion and ophiolites (Zoheir & Moritz, 2014). The El Sid deposit is a mesothermal mineralization with quart and quartz carbonate veins hosted in fault/shear system (Zoheir & Moritz, 2014). Fluid inclusion data for the El Sid gold deposition indicate a complex history of fluid immiscibility, mixing and wall-rock alteration with low salinity carbonic fluid in the early stage and more saline fluids in the later stage (Zoheir & Moritz, 2014). The gold deposition is described to mostly have been precipitated by decrease in pressure because of the fault-fracture meshes and during destabilization of gold-disulphide/chlorite complexes (Zoheir & Moritz, 2014). Comparably, the fluid inclusion data for Lykling reveal neutral and moderately salinity at the ductile quartz-carbonate mineralization, while the brittle mineralization reflects mixing of moderately saline ore-bearing fluids with diluted and colder fluid.

The Silurian-Devonian Viking orogenic gold deposit in White Bay, Newfoundland, is another orogenic system that has similarities to the Lykling area. The Viking deposit have been interpreted to have formed during a prolonged strike-slip movement and represent the tectonic setting of a gold-rich epizonal deposit (Fig. 5.8) (Abdelnasser & Kumral, 2017). The deposit has been suggested to have formed at a depth of 3 km, with pressures from 4 to 11 km depth and temperatures ranging from 237 ºC to 320 ºC (Abdelnasser & Kumral, 2017). Similar temperatures have been suggested for the Lykling deposit. The gold mineralization in the Viking deposit is hosted in quartz, calcite, and sulphide veins in sericite-altered host rock. The host rock is not the same as seen in Lykling, with the Viking being hosted in a granodiorite, but the mineralization is associated with calc-alkaline dikes, just like the Lykling NNE-SSW calc-alkaline dikes. Also comparable is the sulphide assemblage, the Viking sulphides consist of pyrite, galena, sphalerite, and chalcopyrite. The fluid inclusion data revealed boiling and mixing of fluids in the Viking deposit that just as the Lykling deposit led to precipitation of the mineralizing gold-bearing fluids.

8 CONCLUSION

The main aim of this study has been to determine the mineralogical, geochemical, and stable isotope characteristics of the gold-bearing quartz veins, their host rocks and associated alteration products in the Lykling area. The study has also provided a better understanding of the mineralizing fluids associated with deposition of gold in the study area. The following conclusions can be drawn from the present study:

- The gold-bearing quartz veins are hosted by the Lykling Ophiolite Complex and the intruding trondhjemite. Both host lithologies have been hydrothermally altered. The typical alteration assemblages consist of quartz, chlorite, sulphides and saussurite resembling greenschist facies alteration.
- The gold-bearing quartz veins in the Lykling area are spatially associated with at least two generation dikes that crosscuts the Lykling Ophiolite and the intruding trondhjemite. Field relationships suggest that the ESE-WNW trending generation of mafic dikes are older than the NNE-SSW oriented dikes. The ESE-WNW oriented dikes have tholeiitic character and have been suggested to represent the sheeted dike complex of the Lykling Ophiolite Complex. In contrast, the NNE-SSW oriented dikes have calc-alkaline character and have been genetically associated with the Siggjo Complex.
- The gold-bearing mineralization are structurally the youngest and can be divided into two types: I) sulphide-rich quartz veins hosted by steeply dipping brittle faults and (II) quartz-carbonate veins hosted by low-angle ductile shear zones.
- The ductile mineralization, hosted by low-angled shear zones might be related to a compressional regime, whereas the brittle type of the mineralization is suggested to have deposited during an extensional regime.
- There are two suggested theories for the possible timing for the mineralization of both brittle and ductile gold-bearing quartz veins: (I) The ductile and brittle mineralization might be related to the change from compressional to the extensional regime during the orogenic collapse following the Taconian Orogenes and the formation of the Siggjo Complex. (II) The ductile mineralization, hosted by low-angled shear zones might be related to the compressional stage of the Caledonian Orogeny and the brittle type of the mineralization is suggested to have deposited during the extensional regime related to the formation of the Hardanger Fault Zone (HFZ) and the Sunnhordland Fault Zone (SFZ) during the Caledonian post-orogeny extension.

- The typical ductile mineral assemblage consists of carbonates (predominantly ankerite), quartz and hydrous silicates, mostly chlorite and epidote. The mineral assemblage indicates that hydrothermal fluids had a near-natural pH value, a high CO_2 fugacity and a low sulphur fugacity. The fluid inclusion study revealed boiling as a trigger for precipitation of gold from gold-bisulphide complexes.
- The typical brittle mineralization consists of quartz and sulphides, predominantly pyrite and locally chalcopyrite. The mineral assemblage reflects a high sulphur fugacity. Fluid inclusions revealed mixing of a low temperature and low salinity fluid with higher temperature and moderate salinity fluids and consequent destabilisation of Au-chloride complexes as the trigger for precipitation of native gold and base-metal sulphides.
- Stabile isotope characteristics of the Lykling mineralization disclosed magmatic source of sulphur and CO_2 in both types of the mineralization.
- The mineralization in the Lykling area can be categorized as an orogenic gold deposit.

9 FURTHER RESEARCH

This study has provided useful knowledge about the gold-bearing quartz veins mineralization in Lykling. In further research, Ar-Ar geochronology of the chlorite minerals in both the brittle and ductile mineralization and hosted shear zones could be useful to establish the timing of the mineralization. Another method to establish timing of mineralization that could be used is sulphide mineral dating from the brittle and ductile mineralization using Re-Os geochronology to determine if the brittle and ductile mineralization is connected to the same event or at two different times. The Lykling area has a very complex structural composition, hence detailed structure mapping of the Lykling area can give an even better understating to the tectonic history and fluid flow. Further research into other mapped gold mines on the island Bømlo and in SW Norway may provide a better understanding on the hydrothermal fluids and to what extent the mineralization has happened.

REFERENCES

Amaliksen, K.G. (1980a) Gullforekomster på Bømlo. NGU-1750/35A, Norges geologiske undersøkelse.

Amaliksen, K.G. (1980b) Gullforekomster på Bømlo. BV-3773, Bergvesenet.

Amaliksen, K.G. (1983) *The geology of the Lykling Ophiolitic Complex, Bømlo, SW Norway*. Unpubl. Cand. Real. Thesis, University of Bergen.

Amaliksen, K.G & Sturt, B.A. (1986) The Søre Lyklingholmen Formation: Coarse Sedimentary Breccias Related to Submarine Faulting in the Iapetus Ocean. *The Journal of geology*, 94(1), pp.109–120.

Abdelnasser A. & Kumral M. (2017) The nature of gold-bearing fluids in Atud gold deposit, Central Eastern Desert, Egypt, *International Geology Review*, 59(15), pp.1845-1860.

Anders, E. & Grevesse, N. (1989) Abundances of the elements: Meteoritic and solar. Geochimica et Cosmochimica acta, 53(1), pp.197-214.

Andersen, T.B. & Andresen, A. (1994) Stratigraphy, tectonostratigraphy and the accretion of outboard terranes in the Caledonides of Sunnhordland, W. Norway. *Tectonophysics*, 231(1-3), pp.71-84.

Andersen, T.B., & Jansen, Ø.J. (1987) The Sunnhordland Batholith, W. Norway: regional setting and internal structure, with emphasis on the granitoid plutons. *Norsk geologisk tidsskrift*, 67(3), pp.159-183.

Atkinson Jr, A.B. (2002) *A model for the PTX properties of H_2O-NaCl*. Doctoral dissertation Virginia Tech.

Bodnar, R.J. (1983) A method of calculating fluid inclusions volumes based on vapor bubble diameters and P-V-T-X properties of inclusion fluids. *Economic Geology*, v.78, pp.535-542.

Bodnar, R.J. (1993) Revised equation and table for determining the freezing point depression of H_2O-NaCl solutions. *Geochimica et Cosmochimica Acta*, v.57, pp.683-684.

Bodnar, R.J. & Vityk, M.O. (1994) Interpretation of microthermometric data for H_2O-NaCl fluid inclusions. B. De Vivo & M.L. Frezzotti, eds. Fluid Inclusions in Minerals, Methods and Applications. Blacksburg: Virginia Tech, VA, pp.117-130.

Bodnar, R.J. (2003) Introduction to aqueous-electrolyte fluid inclusions. Fluid inclusions: Analysis and interpretation, v.32, pp.81-100.

Bodnar, R.J. (2018) Fluid Inclusions, Encyclopedia of Earth Sciences Series. *Springer International Publishing*, pp.488-492.

Bodnar, R.J., Lecumberri-Sanchez, P., Moncada, D. & Steele-MacInnis, M. (2014) Fluid inclusions in hydrothermal ore deposits. Treatise on geochemistry. 2nd edn. Elsevier, Oxford, v.13, pp.119-142.

Bohlke, J.K. (1982) Orogenic (metamorphic-hosted) gold-quartz veins. US Geological Survey Open-File Report, 795, pp.70-76.

Brekke, H., Furnes, H., Nordås, J., & Hertogen, J. (1984). Lower Palaeozoic convergent plate margin volcanism on Bømlo, SW Norway, and its bearing on the tectonic

environments of the Norwegian Caledonides. *Journal of the Geological Society*, 141(6) pp. 1015-1032.

Briscoe, H.V.A. & Robinson, P.L. (1925) XCIX.—A redetermination of the atomic weight of boron. Journal of the Chemical Society, Transactions, v.127, pp.696-720.

Cathelineau, M. (1988) Cation site occupancy in chlorites and illites as a function of temperature. Clay minerals, 23(4), pp.471-485.

Chistensen, K., Stendal, H. (1995) Gold mineralization at Lykling, Bømlo, the Caledonides of Southwestern Norway. *Grønlands geologiske undersøgele*, 95(10), pp. 20-23.

Christensen, K. (1994) *En geologisk undersøgelse af guldmineraliseringerne i Lykling, Bømlo, SW-Norge*. Unpublished thesis from the University of Copenhagen.

Corfu, F., Andersen, T.B. & Gasser, D. (2014) The Scandinavian Caledonides: main features, conceptual advances and critical questions. *Geological Society*, London, Special Publications, 390(1), pp.9-43.

Cox, K. G., Bell, J. D., & Pankhurst, R. J. (1979) *The Interpretation of Igneous Rocks*. London: Allen & Unwin.

Criss, R.E. (1999) *Principles of stable isotope distribution*. Oxford University.

Davis, D.W., Lowenstein, T.K., Spencer, R.J. (1990) Melting behavior of fluid inclusions in laboratory-grown halite crystals in the systems NaCl-H2O, NaCl-KCl-H2O, NaCl-MgCl2-H2O, and NaCl-CaCl-H2O. *Geochemica et Cosmochimica Acta*, 54(3), pp. 591-601.

Dunning, G.R., & Pedersen, R.B. (1988) U/Pb ages of ophiolites and arc-related plutons of the Norwegian Caledonides: implications for the development of Iapetus. *Contributions to Mineralogy and Petrology*, 98(1), pp. 13-23.

Duuring, P., Cassidy, K. F. & Hagemann, S. G. (2007) Granitoid-associated orogenic, intrusion-related, and porphyry style metal deposits in the Archean Yilgarn Craton, Western Australia. *Ore Geology Reviews*, v.32, pp.157-186.

Fjellet, T. (2021) *Geochemical characteristics of the volcanogenic massive sulfide mineralization on Bømlo and Stord islands, Sunnhordaland, SW Norway*. Master Thesis, University of Bergen, Norway.

Fonneland, H.C. (2002) *Radiogenic isotope systematics of clastic sedimentary rocks-with emphasis on detrital zircon geochronology.* Ph.D. Thesis University of Bergen.

Fossen, H. & Robin, B. (2015) *Lykling – Gull*. Available at: https://www.grind.no/sunnhordland/bomlo/lykling-gull (Accesed: 31.05.2021).

Fossen, H. & Dunlap, W.J. (1998) Timing and kinematics of Caledonian thrusting and extensional collapse, southern Norway: evidence from 40Ar/39Ar thermochronology. *Journal of structural geology*, 20(6), pp.765-781.

Fossen, H. (1992) The role of extensional tectonics in the Caledonides of south Norway. *Journal of structural geology*, 14(8), pp. 1033-1046.

Fossen, H. (2000) Extensional tectonics in the Caledonides: Synorogenic or postorogenic?. *Tectonics*, 19(2), pp.213-224.

Fossen, H. & Hurich, C.A. (2005) The Hardangerfjord Shear Zone in SW Norway and the North Sea: a large-scale low-angle shear zone in the Caledonian crust. *Journal of the Geological Society*, 162(4), pp.675-687.

Fossen, H., Gabrielsen, R.H., Faleide, J.I. & Hurich, C.A. (2014) Crustal stretching in the Scandinavian Caledonides as revealed by deep seismic data. *Geology*, 42(9), pp.791-794.

Fossen, H., Khani, H.F., Faleide, J.I., Ksienzyk, A.K. & Dunlap, W.J. (2017) Post-Caledonian extension in the West Norway–northern North Sea region: the role of structural inheritance. *Geological Society*, London, Special Publications, 439(1), pp.465-486.

Furnes, H., Brekke, H., Nordås, J., & Hertogen, J. (1986) Lower Palaeozoic convergent plate margin volcanism on Bømlo, southwest Norwegian Caledonides: geochemistry and petrogenesis*: Geological Magazine*, 123(2), pp.123-142.

Gaboury, D. (2019) Parameters for the formation of orogenic gold deposits. *Applied Earth Science*, 128(3), pp.124-133.

Gale, G. H. & Roberts, D. (1974) Trace element geochemistry of Norwegian Lower Palaeozoic basic volcanics and its tectonic implications. *Earth and Planetary Science Letters*, 22(4), pp. 380-390.

Gammons, C.H. & Williams-Jones, A.E. (1997) Chemical mobility of gold in the porphyry-epithermal environment. *Economic Geology*, 92(1), pp.45-59.

Gee, D. G., 1975. A tectonic model for the central part of the Scandinavian Caledonides. *American Journal of Science*, 275(A), pp. 468-515.

Gee, D.G., & Sturt, A. B., eds. *The Caledonide orogen* (1985) Scandinavia and related areas. John Wiley & Sons, v.27.

Giesemann, A., Jäger, H.J., Norman, A.L., Krouse, H.R. & Brand, W.A., 1994. Online sulfur-isotope determination using an elemental analyzer coupled to a mass spectrometer. *Analytical Chemistry*, 66(18), pp.2816-2819.

Goldfarb, R., Baker, T., Dubé, B., Groves, D.I., Hart, C.J. & Gosselin, P. (2005) Distribution, character and genesis of gold deposits in metamorphic terranes. *Society of Economic Geologists*.

Goldfarb, R.J. & Groves, D.I. (2015) Orogenic gold: Common or evolving fluid and metal s ources through time. *Lithos*, v.233, pp.2-26.

Goldfarb, R.J., Groves, D.I. & Gardoll, S. (2001) Orogenic gold and geologic time: a global synthesis. *Ore geology reviews*, 18(1-2), pp.1-75.

Goldstein, R.H. (2003) Petrographic analysis of fluid inclusions, In I. Samson, A. Anderson, & D. Marshall. (eds.) *Fluid Inclusions: Analysis and Interpretation*. Mineral. Assoc. Can., Short Course Ser. v.32, pp.9-53.

Goldstein, R.H. & Reynolds, T.J. (1994) *Fluid inclusion microthermometry*.

Google Maps, 2021. *Lykling map*. Google Maps (online) Available at: https://www.google.com/maps/place/5437+Lykling/(Accessed: 26.05.2021).

Grenne, T., Ihlen, P. M. & Vokes, F. M. (1999) Scandinavian Caledonide Metallogeny in a plate tectonic perspective. *Mineralium Deposita*, 34(5-6), pp. 422-471.

Griffin, W. L. & Brueckner, H. K. (1980) Caledonian Sm–Nd ages and a crustal origin for Norwegian eclogites. Nature, 285(5763), pp.319-321.

Groves, D.I., Goldfarb, R.J., Gebre-Mariam, M., Hagemann, S.G. & Robert, F. (1998) Orogenic gold deposits: a proposed classification in the context of their crustal

distribution and relationship to other gold deposit types. *Ore geology reviews*, 13(1-5), pp.7-27.

Groves, D.I., Goldfarb, R.J., Robert, F. & Hart, C.J. (2003) Gold deposits in metamorphic belts: overview of current understanding, outstanding problems, future research, and exploration significance. *Economic geology*, 98(1), pp.1-29.

Groves, D. I., Santosh, M., Goldfarb, R. J., & Zhang, L. (2018) Structural geometry of orogenic gold deposits: Implications for exploration of world-class and giant deposits. *Geoscience Frontiers*, 9(4), pp.1163-1177.

Helland, A. (1884) *Guldet paa Bømmeløen og dets Gange*. Kristiania: Writers publisher.

Hoefs, J. (2018) *Stable isotope geochemistry*, eighth edition. Springer, Berlin, vol.285.

Hollocher, K., Robinson, P., Walsh, E. & Terry, M. P. (2007) The Neoproterozoic Ottfjallet dike swarm of the Middle Allochthon, traced geochemically into the Scandian Hinterland, Western Gneiss Region, Norway. *American Journal of Science*, 307(6), pp. 901-953.

Hollocher, K., Robinson, P., Walsh, E., & Roberts, D. (2012) Geochemistry of amphibolite-facies volcanics and gabbros of the Støren Nappe in extensions west and southwest of Trondheim, Western Gneiss Region, Norway: a key to correlations and paleotectonic settings. *American Journal of Science*, v. 312, pp. 357-416.

Hossack, J. R. & Cooper, M. A. (1986) Collision tectonics in the Scandinavian Caledonides. *Geological Society*, London, Special Publications, 19(1), pp. 285-304.

Irvine, T.N. & Baragar, W.R.A. (1971) A guide to the chemical classification of the common volcanic rocks. *Canadian journal of earth sciences*, 8(5), pp.523-548.

Jowett, E. C. (1991) Fitting iron and magnesium into the hydrothermal chlorite geothermometer. GAC/MAC/SEG Joint Annual Meeting, Program with Abstract, v. 16.

Kranidiotis, P. & MacLean, W.H. (1987) Systematics of chlorite alteration at the Phelps Dodge massive sulfide deposit, Matagami, Quebec. *Economic geology*, 82(7), pp.1898-1911.

Krogh, E. J. (1977) Evidence of Precambrian continent–continent collision in Western Norway. *Nature*, 267(5606), pp. 17-19.

Lambrecht, G. & Diamond, L.W. (2014) Morphological ripening of fluid inclusions and coupled zone-refining in quartz crystals revealed by cathodoluminescence imaging: Implications for CL-petrography, fluid inclusion analysis and trace-element geothermometry. *Geochimica et Cosmochimica Acta*, v. 141, pp.381-406.

Lindgren, W. (1907) The relation of ore-deposition to physical conditions. *Economic Geology*, 2(2), pp.105-127.

Lindgren, W. (1933) Chapter XXIV: Epithermal Deposits–Metalliferous Deposits Formed Near the Surface by Ascending Thermal Waters and in Genetic Connection With Igneous Rocks, Mineral Deposits. Mineral Deposits, fourth edition. McGraw-Hill Book Company, Inc., New York and London, pp.444-513.

McDonough, W.F. & Sun, S.S. (1995) The composition of the Earth. *Chemical geology*, 120(3-4), pp.223-253.

Nordås, J. (1985) *A volcanological and geochemical study of the lower palaeozoic Lykling ophiolithic complex and Siggjo complex, Central Bømlo, Western Norway*. Unpubl. Cand. Real. Thesis. University of Bergen, Norway.

O'Connor, J.T. (1965) A classification for quartz-rich igneous rocks based on feldspar ratios. *US geological survey professional paper B*, v.525, pp.79-84.

Pedersen, R. B. & Dunning, G. R. (1997) Evolution of arc crust and relations between contrasting sources: U-Pb (age), Nd and Sr isotope systematics of the ophiolitic terrain of SW Norway. *Contributions to Mineralogy and Petrology*, 128(1), pp. 1-15.

Pedersen, R. B. & Furnes, H. (1991) Geology, magmatic affinity and geotectonic environment of some Caledonian ophiolites in Norway. *Journal of Geodynamics*, 13(2-4), pp. 183-203.

Pedersen, R. B., Bruton, D. L. & Furnes, H. (1992) Ordovician faunas, island arcs and ophiolites in the Scandinavian Caledonides. *Wiley-Blackwell*, 4(2), pp.217-222

Pedersen, R.B., Furnes, H., & Dunning, G. (1988) Some Norwegian ophiolite complexes reconsidered. *Norges Geologiske Undersokelse,* Special Publication, v. 3, pp.80-85.

Phillips, G.N. and Evans, K.A. (2004) Role of CO 2 in the formation of gold deposits. *Nature*, 429(6994), pp.860-863.

Randive, K.R., Hari, K.R., Dora, M.L., Malpe, D.B. & Bhondwe, A.A. (2014) Study of fluid inclusions: methods, techniques and applications. *Geol. Mag*, v. 29, pp.19-28.

Reusch, H. (1888) *Bømmeløen og Karmøen med omgivelser*. GFF, 10(5), pp.392-396.

Rey, P., Burg, J.-P. & Casey, M. (1997) The Scandinavian Caledonides and their relationship to the Variscan belt. In: Burg, J.-P. & Ford, M. (eds) *Geological Society*, London, Special Publications, v. 121, pp.179–200.

Ridley J.R. & Diamond L.W. (2000) Fluid chemistry of lode-gold deposits and implications for genetic models. In: Hagemann S.G., Brown P. (Eds.), *Gold in 2000*. Economic Geology. Society of Economic Geologists, Inc., v. 13, pp.141-162.

Roberts, D. & Gee, D. G. (1985) An introduction to the structure of the Scandinavian Caledonides. *The Caledonide orogen–Scandinavia and related areas*, v. 1, pp.55-68.

Roberts, D. (2003) The Scandinavian Caledonides: event chronology, palaeogeographic settings and likely modern analogues. *Tectonophysics*, 365(1-4), pp.283-299.

Roedder, E. & Bodnar, R.J. (1980) Geologic pressure determinations from fluid inclusion studies. *Annual review of earth and planetary sciences*, 8(1), pp.263-301.

Roedder, E. (1984) Fluid inclusion, Reviews in mineralogy. Mineralogical society of Amerika, v. 12.

Rowe, R.R. & Zhou, X. (2007) Models and exploration methods for major gold deposit types. In *Proceedings of exploration*, v.7, pp.691-711.

Saltvedt, S. (2021) *The formation of the ophiolitic terrane of SW Norway - relationships between immature island arc sequences and trondhjemitic complexes on Bømlo*. Master Thesis, University of Bergen.

Saunders, J.A., Hofstra, A.H., Goldfarb, R.J. & Reed, M.H. (2014) Geochemistry of hydrothermal gold deposits. *Treatise on geochemistry*. 2nd edn. Elsevier, Oxford, v. 13, pp.383-424.

Seward, T. M. (1973) Thio complexes of gold and the transport of gold in hydrothermal ore solutions. *Geochimica et Cosmochimica Acta*, 37(3), 379-399.

Shanks, Pat. W.C. (2014) Stable Isotope Geochemistry of Mineral Deposits In. *Treatise on geochemistry*. 2nd edn. Elsevier, Oxford, v.13, pp. 59-85.

Sharp, Z. (2017) *Principles of stable isotope geochemistry*, 2nd edition.

Sherpherd, T.J., Rankin, A.H., Alderton. (1985) *A Practical Guide to Fluid Inclusion Studies.* Chapman & Hall, New York.

Simpson, M. P., Strmic Palinkas, S., Mauk, J. L., & Bodnar, R. J. (2015) Fluid inclusion chemistry of adularia-sericite epithermal Au-Ag deposits of the southern Hauraki Goldfield, New Zealand. *Economic Geology*, 110(3), 763-786.

Slotnes, M. S. (2021) *Detrital zircon provenance of the Bremnes Migmatite Complex on Bømlo, SW Norway*. Master Thesis, University of Bergen.

Solyom, Z. (1979) The Ottfjaell dolerites. Geochemistry of the dykee swarm in relation to the geo dynamics of the Caledonide Orogen of Central Scandinavia. *Sver. Geol. Unders. Ser.*, 756(C), p. 38.

SRK Exploration Services Ltd. (2018) *Competent person's report on the Bømlo and Bjerkheim projects, Norway*. ES7775, SRK Exploration Services Ltd.

Stakes, D. S. & O'Neil, J.R. (1982) Mineralogy and stable isotope geochemistry of hydrothermally altered oceanic rocks. *Earth and Planetary Science Letters*, 57(2), pp.285-304.

Stautland, B. (2000) *Gullgravarane på Lykling*, Bømlo, Bømlo kommune.

Steele-MacInnis, M., Lecumberri-Sanchez, P., Bodnar, R.J., 2012. HOKIEFLINCKS_H2O-NACL: A Microsoft Excel spreadsheet for interpreting microthermometric data from f luid inclusions based on the PVTX properties of H2O-NaCl. Computers & Geosciences.

Stefánsson, A. & Seward, T.M. (2004) Gold (I) complexing in aqueous sulphide solutions to 500 C at 500 bar. *Geochimica et Cosmochimica Acta*, 68(20), pp.4121-4143.

Stephens, M. B. & Gee, D. G. (1985) A tectonic model for the evolution of the eugeoclinal terranes in the central Scandinavian Caledonides. The Caledonide Orogen: Scandinavia and Related Areas. *Wiley*, Chichester, v.953, p. 978.

Stephens, M. B. & Gee, D. G. (1989) Terranes and polyphase accretionary history in the Scandinavian Caledonides. *Geological Society of America*, Special Paper, v.230, pp. 17-30.

Stephens, M. B. (1988) The Scandinavian Caledonides: a complexity of collisions. *Geology Today*, 4(1), pp. 20-26.

Sun, S.S. & McDonough, W.F. (1989) Chemical and isotopic systematics of oceanic basalts: implications for mantle composition and processes. *Geological Society*, London, Special Publications, 42(1), pp.313-345.

Tomkins, A.G. (2013) On the source of orogenic gold. *Geology*, 41(12), pp.1255-1256.

Urey, H.C. (1947) The thermodynamic properties of isotopic substances. Journal of the Chemical Society, pp.562-581.

Veizer, J. & Hoefs, J. (1976) The nature of O18/O16 and C13/C12 secular trends in sedimentary carbonate rocks. *Geochimica et Cosmochimica Acta*, 40(11), pp.1387-1395.

Viken, A.L. (2017) *Accretionary history of Lower Ordovician island arc complexes on Bømlo: evidence from detrital zircon dating and geochemical data*. Master thesis, University of Bergen, Bergen, Norway.

Wilkinson, J.J. (2001) Fluid inclusions in hydrothermal ore deposits. *Lithos*, 55(1-4), pp.229-272.

Wilks, W.J. & Cuthbert, S.J. (1994) The evolution of the Hornelen Basin detachment system, western Norway: implications for the style of late orogenic extension in the southern Scandinavian Caledonides. *Tectonophysics*, 238(1-4), pp.1-30.

Wulff, P.W. (1996) *En befaring af cirka 100 mineraliseringer i Sunnhordland, SV-Norge*. NGU-96/139, Norges geologiske undersøkelse.

Zhu, Y., An, F. & Tan, J. (2011) Geochemistry of hydrothermal gold deposits: a review. *Geoscience Frontiers*, 2(3), pp.367-374.

Zoheir, B. and Moritz, R. (2014) Fluid evolution in the el-Sid gold deposit, Eastern Desert, Egypt. Geological Society, *London, Special Publications*, 402(1), pp.147-175.

Zoheir, B.A., Johnson, P.R., Goldfarb, R.J. and Klemm, D.D. (2019) Orogenic gold in the Egyptian Eastern Desert: widespread gold mineralization in the late stages of Neoproterozoic orogeny. *Gondwana Research*, v.75, pp.184-217.

Zoheir, B., Steele-MacInnis, M., & Garbe-Schönberg, D. (2019) Orogenic gold formation in an evolving, decompressing hydrothermal system: Genesis of the Samut gold deposit, Eastern Desert, Egypt. *Ore Geology Reviews*, 105, 236-257.

APPENDIX

Appendix A – Sample overview

Appendix B – Fluid inclusion data

Appendix C – SEM-EDS point analysis

Appendix D – LA-ICP-MS maps

Appendix E – LA-ICP-MS point analysis

Appendix F – Chlorite thermometry

Appendix A – Sample overview

Sample name	Mineralization	Minerals	Analysis	Coordinates	Host	Direction
19LYK1A	Brittle-ductile		Au assay, XRD	59.708467, 5.16848	Lykling Ophiolite	E-W
19LYK2A	Mafic dike with mineralization	Qtz, Py	RLM, FIs, lithogeochemistry, $d^{13}C$, $d^{18}O$, Au Assay, $d^{34}S$	59.711122, 5.166439	Lykling Ophiolite	NNE-SSW
19LYK4A	Brittle	Qtz	FIs	59.711122, 5.166439	Lykling Ophiolite	NNE-SSW
20LYK3B	Brittle-ductile	Qtz, C,	$d^{13}C$, $d^{18}O$, RLM, SEM-EDS, chlorite thermometry	59.708467, 5.16848	Lykling Ophiolite	NNE-SSW
20LYK4C	Brittle	Qtz, Cpy	RLM, SEM-EDS, FIs, Au assay, $d^{34}S$	59.709199, 5.168484	Lykling Ophiolite	NNE-SSW
20LYK4D	Brittle	Qtz, Cpy	RLM, LA-ICP-MS, Fis, $d^{34}S$	59.709199, 5.168484	Lykling Ophiolite	NNE-SSW
20LYK6	Brittle-ductile	Qtz, C	FIs, $d^{13}C$, $d^{18}O$, XRD	59.711078, 5.17014	Lykling Ophiolite	NNE-SSW
20LYK7A	Gabbro		TLM	59.712653, 5.176204	Lykling Ophiolite	
20LYK7D	Brittle-ductile	Qtz, C, Greenschist	$d^{13}C$, $d^{18}O$, XRD	59.712653, 5.176204	Lykling Ophiolite	NNE-SSW
20LYK10C	Brittle-ductile	Qtz, C, Greenschist	$d^{13}C$, $d^{18}O$	59.713481, 5.168642	Lykling Ophiolite	NNE-SSW
20LYK12	Mafic dike without mineralization		Lithogeochemistry	59.714744, 5.170215	Lykling Ophiolite	ESE-WNW
20LYK13A	Brittle	Qtz	Au Assay	59.714924, 5.170002	Lykling Ophiolite	NNE-SSW
20LYK13B	Brittle, mafic dike with mineralization		TLM, lithogeochemistry, SEM-EDS, chlorite thermometry	59.714924, 5.170002	Lykling Ophiolite	ESE-WNW
20LYK14B	Brittle	Qtz, Py	RLM, LA-ICP-MS, $d^{34}S$	59.714478, 5.170965	Lykling Ophiolite	NNE-SSW
20LYK15D	Brittle-ductile	Qtz, C, Greenschist	FIs, $d^{13}C$, $d^{18}O$, Au Assay	59.715817, 5.171756	Trondhjemite	NNE-SSW
20LYK16C	Trondhjemite		TLM	59.717081, 5.173501	Trondhjemite	
20LYK17A	Brittle	Qtz	FIs	59.717341, 5.169952	Trondhjemite	NNE-SSW
20LYK17B	Mafic dike with mineralization		TLM, lithogeochemistry	59.717341, 5.169952	Trondhjemite	NNE-SSW
20LYK18A	Brittle, qtz	Qtz	FIs, Au Assay	59.717574, 5.170895	Trondhjemite	NNE-SSW
20LYK19C	Mafic dike with mineralization	Qtz	TLM, SEM-EDS, chlorite thermometry	59.716538, 5.170148	Trondhjemite	NNE-SSW

20LYK20B	Brittle	Qtz, Py	RLM, LA-ICP-MS, FIs, Au Assay, $d^{34}S$	59.714914, 5.16724	Trondhjemite	NNE-SSW
20LYK20H	Brittle, Quartz crystal	Qtz	FIs	59.714914, 5.16724	Trondhjemite	NNE-SSW
20LYK20J	Mafic dike with mineralization	C	$d^{13}C$, $d^{18}O$	59.714914, 5.16724	Trondhjemite	NNE-SSW
20LYK20K	Mafic dike with mineralization, East		Lithogeochemistry	59.714914, 5.16724	Trondhjemite	NNE-SSW
20LYK20L	Mafic dike with mineralization, West		Lithogeochemistry	59.714914, 5.16724	Trondhjemite	NNE-SSW
20LYK21B	Brittle-ductile	Qtz, Py, C	$d^{13}C$, $d^{18}O$	59.712743, 5.166402	Lykling Ophiolite	NNE-SSW
20LYK21C	Brittle-ductile	Qtx, Py, C	RLM, SEM-EDS, $d^{13}C$, $d^{18}O$,	59.712743, 5.166402	Lykling Ophiolite	NNE-SSW
20LYK24A	Brittle-ductile	Qtz, C	FIs, $d^{13}C$, $d^{18}O$,	59.716606, 5.174508	Trondhjemite	E-W
20LYK24B	Brittle-ductile	Qtz, C	$d^{13}C$, $d^{18}O$, Au Assay	59.716606, 5.174508	Trondhjemite	E-W
20LYK25B	Brittle-ductile	Qtz, C	$d^{13}C$, $d^{18}O$, Au Assay	59.717081, 5.173501	Trondhjemite	NNE-SSW
20LYK25C	Brittle	Qtz	FIs	59.717081, 5.173501	Trondhjemite	NNE-SSW
20LYK26C	Trondhjemite		TLM, lithogeochemistry	59.716308, 5.173487	Trondhjemite	
20LYK27B	Brittle-ductile	Qtz, Py, C	RLM, LA-ICP-MS, $d^{34}S$	59.716293, 5.172138	Trondhjemite	NNE-SSW
20LYK27D	Trondhjemite		TLM	59.716293, 5.172138	Trondhjemite	
20LYK27E1	Mafic dike with mineralization		TLM, lithogeochemistry	59.716293, 5.172138	Trondhjemite	ESE-WNW
20LYK37C	Brittle-ductile	Qtz, C, Py	RLM, SEM-EDS, FIs, $d^{13}C$, $d^{18}O$, Au Assay, $d^{34}S$	59.704453, 5.166965	Lykling Ophiolite	ESE-WNW
20LYK38C	Mafic dike		Lithogeochemistry	59.704516, 5.167037	Lykling Ophiolite	ESE-WNW
20LYK39A	Brittle,	Qtz, Py, Cpy, C	RLM, SEM-EDS, chlorite thermometry FIs, $d^{13}C$, $d^{18}O$, Au Assay, $d^{34}S$	59.704912, 5.165151	Lykling Ophiolite	ESE-WNW
20LYK39C	Brittle	Qtz, Py	RLM, LA-ICP-MS, FIs, Au Assay, $d^{34}S$	59.704912, 5.165151	Lykling Ophiolite	ESE-WNW

Appendix B – Fluid Inclusion data

Sample name	FI #	Te	Tm – ice (ºC)	Th (ºC)	Salinity (w%. NaCl eq)	Density. δ (g/cm^3)	dP/dT (bar/ ºC)
19LYK2A – Brittle, hosted in gabbro							
FIA - 1	1	-21	-0.1	125	0.18	0.945	18.2
	2	-21	-0.1	128	0.18	0.943	18.1
	3	-21	-0.2	125	0.35	0.946	18.2
	4	-21	-0.2	127	0.35	0.945	18.2
	5	-21	-0.2	127	0.35	0.945	18.2
	6	-21	-0.5	127	0.88	0.948	18.2
FIA - 2	1	-52	-8.3	177	12.05	0.980	19.0
	2	-52	-8.4	177	12.16	0.981	19.0
	3	-52	-8.4	175	12.16	0.983	19.1
	4	-52	-8.0	178	11.70	0.977	18.8
	5	-52	-8.2	175	11.93	0.981	19.1
	6	-52	-8.2	178	11.93	0.979	18.9
	7	-52	-8.0	180	11.70	0.975	18.7
FIA - 3	1		-5.0	128	7.86	0.993	20.6
	2		-4.8	129	7.59	0.990	20.4
	3		-5.0	131	7.86	0.990	20.4
	4		-5.0	130	7.86	0.991	20.5
	5		-5.1	129	8.00	0.993	20.6
	6		-5.2	132	8.14	0.992	20.5
	7		-5.0	130	7.86	0.991	20.5
FIA - 4	1		-3.0	125	4.96	0.975	19.5
	2		-3.3	125	5.41	0.978	19.7
	3		-3.5	127	5.71	0.979	19.8
	4		-3.0	124	4.96	0.976	19.6
19LYK4A – Brittle, hosted in gabbro							

FIA – 3	1		-0.5	125	0.88	0.949	18.3
	2		-0.2	120	0.35	0.950	18.3
	3		-0.2	120	0.35	0.950	18.3
	4		-0.3	123	0.53	0.949	18.3
20LYK24A – Ductile, hosted in Trondhjemite							
FIA – 2	1		-3.4	182	5.56	0.928	16.9
	2		-4.0	178	6.45	0.938	17.3
	3		-3.5	180	5.71	0.931	17.0
	4		-2.9	179	4.80	0.925	16.9
	5		-2.9	180	4.80	0.924	16.8
FIA – 3	1		-2.0	178	3.39	0.917	16.7
	2		-2.1	180	3.55	0.916	16.6
	3		-2.2	182	3.71	0.915	16.5
	4		-1.9	179	3.23	0.914	16.6
	5		-2.0	178	3.39	0.917	16.7
FIA - 4	1		-2.1	180	3.55	0.916	16.6
	2		-2.0	182	3.39	0.912	16.5
	3		-1.9	180	3.23	0.913	16.6
20LYK4D – Brittle (cpy-rich), hosted in gabbro							
FIA 1	1	-21	-3.5	162	5.71	0.949	17.9
	2	-21	-3.7	162	6.01	0.951	18.0
	3	-21	-3.4	165	5.56	0.945	17.7
	4	-21	-3.6	160	5.86	0.952	18.1
	5	-21	-3.5	165	5.71	0.946	17.8
FIA – 2	1		-3.4	165	5.56	0.945	17.7
	2		-3.4	164	5.56	0.946	17.8
	3		-3.5	165	5.71	0.946	17.8
	4		-3.5	162	5.71	0.949	17.9
	5		-3.6	168	5.86	0.944	17.7
FIA – 3	1		-3.4	165	5.56	0.945	17.7
	2		-3.4	168	5.56	0.942	17.6
	3		-3.6	164	5.86	0.948	17.9

20LYK18A – Brittle, hosted in Trondhjemite							
FIA 1	1	-52	-2.0	153	3.39	0.941	17.8
	2	-52	-2.0	151	3.39	0.943	17.9
	3	-52	-2.5	154	4.18	0.946	17.9
	4	-52	-2.0	150	3.39	0.944	17.9
	5	-52	-1.9	150	3.23	0.943	17.9
FIA 2	1		-0.5	131	0.88	0.945	18.1
	2		-1.0	132	1.74	0.949	18.3
	3		-0.5	129	0.88	0.946	18.2
	4		-0.5	130	0.88	0.945	18.2
	5		-1.1	133	1.91	0.949	18.3
20LYK39A Brittle, hosted in gabbro							
FIA – 2	1		-8.0	167	11.70	0.987	19.5
	2		-7.9	165	11.58	0.988	19.6
	3		-8.0	165	11.70	0.989	19.7
	4		-8.1	168	11.81	0.987	19.5
	5		-8.0	168	11.70	0.986	19.5
	6		-8.2	168	11.93	0.988	19.5
FIA – 3	1		-7.9	185	11.58	0.969	18.3
	2		-7.5	189	11.10	0.962	17.9
	3		-7.5	182	11.10	0.968	18.3
	4		-8.0	180	11.70	0.975	18.7
FIA - 4	1		-7.2	160	10.73	0.986	19.7
	2		-7.1	160	10.61	0.985	19.6
	3		-7.2	162	10.73	0.984	19.5
	4		-7.5	158	11.10	0.991	19.9
20LYK39C Brittle. hosted in gabbro							
FIA - 1	1		-3.0	150	4.96	0.955	18.3
	2		-3.5	150	5.71	0.960	18.6
	3		-3.2	145	5.26	0.961	18.7
	4		-3.5	155	5.71	0.955	18.3
FIA - 2	1		-3.0	120	4.96	0.979	19.8

	2		-3.5	125	5.71	0.980	19.9
	3		-3.2	122	5.26	0.980	19.8
	4		-3.2	128	5.26	0.975	19.5
	5		-3.1	122	5.11	0.979	19.8
	6		-3.0	123	4.96	0.977	19.6
	7		-3.2	130	5.26	0.973	19.4
20LYK6 Brittle, hosted in gabbro							
FIA 1	1		-4.0	120	6.45	0.989	20.4
	2		-4.1	123	6.59	0.988	20.3
	3		-4.2	125	6.74	0.987	20.3
	4		-4.0	120	6.45	0.989	20.4
	5		-4.0	123	6.45	0.987	20.3
FIA 2	1		-4.2	125	6.74	0.987	20.3
	2		-4.0	120	6.45	0.989	20.4
	3		-4.3	120	6.88	0.992	20.6
	4		-4.3	125	6.88	0.988	20.4
FIA 3	1		-3.2	132	5.26	0.972	19.3
	2		-3.0	131	4.96	0.971	19.3
	3		-3.1	135	5.11	0.968	19.1
20LYK37C Ductile, boiling FIA. hosted in gabbro							
FIA 1	1		-3.2	165	5.26	0.943	17.7
	2		-3.3	168	5.41	0.941	17.5
	3	V-rich		165	0		
	4		-3.2	167	5.26	0.941	17.6
	5	V-rich		165	0		
	6		-3.0	166	4.96	0.940	17.5
	7	V-rich		168	0		
FIA 2	1		-3.5	170	5.71	0.941	17.5
	2	V-rich		168	0		
	3		-3.2	165	5.26	0.943	17.7
	4		-3.4	165	5.56	0.945	17.7
FIA 3	1	-21	-3.4	170	5.56	0.940	17.5

	2	-21	-3.5	171	5.71	0.940	17.5
	3	-21	-3.5	170	5.71	0.941	17.5
	4	-21	-3.2	169	5.26	0.939	17.5
	5	-21	-3.5	169	5.71	0.942	17.6
FIA 4	1		-3.0	172	4.96	0.934	17.2
	2		-3.1	165	5.11	0.942	17.6
	3		-3.1	171	5.11	0.936	17.3
	4		-3.2	170	5.26	0.938	17.4
	5		-3.2	170	5.26	0.938	17.4
20LYK25B Ductile, hosted in Trondhjemite							
FIA 1	1		-3.0	180	4.96	0.925	16.8
	2		-2.9	178	4.80	0.926	16.9
	3		-2.9	176	4.80	0.929	17.0
FIA 2	1		-2.8	176	4.65	0.927	17.0
	2		-2.9	179	4.80	0.925	16.9
	3		-2.6	175	4.34	0.926	17.0
	4		-3.0	176	4.96	0.930	17.0
FIA 3	1		-3.1	181	5.11	0.926	16.8
	2		-2.9	178	4.80	0.926	16.9
	3		-2.9	178	4.80	0.926	16.9
20LYK25C Brittle, hosted in Trondhjemite							
FIA 1	1		-4.0	125	6.45	0.985	20.2
	2		-3.9	125	6.30	0.984	20.1
	3		-3.8	123	6.16	0.985	20.2
	4		-4.0	123	6.45	0.987	20.3
	5		-4.0	123	6.45	0.987	20.3

Appendix C – SEM-EDS point analysis

Sample 20LYK4C - A

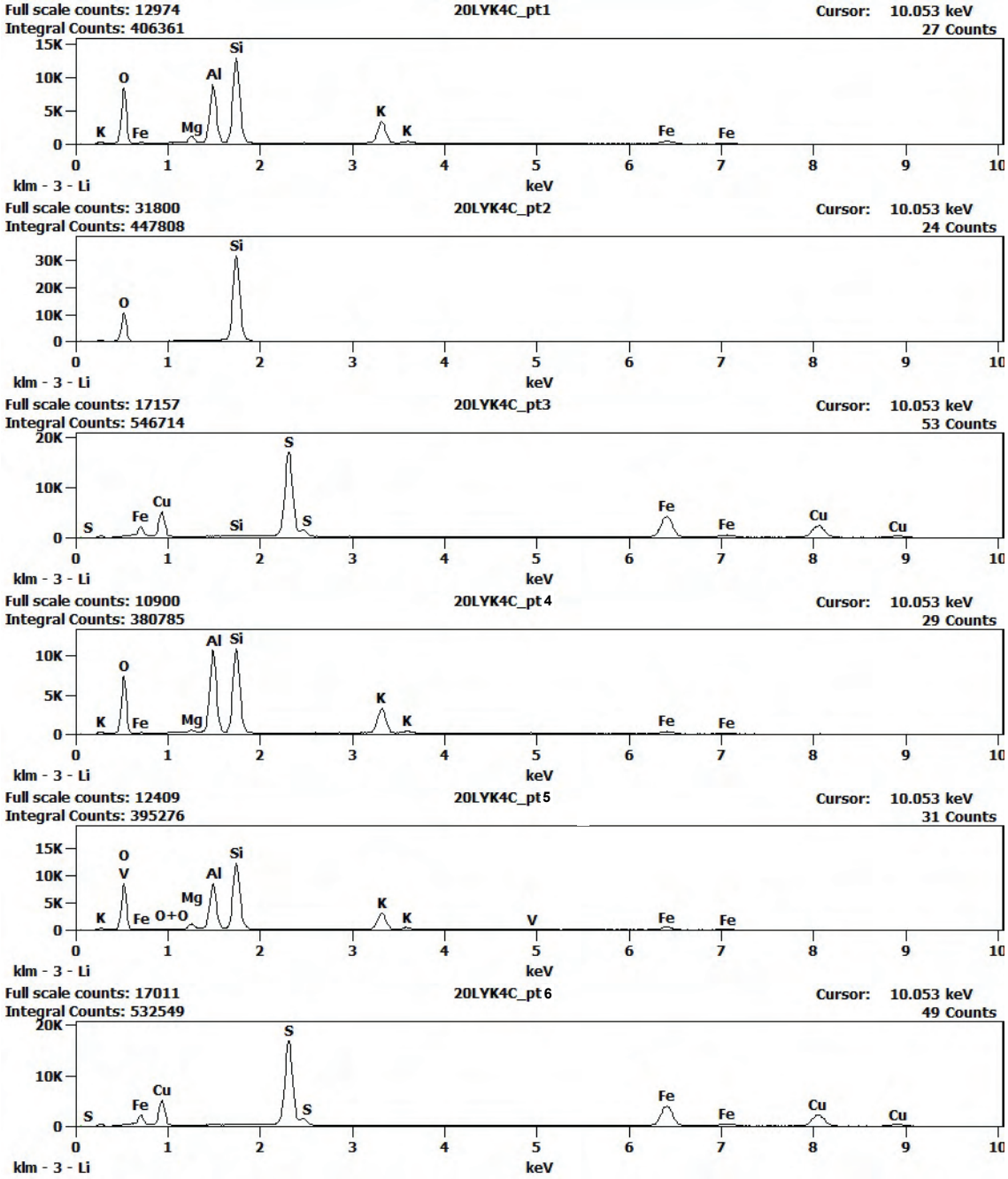

Sample 20LYK4C - B

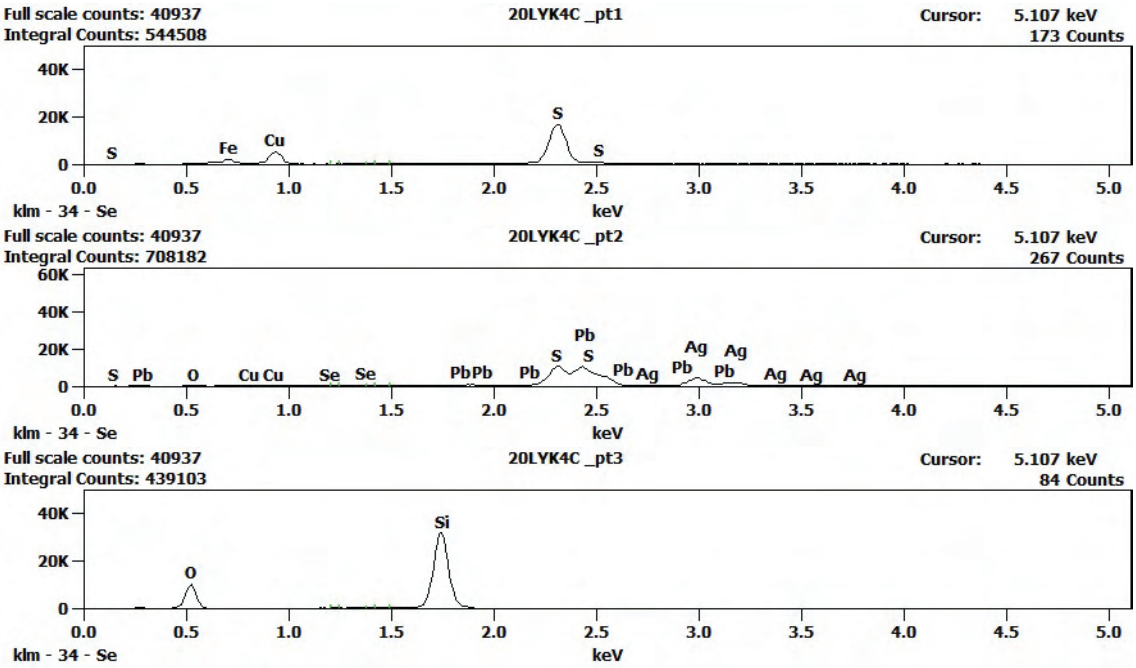

Sample 20LYK39A - A

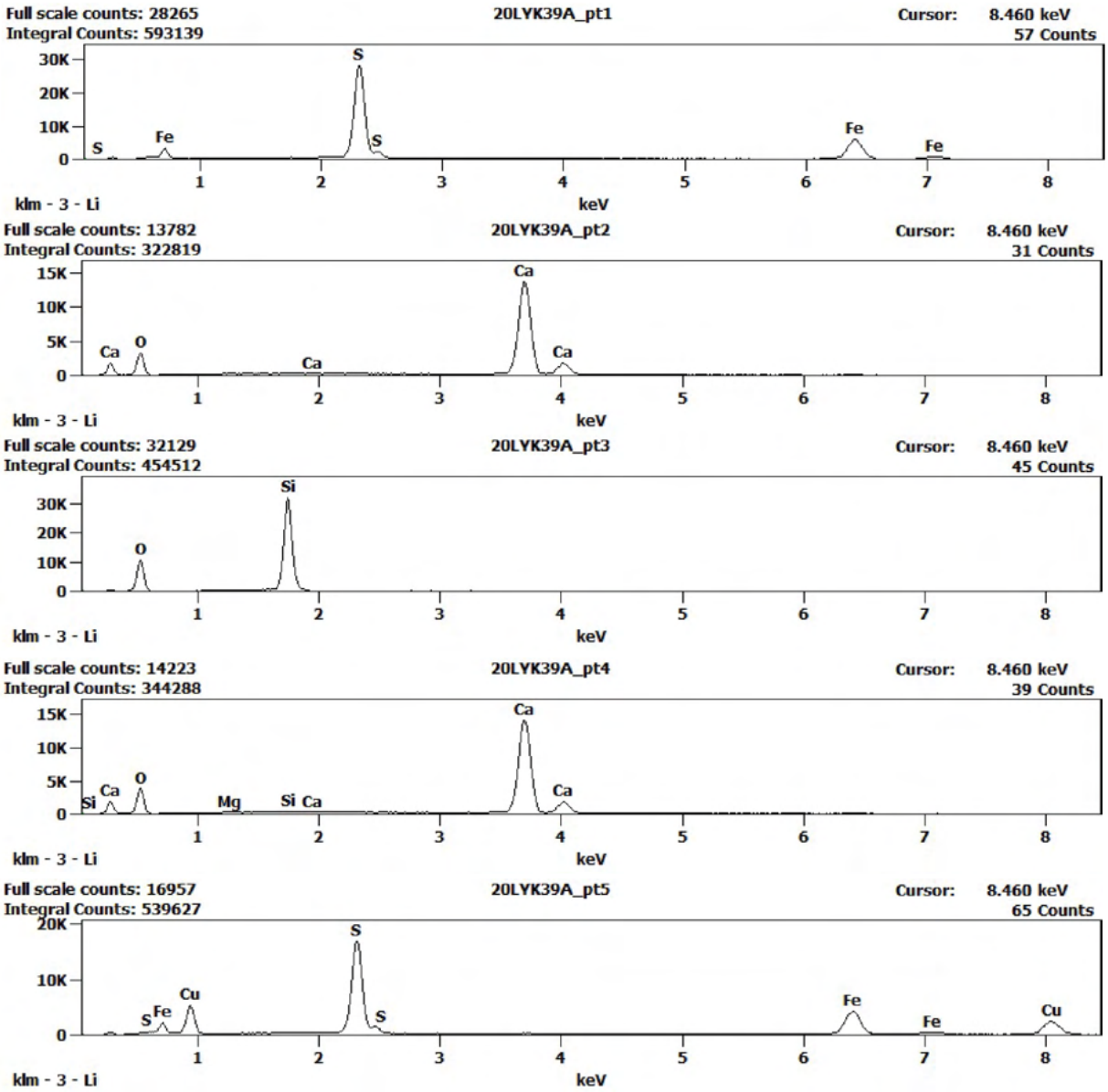

Sample 20LYK39A - B

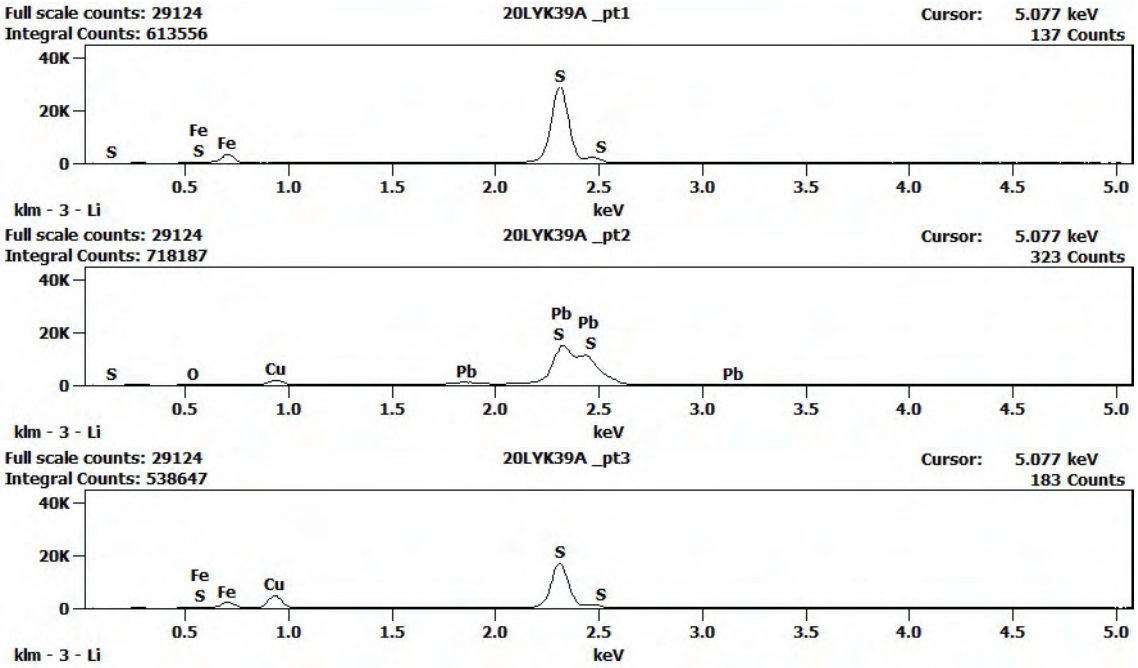

Sample 20LYK37C

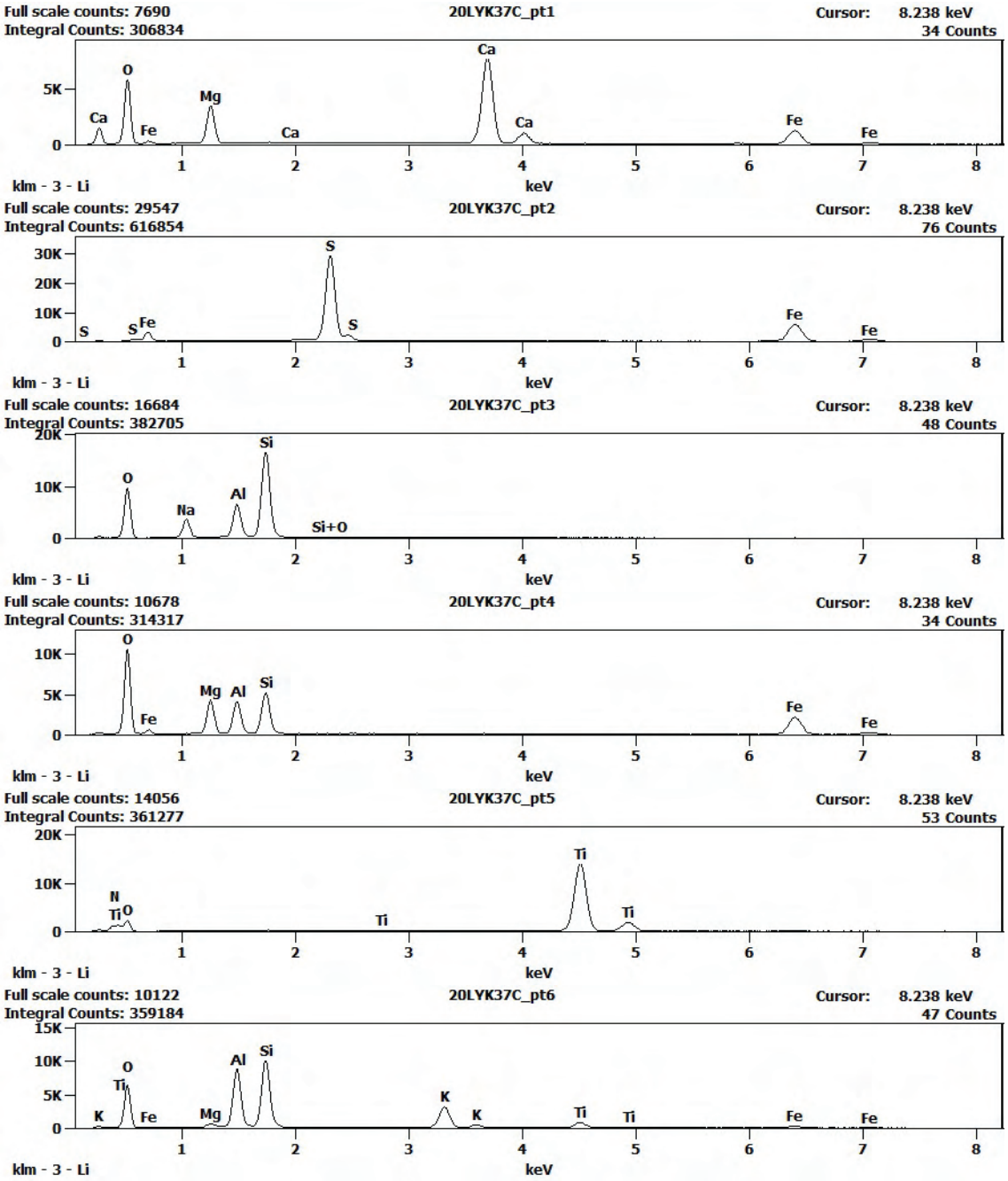

Sample 20LYK21C

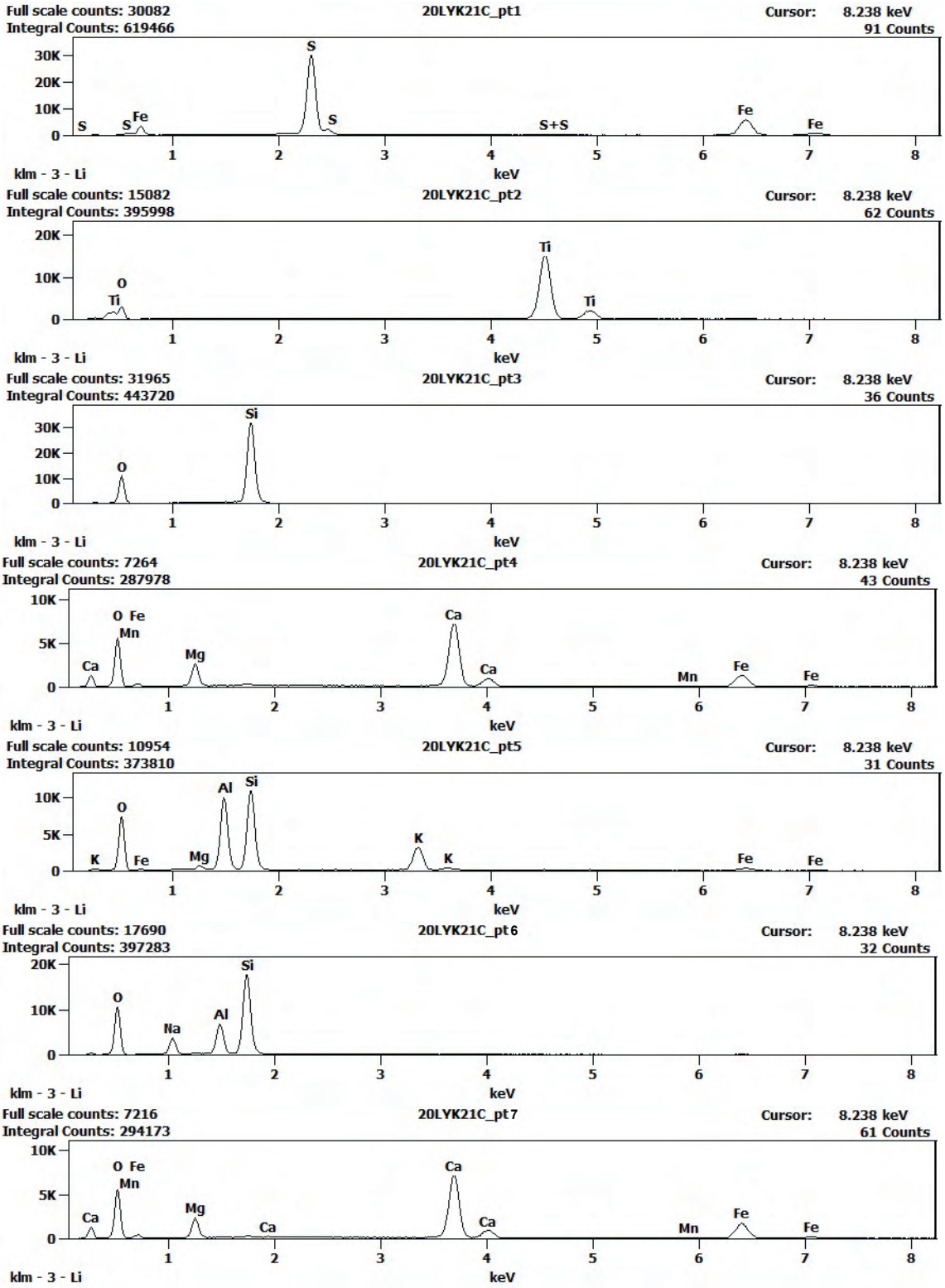

Appendix D – LA-ICP-MS maps

20LYK14B Area 2

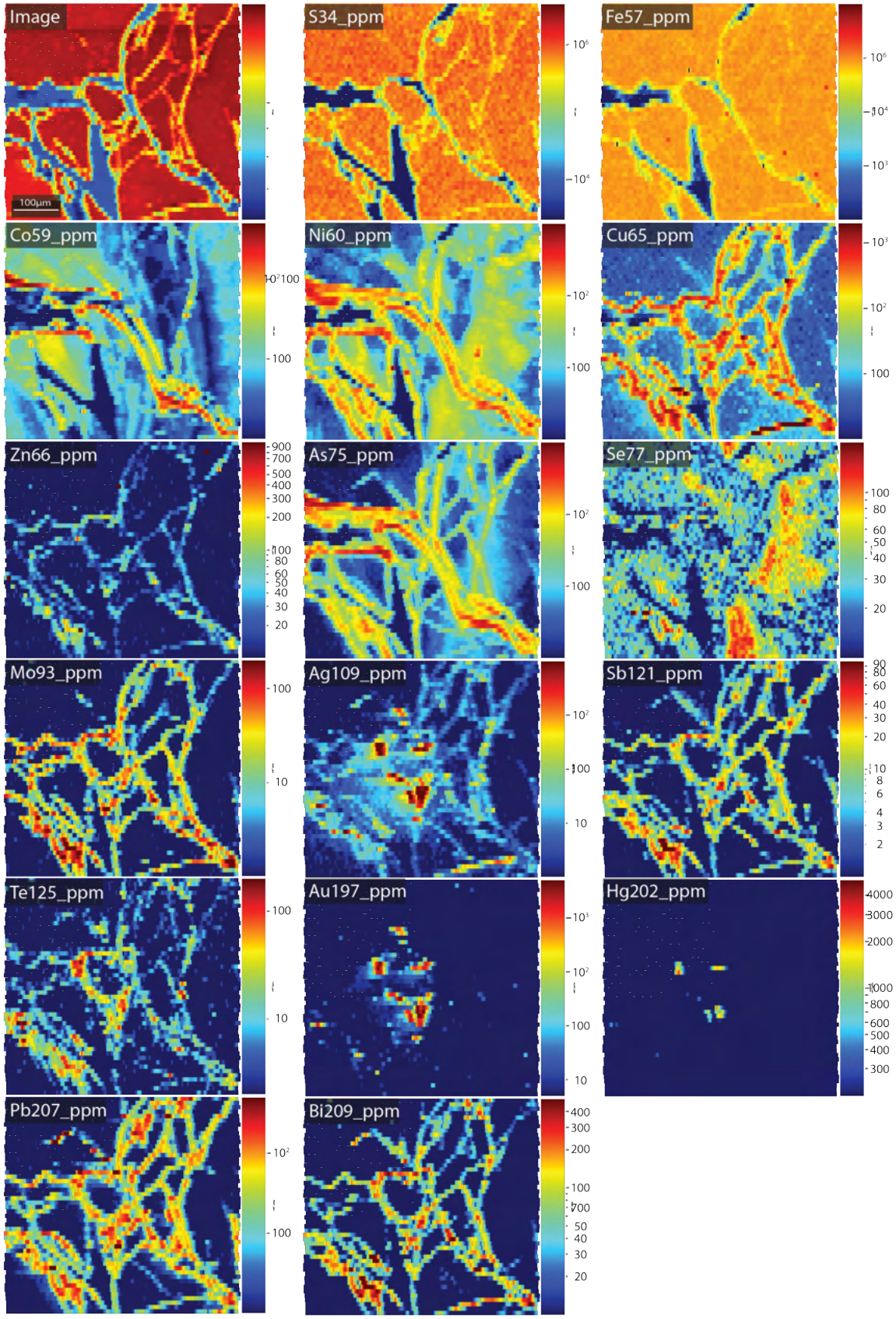

20LYK20B Area 1

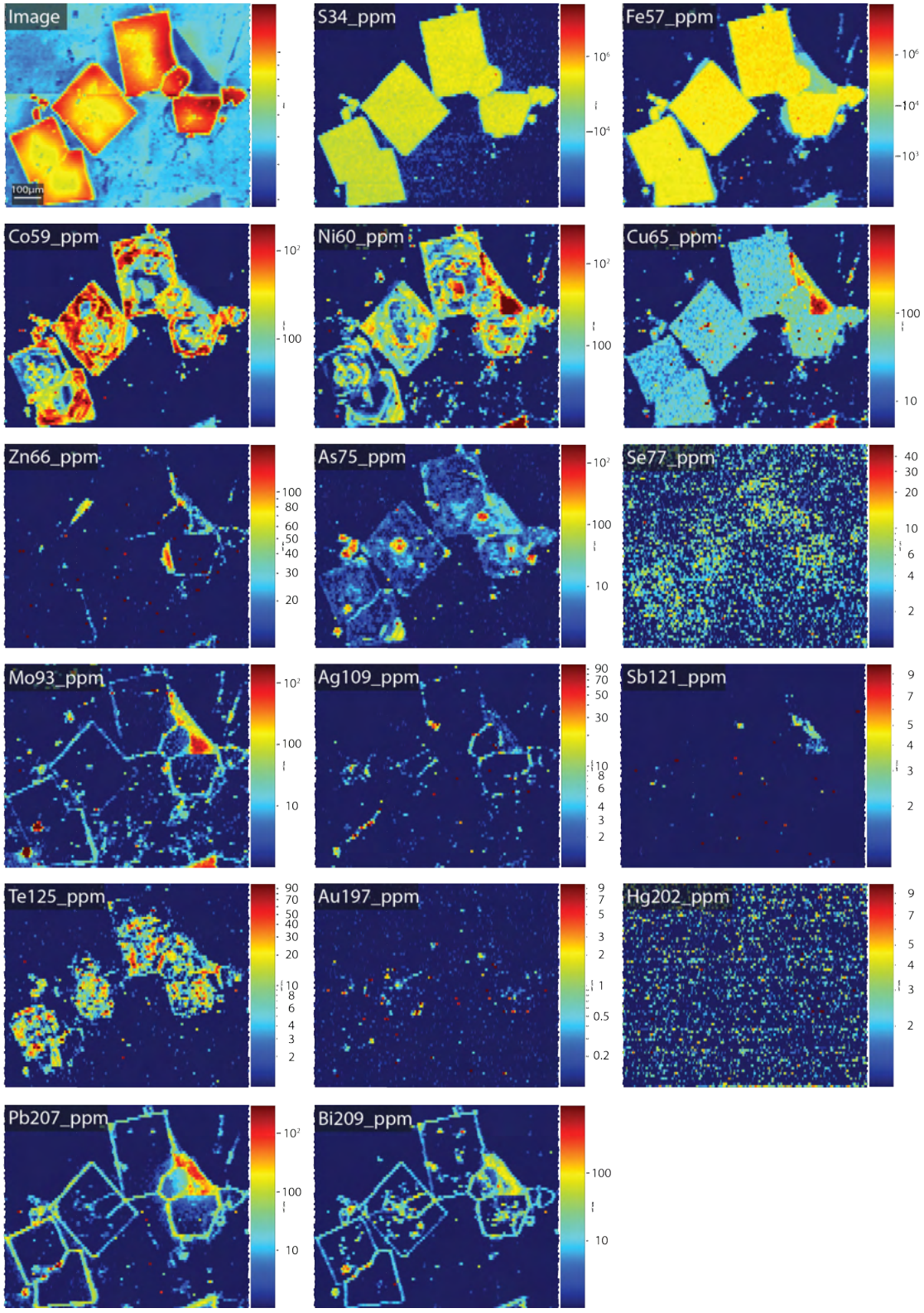

20LYK20B Area 1B

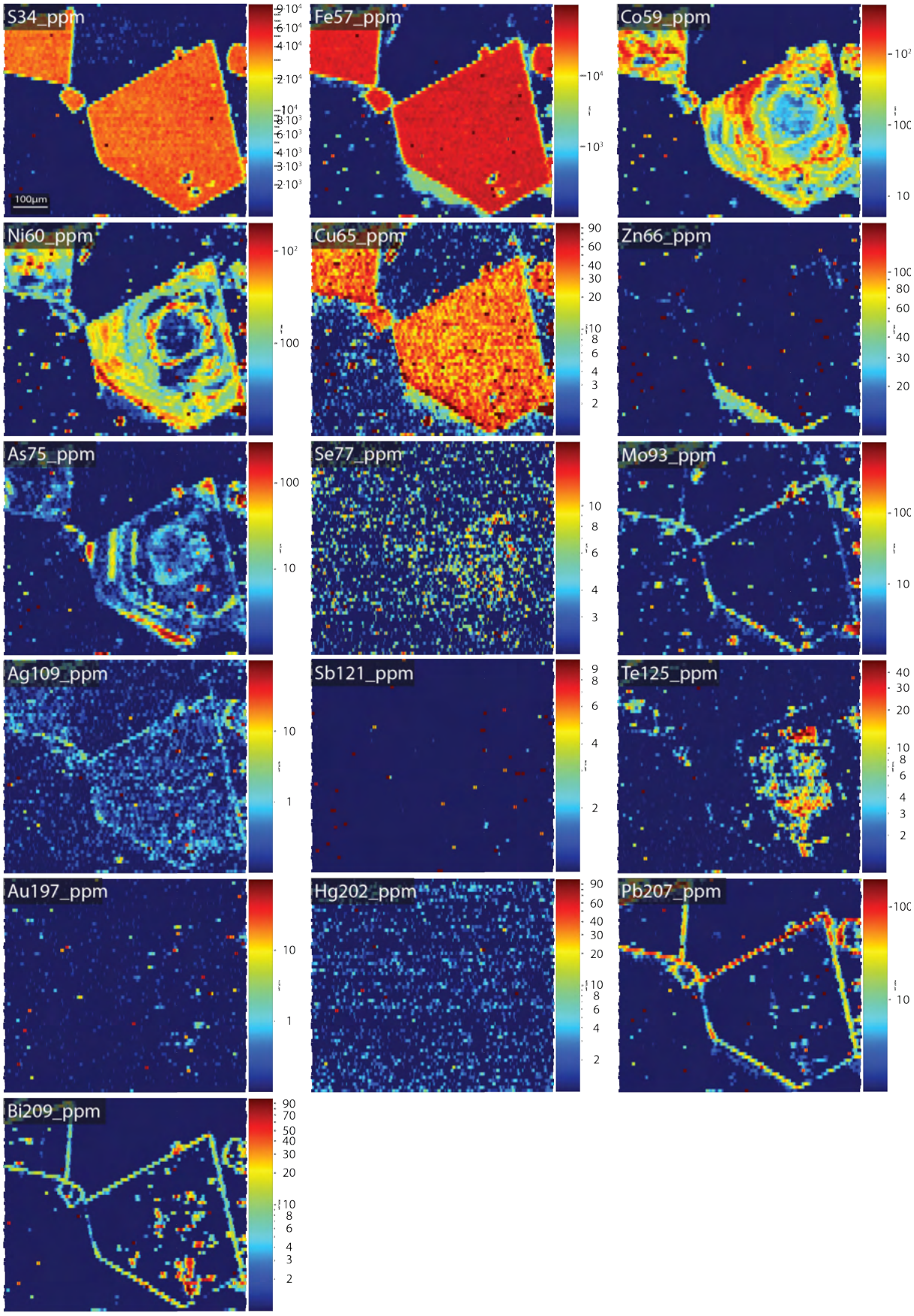

20LYK27B Area 1

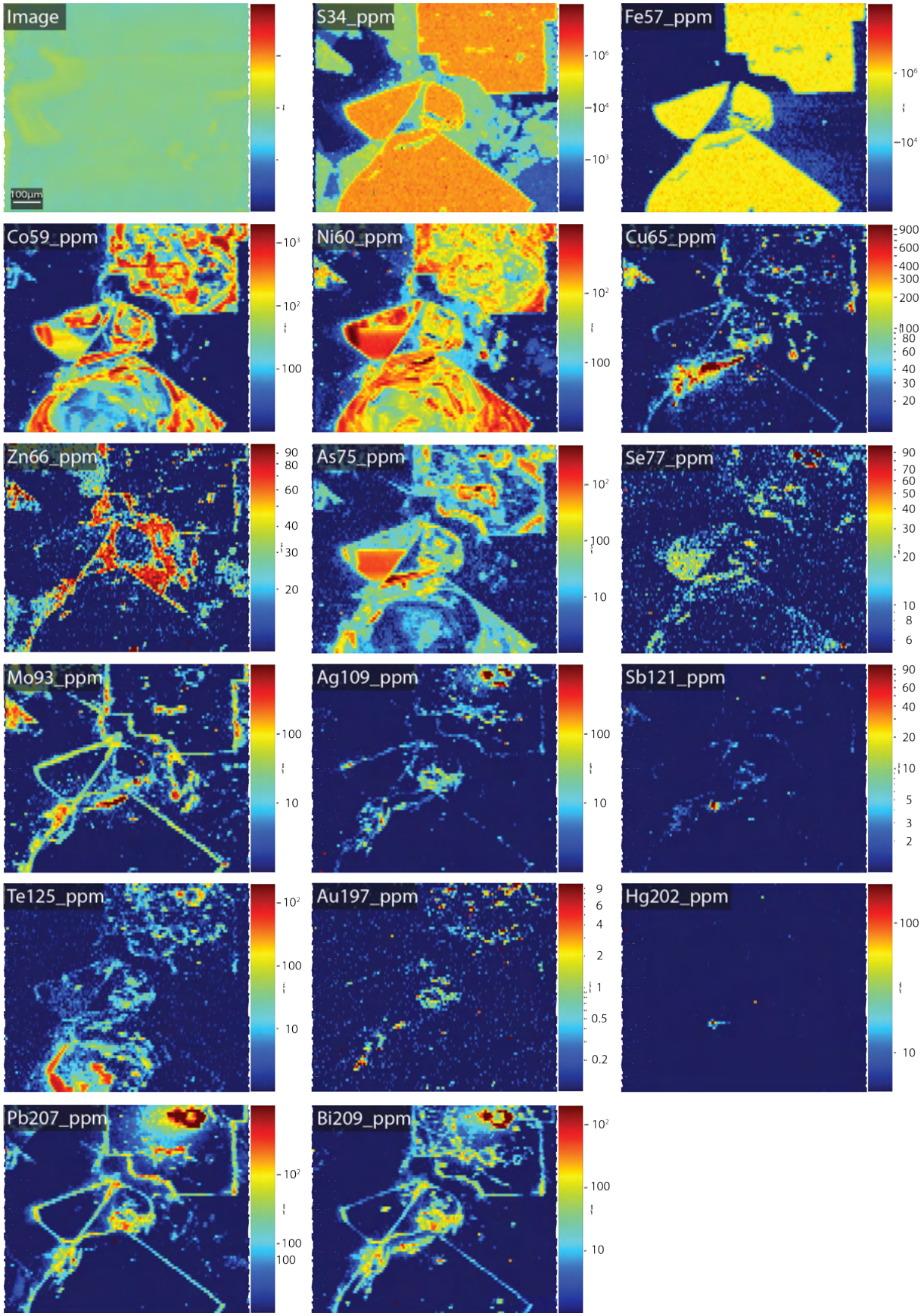

20LYK27B Area 2

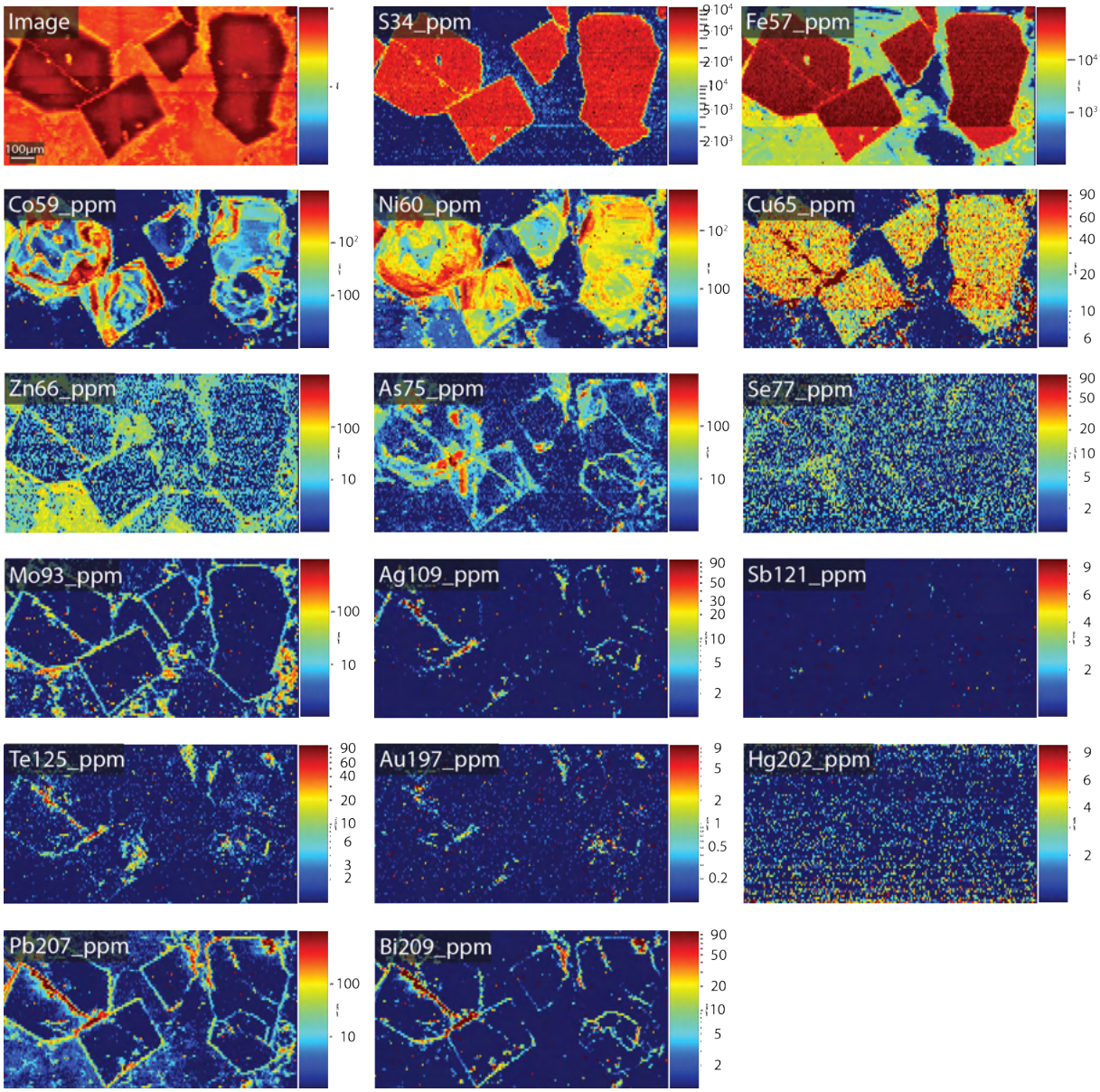

20LYK39C Area 1

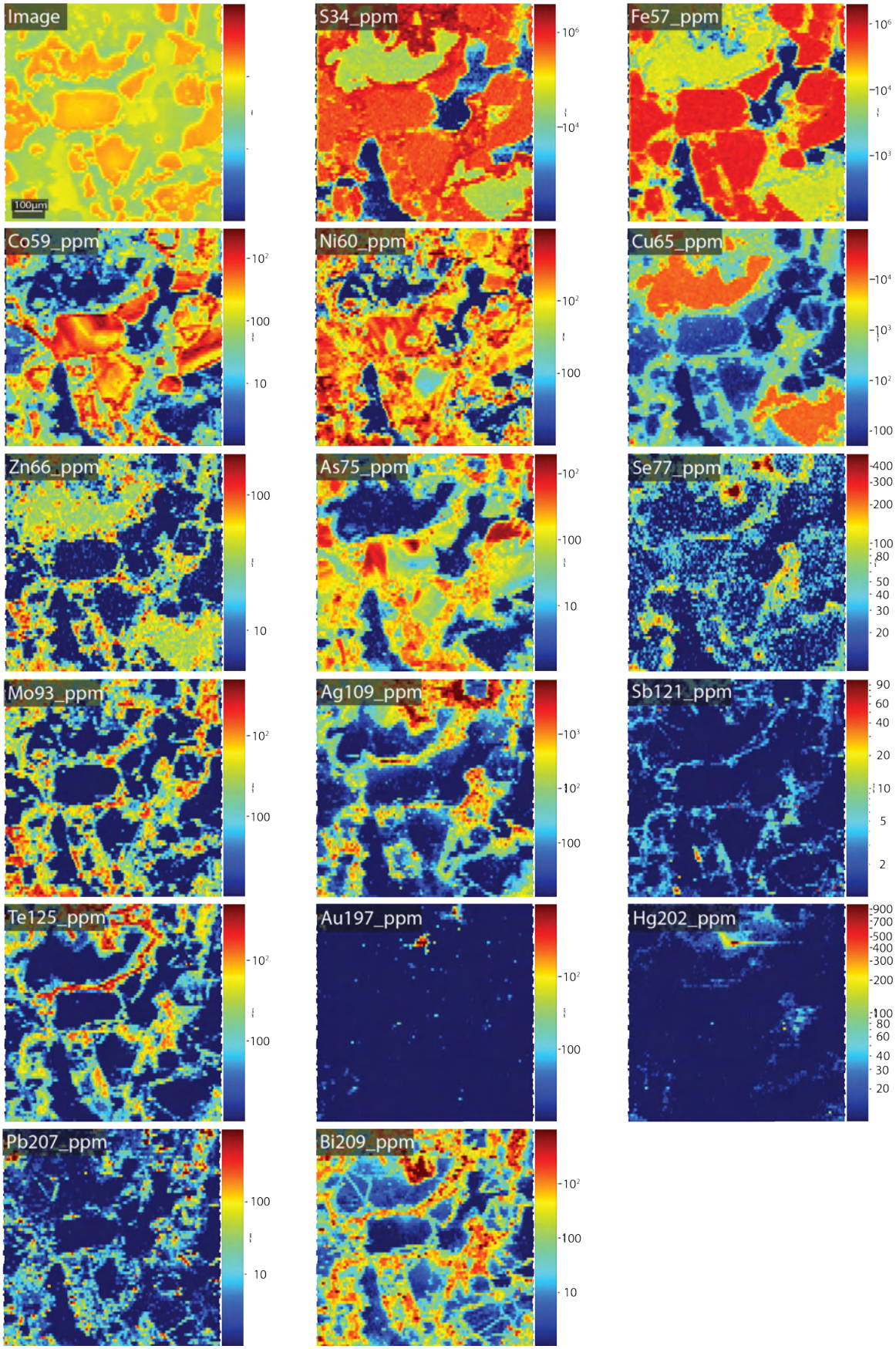

20LYK39C Area 2

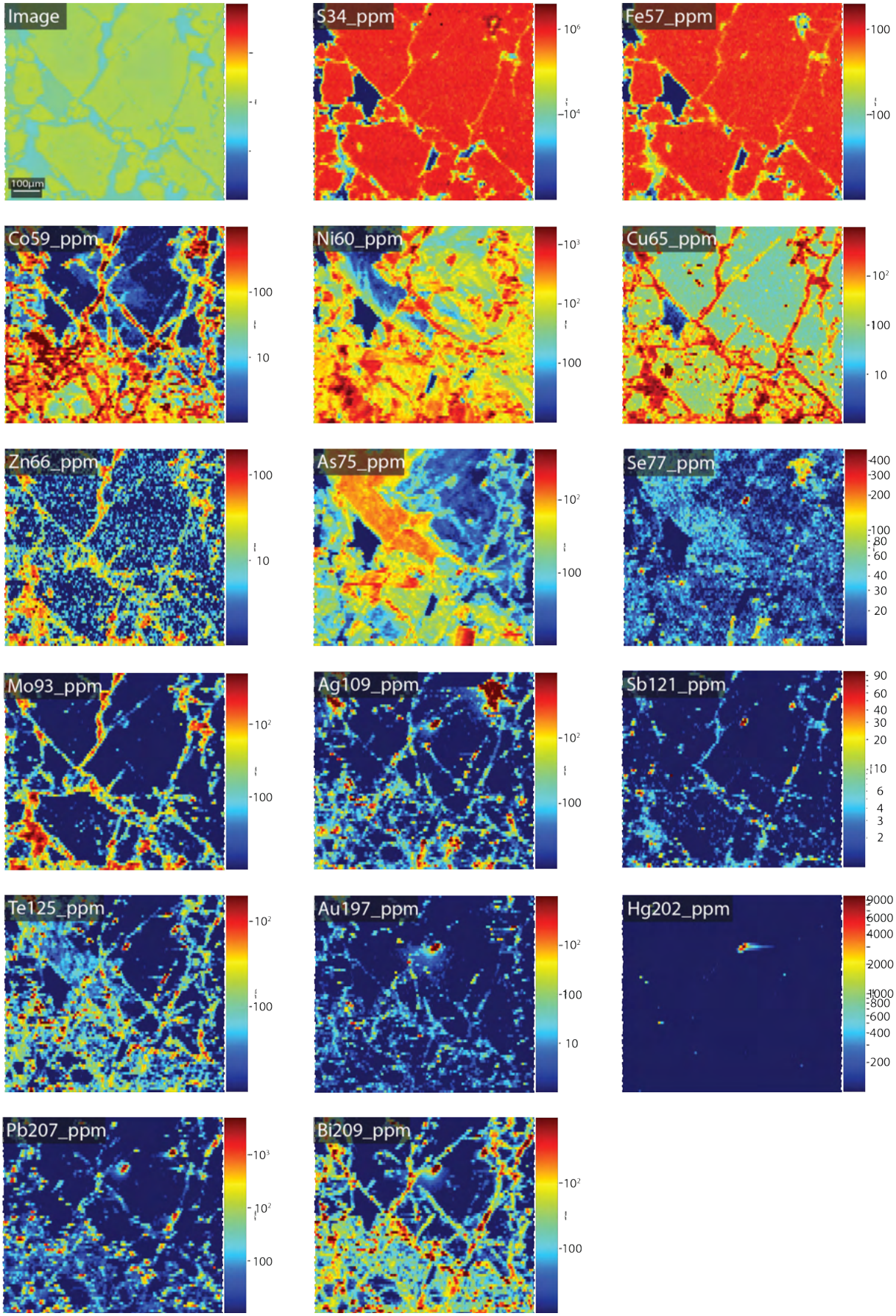

Appendix E – LA-ICP-MS point analysis

Pyrite

	20LYK14B							
Pyrite ppm	20LYK14B Area 1.1	20LYK14B Area 1.2	20LYK14B Area 1.3	20LYK14B Area 1.4	20LYK14B Area 2.1	20LYK14B Area 2.3	20LYK14B Area 2.4	20LYK14B Area 2.5
S34 value	707308	656543	563261	590103	669352	599586	681532	676121
S34 STD	75841	61081	44969	49939	57382	60816	71861	73734
S34 LOD	9325	8460	8034	8142	9078	8383	8960	7657
Co59 value	137.7	23.0	116.7	17.9	70.1	146.3	24.3	28.0
Co59 STD	13.3	2.7	14.8	1.6	5.3	70.2	2.8	3.0
Co59 LOD	0.2	0.2	0.2	0.2	0.2	0.2	0.2	0.2
Ni60 value	153.5	50.0	33.3	69.8	13.3	60.5	281.3	10.9
Ni60 STD	14.4	7.6	5.3	6.7	2.3	14.1	27.6	1.9
Ni60 LOD	2.8	2.5	2.4	2.4	2.6	2.6	2.6	2.2
Cu65 value	<d.l	<d.l	4.2	<d.l	<d.l	956.1	<d.l	<d.l
Cu65 STD	0.6	0.6	3.9	0.6	0.8	408.7	0.5	0.7
Cu65 LOD	1.3	0.9	0.8	0.9	1.5	0.8	1.1	1.0
Zn66 value	<d.l	<d.l	<d.l	<d.l	23.7	<d.l	<d.l	<d.l
Zn66 STD	2.2	1.9	1.8	2.2	31.6	3.2	2.6	2.6
Zn66 LOD	5.0	4.6	4.1	3.8	5.1	4.7	4.5	4.2
As75 value	60.0	31.7	48.5	27.4	6.2	217.0	37.4	4.6
As75 STD	4.9	5.0	4.8	2.6	0.9	109.8	3.3	0.7
As75 LOD	0.9	0.9	0.8	0.8	1.0	0.8	0.8	0.8
Se77 value	12.2	9.6	10.6	16.8	15.2	10.8	56.6	21.4
Se77 STD	4.3	3.2	3.6	3.5	3.8	2.8	6.6	5.1
Se77 LOD	5.3	4.7	5.0	4.1	5.6	4.5	4.8	3.3
Mo92 value	<d.l	<d.l	<d.l	<d.l	<d.l	0.9	<d.l	<d.l
Mo92 STD	0.0	0.0	0.0	0.1	0.1	0.5	0.1	0.0
Mo92 LOD	0.3	0.2	0.0	0.2	0.2	0.0	0.2	0.2
Ag109 value	<d.l	<d.l	<d.l	<d.l	<d.l	11.2	<d.l	<d.l
Ag109 STD	0.1	0.1	0.1	0.1	0.1	5.5	0.1	0.1
Ag109 LOD	0.2	0.2	0.1	0.1	0.2	0.2	0.2	0.1
Sn117 value	<d.l	<d.l	<d.l	<d.l	<d.l	<d.l	<d.l	<d.l
Sn117 STD	0.9	0.7	0.7	0.5	0.5	0.8	0.8	0.6
Sn117 LOD	1.5	1.1	1.3	1.2	1.4	1.6	1.5	1.3
Sb121 value	<d.l	<d.l	<d.l	<d.l	<d.l	4.3	<d.l	<d.l
Sb121 STD	0.1	0.1	0.1	0.1	0.1	1.6	0.1	0.1
Sb121 LOD	0.2	0.2	0.2	0.2	0.2	0.2	0.2	0.2
Te125 value	<d.l	<d.l	<d.l	<d.l	<d.l	3.2	<d.l	<d.l
Te125 STD	0.1	0.1	0.2	0.1	0.0	1.4	0.2	0.1
Te125 LOD	0.6	0.4	0.4	0.4	0.6	0.1	0.4	0.4
Au197 value	<d.l	<d.l	<d.l	<d.l	<d.l	0.3	<d.l	<d.l
Au197 STD	0.07	0.05	0.05	0.05	0.05	0.12	0.05	0.04
Au197 LOD	0.12	0.11	0.10	0.10	0.11	0.09	0.11	0.08
Hg202 value	<d.l	<d.l	<d.l	<d.l	<d.l	<d.l	<d.l	<d.l
Hg202 STD	0.4	0.4	0.3	0.3	0.3	0.3	0.4	0.4
Hg202 LOD	1.0	0.9	0.8	0.9	0.9	0.8	0.8	0.7
Pb207 value	<d.l	<d.l	0.7	<d.l	0.3	451.4	<d.l	<d.l
Pb207 STD	0.1	0.1	0.7	0.1	0.2	137.4	0.1	0.1
Pb207 LOD	0.1	0.2	0.2	0.1	0.2	0.2	0.1	0.2
Bi209 value	<d.l	<d.l	0.2	<d.l	<d.l	37.5	<d.l	0.1
Bi209 STD	0.0	0.0	0.2	0.0	0.0	15.5	0.0	0.0
Bi209 LOD	0.0	0.0	0.0	0.0	0.0	0.0	0.0	0.0

	20LYK20B									
Pyrite ppm	20LYK20B Area 1B.1	20LYK20B Area 1B.2	20LYK20B Area 1B.3	20LYK20B Area 1B.4	20LYK20B Area 1.1	20LYK20B Area 1.2	20LYK20B Area 1.3	20LYK20B Area 1.4	20LYK20B Area 1.5	20LYK20B Area 1.6
S34 value	593090	610893	623077	612969	594283	595077	581098	619663	594166	617322
S34 STD	42234	40580	39229	33896	37377	30378	38336	43183	36264	39325
S34 LOD	9609	10640	10555	11164	10306	10534	10784	10852	9751	8696
Co59 value	1172.0	144.2	538.6	370.6	933.8	42.3	52.5	218.9	350.3	33.4
Co59 STD	162.8	40.8	61.7	21.3	117.0	3.1	12.7	26.6	49.4	3.6
Co59 LOD	0.2	0.2	0.2	0.2	0.2	0.2	0.2	0.2	0.2	0.2
Ni60 value	104.3	219.5	114.2	143.1	238.4	18.6	12.7	66.8	29.4	388.2
Ni60 STD	16.2	68.8	11.0	10.6	43.0	3.1	2.1	8.7	4.7	60.2
Ni60 LOD	2.9	3.2	3.4	3.6	3.1	3.1	3.2	3.3	2.9	2.7
Cu65 value	<d.l	<d.l	<d.l	<d.l	<d.l	<d.l	9.7	<d.l	<d.l	3.0
Cu65 STD	0.6	0.5	0.5	0.5	0.8	0.7	3.1	0.8	0.7	1.5
Cu65 LOD	2.2	1.2	1.3	1.5	1.0	2.0	1.1	1.5	1.3	1.2
Zn66 value	<d.l	<d.l	<d.l	<d.l	<d.l	<d.l	<d.l	<d.l	<d.l	<d.l
Zn66 STD	2.4	2.2	2.4	2.4	3.0	2.5	1.9	2.8	2.3	2.9
Zn66 LOD	5.5	5.5	5.8	5.9	5.7	5.8	5.9	5.3	5.1	4.6
As75 value	3.9	11.3	3.7	11.7	12.2	1.7	24.5	1.7	3.3	8.6
As75 STD	0.6	1.8	0.8	1.2	3.6	0.5	4.1	0.5	0.6	1.2
As75 LOD	0.9	1.0	1.1	1.1	1.1	1.0	1.1	1.0	0.9	0.9
Se77 value	<d.l	6.7	<d.l	<d.l	<d.l	6.6	<d.l	<d.l	<d.l	7.2
Se77 STD	2.5	2.6	2.2	2.7	3.0	2.7	2.6	2.4	2.6	3.7
Se77 LOD	5.5	5.8	5.4	4.8	5.2	5.7	4.8	6.1	5.2	5.2
Mo92 value	<d.l	<d.l	0.4	0.2	1.0	<d.l	<d.l	<d.l	<d.l	<d.l
Mo92 STD	0.0	0.1	0.4	0.2	0.8	0.0	0.0	0.0	0.0	0.1
Mo92 LOD	0.1	0.3	0.3	0.1	0.1	0.1	0.1	0.3	0.1	0.2
Ag109 value	<d.l	<d.l	<d.l	<d.l	<d.l	<d.l	0.5	<d.l	<d.l	<d.l
Ag109 STD	0.1	0.1	0.1	0.1	0.1	0.1	0.2	0.1	0.1	0.1
Ag109 LOD	0.2	0.2	0.2	0.2	0.2	0.1	0.1	0.2	0.2	0.1
Sn117 value	<d.l	<d.l	<d.l	<d.l	<d.l	<d.l	<d.l	<d.l	<d.l	<d.l
Sn117 STD	0.6	0.6	0.7	0.6	0.6	0.6	0.5	0.7	0.6	0.9
Sn117 LOD	1.6	1.7	1.5	1.5	1.5	1.6	1.6	1.5	1.5	1.4
Sb121 value	<d.l	<d.l	<d.l	<d.l	<d.l	<d.l	<d.l	<d.l	<d.l	<d.l
Sb121 STD	0.1	0.1	0.1	0.1	0.1	0.1	0.1	0.1	0.1	0.2
Sb121 LOD	0.2	0.2	0.2	0.3	0.2	0.2	0.2	0.3	0.2	0.2
Te125 value	<d.l	1.8	<d.l	<d.l	1.4	4.0	42.3	5.3	<d.l	10.8
Te125 STD	0.1	0.6	0.2	0.1	0.5	0.9	12.0	1.1	0.1	2.1
Te125 LOD	0.3	0.5	0.4	0.4	0.1	0.1	0.4	0.5	0.6	0.4
Au197 value	<d.l	<d.l	<d.l	<d.l	<d.l	<d.l	<d.l	<d.l	<d.l	0.1
Au197 STD	0.05	0.04	0.04	0.04	0.04	0.04	0.06	0.04	0.04	0.05
Au197 LOD	0.08	0.10	0.09	0.09	0.10	0.11	0.10	0.10	0.09	0.07
Hg202 value	<d.l	<d.l	<d.l	<d.l	<d.l	<d.l	<d.l	<d.l	<d.l	<d.l
Hg202 STD	0.4	0.4	0.4	0.3	0.4	0.4	0.3	0.4	0.4	0.5
Hg202 LOD	0.9	1.0	1.0	1.0	1.1	1.1	1.0	1.0	0.9	1.0
Pb207 value	<d.l	<d.l	<d.l	<d.l	12.6	<d.l	2.0	<d.l	<d.l	2.2
Pb207 STD	0.1	0.1	0.1	0.1	7.7	0.1	0.5	0.1	0.1	0.7
Pb207 LOD	0.2	0.2	0.2	0.2	0.2	0.2	0.2	0.2	0.2	0.2
Bi209 value	0.1	0.2	<d.l	<d.l	1.5	0.7	46.0	<d.l	<d.l	24.2
Bi209 STD	0.0	0.1	0.0	0.0	0.9	0.2	12.5	0.0	0.0	6.8
Bi209 LOD	0.0	0.0	0.1	0.0	0.0	0.1	0.0	0.1	0.0	0.0

	20LYK27B								
Pyrite ppm	20LYK27B Area 1.1	20LYK27B Area 1.4	20LYK27B Area 1.5	20LYK27B Area 2.1	20LYK27B Area 2.2	20LYK27B Area 2.3	20LYK27B Area 2.4	20LYK27B Area 2.5	20LYK27B Area 2.6
S34 value	534557	640649	598634	620342	650341	579259	519038	555294	554626
S34 STD	46876	50485	52505	56557	68262	51753	51009	44529	50431
S34 LOD	9174	8495	7928	7909	7996	7157	5889	7371	7057
Co59 value	297.0	245.0	68.5	6.8	1414.2	190.2	1350.4	666.5	25.5
Co59 STD	31.6	24.5	9.2	0.7	180.8	22.8	117.4	205.1	2.3
Co59 LOD	0.2	0.2	0.2	0.2	0.2	0.2	0.1	0.1	0.1
Ni60 value	1101.4	1676.8	320.1	56.4	911.8	1082.7	508.7	533.6	252.4
Ni60 STD	93.9	135.8	45.6	4.8	80.6	98.8	52.8	60.0	23.0
Ni60 LOD	2.7	2.5	2.4	2.2	2.3	2.0	1.8	2.2	2.2
Cu65 value	9.8	<d.l	2.0	1.7	12.7	<d.l	2.6	<d.l	<d.l
Cu65 STD	5.9	0.4	0.7	1.0	2.7	0.4	1.7	0.4	0.5
Cu65 LOD	1.2	1.0	1.0	1.0	1.1	0.8	0.7	0.8	0.9
Zn66 value	16.6	<d.l	<d.l	<d.l	11.3	<d.l	3.5	<d.l	<d.l
Zn66 STD	11.1	2.5	2.0	1.7	5.9	1.8	2.2	1.9	1.5
Zn66 LOD	5.0	4.1	4.2	4.0	4.5	3.6	3.2	4.2	4.0
As75 value	327.3	9.7	4.2	0.9	99.7	16.7	7.6	3.6	<d.l
As75 STD	24.3	1.0	1.3	0.4	37.0	1.5	1.4	0.7	0.4
As75 LOD	0.9	0.8	0.8	0.7	0.8	0.7	0.6	0.7	0.8
Se77 value	6.7	<d.l	<d.l	<d.l	<d.l	3.7	<d.l	<d.l	<d.l
Se77 STD	5.1	1.8	1.9	1.9	2.4	2.4	1.6	1.8	1.8
Se77 LOD	4.0	3.9	3.1	3.1	4.0	3.3	3.4	3.5	3.8
Mo92 value	20.1	0.1	<d.l	<d.l	<d.l	<d.l	3.9	<d.l	<d.l
Mo92 STD	8.9	0.1	0.0	0.0	0.1	0.1	3.2	0.0	0.0
Mo92 LOD	0.0	0.0	0.0	0.2	0.3	0.2	0.2	0.2	0.0
Ag109 value	1.9	<d.l	<d.l	<d.l	0.4	<d.l	<d.l	<d.l	<d.l
Ag109 STD	0.8	0.1	0.1	0.1	0.2	0.1	0.1	0.1	0.0
Ag109 LOD	0.2	0.2	0.2	0.1	0.1	0.1	0.1	0.1	0.1
Sn117 value	<d.l	<d.l	<d.l	<d.l	<d.l	<d.l	<d.l	<d.l	<d.l
Sn117 STD	0.7	0.7	0.6	0.5	0.6	0.5	0.4	0.5	0.5
Sn117 LOD	1.5	1.2	1.4	1.1	1.5	1.1	1.0	1.1	1.1
Sb121 value	0.5	<d.l	<d.l	<d.l	<d.l	<d.l	<d.l	<d.l	<d.l
Sb121 STD	0.4	0.1	0.1	0.1	0.1	0.1	0.1	0.1	0.1
Sb121 LOD	0.2	0.2	0.2	0.2	0.2	0.2	0.1	0.2	0.2
Te125 value	4.6	<d.l	7.0	0.7	9.2	<d.l	0.2	1.0	0.4
Te125 STD	2.2	0.2	1.5	0.3	2.5	0.1	0.3	0.5	0.2
Te125 LOD	0.4	0.3	0.3	0.4	0.5	0.3	0.1	0.4	0.1
Au197 value	<d.l	<d.l	<d.l	<d.l	<d.l	<d.l	<d.l	<d.l	<d.l
Au197 STD	0.07	0.04	0.05	0.04	0.06	0.03	0.03	0.03	0.04
Au197 LOD	0.10	0.08	0.09	0.09	0.08	0.07	0.06	0.08	0.06
Hg202 value	<d.l	<d.l	<d.l	<d.l	<d.l	<d.l	<d.l	<d.l	<d.l
Hg202 STD	0.4	0.3	0.3	0.3	0.4	0.2	0.3	0.2	0.3
Hg202 LOD	0.9	0.8	0.7	0.7	0.8	0.6	0.5	0.7	0.6
Pb207 value	424.4	<d.l	<d.l	0.5	8.6	<d.l	18.1	<d.l	<d.l
Pb207 STD	211.6	0.1	0.1	0.2	1.8	0.1	13.5	0.1	0.1
Pb207 LOD	0.2	0.2	0.2	0.1	0.2	0.1	0.1	0.2	0.1
Bi209 value	33.6	0.0	<d.l	0.1	41.0	0.1	1.5	<d.l	<d.l
Bi209 STD	17.9	0.0	0.0	0.0	9.1	0.0	1.0	0.0	0.0
Bi209 LOD	0.0	0.0	0.0	0.0	0.0	0.0	0.0	0.0	0.0

	20LYK39C									
Pyrite ppm	20LYK39C Area 1.1	20LYK39C Area 1.2	20LYK39C Area 1.3	20LYK39C Area 1.4	20LYK39C Area 1.5	20LYK39C Area 2.1	20LYK39C Area 2.2	20LYK39C Area 2.3	20LYK39C Area 2.4	20LYK39C Area 2.5
S34 value	660256	613218	581964	615915	625100	597804	635791	598476	577434	603786
S34 STD	48455	50421	36884	45957	39968	40439	48145	38342	40942	38171
S34 LOD	9566	9509	10033	9024	9167	9397	9999	9923	9048	9694
Co59 value	943.2	235.0	105.3	478.4	111.0	<d.l	4.0	23.2	0.5	49.8
Co59 STD	55.3	19.9	6.1	31.0	8.4	0.1	1.9	14.8	0.1	8.6
Co59 LOD	0.2	0.2	0.2	0.2	0.2	0.2	0.2	0.2	0.2	0.2
Ni60 value	2274.9	325.0	49.4	899.3	621.2	24.9	28.1	456.0	95.3	944.2
Ni60 STD	126.8	41.6	4.0	67.0	36.0	11.5	3.2	38.3	10.5	57.4
Ni60 LOD	3.1	2.9	3.1	2.7	2.7	2.9	3.1	3.1	2.7	2.9
Cu65 value	<d.l	<d.l	3.2	<d.l	4.3	<d.l	<d.l	21.6	<d.l	92.1
Cu65 STD	0.5	0.6	2.0	0.8	2.0	0.7	0.7	13.1	0.4	58.4
Cu65 LOD	1.5	1.4	1.8	1.1	1.1	1.4	1.2	1.4	1.0	1.2
Zn66 value	<d.l	<d.l	<d.l	<d.l	<d.l	<d.l	<d.l	<d.l	<d.l	<d.l
Zn66 STD	2.1	1.8	2.6	2.3	2.4	2.7	1.8	2.7	1.8	2.3
Zn66 LOD	5.5	5.5	5.3	4.8	4.9	5.4	5.2	5.0	4.9	5.3
As75 value	1745.5	58.8	29.2	56.8	98.3	588.9	658.3	30.5	12.6	188.2
As75 STD	119.4	4.3	2.2	4.4	6.1	50.2	33.9	6.2	1.5	12.4
As75 LOD	1.1	1.0	1.0	0.9	0.9	0.9	1.0	0.9	0.8	1.0
Se77 value	14.7	6.8	8.5	11.7	16.5	15.1	15.2	18.4	6.9	8.0
Se77 STD	3.6	2.3	2.5	3.4	3.4	4.2	3.6	3.0	3.0	3.1
Se77 LOD	3.7	5.0	4.1	4.6	4.7	5.7	5.3	5.8	3.9	5.3
Mo92 value	0.2	<d.l	<d.l	<d.l	<d.l	<d.l	<d.l	0.3	<d.l	<d.l
Mo92 STD	0.2	0.2	0.1	0.0	0.1	0.0	0.0	0.2	0.0	0.0
Mo92 LOD	0.1	0.3	0.3	0.1	0.4	0.1	0.3	0.1	0.1	0.1
Ag109 value	<d.l	<d.l	<d.l	0.6	0.6	<d.l	1.5	1.3	<d.l	19.5
Ag109 STD	0.1	0.1	0.1	0.3	0.2	0.1	0.7	0.6	0.1	8.1
Ag109 LOD	0.2	0.2	0.2	0.2	0.2	0.2	0.2	0.2	0.1	0.2
Sn117 value	<d.l	<d.l	<d.l	<d.l	<d.l	<d.l	<d.l	<d.l	<d.l	<d.l
Sn117 STD	0.6	0.7	0.7	0.5	0.6	0.7	0.6	0.7	0.6	0.5
Sn117 LOD	1.7	1.6	1.7	1.5	1.5	1.4	1.3	1.5	1.5	1.4
Sb121 value	<d.l	<d.l	<d.l	<d.l	<d.l	<d.l	<d.l	<d.l	<d.l	0.4
Sb121 STD	0.1	0.1	0.1	0.1	0.1	0.1	0.1	0.1	0.1	0.1
Sb121 LOD	0.2	0.3	0.3	0.2	0.2	0.2	0.2	0.2	0.2	0.2
Te125 value	0.5	<d.l	0.6	0.6	2.0	11.7	17.6	2.9	<d.l	32.2
Te125 STD	0.3	0.2	0.2	0.3	0.7	1.6	1.8	1.7	0.0	6.2
Te125 LOD	0.4	0.4	0.1	0.1	0.1	0.5	0.5	0.6	0.3	0.3
Au197 value	<d.l	<d.l	<d.l	<d.l	<d.l	<d.l	0.1	0.3	<d.l	1.1
Au197 STD	0.06	0.04	0.05	0.03	0.05	0.03	0.06	0.21	0.04	0.48
Au197 LOD	0.10	0.10	0.10	0.09	0.08	0.09	0.09	0.08	0.07	0.09
Hg202 value	<d.l	<d.l	<d.l	<d.l	<d.l	<d.l	<d.l	<d.l	<d.l	1.1
Hg202 STD	0.4	0.4	0.3	0.4	0.4	0.4	0.3	0.4	0.3	0.4
Hg202 LOD	1.1	1.1	1.1	0.9	1.0	0.9	1.1	1.0	0.9	0.9
Pb207 value	<d.l	0.3	2.1	3.8	3.2	2.6	13.6	1.2	<d.l	136.4
Pb207 STD	0.1	0.2	0.4	1.6	1.2	1.1	7.3	0.6	0.1	70.5
Pb207 LOD	0.2	0.2	0.2	0.2	0.2	0.3	0.2	0.1	0.2	0.2
Bi209 value	<d.l	0.1	6.8	4.2	5.3	5.6	5.6	14.2	0.0	94.8
Bi209 STD	0.0	0.0	1.7	1.7	1.9	1.8	2.7	7.1	0.0	24.7
Bi209 LOD	0.0	0.0	0.0	0.0	0.0	0.0	0.0	0.0	0.0	0.0

Chalcopyrite

	20LYK4D				20LYK14B		
Chalcopyrite ppm	20LYK4D Area 1.1	20LYK4D Area 1.2	20LYK4D Area 1.3	20LYK4D Area 1.4	20LYK14B Area 1.1	20LYK14B Area 1.2	20LYK14B Area 1.3
S34 value	436746	454462	481750	453493	744686	530716	688294
S34 STD	20855	23076	18559	22577	129093	25027	90704
S34 LOD	16490	17640	19945	15748	30434	21657	30668
Co59 value	67.6	<d.l	1.1	198.3	<d.l	1.5	1.5
Co59 STD	133.6	0.2	1.0	202.2	0.7	0.6	0.8
Co59 LOD	0.6	0.7	0.6	0.5	1.0	0.8	1.0
Ni60 value	<d.l	<d.l	<d.l	22.6	<d.l	<d.l	<d.l
Ni60 STD	3.8	3.9	4.1	27.4	7.3	5.9	7.6
Ni60 LOD	8.9	9.1	10.4	8.1	15.4	10.5	14.4
Cu65 value	364655	376713	379707	365405	376723	383017	377736
Cu65 STD	13578	21377	10540	13893	10376	17953	8292
Cu65 LOD	9.6	8.6	12.0	4.3	10.8	6.3	6.7
Zn66 value	256.3	214.8	229.2	201.3	160.0	148.0	317.0
Zn66 STD	17.3	15.1	16.6	28.9	18.3	16.9	43.3
Zn66 LOD	13.1	13.7	16.4	12.0	21.9	14.5	21.7
As75 value	<d.l	<d.l	<d.l	748.0	<d.l	6.4	15.7
As75 STD	0.8	0.9	1.3	327.6	2.5	9.7	13.3
As75 LOD	2.2	2.2	2.5	2.1	4.3	2.8	3.9
Se77 value	24.7	20.2	26.8	22.3	<d.l	<d.l	<d.l
Se77 STD	7.0	7.2	7.6	6.4	16.6	9.1	12.6
Se77 LOD	11.1	13.4	13.9	9.2	23.5	16.5	22.4
Mo92 value	<d.l	<d.l	<d.l	<d.l	<d.l	0.9	<d.l
Mo92 STD	0.0	0.0	0.0	0.2	0.3	0.9	0.1
Mo92 LOD	0.2	1.1	1.2	0.8	0.3	0.9	1.1
Ag109 value	9.8	1.8	3.8	7.0	15.8	127.3	185.3
Ag109 STD	2.3	0.6	1.3	0.9	17.4	102.1	156.2
Ag109 LOD	0.5	0.6	0.5	0.5	1.0	0.7	0.8
Sn117 value	4.6	5.1	<d.l	3.7	<d.l	<d.l	<d.l
Sn117 STD	2.3	1.8	1.9	1.8	3.5	2.0	3.3
Sn117 LOD	3.4	3.7	4.3	3.4	5.4	4.0	5.7
Sb121 value	0.9	<d.l	1.1	2.7	8.9	8.2	22.7
Sb121 STD	0.3	0.2	0.4	0.5	1.7	2.3	5.7
Sb121 LOD	0.6	0.5	0.7	0.5	1.0	0.6	0.9
Te125 value	<d.l	<d.l	<d.l	1.7	<d.l	2.6	<d.l
Te125 STD	0.0	0.4	0.6	0.8	1.1	1.7	1.3
Te125 LOD	0.8	1.1	1.5	1.1	2.1	1.5	2.7
Au197 value	<d.l	<d.l	<d.l	<d.l	<d.l	3.1	2.4
Au197 STD	0.1	0.1	0.1	0.1	0.3	1.5	1.3
Au197 LOD	0.3	0.3	0.4	0.2	0.5	0.4	0.5
Hg202 value	6.8	8.2	<d.l	<d.l	<d.l	4.6	6.6
Hg202 STD	1.6	2.0	1.3	1.3	2.4	2.4	3.1
Hg202 LOD	3.4	3.2	4.1	3.0	6.0	4.1	5.5
Pb207 value	3.8	<d.l	12.7	32.6	11.2	40.1	54.0
Pb207 STD	1.3	0.2	3.5	4.0	3.6	25.9	39.4
Pb207 LOD	0.8	0.6	0.8	0.7	1.1	0.7	0.8
Bi209 value	11.1	<d.l	8.7	26.8	6.4	26.7	27.1
Bi209 STD	3.0	0.0	2.2	3.3	1.9	14.3	12.8
Bi209 LOD	0.1	0.1	0.1	0.1	0.1	0.2	0.2

	20LYK39C						
Chalcopyrite ppm	20LYK39C Area 1.1	20LYK39C Area 1.2	20LYK39C Area 1.3	20LYK39C Area 1.4	20LYK39C Area 1.5	20LYK39C Area 1.6	20LYK39C Area 2.1
S34 value	527332	493090	472033	469101	519029	513360	501771
S34 STD	38725	28922	19971	24271	38260	34616	32227
S34 LOD	24960	23646	23771	23565	25446	23841	17044
Co59 value	13.2	<d.l	<d.l	<d.l	<d.l	<d.l	284.3
Co59 STD	26.6	0.3	0.3	0.4	0.3	0.3	85.8
Co59 LOD	0.8	0.7	0.7	0.8	0.7	0.7	0.6
Ni60 value	<d.l	<d.l	<d.l	<d.l	<d.l	<d.l	99.8
Ni60 STD	6.8	4.9	4.8	5.4	5.4	4.1	23.1
Ni60 LOD	11.9	10.8	11.6	11.4	12.2	11.8	8.5
Cu65 value	384398	369220	369970	366342	372966	378329	262433
Cu65 STD	12900	11933	12727	14268	12169	10720	32112
Cu65 LOD	10.4	10.4	17.8	13.3	10.4	7.8	3.7
Zn66 value	127.7	94.9	97.4	290.2	100.7	91.1	88.1
Zn66 STD	38.0	11.6	13.5	324.3	11.2	10.6	12.0
Zn66 LOD	17.4	16.9	21.9	16.7	18.8	17.5	12.7
As75 value	<d.l	<d.l	<d.l	<d.l	<d.l	<d.l	92.8
As75 STD	1.9	0.9	1.3	1.3	1.6	1.1	24.2
As75 LOD	3.3	2.8	3.0	3.2	3.3	3.1	2.2
Se77 value	34.5	23.2	28.7	26.6	23.3	20.7	21.3
Se77 STD	10.8	9.7	9.0	8.7	9.3	8.4	9.4
Se77 LOD	16.3	14.6	15.3	18.4	17.1	19.7	11.8
Mo92 value	<d.l	<d.l	<d.l	<d.l	<d.l	<d.l	<d.l
Mo92 STD	0.0	0.0	0.1	0.1	0.0	0.0	0.0
Mo92 LOD	0.2	0.9	1.7	1.4	1.0	0.2	0.2
Ag109 value	1.5	0.9	3.5	1.1	2.9	1.7	134.7
Ag109 STD	0.4	0.5	1.6	0.4	0.7	0.5	14.1
Ag109 LOD	0.7	0.7	0.6	0.7	0.8	0.7	0.5
Sn117 value	5.3	<d.l	6.0	7.0	7.3	8.4	5.0
Sn117 STD	2.2	2.2	2.3	2.4	2.4	3.2	2.3
Sn117 LOD	5.1	5.2	4.7	5.0	5.6	4.4	3.9
Sb121 value	<d.l	<d.l	<d.l	<d.l	1.2	<d.l	0.9
Sb121 STD	0.3	0.4	0.3	0.3	0.5	0.3	0.4
Sb121 LOD	0.8	0.8	0.7	0.8	0.8	0.8	0.6
Te125 value	<d.l	<d.l	<d.l	<d.l	<d.l	<d.l	6.7
Te125 STD	0.6	0.6	0.0	0.7	0.7	0.4	2.1
Te125 LOD	2.2	1.8	1.7	1.9	1.6	1.1	0.2
Au197 value	<d.l	<d.l	<d.l	<d.l	<d.l	<d.l	<d.l
Au197 STD	0.2	0.1	0.1	0.2	0.2	0.2	0.1
Au197 LOD	0.3	0.4	0.4	0.4	0.4	0.4	0.3
Hg202 value	19.8	7.8	14.3	5.0	<d.l	9.0	11.9
Hg202 STD	2.7	2.4	2.5	2.1	1.7	2.4	1.7
Hg202 LOD	4.6	4.0	4.3	4.7	4.7	4.3	2.9
Pb207 value	<d.l	2.1	<d.l	2.5	6.4	4.8	11.8
Pb207 STD	0.3	0.7	0.4	0.8	1.5	1.1	2.9
Pb207 LOD	0.8	0.9	0.9	0.9	0.9	0.8	0.4
Bi209 value	1.5	5.9	1.7	5.6	40.6	11.8	47.2
Bi209 STD	0.3	1.6	0.3	0.9	7.0	1.4	11.5
Bi209 LOD	0.1	0.1	0.1	0.1	0.1	0.1	0.1

Appendix F – Chlorite thermometry

Table 7. Chlorite formula unit calculator and variety namer. BAsed on 28 oxygen and with Fe^{2+}/Fe^{3+} and OH calculated assuming full site occupancy.

	20LYK-3B site1					**20LYK-3B 2-site1**			**20LYK-13B site1**				**20LYK-13B site2**					**20LYK-19C 1-site1**			**20LYK-19C 1-site2**			**20LYK-19C 2-site1**				**20LYK-39A 1-site1**				
Spec	**#36**	**#37**	**#38**	**#39**	**#40**	**#58**	**#59**	**#60**	**#3**	**#13**	**#14**	**#15**	**#25**	**#26**	**#27**	**#34**	**#35**	**#91**	**#92**	**#93**	**#105**	**#106**	**#116**	**#122**	**#123**	**#124**	**#127**	**#133**	**#135**	**#136**	**#137**	**#138**
SiO2	28.24	28.03	28.67	28.03	28.24	28.88	29.1	28.67	14.98	27.60	27.60	28.03	28.24	27.60	27.38	28.03	28.03	28.67	27.81	28.24	27.81	28.45	28.45	26.96	26.53	26.10	27.38	31.66	31.88	32.52	32.09	33.16
TiO2																																
Al2O3	19.65	19.65	19.84	20.78	19.65	19.27	19.08	19.46	10.77	20.22	20.60	20.03	20.22	20.22	20.78	20.41	20.60	21.73	21.73	21.92	22.11	21.73	21.92	21.54	20.60	20.97	21.54	18.89	19.46	19.08	18.89	19.27
FeO	27.27	28.17	27.53	27.27	26.89	27.15	27.27	27.79	16.60	31.13	31.65	31.52	31.13	31.26	31.52	31.00	31.13	35.12	37.44	36.28	35.25	34.86	34.86	32.68	35.38	34.09	35.89	21.23	20.97	21.10	20.58	21.74
MnO																																
MgO	17.25	16.58	17.58	17.08	17.41	18.08	17.25	16.42	7.79	14.43	13.93	14.10	14.43	13.93	14.10	14.26	14.26	12.44	10.61	10.94	11.11	11.44	11.94	11.94	10.45	10.94	11.28	23.55	24.05	23.55	24.05	24.38
CaO																																
Na2O																																
K2O																																
BaO																																
Rb2O																																
Cs2O																																
ZnO																																
F																																
Cl																																
Cr2O3																																
NiO																																
No. of oxygens	28	28	28	28	28	28	28	28	28	28	28	28	28	28	28	28	28	28	28	28	28	28	28	28	28	28	28	28	28	28	28	28

Reformatted oxide percentages based on 28 oxygens (with Fe2+/Fe3+ and OH calculated assuming full site occupancy)

	20LYK-3B site 1					**20LYK-3B-2-site1**			**20LYK-13B site1**				**20LYK-13B site2**					**20LYK-19C 1-site1**			**20LYK-19C 1-site2**			**20LYK-19C 2-site1**				**20LYK-39A 1-site1**				
Spec	**#36**	**#37**	**#38**	**#39**	**#40**	**#58**	**#59**	**#60**	**#3**	**#13**	**#14**	**#15**	**#25**	**#26**	**#27**	**#34**	**#35**	**#91**	**#92**	**#93**	**#105**	**#106**	**#116**	**#122**	**#123**	**#124**	**#127**	**133**	**#135**	**#136**	**#137**	**#138**
SiO2	28.24	28.03	28.67	28.03	28.24	28.88	29.1	28.67	14.98	27.6	27.6	28.03	28.24	27.6	27.38	28.03	28.03	28.67	27.81	28.24	27.81	28.45	28.45	26.96	26.53	26.1	27.38	31.66	31.88	32.52	32.09	33.16
TiO2	0	0	0	0	0	0	0	0	0	0	0	0	0	0	0	0	0	0	0	0	0	0	0	0	0	0	0	0	0	0	0	0
Al2O3	19.65	19.65	19.84	20.78	19.65	19.27	19.08	19.46	10.77	20.22	20.6	20.03	20.22	20.22	20.78	20.41	20.6	21.73	21.73	21.92	22.11	21.73	21.92	21.54	20.6	20.97	21.54	18.89	19.46	19.08	18.89	19.27
Cr2O3	0	0	0	0	0	0	0	0	0	0	0	0	0	0	0	0	0	0	0	0	0	0	0	0	0	0	0	0	0	0	0	0
Fe2O3	0	0	0	0	0	0	0.285219161	0.387484821	0.05622918 5	0	0.089284713	0.215458667	0.293370174	0.170601 061	0	0.332526 49	0.312505744	0.566536447	0.375836349	0.828039 5	0.830730392	1.089753314	0.828034 96	0.629175466	0.262514237	0.193909419	0.222664846	0.074141952	0.062775315	0.626428421	0.242528522	0.339205495
FeO	27.27	28.17	27.53	27.27	26.89	27.15	27.0 1334639	27.4 4132 29	16.5494023 3	31.13	31.5696574 2	31.3261201 6	30.8660090 2	31.1064833 4	31.52	30.7007770 3	30.8487926 4	34.6102038 6	37.1018047 8	35.5389556 1	34.5024697 3	33.8793887 2	34.1148952	32.1138365 3	35.1414377 4	33.9155111 9	35.6896357	21.1632835 9	20.9135118 2	20.5363102 5	20.3618514 2	21.4347669 4
MnO	0	0	0	0	0	0	0	0	0	0	0	0	0	0	0	0	0	0	0	0	0	0	0	0	0	0	0	0	0	0	0	0
MgO	17.25	16.58	17.58	17.08	17.41	18.08	17.25	16.42	7.79	14.43	13.93	14.1	14.43	13.93	14.1	14.26	14.26	12.44	10.61	10.94	11.11	11.44	11.94	11.94	10.45	10.94	11.28	23.55	24.05	23.55	24.05	24.38
NiO	0	0	0	0	0	0	0	0	0	0	0	0	0	0	0	0	0	0	0	0	0	0	0	0	0	0	0	0	0	0	0	0
ZnO	0	0	0	0	0	0	0	0	0	0	0	0	0	0	0	0	0	0	0	0	0	0	0	0	0	0	0	0	0	0	0	0
CaO	0	0	0	0	0	0	0	0	0	0	0	0	0	0	0	0	0	0	0	0	0	0	0	0	0	0	0	0	0	0	0	0
Na2O	0	0	0	0	0	0	0	0	0	0	0	0	0	0	0	0	0	0	0	0	0	0	0	0	0	0	0	0	0	0	0	0
K2O	0	0	0	0	0	0	0	0	0	0	0	0	0	0	0	0	0	0	0	0	0	0	0	0	0	0	0	0	0	0	0	0
BaO	0	0	0	0	0	0	0	0	0	0	0	0	0	0	0	0	0	0	0	0	0	0	0	0	0	0	0	0	0	0	0	0
Rb2O	0	0	0	0	0	0	0	0	0	0	0	0	0	0	0	0	0	0	0	0	0	0	0	0	0	0	0	0	0	0	0	0
F	0	0	0	0	0	0	0	0	0	0	0	0	0	0	0	0	0	0	0	0	0	0	0	0	0	0	0	0	0	0	0	0
Cl	0	0	0	0	0	0	0	0	0	0	0	0	0	0	0	0	0	0	0	0	0	0	0	0	0	0	0	0	0	0	0	0
H2O*	11.9706827 2	11.9136255 1	12.1338948	12.08413978	11.9638903 9	12.1201681 9	12.0316923 5	11.9468414	6.38159461 9	11.8637969 3	11.8947550 3	11.8944903 2	11.9734442 7	11.8092622 6	11.8967205	11.9352208 6	11.9733105 6	12.3075433 2	12.0927287 5	12.1542101 6	12.0572349 6	12.1235292 3	12.2161535 9	11.7471501 6	11.5342781 7	11.4868007 6	11.9647954 5	12.8132770 7	12.9825186 2	12.9800786 4	12.9042275 5	13.2703404 8

Total	104.380682	104.343625	105.753894	105.24413	104.153890	105.500168	104.760257	104.325649	56.5272261	105.243796	105.683697	105.596069	106.022826	104.836348	105.676720	105.668524	106.024608	110.324283	109.720369	109.616688	108.420435	108.712671	109.469083	104.930164	104.520830	103.606221	108.077096	108.150702	109.348805	109.292817	108.538507	111.854312
	7	5	8	98	4	2	9		4	9	2	1	5	7	5	4	9	6	9	4	1	3	8	2	2	4		6	7	3	5	9
O=F,Cl	0	0	0	0	0	0	0	0	0	0	0	0	0	0	0	0	0	0	0	0	0	0	0	0	0	0	0	0	0	0	0	0
TOTAL	104.380682	104.343625	105.753894	105.24413	104.153890	105.500168	104.760257	104.325649	56.5272261	105.243796	105.683697	105.596069	106.022826	104.836348	105.676720	105.668524	106.024608	110.324283	109.720369	109.616688	108.420435	108.712671	109.469083	104.930164	104.520830	103.606221	108.077096	108.150702	109.348805	109.292817	108.538507	111.854312
	7	5	8	98	4	2	9		4	9	2	1	5	7	5	4	9	6	9	4	1	3	8	2	2	4		6	7	3	5	9
Si	5.65409141	5.63810536	5.66293537	5.5624499	5.65821614	5.70763980	5.79669841	5.74998819	5.62866536	5.57781095	5.56409673	5.64897843	5.65260829	5.60312466	5.51805162	5.62793344	5.61034789	5.57902840	5.51046158	5.56079193	5.51996085	5.61232584	5.57373248	5.49521136	5.51278869	5.44692414	5.48547051	5.92537520	5.88894951	5.99990409	5.96102510	5.98853975
	8		5	02		2	3		6			5	9	5	7	7	6	1	9	4	2	8	3	7	4	7	2	7	8	4	1	8
Al iv	2.34590858	2.36189464	2.33706462	2.4375500	2.34178386	2.29236019	2.20330158	2.25001181	2.37133463	2.42218905	2.43590327	2.35102156	2.34739170	2.39687533	2.48194837	2.37206655	2.38965210	2.42097159	2.48953841	2.43920806	2.48003914	2.38767415	2.42626751	2.50478863	2.48721130	2.55307585	2.51452948	2.07462479	2.11105048	2.00009590	2.03897489	2.01146024
	2		5	98		8	7		4			5	1	5	3	3	4	9	1	6	8	2	7	3	6	3	8	3	2	6	9	2
Al vi	2.29488405	2.30112386	2.28557429	2.4240399	2.30164352	2.20255597	2.28002298	2.3550797	2.39994663	2.39624563	2.46030910	2.40981903	2.42691795	2.44381066	2.45623046	2.46253930	2.47443677	2.57059514	2.59069824	2.65952572	2.70425396	2.67965589	2.64661254	2.67917215	2.56202072	2.60809066	2.57513260	2.09330379	2.12667101	2.15565564	2.09957765	2.09387075
	7	9	5	27	3	9	4		8	1	3	8	4	8	1	4	9	2	6	1			4	3		7	1	8		7	1	
Ti	0	0	0	0	0	0	0	0	0	0	0	0	0	0	0	0	0	0	0	0	0	0	0	0	0	0	0	0	0	0	0	0
Cr	0	0	0	0	0	0	0	0	0	0	0	0	0	0	0	0	0	0	0	0	0	0	0	0	0	0	0	0	0	0	0	0
Fe3+	0	0	0	0	0	0	0.04275732	0.05848413	0.01590008	0	0.01354586	0.03267795	0.04419251	0.02606466	0	0.05024539	0.04707266	0.08296651	0.05604409	0.12203702	0.12409069	0.16178301	0.12208340	0.09651210	0.04145827	0.03045466	0.03357192	0.01044270	0.00872675	0.08697798	0.03389058	0.04610132
							5		8		7	8	5	5			8	6	9	5	7	4	7	6	8	6	3	7		5	5	6
Fe2+	4.58744964	4.76411316	4.56913707	4.5315201	4.52258133	4.52475110	4.50030072	4.60277	5.20057498	5.27230892	5.32268653	5.27993845	5.16701961	5.28138163	5.32342152	5.15526096	5.16392941	5.63262019	6.14833408	5.85264316	5.72744099	5.58948254	5.58963336	5.47434467	6.10701594	5.91949446	5.97995598	3.31255752	3.23088809	3.16877658	3.16332584	3.23743168
	4	3	4	28	9	1	6	49	1		1	2		2	5	1	8	9	7		7	9	8	2	1	5	6	2	7	1	1	4
Mn	0	0	0	0	0	0	0	0	0	0	0	0	0	0	0	0	0	0	0	0	0	0	0	0	0	0	0	0	0	0	0	0
Mg	5.14845165	4.97146082	5.17633278	5.0526624	5.19999609	5.32656463	5.12231429	4.90909931	4.36335431	4.34720825	4.18625916	4.23599401	4.30566202	4.21562261	4.23604762	4.26810197	4.25476547	3.60861596	3.13394795	3.21128374	3.28729344	3.36415531	3.48704524	3.62792455	3.23697833	3.40343568	3.36882884	6.57030095	6.62253108	6.47700286	6.65971616	6.56340982
	5	6	4	67	9		1		3	2	8	2	2	3	5		2		8	5	4	2	5		4	3	1	1	1		5	
Ni	0	0	0	0	0	0	0	0	0	0	0	0	0	0	0	0	0	0	0	0	0	0	0	0	0	0	0	0	0	0	0	0
Zn	0	0	0	0	0	0	0	0	0	0	0	0	0	0	0	0	0	0	0	0	0	0	0	0	0	0	0	0	0	0	0	0
Ca	0	0	0	0	0	0	0	0	0	0	0	0	0	0	0	0	0	0	0	0	0	0	0	0	0	0	0	0	0	0	0	0
Na	0	0	0	0	0	0	0	0	0	0	0	0	0	0	0	0	0	0	0	0	0	0	0	0	0	0	0	0	0	0	0	0
K	0	0	0	0	0	0	0	0	0	0	0	0	0	0	0	0	0	0	0	0	0	0	0	0	0	0	0	0	0	0	0	0
Ba	0	0	0	0	0	0	0	0	0	0	0	0	0	0	0	0	0	0	0	0	0	0	0	0	0	0	0	0	0	0	0	0
Rb	0	0	0	0	0	0	0	0	0	0	0	0	0	0	0	0	0	0	0	0	0	0	0	0	0	0	0	0	0	0	0	0

F	0	0	0	0	0	0	0	0	0	0	0	0	0	0	0	0	0	0	0	0	0	0	0	0	0	0	0	0	0	0	0	0
Cl	0	0	0	0	0	0	0	0	0	0	0	0	0	0	0	0	0	0	0	0	0	0	0	0	0	0	0	0	0	0	0	0
OH*	16	16	16	16	16	16	16	16	16	16	16	16	16	16	16	16	16	16	16	16	16	16	16	16	16	16	16	16	16	16	16	16
Total	36.0307853 6	36.0366978 6	36.0310441 5	36.008222 52	36.0242209 6	36.0538717 1	35.9453953 3	35.925438	35.9797760 2	36.0157628	35.9828006 7	35.9584294 6	35.9437921	35.9668795 8	36.0156996 1	35.9361476 3	35.9402043 4	35.8947978 2	35.9290243 9	35.8454896 5	35.8430791	35.7950767 7	35.8453745 6	35.8779534 8	35.9474732 7	35.9614754 8	35.9574893 5	35.9866049 8	35.9888169 4	35.8884130 7	35.9565102 4	35.9408135 8
Oxidized	yes	yes	yes	yes	yes	yes	yes	yes	yes	yes	yes	yes	yes	yes	yes	yes	yes	yes	yes	yes	yes	yes	yes	yes	yes	yes	yes	yes	yes	yes	yes	yes
Fe/Fe+Mg	0.47118900 5	0.48935103	0.46884728 4	0.4728123 74	0.46516279 9	0.45930424 2	0.47003445 8	0.48705167	0.54452692 8	0.54808456 9	0.56038195 1	0.55637586 8	0.54757602 6	0.55732520 1	0.55687417 8	0.54947451 6	0.55051025 2	0.61298396 4	0.66439938 9	0.65041407	0.64029364 9	0.63093801 6	0.62092233 3	0.60560813 2	0.65510684 6	0.63612791	0.64094001 8	0.33588386 4	0.32848985 1	0.33451512 5	0.32436220 9	0.33345710 1
Variety	pyc noc hlor ite	pyc noc hlor ite	pyc noc hlor ite	ripi doli te	pyc noc hlor ite	pyc noc hlor ite	pyc noc hlor ite	pyc noc hlor ite	bru nsvi gite	ripi doli te	ripi doli te	bru nsvi gite	bru nsvi gite	bru nsvi gite	ripi doli te	bru nsvi gite	bru nsvi gite	ripi doli te	ripi doli te	ripi doli te	ripi doli te	bru nsvi gite	ripi doli te	ripi doli te	ripi doli te	ripi doli te	ripi doli te	pyc noc hlor ite	pyc noc hlor ite	pyc noc hlor ite	pyc noc hlor ite	pyc noc hlor ite
Al total	4.64079263 9	4.66301851	4.62263892	4.8615900 24	4.64342738 3	4.49491617 7	4.48332457 1	4.60509151	4.77128127 2	4.81843468	4.89621237 3	4.76084060 3	4.77430965 4	4.84068600 4	4.93817883 4	4.83460585 7	4.86408888 3	4.99156674 2	5.08023665 7	5.09873378 6	5.18429310 8	5.06733004 2	5.07288006 1	5.18396078 7	5.04923202 7	5.16116652	5.08966209	4.16792859 2	4.23772149 2	4.15575155 3	4.13855255	4.10533099 2
Al iv (1)	2.34590858 2	2.36189464	2.33706462 5	2.4375500 98	2.34178386	2.29236019 8	2.20330158 7	2.25001181	2.37133463 4	2.42218905	2.43590327	2.35102156 5	2.34739170 1	2.39687533 5	2.48194837 3	2.37206655 3	2.38965210 4	2.42097159 9	2.48953841 1	2.43920806 6	2.48003914 8	2.38767415 2	2.42626751 7	2.50478863 3	2.48721130 6	2.55307585 3	2.51452948 8	2.07462479 3	2.11105048 2	2.00009590 6	2.03897489 9	2.01146024 2
Al iv (2)	2.34590858 2	2.36189464	2.33706462 5	2.4375500 98	2.34178386	2.29236019 8	2.20330158 7	2.25001181	2.37133463 4	2.42218905	2.43590327	2.35102156 5	2.34739170 1	2.39687533 5	2.48194837 3	2.37206655 3	2.38965210 4	2.42097159 9	2.48953841 1	2.43920806 6	2.48003914 8	2.38767415 2	2.42626751 7	2.50478863 3	2.48721130 6	2.55307585 3	2.51452948 8	2.07462479 3	2.11105048 2	2.00009590 6	2.03897489 9	2.01146024 2
Al vi	2.29488405 7	2.30112386 9	2.28557429 5	2.4240399 27	2.30164352 3	2.20255597 9	2.28002298 4	2.3550797	2.39994663 8	2.39624563 1	2.46030910 3	2.40981903 8	2.42691795 4	2.44381066 8	2.45623046 1	2.46253930 4	2.47443677 9	2.57059514 2	2.59069824 6	2.65952572 1	2.70425396	2.67965589	2.64661254 4	2.67917215 3	2.56202072	2.60809066 7	2.57513260 1	2.09330379 8	2.12667101	2.15565564 7	2.09957765 1	2.09387075
Si	5.65409141 8	5.63810536	5.66293537 5	5.5624499 02	5.65821614	5.70763980 2	5.79669841 3	5.74998819	5.62866536 6	5.57781095	5.56409673	5.64897843 5	5.65260829 9	5.60312466 5	5.51805162 7	5.62793344 7	5.61034789 6	5.57902840 1	5.51046158 9	5.56079193 4	5.51996085 2	5.61232584 8	5.57373248 3	5.49521136 7	5.51278869 4	5.44692414 7	5.48547051 2	5.92537520 7	5.88894951 8	5.99990409 4	5.96102510 1	5.98853975 8
Fe/Fe+Mg	0.47118900 5	0.48935103	0.46884728 4	0.4728123 74	0.46516279 9	0.45930424 2	0.47003445 8	0.48705167	0.54452692 8	0.54808456 9	0.56038195 1	0.55637586 8	0.54757602 6	0.55732520 1	0.55687417 8	0.54947451 6	0.55051025 2	0.61298396 4	0.66439938 9	0.65041407	0.64029364 9	0.63093801 6	0.62092233 3	0.60560813 2	0.65510684 6	0.63612791	0.64094001 8	0.33588386 4	0.32848985 1	0.33451512 5	0.32436220 9	0.33345710 1

Namer	FALSE	FALSE	FALSE	FALSE	FALSE	FALSE	FALSE	FALSE	FALSE	FALSE	FALSE	FALSE	FALSE	FALSE	FALSE	FALSE	FALSE	FALSE	FALSE	FALSE	FALSE	FALSE	FALSE	FALSE	FALSE	FALSE	FALSE	FALSE	FALSE	FALSE	FALSE	FALSE
	FALSE	FALSE	FALSE	FALSE	FALSE	FALSE	FALSE	FALSE	FALSE	FALSE	FALSE	FALSE	FALSE	FALSE	FALSE	FALSE	FALSE	FALSE	FALSE	FALSE	FALSE	FALSE	FALSE	FALSE	FALSE	FALSE	FALSE	FALSE	FALSE	FALSE	FALSE	FALSE
	FALSE	FALSE	FALSE	FALSE	FALSE	FALSE	FALSE	FALSE	FALSE	FALSE	FALSE	FALSE	FALSE	FALSE	FALSE	FALSE	FALSE	FALSE	FALSE	FALSE	FALSE	FALSE	FALSE	FALSE	FALSE	FALSE	FALSE	FALSE	FALSE	FALSE	FALSE	FALSE
	FALSE	FALSE	FALSE	FALSE	FALSE	FALSE	FALSE	FALSE	FALSE	FALSE	FALSE	FALSE	FALSE	FALSE	FALSE	FALSE	FALSE	FALSE	FALSE	FALSE	FALSE	FALSE	FALSE	FALSE	FALSE	FALSE	FALSE	FALSE	FALSE	FALSE	FALSE	FALSE
	FALSE	FALSE	FALSE	FALSE	FALSE	FALSE	FALSE	FALSE	FALSE	FALSE	FALSE	FALSE	FALSE	FALSE	FALSE	FALSE	FALSE	FALSE	FALSE	FALSE	FALSE	FALSE	FALSE	FALSE	FALSE	FALSE	FALSE	FALSE	FALSE	FALSE	FALSE	FALSE
	FALSE	FALSE	FALSE	FALSE	FALSE	FALSE	FALSE	FALSE	FALSE	FALSE	FALSE	FALSE	FALSE	FALSE	FALSE	FALSE	FALSE	FALSE	FALSE	FALSE	FALSE	FALSE	FALSE	FALSE	FALSE	FALSE	FALSE	FALSE	FALSE	FALSE	FALSE	FALSE
	FALSE	FALSE	FALSE	ripidolite	FALSE	FALSE	FALSE	FALSE	FALSE	ripidolite	ripidolite	FALSE	FALSE	FALSE	ripidolite	FALSE	FALSE	ripidolite	ripidolite	ripidolite	ripidolite	FALSE	ripidolite	ripidolite	ripidolite	ripidolite	ripidolite	FALSE	FALSE	FALSE	FALSE	FALSE
	FALSE	FALSE	FALSE	FALSE	FALSE	FALSE	FALSE	FALSE	FALSE	FALSE	FALSE	FALSE	FALSE	FALSE	FALSE	FALSE	FALSE	FALSE	FALSE	FALSE	FALSE	FALSE	FALSE	FALSE	FALSE	FALSE	FALSE	FALSE	FALSE	FALSE	FALSE	FALSE
	pycnochlorite	pycnochlorite	pycnochlorite	FALSE	pycnochlorite	pycnochlorite	pycnochlorite	pycnochlorite	FALSE	FALSE	FALSE	FALSE	FALSE	FALSE	FALSE	FALSE	FALSE	FALSE	FALSE	FALSE	FALSE	FALSE	FALSE	FALSE	FALSE	FALSE	FALSE	pycnochlorite	pycnochlorite	pycnochlorite	pycnochlorite	pycnochlorite
	FALSE	FALSE	FALSE	FALSE	FALSE	FALSE	FALSE	FALSE	brunsvigite	FALSE	FALSE	brunsvigite	brunsvigite	brunsvigite	FALSE	brunsvigite	brunsvigite	FALSE	FALSE	FALSE	FALSE	brunsvigite	FALSE	FALSE	FALSE	FALSE	FALSE	FALSE	FALSE	FALSE	FALSE	FALSE
	FALSE	FALSE	FALSE	FALSE	FALSE	FALSE	FALSE	FALSE	FALSE	FALSE	FALSE	FALSE	FALSE	FALSE	FALSE	FALSE	FALSE	FALSE	FALSE	FALSE	FALSE	FALSE	FALSE	FALSE	FALSE	FALSE	FALSE	FALSE	FALSE	FALSE	FALSE	FALSE
Variety inter	pycnochlorite	pycnochlorite	pycnochlorite	ripidolite	pycnochlorite	pycnochlorite	pycnochlorite	pycnochlorite	brunsvigite	ripidolite	ripidolite	brunsvigite	brunsvigite	brunsvigite	ripidolite	brunsvigite	brunsvigite	ripidolite	ripidolite	ripidolite	ripidolite	brunsvigite	ripidolite	ripidolite	ripidolite	ripidolite	ripidolite	pycnochlorite	pycnochlorite	pycnochlorite	pycnochlorite	pycnochlorite
Variety final	pycnochlorite	pycnochlorite	pycnochlorite	ripidolite	pycnochlorite	pycnochlorite	pycnochlorite	pycnochlorite	brunsvigite	ripidolite	ripidolite	brunsvigite	brunsvigite	brunsvigite	ripidolite	brunsvigite	brunsvigite	ripidolite	ripidolite	ripidolite	ripidolite	brunsvigite	ripidolite	ripidolite	ripidolite	ripidolite	ripidolite	pycnochlorite	pycnochlorite	pycnochlorite	pycnochlorite	pycnochlorite
anion props. (E), raw anions																																
Si	0.939923448	0.932933932	0.954235314	0.932933932	0.939923448	0.961224829	0.968547179	0.95423531	0.498585455	0.918622067	0.918622067	0.932933932	0.939923448	0.918622067	0.911299717	0.932933932	0.932933932	0.954235314	0.925611583	0.939923448	0.925611583	0.946912964	0.946912964	0.897320686	0.88300882	0.868696955	0.911299717	1.053752704	1.061075054	1.082376435	1.06806457	1.103677817
Ti	0	0	0	0	0	0	0	0	0	0	0	0	0	0	0	0	0	0	0	0	0	0	0	0	0	0	0	0	0	0	0	0

Al	0.57816790 9	0.57816790 9	0.58375833 7	0.6114162 42	0.57816790 9	0.56698705 4	0.56139662 6	0.57257748	0.31688897 6	0.59493919 2	0.60612004 7	0.58934876 4	0.59493919 2	0.59493919 2	0.61141624 2	0.60052961 9	0.60612004 7	0.63936838	0.63936838	0.64495880 7	0.65054923 5	0.63936838	0.64495880 7	0.63377795 2	0.60612004 7	0.61700666 9	0.63377795 2	0.55580619 9	0.57257748 1	0.56139662 6	0.55580619 9	0.56698705 4
Cr	0	0	0	0	0	0	0	0	0	0	0	0	0	0	0	0	0	0	0	0	0	0	0	0	0	0	0	0	0	0	0	0	0
Fe3+	0	0	0	0	0	0	0	0	0	0	0	0	0	0	0	0	0	0	0	0	0	0	0	0	0	0	0	0	0	0	0	0	0
Fe2+	0.37954071	0.39206680 6	0.38315936	0.3795407 1	0.37425191 4	0.37787056 4	0.37954071	0.38677801	0.23103688 2	0.43326374 4	0.44050104 4	0.43869171 9	0.43326374 4	0.43507306 9	0.43869171 9	0.43145441 9	0.43326374 4	0.48879610 3	0.52108559 5	0.50494084 9	0.49060542 8	0.48517745 3	0.48517745 3	0.45483646 5	0.49241475 3	0.47446068 2	0.49951287 4	0.29547668 8	0.29185803 8	0.29366736 3	0.28643006 3	0.30257480 9
Mn	0	0	0	0	0	0	0	0	0	0	0	0	0	0	0	0	0	0	0	0	0	0	0	0	0	0	0	0	0	0	0	0	0
Mg	0.42793351 5	0.41131232 9	0.43612006 9	0.4237161 99	0.43190275 4	0.44852393 9	0.42793351 5	0.40734309	0.19325229 5	0.35797568 8	0.34557181 8	0.34978913 4	0.35797568 8	0.34557181 8	0.34978913 4	0.35375837 3	0.35375837 3	0.30860828 6	0.26321012 2	0.27139667 6	0.27561399 2	0.28380054 6	0.29620441 6	0.29620441 6	0.25924088 3	0.27139667 6	0.27983130 7	0.58422227 7	0.59662614 7	0.58422227 7	0.59662614 7	0.60481270 2
Ni	0	0	0	0	0	0	0	0	0	0	0	0	0	0	0	0	0	0	0	0	0	0	0	0	0	0	0	0	0	0	0	0	0
Zn	0	0	0	0	0	0	0	0	0	0	0	0	0	0	0	0	0	0	0	0	0	0	0	0	0	0	0	0	0	0	0	0	0
Ca	0	0	0	0	0	0	0	0	0	0	0	0	0	0	0	0	0	0	0	0	0	0	0	0	0	0	0	0	0	0	0	0	0
Na	0	0	0	0	0	0	0	0	0	0	0	0	0	0	0	0	0	0	0	0	0	0	0	0	0	0	0	0	0	0	0	0	0
K	0	0	0	0	0	0	0	0	0	0	0	0	0	0	0	0	0	0	0	0	0	0	0	0	0	0	0	0	0	0	0	0	0
Ba	0	0	0	0	0	0	0	0	0	0	0	0	0	0	0	0	0	0	0	0	0	0	0	0	0	0	0	0	0	0	0	0	0
Rb	0	0	0	0	0	0	0	0	0	0	0	0	0	0	0	0	0	0	0	0	0	0	0	0	0	0	0	0	0	0	0	0	0
F	0	0	0	0	0	0	0	0	0	0	0	0	0	0	0	0	0	0	0	0	0	0	0	0	0	0	0	0	0	0	0	0	0
Cl	0	0	0	0	0	0	0	0	0	0	0	0	0	0	0	0	0	0	0	0	0	0	0	0	0	0	0	0	0	0	0	0	0
Total	2.32556558 2	2.31448097 7	2.35727308	2.3476070 83	2.32424602 5	2.35460638 6	2.33741803	2.32093 39	1.23976360 8	2.30480069 1	2.31081497 6	2.31076355	2.32610207 2	2.29420614 6	2.31119681 2	2.31867634 3	2.32607609 6	2.39100808 2	2.34927567 9	2.36121978	2.34238023 7	2.35525934 2	2.37325364	2.28213951 8	2.24078450 3	2.23156098 2	2.32442185 1	2.48925786 8	2.52213672	2.52166270 1	2.50692697 8	2.57805238 1
F,Cl corr	2.32556558 2	2.31448097 7	2.35727308	2.3476070 83	2.32424602 5	2.35460638 6	2.33741803	2.32093 39	1.23976360 8	2.30480069 1	2.31081497 6	2.31076355	2.32610207 2	2.29420614 6	2.31119681 2	2.31867634 3	2.32607609 6	2.39100808 2	2.34927567 9	2.36121978	2.34238023 7	2.35525934 2	2.37325364	2.28213951 8	2.24078450 3	2.23156098 2	2.32442185 1	2.48925786 8	2.52213672	2.52166270 1	2.50692697 8	2.57805238 1
no. of O	12.0400818 7	12.0977447 1	11.8781316 6	11.927038 47	12.0469174 5	11.8915841 6	11.9790297	12.0641092	22.5849507 2	12.1485558 9	12.1169372 2	12.1172068 9	12.0373049 5	12.2046573 9	12.1149353 7	12.0758553	12.0374393 8	11.7105417 6	11.9185671 8	11.8582777 6	11.9536527 7	11.8882874 2	11.7981489 7	12.2691885 3	12.4956237 2	12.5472708 3	12.0460061 9	11.2483324 3	11.1016979 3	11.1037848 1	11.1690528 9	10.8609119 9
raw cations																																	
Si	0.46996172 4	0.46646696 6	0.47711765 7	0.4664669 66	0.46996172 4	0.48061241 5	0.48427359	0.47711766	0.24929272 8	0.45931103 3	0.45931103 3	0.46646696 6	0.46996172 4	0.45931103 3	0.45564985 9	0.46646696 6	0.46646696 6	0.47711765 7	0.46280579 1	0.46996172 4	0.46280579 1	0.47345648 2	0.47345648 2	0.44866034 3	0.44150441	0.43434847 7	0.45564985 9	0.52687635 2	0.53053752 7	0.54118821 8	0.53403228 5	0.55183890 8
Ti	0	0	0	0	0	0	0	0	0	0	0	0	0	0	0	0	0	0	0	0	0	0	0	0	0	0	0	0	0	0	0	0	0
Al	0.38544	0.38544	0.38917	0.4076	0.38544	0.37799	0.37426	0.38171832	0.21125	0.39662	0.40408	0.39289	0.39662	0.39662	0.40761	0.40035308	0.40408	0.42624	0.42624	0.42997	0.43369949	0.42624	0.42997	0.42251	0.40408	0.41133778	0.42251	0.37053	0.38171	0.37426	0.37053	0.37799

	5273	5273	2224	10828	5273	1369	4417		9317	6128	0031	9176	6128	6128	0828		0031	5587	5587	2538		5587	2538	8635	0031		8635	7466	8321	4417	7466	1369
Cr	0	0	0	0	0	0	0	0	0	0	0	0	0	0	0	0	0	0	0	0	0	0	0	0	0	0	0	0	0	0	0	0
Fe3+	0	0	0	0	0	0	0	0	0	0	0	0	0	0	0	0	0	0	0	0	0	0	0	0	0	0	0	0	0	0	0	0
Fe2+	0.37954071	0.39206680	0.38315936	0.3795407	0.37425191	0.37787056	0.37954071	0.38677801	0.23103688	0.43326374	0.44050104	0.43869171	0.43326374	0.43507306	0.43869171	0.43145441	0.43326374	0.48879610	0.52108559	0.50494084	0.49060542	0.48517745	0.48517745	0.45483646	0.49241475	0.47446068	0.49951287	0.29547668	0.29185803	0.29366736	0.28643006	0.30257480
Mn	0	0	0	0	0	0	0	0	0	0	0	0	0	0	0	0	0	0	0	0	0	0	0	0	0	0	0	0	0	0	0	0
Mg	0.42793351	0.41131232	0.43612006	0.4237161	0.43190275	0.44852393	0.42793351	0.40734309	0.19325229	0.35797568	0.34557181	0.34978913	0.35797568	0.34557181	0.34978913	0.35375837	0.35375837	0.30860828	0.26321012	0.27139667	0.27561399	0.28380054	0.29620441	0.29620441	0.25924088	0.27139667	0.27983130	0.58422227	0.59662614	0.58422227	0.59662614	0.60481270
Ni	0	0	0	0	0	0	0	0	0	0	0	0	0	0	0	0	0	0	0	0	0	0	0	0	0	0	0	0	0	0	0	0
Zn	0	0	0	0	0	0	0	0	0	0	0	0	0	0	0	0	0	0	0	0	0	0	0	0	0	0	0	0	0	0	0	0
Ca	0	0	0	0	0	0	0	0	0	0	0	0	0	0	0	0	0	0	0	0	0	0	0	0	0	0	0	0	0	0	0	0
Na	0	0	0	0	0	0	0	0	0	0	0	0	0	0	0	0	0	0	0	0	0	0	0	0	0	0	0	0	0	0	0	0
K	0	0	0	0	0	0	0	0	0	0	0	0	0	0	0	0	0	0	0	0	0	0	0	0	0	0	0	0	0	0	0	0
Ba	0	0	0	0	0	0	0	0	0	0	0	0	0	0	0	0	0	0	0	0	0	0	0	0	0	0	0	0	0	0	0	0
Rb	0	0	0	0	0	0	0	0	0	0	0	0	0	0	0	0	0	0	0	0	0	0	0	0	0	0	0	0	0	0	0	0
F	0	0	0	0	0	0	0	0	0	0	0	0	0	0	0	0	0	0	0	0	0	0	0	0	0	0	0	0	0	0	0	0
Cl	0	0	0	0	0	0	0	0	0	0	0	0	0	0	0	0	0	0	0	0	0	0	0	0	0	0	0	0	0	0	0	0
Total	1.66288122	1.65529137	1.68556931	1.6773347	1.66156166	1.68499828	1.66601223	1.65295708	0.88484122	1.64717659	1.64946392	1.64784699	1.65782728	1.63658204	1.65174153	1.65203283	1.65756911	1.70076763	1.67334709	1.67627178	1.66272470	1.66868007	1.68481089	1.62221985	1.59724008	1.59154361	1.65751267	1.77711278	1.80074003	1.79334227	1.78762596	1.83721778
formula based on 36 O																																
Si	5.65837763	5.64319827	5.66726634	5.5635694	5.66159009	5.71524297	5.80112771	5.75599952	5.63026396	5.57996575	5.56544295	5.65227673	5.65707259	5.60573	5.52016858	5.63298758	5.61506782	5.58730624	5.51598191	5.57293665	5.53221972	5.62858673	5.58591010	5.50469833	5.51687298	5.44988797	5.48876101	5.92648035	5.88986736	6.00923751	5.96463483	5.99347381
Ti	0	0	0	0	0	0	0	0	0	0	0	0	0	0	0	0	0	0	0	0	0	0	0	0	0	0	0	0	0	0	0	0
Al	4.64079263	4.66301851	4.62263892	4.8615900	4.64342738	4.49491617	4.48332457	4.60509151	4.77128127	4.81843468	4.89621237	4.76084060	4.77430965	4.84068600	4.93817883	4.83460585	4.86408888	4.99156674	5.08023665	5.09873378	5.18429310	5.06733004	5.07288006	5.18396078	5.04923202	5.16116652	5.08966209	4.16792859	4.23772149	4.15575155	4.13855255	4.10533099
Cr	0	0	0	0	0	0	0	0	0	0	0	0	0	0	0	0	0	0	0	0	0	0	0	0	0	0	0	0	0	0	0	0
Fe3+	0	0	0	0	0	0	0	0	0	0	0	0	0	0	0	0	0	0	0	0	0	0	0	0	0	0	0	0	0	0	0	0
Fe2+	4.56970121	4.74312412	4.55121732	4.5267966	4.50858191	4.49347960	4.54652943	4.66613215	5.21795660	5.26352880	5.52752349	5.31571831	5.21532781	5.30991774	5.31472182	5.21018113	5.21538605	5.72406717	6.21059367	5.98772883	5.86452693	5.76792900	5.72419587	5.58047433	6.15302946	5.95318667	6.01713517	3.32362000	3.24011977	3.26081	3.19915251	3.28623836
Mn	0	0	0	0	0	0	0	0	0	0	0	0	0	0	0	0	0	0	0	0	0	0	0	0	0	0	0	0	0	0	0	0

Mg	5.15235455 8	4.97595155 9	5.18029160 5	5.0536794 12	5.20309682 1	5.33366017 3	5.12622828 7	4.91423154	4.36459355 3	4.34888765 6	4.18727203	4.23846730 6	4.30906252 8	4.21758564 8	4.23767275 4	4.27193491 7	4.25834496 6	3.61397021 9	3.13708751 6	3.21829716 4	3.29459395 3	3.37390245 7	3.49466382 4	3.63418782	3.23937653	3.40528759 2	3.37084966 1	6.57152638 9	6.62356326 3	6.48707844 9	6.66374899 3	6.56881752
Ni	0	0	0	0	0	0	0	0	0	0	0	0	0	0	0	0	0	0	0	0	0	0	0	0	0	0	0	0	0	0	0	0	0
Zn	0	0	0	0	0	0	0	0	0	0	0	0	0	0	0	0	0	0	0	0	0	0	0	0	0	0	0	0	0	0	0	0	0
Ca	0	0	0	0	0	0	0	0	0	0	0	0	0	0	0	0	0	0	0	0	0	0	0	0	0	0	0	0	0	0	0	0	0
Na	0	0	0	0	0	0	0	0	0	0	0	0	0	0	0	0	0	0	0	0	0	0	0	0	0	0	0	0	0	0	0	0	0
K	0	0	0	0	0	0	0	0	0	0	0	0	0	0	0	0	0	0	0	0	0	0	0	0	0	0	0	0	0	0	0	0	0
Ba	0	0	0	0	0	0	0	0	0	0	0	0	0	0	0	0	0	0	0	0	0	0	0	0	0	0	0	0	0	0	0	0	0
Rb	0	0	0	0	0	0	0	0	0	0	0	0	0	0	0	0	0	0	0	0	0	0	0	0	0	0	0	0	0	0	0	0	0
F	0	0	0	0	0	0	0	0	0	0	0	0	0	0	0	0	0	0	0	0	0	0	0	0	0	0	0	0	0	0	0	0	0
Cl	0	0	0	0	0	0	0	0	0	0	0	0	0	0	0	0	0	0	0	0	0	0	0	0	0	0	0	0	0	0	0	0	0
Total	20.0212260 5	20.0252924 7	20.0214141 9	20.005635 54	20.0166962 1	20.0372989 3	19.9572 1	19.9414547	19.9840954	20.0108169	19.9864508 6	19.9673029 6	19.9557725 8	19.9739232	20.0107 42	19.9497094 9	19.9528877 3	19.9169103 8	19.9438997 6	19.8776964 5	19.8756337 2	19.8377482 4	19.8776498 6	19.9033212 8	19.9585110 1	19.9695287 6	19.9664079 4	19.9895553 5	19.9912718 9	19.9128867 1	19.9660888 9	19.9538606 9
Fe3+	-0.02122604 8	-0.02529247 1 0	-0.02141419 4 0	-0.0056355 36 0	-0.01669621 2 0	-0.03729893 5 0	0.04278999 7 0.04278999 7	0.05854528 0.05854528	0.01590460 4 0.01590460 4	-0.01081690 1 0	0.01354914 5 0.01354914 5	0.03269703 7 0.03269703 7	0.04422741 7 0.04422741 7	0.02607680 2 0.02607680 2	-0.01074199 6 0	0.05029051 2 0.05029051 2	0.04711227 0.04711227	0.08308961 7 0.08308961 7	0.05610024 3 0.05610024 3	0.12230355 3 0.12230355 3	0.12436628 1 0.12436628 1	0.16225175 7 0.16225175 7	0.12235013 8 0.12235013 8	0.09667872 5 0.09667872 5	0.04148899 4 0.04148899 4	0.03047123 7 0.03047123 7	0.03359206 1 0.03359206 1	0.01044465 4 0.01044465 4	0.00872811 0.00872811	0.08711328 7 0.08711328 7	0.03391110 8 0.03391110 8	0.04613930 9 0.04613930 9
Fe3+ = 0 if Fe3+ < 0																																	
Fe2+ = total	4.59092726 6	4.76841659 8	4.57263151 7	4.5324321 83	4.52527812 4	4.53077854 3	4.50373943 7	4.60758687	5.20205 2	5.27434570 7	5.32397435	5.28302128	5.17110039 4	5.28384094 5	5.32546381 7	5.15989061 7	5.16827378 3	5.64097756	6.15449342 7	5.86542528 6	5.74016065	5.60567725 2	5.60184573 2	5.48379561 2	6.11154047 5	5.92271543 5	5.98354311 1	3.31317535 3	3.23139166 1	3.17370591 2	3.16524141	3.24009905 6
Fe2+ - Fe3+																																	
Fe3+ = total	0	0	0	0	0	0	0.04278999 7	0.05854528	0.01590460 4	0	0.01354914 5	0.03269703 7	0.04422741 7	0.02607680 2	0	0.05029051 2	0.04711227	0.08308961 7	0.05610024 3	0.12230355 3	0.12436628 1	0.16225175 7	0.12235013 8	0.09667872 5	0.04148899 4	0.03047123 7	0.03359206 1	0.01044465 4	0.00872811	0.08711328 7	0.03391110 8	0.04613930 9
Fe2+ if Fe3+ > total																																	

Fe2+																																	
Fe2+ = 0 if Fe3+ > total Fe2+	4.590927266	4.768416598	4.572631517	4.532432183	4.525278124	4.530778543	4.503737937	4.607587687	5.202052	5.274345707	5.323974357	5.283021 28	5.171100394	5.283844945	5.325463817	5.159890617	5.168273783	5.640970756	6.154493427	5.864205426	5.740160 65	5.605677252	5.601847232	5.483795612	6.111547045	5.922715435	5.983543111	3.313175353	3.231391661	3.173705912	3.165241 41	3.240099056
Intermediate 36 O																																	
Si	11.3167552 7	11.2863965 5	11.3345326 9	11.127138 9	11.3231801 9	11.4304859 5	11.6022554 2	11.5119 99	11.2605279 3	11.1599315 2	11.1308859 2	11.3045534 7	11.3141451 8	11.2114676	11.0403371 7	11.2659751 7	11.2301356 6	11.1746124 9	11.0319638 3	11.1458733 2	11.0644394 5	11.2571734 7	11.1718202 1	11.0093966 6	11.0337459 6	10.8997759 5	10.9775220 3	11.8529607 2	11.7797347 3	12.0184750 2	11.9292696 7	11.9869476 3
Ti	0	0	0	0	0	0	0	0	0	0	0	0	0	0	0	0	0	0	0	0	0	0	0	0	0	0	0	0	0	0	0	0	0
Al	6.96118895 8	6.99452776 4	6.93395838	7.2923850 37	6.96514107 4	6.74237426 6	6.72498685 6	6.90763727	7.15692190 9	7.22765202	7.34431856	7.14126090 5	7.16146448 2	7.26102900 6	7.40726825 1	7.25190878 5	7.29613332 4	7.48735011 2	7.62035498 6	7.64810068	7.77643966 2	7.60099506 3	7.60932009 2	7.77594118	7.57384804	7.74174978 1	7.63449313 4	6.25189288 8	6.35658223 8	6.23362733	6.20782882 5	6.15799648 8
Cr	0	0	0	0	0	0	0	0	0	0	0	0	0	0	0	0	0	0	0	0	0	0	0	0	0	0	0	0	0	0	0	0	0
Fe3+	0	0	0	0	0	0	0.06418499 5	0.08781792	0.02385690 5	0	0.02032371 7	0.04904555 6	0.06634112 5	0.03911520 3	0	0.07543576 9	0.07066840 5	0.12463442 5	0.08415036 4	0.18345532 9	0.18654942 2	0.24337763 5	0.18352520 6	0.14501808 7	0.06223349 1	0.04570685 6	0.05038809 2	0.01566698 1	0.01309216 5	0.13066993 1	0.05086666 1	0.06920896 4
Fe2+	4.590927266	4.768416598	4.572631517	4.5324321 83	4.525278124	4.530778543	4.503737943 7	4.607587687	5.202052	5.274345707	5.323974357	5.283021 28	5.171100394	5.283844945	5.325463817	5.159890617	5.168273783	5.640970756	6.154493427	5.864205426	5.740160 65	5.605677252	5.601847232	5.483795612	6.111547045	5.922715435	5.983543111	3.313175353	3.231391661	3.173705912	3.165241 41	3.240099056
Mn	0	0	0	0	0	0	0	0	0	0	0	0	0	0	0	0	0	0	0	0	0	0	0	0	0	0	0	0	0	0	0	0	0
Mg	5.15235455 8	4.97595155 9	5.18029160 5	5.0536794 12	5.20309682 1	5.33366017 3	5.12622828 7	4.91423154	4.36459355 3	4.34888765 6	4.18727203	4.23846730 6	4.30906252 8	4.21758564 8	4.23767275 4	4.27193491 7	4.25834496 6	3.61397021 9	3.13708751 6	3.21829716 4	3.29459395 3	3.37390245 7	3.49466382 4	3.63418782	3.23937653	3.40528759 2	3.37084966 1	6.57152638 9	6.62356326 3	6.48707844 9	6.66374899 3	6.56881752
Ni	0	0	0	0	0	0	0	0	0	0	0	0	0	0	0	0	0	0	0	0	0	0	0	0	0	0	0	0	0	0	0	0	0
Zn	0	0	0	0	0	0	0	0	0	0	0	0	0	0	0	0	0	0	0	0	0	0	0	0	0	0	0	0	0	0	0	0	0
Ca	0	0	0	0	0	0	0	0	0	0	0	0	0	0	0	0	0	0	0	0	0	0	0	0	0	0	0	0	0	0	0	0	0
Na	0	0	0	0	0	0	0	0	0	0	0	0	0	0	0	0	0	0	0	0	0	0	0	0	0	0	0	0	0	0	0	0	0
K	0	0	0	0	0	0	0	0	0	0	0	0	0	0	0	0	0	0	0	0	0	0	0	0	0	0	0	0	0	0	0	0	0
Ba	0	0	0	0	0	0	0	0	0	0	0	0	0	0	0	0	0	0	0	0	0	0	0	0	0	0	0	0	0	0	0	0	0
Rb	0	0	0	0	0	0	0	0	0	0	0	0	0	0	0	0	0	0	0	0	0	0	0	0	0	0	0	0	0	0	0	0	0
F	0	0	0	0	0	0	0	0	0	0	0	0	0	0	0	0	0	0	0	0	0	0	0	0	0	0	0	0	0	0	0	0	0
Cl	0	0	0	0	0	0	0	0	0	0	0	0	0	0	0	0	0	0	0	0	0	0	0	0	0	0	0	0	0	0	0	0	0

Total	28.0212260 5	28.0252924 7	28.0214141 9	28.005635 54	28.0166962 1	28.0372989 3	28.0213 95	28.0292726	28.0079523	28.0108169	28.0067745 7	28.0163485 2	28.0221137 1	28.0130384	28.0107 42	28.0251452 6	28.0235561 4	28.0415448 1	28.0280501 2	28.0611517 8	28.0621831 4	28.0811258 8	28.0611750 7	28.0483393 6	28.0207445	28.0152356 2	28.0167960 3	28.0052223 3	28.0043640 6	28.0435566 4	28.0169555 5	28.0230696 5
F factor	0.99924250 1	0.99909751 3	0.99923579 2	0.9997987 71	0.99940406 2	0.99866966 7	0.99923647 6	0.99895564	0.99971607	0.99961383 1	0.99975811	0.99941646 5	0.99921084 8	0.99953456	0.99961650 4	0.99910276 1	0.99915941 7	0.99851845 5	0.99899921 3	0.99782076 7	0.99778409 5	0.99711101 8	0.99781993 9	0.99827657	0.99925967 4	0.99945616 7	0.99940050 1	0.99981352 3	0.99984416 5	0.99844682 2	0.99939481 1	0.99917676 2
Formula based on 36 oxygens inc. Fe2/Fe3																																	
Si	5.65409141 8	5.63810536	5.66293537 5	5.5624499 02	5.65821614	5.70763980 2	5.79669841 3	5.74998819	5.62866536 6	5.57781095	5.56409673	5.64897843 5	5.65260829 9	5.60312466 5	5.51805162 7	5.62793344 7	5.61034789 6	5.57902840 1	5.51046158 9	5.56079193 4	5.51996085 2	5.61232584 8	5.57373248 3	5.49521136 7	5.51278869 4	5.44692414 7	5.48547051 2	5.92537520 7	5.88894951 8	5.99990409 4	5.96102510 1	5.98853975 8
Ti	0	0	0	0	0	0	0	0	0	0	0	0	0	0	0	0	0	0	0	0	0	0	0	0	0	0	0	0	0	0	0	0	0
Al	4.63727724 3	4.65881019 5	4.61910626 2	4.8606117 33	4.64066018 8	4.48893644 3	4.47990144 6	4.60028214	4.76992656 2	4.81657395 2	4.89502802 6	4.75806248 6	4.77054199 8	4.83843295 3	4.93628506 4	4.83026805 9	4.86000021	4.98417151 1	5.07515242	5.08762246	5.17280520 5	5.05269061 4	5.06182087 4	5.17502659 1	5.04549394 7	5.15835970 6	5.08661084 4	4.16715136 9	4.23706110 7	4.14929693	4.13604794 3	4.10195132 8
Cr	0	0	0	0	0	0	0	0	0	0	0	0	0	0	0	0	0	0	0	0	0	0	0	0	0	0	0	0	0	0	0	0	0
Fe3+	0	0	0	0	0	0	0.04275732 5	0.05848413	0.01590008 8	0	0.01354586 7	0.03267795 8	0.04419251 5	0.02606466 5	0	0.05024539	0.04707266 8	0.08296651 6	0.05604409 9	0.12203702 5	0.12409069 7	0.16178301 4	0.12208340 7	0.09651210 6	0.04145827 8	0.03045466 6	0.03357192 3	0.01044270 7	0.00872675	0.08697798 5	0.03389058 5	0.04610132 6
Fe2+	4.58744964 4	4.76411316 3	4.56913707 4	4.5315201 28	4.52258133 9	4.52475110 1	4.50030072 6	4.60277 49	5.20057498 1	5.27230892	5.32268653 1	5.27993845 2	5.16701961	5.28138163 2	5.32342152 5	5.15526096 1	5.16392941 8	5.63262019 9	6.14833408 7	5.85264316	5.72744099 7	5.58948254 9	5.58963336 8	5.47434467 2	6.10701594 1	5.91949446 5	5.97995598 6	3.31255752 2	3.23088809 7	3.16877658 1	3.16332584 1	3.23743168 4
Mn	0	0	0	0	0	0	0	0	0	0	0	0	0	0	0	0	0	0	0	0	0	0	0	0	0	0	0	0	0	0	0	0	0
Mg	5.14845165 5	4.97146082 6	5.17633278 4	5.0526624 67	5.19999609 9	5.32656463	5.12231429 1	4.90909931	4.36335431 3	4.34720825 2	4.18625916 8	4.23599401 2	4.30566202 2	4.21562261 3	4.23604762 5	4.26810197	4.25476547 2	3.60861596	3.13394795 8	3.21128374 5	3.28729344 4	3.36415531 2	3.48704524 5	3.62792455	3.23697833 4	3.40343568 3	3.36882884 1	6.57030095 1	6.62253108 1	6.47700286	6.65971616 5	6.56340982
Ni	0	0	0	0	0	0	0	0	0	0	0	0	0	0	0	0	0	0	0	0	0	0	0	0	0	0	0	0	0	0	0	0	0
Zn	0	0	0	0	0	0	0	0	0	0	0	0	0	0	0	0	0	0	0	0	0	0	0	0	0	0	0	0	0	0	0	0	0
Ca	0	0	0	0	0	0	0	0	0	0	0	0	0	0	0	0	0	0	0	0	0	0	0	0	0	0	0	0	0	0	0	0	0
Na	0	0	0	0	0	0	0	0	0	0	0	0	0	0	0	0	0	0	0	0	0	0	0	0	0	0	0	0	0	0	0	0	0
K	0	0	0	0	0	0	0	0	0	0	0	0	0	0	0	0	0	0	0	0	0	0	0	0	0	0	0	0	0	0	0	0	0
Ba	0	0	0	0	0	0	0	0	0	0	0	0	0	0	0	0	0	0	0	0	0	0	0	0	0	0	0	0	0	0	0	0	0
Rb	0	0	0	0	0	0	0	0	0	0	0	0	0	0	0	0	0	0	0	0	0	0	0	0	0	0	0	0	0	0	0	0	0
F	0	0	0	0	0	0	0	0	0	0	0	0	0	0	0	0	0	0	0	0	0	0	0	0	0	0	0	0	0	0	0	0	0
Cl	0	0	0	0	0	0	0	0	0	0	0	0	0	0	0	0	0	0	0	0	0	0	0	0	0	0	0	0	0	0	0	0	0
OH*	16	16	16	16	16	16	16	16	16	16	16	16	16	16	16	16	16	16	16	16	16	16	16	16	16	16	16	16	16	16	16	16	16
Total	36.0272	36.0324	36.0275	36.007	36.0214	36.0478	35.9419722	35.9206287	35.9784	36.0139	35.9816	35.9556	35.9400	35.9646	36.0138	35.9318	35.9361	35.8874	35.9239	35.8343	35.8315912	35.7804	35.8343	35.8690	35.9437	35.9586	35.9544381	35.9858	35.9881	35.8819	35.9540	35.9374

	6996	8954	1149	24423	5377	9198			2131	0207	1632	5134	2444	2653	0584	0983	1566	0259	4015	7832		3734	1538	1929	3519	6867		2776	5655	5845	0563	3392
FeO calc	27.27	28.17	27.53	27.27	26.89	27.15	27.01334639	27.41322 9	16.5494023 3	31.13	31.5696574 2	31.3261201 6	30.8660090 2	31.1064833 4	31.52	30.7007770 3	30.8487926 4	34.6102038 6	37.1018047 8	35.5389556 1	34.5024697 3	33.8793887 2	34.1148952	32.1138365 3	35.1414377 4	33.9155111 9	35.6896357	21.1632835 9	20.9135118 2	20.5363102 5	20.3618514 2	21.4347669 4
Fe2O3 calc	0	0	0	0	0	0	0.28521916 1	0.38748482	0.05622918 5	0	0.08928471 3	0.21545866 7	0.29337317 4	0.17060306 1	0	0.33252649	0.31250574 4	0.56653644 7	0.37583634 9	0.82352263 5	0.83073039 2	1.08975331 4	0.82803496	0.62917746 6	0.26511423 7	0.19390941 9	0.22266484 6	0.07414195 2	0.06277531 4	0.62642842 1	0.24242852 2	0.33920549 8
Cathelineau (1988)	315.7	318.3	314.3	330.5	315.1	307.1	292.8	300.3	319.8	328.0	330.2	316.6	316.0	324.0	337.6	320.0	322.8	327.8	338.9	330.8	337.3	322.5	328.7	341.3	338.5	349.1	342.9	272.1	277.9	260.1	266.3	261.9
Jowett (1991)	320.2	323.3	318.7	334.9	319.4	311.3	297.3	305.3	326.6	334.8	337.4	323.7	322.8	331.0	344.6	326.8	329.6	336.6	349.2	340.7	346.8	331.7	337.6	349.7	348.6	358.5	352.5	272.6	278.2	260.5	266.5	262.4